ITER PHYSICS BASIS

CHAPTER 3

MHD STABILITY, OPERATIONAL LIMITS AND DISRUPTIONS

TABLE OF CONTENTS

3. MHD STABILITY, OPERATIONAL LIMITS AND DISRUPTIONS

MHD stability and the microscopic and macroscopic effects of MHD instability are believed to underlie essentially all aspects of achievable plasma performance in tokamaks, and macroscopic global and local MHD stability considerations underlie the factors that set the principal operational limits for tokamaks — maximum plasma current and maximum plasma pressure (beta) and pressure gradient — and the closely-related operational limits on maximum achievable or usable plasma density. The beta and density limits are two of the three key physics basis considerations — energy confinement is the third — that govern the basic design and plasma performance feasibility of reactor tokamaks. The combination of these three considerations determines the achievable fusion power and neutron wall loading and fusion power gain ($Q = P_{fus}/P_{aux}$).

In contrast, disruptions, which arise from the immediate or eventual consequences of MHD instability, set a second type of operational feasibility constraint for reactor tokamaks — one of the operational lifetime of the disruption-affected components, especially those associated with plasma power and particle exhaust and the maintenance of the primary torus vacuum. Since occurrence of at least a small number of disruptions in any tokamak is inevitable, accommodation of the immediate effects of disruptions is required and it is desirable to minimize of the number of disruptions that do occur. Disruption accommodation and avoidance of unnecessary occurrence of disruption therefore constitute a second set of design and operation requirements for reactor tokamaks.

3.1. INTRODUCTION

This Chapter addresses the basis of macroscopic and localized MHD stability in tokamaks, especially as this basis and its consequences applies to ITER and/or a similar reactor-scale tokamak. The focus is divided between presentation of the bases for MHD stability and consideration of the consequences of instability. Presentation is organized into three major Sections. Section 3.2 deals with the various origins of MHD instability in tokamaks and on the

resulting directly-associated operational limits on current, pressure (beta) and pressure gradient. This Section also addresses the MHD-limit-relaxation phenomena of sawteeth and ELMs (Edge Localized Modes) —two instability mechanisms that are predicted to be of major importance for ITER. Section 3.3 deals with on the indirect limit on achievable plasma density that MHD stability and confinement and impurity radiation effects lead to. Section 3.4 addresses the effects of global MHD instability: major disruption and the ensuing related events of vertical instability (VDE), halo current and runaway electron current conversion that disruption produces. In this Section, the principal emphasis is on the consequential effects of disruptions and on means for disruption avoidance and effect amelioration in reactor tokamak operation.

Aspects of plasma control, both magnetic and kinetic, that ultimately center on the achievement of the plasma conditions needed for adequate MHD stability and confinement performance are presented in Chapter 8. The direct turbulence-level effects of MHD instability on plasma transport and global energy and particle confinement are respectively addressed in Chapters 2 and 4.

An introductory presentation of the requirements for ITER plasma performance and operation follows below. This introduction provides a context and set of representative parameters to support the more specialized discussions that follow in Sections 3.2–3.4. Additional details of how energy confinement, power and particle exhaust, heating and current drive and the availability of plasma diagnostic information affect achievement of reactor tokamak performance and operational reliability will be respectively found in Chapters 2, 4, 6, and 7. The overall integration in ITER of MHD-related issues with the issues addressed in the Chapters cited will be found in Chapter 9.

3.1.1. ITER Plasma Performance and Operational Requirements

Table 3-I summarizes the key plasma performance and disruption-effect related parameters for the projected operation of the present (circa 1997) ITER design. These parameters are intended to be representative rather than definitive and are presented here to provide a context for the

discussions of the MHD stability, beta-limit, density-limit and disruption issues that follow. Table 3-I and Fig. 3-1 show the importance in ITER of achieving ELMy H-mode (or equivalent) energy confinement at a plasma current of approximately 21 MA (to in turn be achieved at a plasma edge safety factor $q_{95} \cong 3$, where the notation q_{95} denotes the safety factor evaluated at 95% poloidal magnetic flux) with normalized volume-average betas [$\beta_N = \beta(\%)a(m)B(T)/I(MA)$] in the range of 2-2.5 and densities at or slightly above the empirical Greenwald 'limit' density n_{GW} (10^{20} m^{-3}) = $I(MA)/\pi a^{2(}m)$.

Table 3-I also presents the corresponding disruption-related plasma thermal and magnetic energies, which are the key parameters for the ITER in-vessel and vessel design. As the Table demonstrates, these energies are nearly independent of plasma density. While plasma thermal energy will clearly depend on beta and indirectly on fusion power, in the context of operation of ITER at reactor-like powers (1-1.5 GW), the basis for disruption design is insensitive to density and beta-limit issues. However, disruption frequency may be sensitive to proximity to the beta and/or density 'limits': these frequency issues are addressed in Sections 3.2 and 3.4.

Figure 3-1 shows the effect of beta and density limits on ITER performance (attainable fusion power) in a sustained-ignition mode with ELMy H-mode confinement. Given the assumption of this energy confinement scaling basis, the achievable fusion power depends parametrically on attainable density (quantified relative to the Greenwald density) and normalized confinement factor H_H. There are also operational limit constraints imposed by limits on attainable density ($n/n_{GW} \leq 1.5$), normalized beta ($\beta_N \leq 2.5$) and the separate requirement to maintain sufficient plasma edge power flow to ensure sustainment of H-mode (see Chapter 2). These limits determine an operation domain that is centered upon 1.5 GW fusion power and $H_H = 1$. At $H_H = 1$, the lower and upper limits on obtainable fusion power are respectively ~1.0 GW, set by the H-mode power threshold requirement, and ~1.8 GW, set by the design basis beta limit assumption of $\beta_N \leq 2.5$.

Figure 3-1 also shows that for a given fusion power, the confinement and beta and density limit requirements are interrelated in a parametric sense, and changes in the confinement or density

limit basis affect the corresponding beta requirement, and vice versa [3.1]. At fixed fusion power, confinement and beta requirements are inversely correlated: better/worse confinement requires increased/decreased β_N.

There may also be a plasma collisionality dependence inherent in the neoclassical island MHD aspect of the ITER beta limit (see Section 3.2.3), and hence achievable beta may be sensitive to plasma density and temperature. In addition, proximity to the H-mode density limit (Section 3.3.3) is anticipated to affect achievable confinement (i.e., H_H), so again there are additional dependencies beyond what is explicitly shown in Fig. 3-1. The experimental study of these dependencies and their collective integration in a reactor-regime plasma is one of the key scientific goals for ITER operation and a goal that must await operation of an ITER-class experiment (see Chapter 9). It is in this context of inter-relationship and ultimate interaction that the contents of this Chapter are approached.

Table 3-I. ITER Plasma Parameters for Sustained Ignition, with Equilibrium He Fraction and with Ar Seeding for ≤50 MW to Divertor

Parameter	At Optimum n_e	At Greenwald n_e
Plasma Current (MA)	21	21
Fusion Power (MW)	1500	1200
Volume-average T (keV)	12.8	12.7
Volume-average n_e (10^{20} m^{-3})	0.98	0.85
n_e/n_{GW}	1.15	1.0
He/Be/Ar fractions: n_i/n_e(%)	9/2/0.17	8/2/0.16
Z_{eff}	1.8	1.8
Volume-average β (%)	3.0	2.6
$\beta_N = \beta$(%) a(m) B(T)/I(MA)	2.25	2.0
β_p	0.81	0.72
Radiated power fraction	0.39	0.39
$\tau_{E,trans}$ (s)*	5.8	6.3
W_{th} (GJ)	1.1	1.0
W_{mag} (GJ)	1.1	1.1

* Basis: ITERH-97P(y) ELMy H-mode scaling plus standard ITER performance modeling basis rules, see Chapter 2.

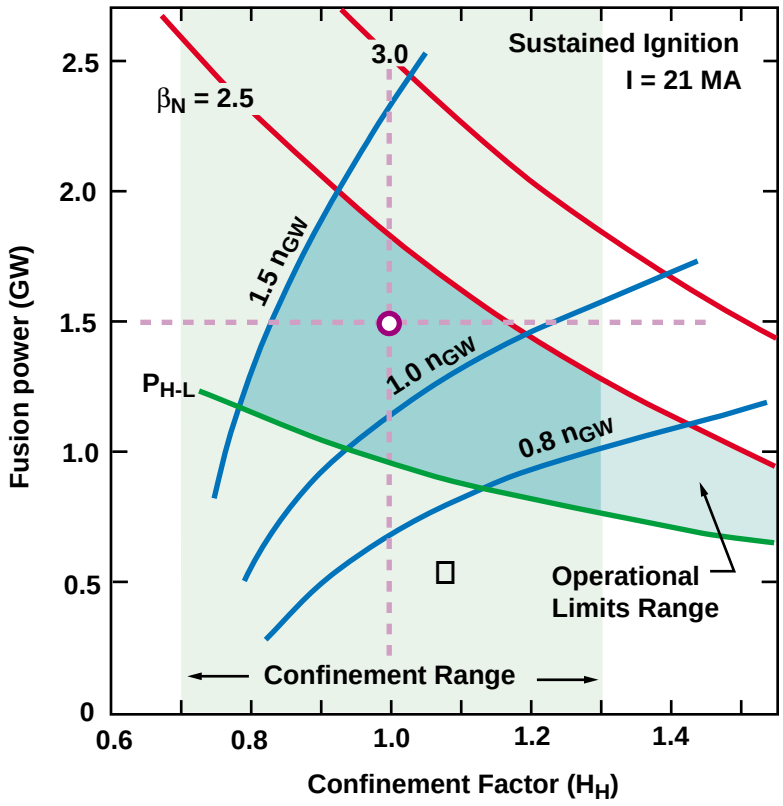

FIG. 3-1. Achievable fusion power for sustained ignition (with equilibrium thermal He) in ITER at I = 21 MA (B = 5.7 T, q_{95} = 3) vs. normalized confinement [H_H, relative to ITERH-97P(y) scaling, see Chapter 2)], for various plasma densities normalized to the Greenwald density. The corresponding operational limits imposed by two possible values of attainable normalized beta (β_N) and the power needed to maintain H-mode (see Chapter 2) are also shown. The overlap of the density, beta and H-mode operational limits and the expected range of confinement (H_H) determine the possible/likely operational domain for sustained ignition. Some of the parameter combinations in this domain exceed the nominal ITER design basis power of 1.5 GW: they are shown to illustrate physics basis parameter sensitivities, independent of hardware power handling capability.

3.1.2. Organization of This Chapter

Figure 3-2 presents the flow of logic and interaction for the MHD stability, operational limit and disruption physics basis issues presented in this Chapter. Ideal MHD stability, whose theoretical basis has been extensively verified in numerous plasma and fusion experiments, sets readily calculable limits on achievable plasma current (essentially set by $q > 2$) and beta in

tokamaks and results in an ideal-MHD-stability beta limit that is $\beta_N \cong 3.5$. This ideal β-limit — commonly described as the 'Troyon limit' — can usually realized in 'short-pulse' tokamak discharges and is comfortably above the requirement of $\beta_N \cong 2.2$ needed in ITER for 1.5 GW fusion power. This aspect of MHD stability and the resulting predictions for the ideal β-limit are discussed in Section 3.2.1.

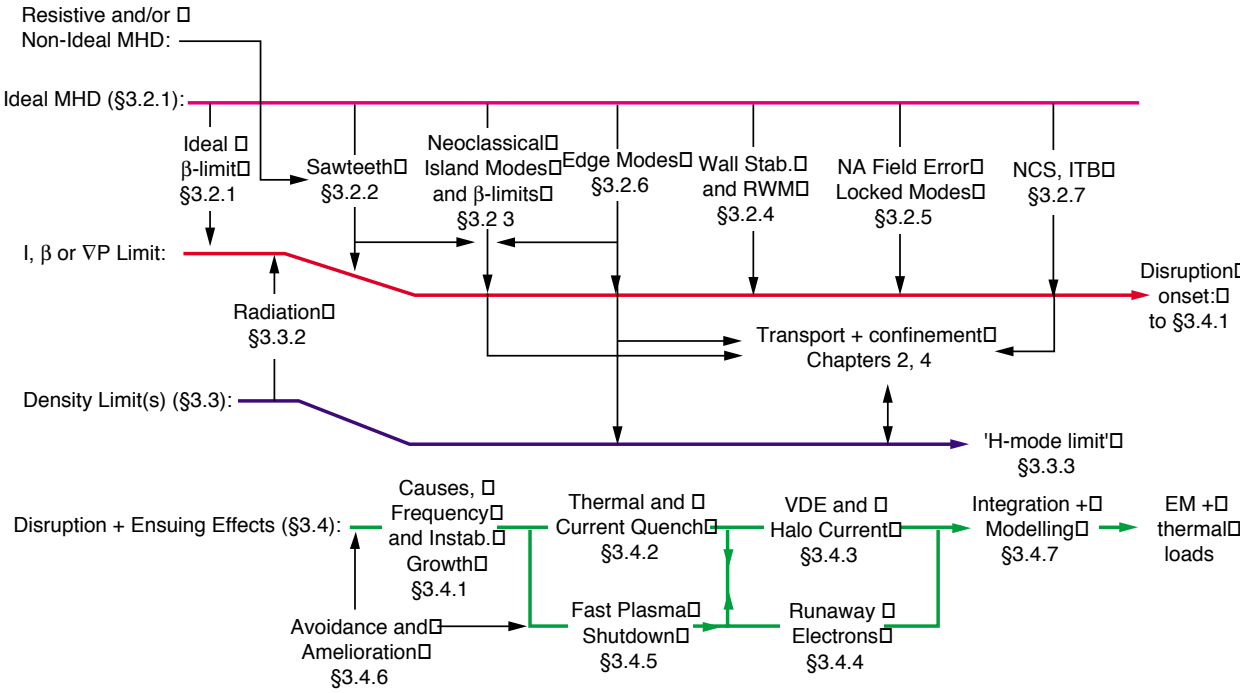

FIG. 3-2. Logic and major cause-effect connections for MHD stability, beta and density limits and disruption physics. The notation §3.x.x indicates the Section of this Chapter where the corresponding physics basis is presented.

However, as indicated in Fig. 3-2, there are additional physics considerations associated with resistive and other non-ideal MHD effects (e.g., fast particle stabilization and the braking of MHD mode rotation by plasma viscosity) that can act to modify ideal MHD behavior and/or reduce achievable stable beta or plasma current in certain phases of the tokamak plasma operation sequence. The most important physics considerations include the effects of sawtooth reconnection (Section 3.2.2), slowly-growing neoclassical island MHD activity driven by the lack of bootstrap current within internal magnetic islands (Section 3.2.3) and the mode-rotation braking effects of

small levels of low-n, low-m field errors that arise from magnet construction and installation tolerances (Section 3.2.5). Of these effects, the limit on β_N set by the onset and uncontrolled growth of neoclassical island modes and the associated propensity of such modes to be triggered by high-amplitude sawtooth and ELM activity raises both the direct concern that such neoclassical modes may limit the achievable β_N in 'long-pulse' reactor tokamaks to values significantly below the Troyon limit, and the indirect concern that uncontrolled sawtooth and ELM activity may unduly excite such modes and hence also lead to disruption. The potentially important inter-relationship among the neoclassical island modes and the resulting non-ideal beta limit, sawteeth and ELMs is indicated schematically in Fig. 3-2.

Also as shown in Fig. 3-2, there are ideal and other MHD stability considerations — especially operation with weak or negative central shear and/or internal transport barriers, described in Section 3.2.7 — which can potentially lead to a mitigation of non-ideal limits of beta and plasma stability and which can also enhance plasma energy confinement relative to 'standard' H-mode confinement. Here the prospects for achievement of ideal or enhanced MHD stability in steady-state reactor tokamaks and in ITER seem however to be critically determined by the need to control the so-called resistive wall mode and thus maintain high beta in a steady-state plasma. This key 'advanced performance' issue of steady-state wall stabilization is addressed in Section 3.2.4.

The effects of MHD instability in the plasma edge are typically manifested as recurring ELMs, and the characteristics (frequency, magnitude and power flow dependence) of ELMs are found to be linked to the plasma edge conditions and the resulting plasma core confinement enhancement in a rather complex manner. The MHD stability aspects of ELMs and their resulting effect on the attainable plasma edge pressure gradient are discussed in Section 3.2.6, with further reference to Chapters 2 and 4 where the confinement and power and particle control aspects of the overall plasma edge physics basis are more extensively presented. In terms of their effect on MHD stability and operational limits, the two most important aspects of ELMs and edge MHD are their effects on the triggering of neoclassical island modes and on the so-called H-mode density limit.

The subject of density limits in reactor tokamaks is addressed in Section 3.3. Here the Section shows that while the well-known Murakami-Hugill and Greenwald empirical density limits provide a reasonably accurate description of the commonly-achieved densities in tokamaks, more detailed study of the causes and manifestation of density limits shows that there are two limits: a radiation/power-balance limit that is affected by plasma boundary power flow (Section 3.3.2), and a so-called H-mode or edge-physics limit in which increasing the plasma core density results in first loss of H-mode confinement quality (marked by a transition from large Type I ELMs to smaller, higher-frequency Type III ELMs) and ultimately a reversion to L-mode and eventual onset of radiative collapse of the plasma edge temperature and disruption (Section 3.3.3). In present edge-fueled (gas-fueled) plasmas, onset of the H-mode density limit typically occurs at densities somewhat below the Greenwald density. However, recent experiments with pellet injection fueling, especially with pellets injected from the high-field-side of the plasma, show that sustained H-mode at greater-than-Greenwald densities and with acceptable H-mode confinement is possible. The means for achieving such high density operation in ITER are focused on this approach.

Figure 3-2 also illustrates that encounters with current, beta and/or density limits lead to onset of disruption. Here, while there is great richness in the non-linear MHD instability physics of the disruption precursor growth and instability onset (global internal reconnection, addressed in Section 3.4.1), from a design basis point of view, it is the resulting characteristics of the thermal and current quench phases of disruption (Section 3.4.2) and the characteristics of the ensuing VDE (vertical displacement event, Section 3.4.3) and runaway electron current conversion phase (Section 3.4.4) that are the most important considerations. In these latter two aspects of the ITER disruption physics basis, there is evidence for an important interaction — disruptions followed by VDEs in present tokamaks are often runaway-free, while disruptions without VDEs can generate high levels of runaways. Differences in the underlying levels of MHD fluctuations seem to be the factor that determines whether or not runaways accumulate. In so far as runaway effects in reactor tokamaks are concerned, there is strong theoretical justification that a new runaway conversion mechanism — the so-called knock-on avalanche — may lead to potentially worrisome levels of

runaway energy deposition in a high-current disruption or loss-of-control VDE or a pellet-injection-initiated fast plasma shutdown (described in Section 3.4.5). The general need for integration of all of the various physics effects involved to arrive at a self-consistent set of predictions of ITER disruptions and ensuing effects is presented in Section 3.4.7. The subject of disruption avoidance and the possibilities for amelioration of disruption effects is addressed in Section 3.4.6.

How plasma control fits into the overall ITER MHD, operational limits and disruption logic is not explicitly presented in Fig. 3-2, but many aspects of plasma control are ultimately closely tied to MHD stability. Here is sufficient to note that the objectives of plasma control are to keep the plasma within all of the various stability and operational limits that apply, and to avoid undue plasma-wall interaction and hence onset of disruption. The operational means how these underlying physics requirements are implemented and certain specialized physics aspects that apply to design and optimization of the plasma operation scenario are addressed in Chapter 8.

3.2. MHD STABILITY

Magnetohydrodynamic (MHD) stability and the microscopic and macroscopic effects of MHD instability are believed to underlie essentially all aspects of the achievable performance in tokamaks and related toroidal magnetic confinement concepts. Global and local MHD stability considerations enter into setting the key operational limits for tokamaks — maximum plasma current and plasma pressure (beta) and edge pressure gradient — and the closely-associated limits on maximum plasma density. The provision of adequate MHD stability and the ability to achieve sufficient current, beta, edge pressure gradient and plasma density are therefore necessary requirements for the design of reactor tokamaks in general and for ITER in particular. As will be presented in this Section, both ideal MHD stability and non-ideal (resistive and/or kinetic) MHD stability enter into setting the various limits that ultimately determine the achievable performance in tokamaks and ITER. Ideal MHD stability and the corresponding limits on plasma current and beta

are addressed below in Section 3.2.1; non-ideal MHD and other more specialized MHD stability considerations are addressed in the balance of Section 3.2.

3.2.1. Ideal MHD: Global Equilibrium and Stability Limits

Ideal MHD stability — which describes the stability of MHD modes in the limit of zero parallel electric field — governs the most fundamental aspects of equilibrium and stability of toroidal magnetic fusion plasmas. As a result of this fundamental importance, the theory of ideal MHD stability [3.2] has been developed to a high degree of computational sophistication and has been successfully applied to explain a wide variety of effects and operation limits observed in tokamaks. The effects described by ideal MHD range from the static equilibrium properties of current-carrying toroidal plasmas to the conditions for onset of the rapidly-growing MHD instabilities that lead to disruption. In these regards, the corresponding static and dynamic effects of ideal MHD are respectively manifested most directly in the control of the axisymmetric equilibrium of the plasma column — effected via the poloidal field (PF) coil system of the tokamak (see Chapter 8) — and in initiation of disruption owing to encroachment of the plasma current or pressure or pressure gradient on the corresponding 'operational limit' for onset of growing MHD instability. The occurrence of prompt disruption whenever the plasma edge safety factor falls below 2 or whenever the plasma beta exceeds the so-called ideal MHD or 'Troyon' beta limit of $\beta(\%) \cong 3.5\, I(MA)/a(m)B(T)$ [3.3] are two well-known examples of effects of ideal MHD instability in tokamaks.

From the viewpoint of plasma behavior, ideal MHD stability applies to situations where the plasma conductivity is so high that any current parallel to the magnetic field can be driven by a vanishingly small electric field. Ideal MHD theory supposes the parallel electric field to be strictly zero. In addition, when applied to tokamaks, the theory typically examines the stability of an initially-axisymmetric plasma column against small perturbations. The evolution of these perturbations is governed by a linearization of the ideal MHD equations about a specified equilibrium, and the resulting predictions of instability onset can usually be correlated in

experiment with the occurrence of either disruption or observable modification of the before-MHD-onset plasma performance. In either of these cases, the subsequent instability development involves a non-linear evolution of the initial mode and often changes in the mode topology and plasma equilibrium state. These non-linear and/or non-ideal aspects of MHD instability and the effects of finite plasma resistivity on ideal MHD behavior are discussed elsewhere in this Chapter (e.g., Sections 3.4.1 and 3.2.2). The principal focus in the presentation in this Section is on the linear-onset aspects of ideal MHD instability and the resulting plasma operation limits.

3.2.1.1. Initial equilibrium

Ideal MHD theory for tokamaks is typically applied to a situation in which the initial plasma equilibrium is axisymmetric — a figure of revolution. It can be then shown that the equilibrium must obey a 2-dimensional nonlinear partial differential equation, called the Grad-Shafranov equation [3.4], for the quantity $\psi = RA_\phi$, where A_ϕ is the toroidal component of the vector potential and R is the major radius. In solving the Grad-Shafranov equation, two free functions of ψ must be supplied to respectively describe the plasma pressure profile and current distribution. In addition, it is also necessary to prescribe boundary conditions which specify the plasma boundary shape and the toroidal magnetic field. Given these inputs, it is then in principle straight-forward to calculate the corresponding plasma equilibrium and magnetic flux surface geometry. For certain pressure and current profile parametrizations and simple boundary shapes, it is possible to obtain an analytic solution; more typically, numerical solutions are used.

In this latter regard, a variety of efficient numerical codes have been developed to solve the Grad-Shafranov equation and compute tokamak plasma equilibria. These 'Grad-Shafranov solvers' can be applied either to generate a series of hypothetical equilibria for subsequent theoretical examinations of MHD stability, or to reconstruct — on the basis of experimental data — the internal flux surface geometry and approximate pressure and current profiles of tokamak plasmas [3.5, 3.6]. Evaluation of the ideal MHD stability of the resulting equilibrium reconstruction of such ‘experimental data’ then allows the stability properties of these plasmas to

be assessed and correlated with the onset of observed MHD activity or disruption. In conducting such comparisons of theory and experiment, it is often important to include allowance for the fact that small variations in the local profile parameterizations can sometimes make the difference between near-marginal stability and onset of instability. Accordingly, consideration of the possible range of profiles that are consistent with the experimental data is often needed. This same need also applies for the use of theoretically-generated equilibria with *ad hoc* profiles: it is important to test the sensitivity of conclusions about stability properties to variations in the exact form of the profile parameterizations. A variant on this procedure is to iteratively optimize the profiles such that the resulting equilibrium is marginally stable to a specified instability throughout the plasma cross-section.

For either use of parameterized equilibria, there are certain ambiguities that effect the choice of the free functions, especially in the vicinity of the magnetic axis and near the separatrix surface. These ambiguities and the non-linearity and ill-posed nature of the free-boundary Grad-Shafranov problem (wherein the plasma boundary is determined by an external separatrix that is separated by some distance from the surface or locations upon which the boundary conditions for ψ are specified) can sometimes result in bifurcation of equilibrium solutions [3.7] and/or variation in the computed poloidal field coil currents for essentially identical reconstructed flux configurations. For separatrix-defined divertor plasmas that are the typical basis for reactor tokamak designs, there are also potential uncertainties related to the precise prescription of the current density profile near/at the separatrix and the resulting exact description of the plasma equilibrium in the vicinity of the separatrix X-point. Consideration of additional experimental data [e.g., j(r) or q(r) or edge temperature, see Chapter 7 and also Section 3.2.7] is sometimes needed in the interpretation of experimental data to resolve such equilibrium-reconstruction-related ambiguities or profile details. With attention to these details and awareness of the potential for bifurcation in highly-shaped plasma configurations (typically more strongly shaped than in ITER and present reactor tokamak proposals), the overall physics basis understanding of static equilibrium prediction and data interpretation can be regarded as being fully satisfactory.

3.2.1.2. Equilibrium perturbations and ideal MHD modes

Within the context of ideal MHD, both axisymmetric ($n = 0$, $m \neq 0$) and non-axisymmetric (n, $m \neq 0$) perturbations to the initial axisymmetric equilibrium are possible. Here n and m are the usual toroidal and poloidal mode numbers. Axisymmetric perturbations are simply neighboring equilibria that are connected — in the context of ideal MHD — by a requirement for the conservation of entropy and safety factor $q(\psi)$. For perturbations that are not inherently stable, the growth rate for axisymmetric perturbations is set by the electrical conductivity of the environment that surrounds the plasma. For typical ITER parameters (with a relatively close-fitting toroidally-continuous shell with ~5 $\mu\Omega$ toroidal resistance), the growth time for the $n = 0$, $m = 1$ 'vertical instability' mode is about 0.5 s and active control of the instability via changes in the PF coil current is required (and provided) to maintain a vertically stable plasma. The active control and stabilization of such slowly-growing axisymmetric perturbations fall in the domain of what is usually described as plasma magnetics control or poloidal field (PF) control, and the principal design issues center around matters of PF power supply current and voltage and the detailed design of the control algorithms (plasma shape controllers) that are used to effect active feedback stabilization of the plasma boundary shape and current magnitude [3.8] (see also Chapter 8).

Axisymmetry-breaking perturbations, which are not affected by PF control, can be classified according to their toroidal mode number n, with the limiting cases $n = 1$ (kink modes) and $n >> 1$ (ballooning modes) being generally the most important because of their propensity to initiate disruption. Moderate-n ideal ballooning modes (with n = 5-10) localized near the plasma edge (called peeling modes, see further discussion below) are also believed to be responsible for the onset of the Edge Localized Modes (ELMs) that are closely associated with H-mode operation. Unlike kink and ballooning instabilities, ELMs are self-limiting and typically do not initiate disruption. In fact, their regular recurrence serves to limit edge pressure gradients (in a time-

average sense) to values that are consistent with ideal MHD stability. Further brief discussion of the MHD aspects of ELMs follows below and additional details appear in Section 3.2.3.

Key mathematical features of all of these ideal MHD modes are that topology is preserved and that infinite current densities can arise in finite times. In other words, a growing perturbation will maintain the nested-toroidal-surfaces topology of the original equilibrium, but often an infinite current sheet can form, leading to non-ideal reconnection and subsequent topology changes. Accordingly, the ultimate development of ideal instability becomes a non-linear and non-ideal process, and mode topology is not always maintained once the non-linear phase begins. But the onset condition, that is, the plasma condition in which the most unstable mode has a finite growth rate, is usually the relevant criterion for defining the pressure or pressure gradient limit.

3.2.1.3. Ideal MHD: wall stabilization effects

The linear operator governing ideal MHD is self-adjoint and hence the growth rate for the most unstable mode can be obtained by minimization of a variational form. However, for kink modes, the results of this type of calculation can be sensitive the assumption made about the location of the perfectly-conducting shell (usually called a wall) which is assumed in the theory to surround the plasma and which provides the boundary condition of zero tangential electric field at the wall surface that ideal MHD theory requires. Accordingly, kink stability calculations typically include an examination of the effects of wall position, which can (in theory) range from at or even inside the plasma surface to very distant: 'wall-at-infinity'. For assessment of kink mode stability, three types of boundary conditions can typically be employed: (1) a fixed, perfectly-conducting wall lying within the separatrix and coinciding with a plasma magnetic surface, (2) a fixed, perfectly-conducting wall outside the separatrix with an intervening vacuum region and a deformable plasma boundary lying inside (or at) the separatrix, and (3) the same as (2) but with the wall at infinity. Boundary conditions (2) and (3) promote greater instability, since a vacuum region can support a parallel electric field and thus is less constrained than a pressureless plasma with $E_{||} = 0$.

Ballooning modes are typically localized in minor radius well within the plasma, and hence their stability is usually insensitive to assumptions about wall position or presence.

From a viewpoint of interpreting experimental data for the onset of kink modes, the most conservative assumption is to place the wall 'at infinity'. This placement is also consistent with the fact that in experiments, while there are conducting structures close to plasma, the resistance of these structures is finite and hence the ultimate stability of kink modes should not be affected. However, there are examples of kink-stable plasma operation at beta values that exceed the 'wall-at-infinity' ideal MHD limit. In these cases, the resulting improvement in stability can be ascribed to the effects of the 'wall stabilization' that arises owing to the presence of a conducting wall close to the plasma. Wall stabilization can be enhanced by the effects of mode rotation: at a sufficiently high angular velocity, such rotation can inhibit growth of the kink instability, at least for the time of plasma operation under consideration. Further discussion of wall stabilization issues and of the importance of the resistive wall mode will be found in Section 3.2.4.

3.2.1.4. Ideal MHD stability limits: theory and experiment

Ideal MHD theory has been shown to adequately predict the upper bound for the beta limit obtainable in present-day tokamak discharges, where it is found empirically that the limit set by onset of ideal MHD instability in situations where wall stabilization and sawtooth instability effects are not significant and where other non-ideal MHD beta-limiting modes are not present or do not grow to large amplitude (see Section 3.2.3) is reasonably well-described by [3.9]

$$\beta_{N,max} \approx 3.5 \qquad (3\text{-}1)$$

where $\beta_N = \beta(\%)/[I(MA)/a(m)B(T)]$ is the so-called 'normalized beta'. Figure 3-3 illustrates typical data that support Eq. (3-1). The upper bound on normalized beta achieved in a broad range of tokamaks with both circular and shaped plasma cross-sections is $3 \leq \beta_N \leq 4$. This general result is commonly referred to as the 'Troyon' or ideal MHD beta limit.

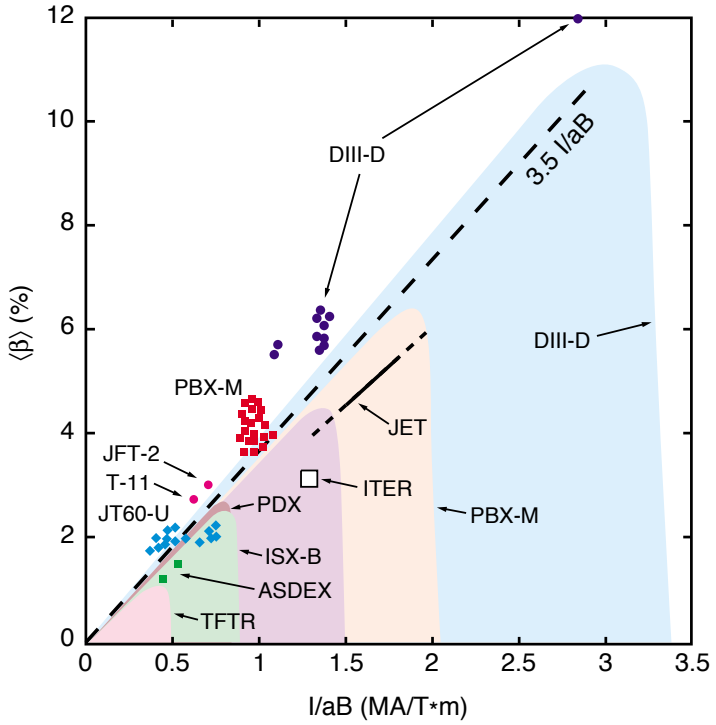

FIG. 3-3. Volume-average β versus I/aB. The shaded regions show the range of beta obtained in the respective experiments. Selected individual high-beta data are also shown. The limit on attainable maximum beta is described by $3 \le \langle\beta\rangle(\%)/[I(MA)/a(M)B(T)] \le 4$ and is consistent with ideal MHD stability. Note that some data appreciably exceed $\beta_N = 3.5$. The basis for this is ascribed either to variations in the plasma current profile (see text below) or to the effect of wall stabilization (Section 3.2.4).

As Fig. 3.3 shows, there can be variation in the data obtained in a given at fixed I/aB and more detailed study shows that the limit on obtainable beta is better described by [3.10]

$$\beta_{N,max} \approx 4\, l_i \qquad (3\text{-}2)$$

where l_i is the plasma internal inductance. The underlying effect here is the degree of radial peaking of the plasma current density profile j(r): l_i is a measure of the degree of profile peaking. Since the internal inductance of typical plasmas with $q(0) \cong 1$ and q_{edge} or q_{95} = 3-4 is l_i = 0.8-1.0,

Eqs. (3-1) and (3-2) give equivalent beta limits for such plasmas. However, for plasmas with higher edge q and/or higher or lower axial q, Eq. (3-2) provides a better description of the ideal MHD beta limit. As Fig. 3-4 demonstrates, Eq. (3-2) provides a relatively good description of the limiting normalized beta obtained in both positive and negative shear plasmas (see section 3.2.7), the latter with q(0) substantially above unity and hence with lower l_i.

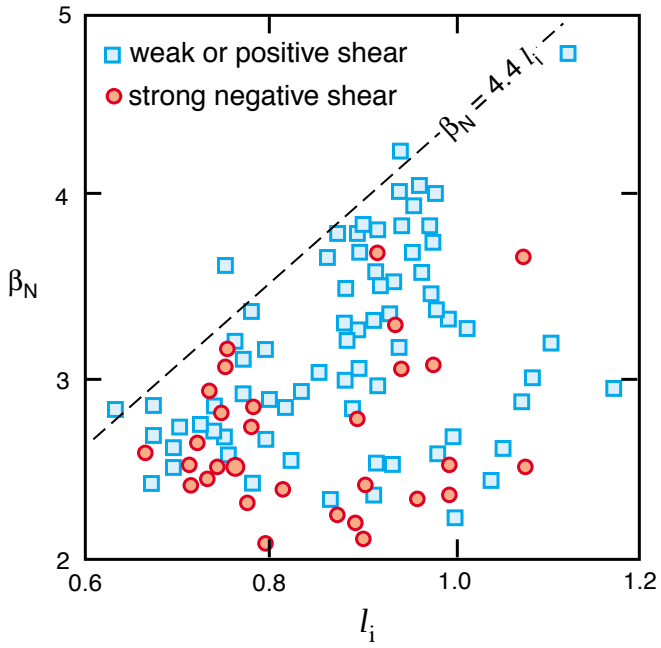

FIG. 3-4. β_N versus internal inductivity l_i in DIII-D. Maximum β_N obtainable in both positive and negative shear plasmas increases with l_i. and is bounded by $\beta_{N,max} \cong 4l_i$.

Ideal beta limits are typically obtained in 'short-pulse' experiments in which heating power is sufficient to produce a continuous rise in beta that is ultimately terminated by onset of rapidly growing MHD instability and subsequent disruption. In such cases, it is often not possible to sustain the highest levels of beta that are obtained at the end of the pulse [3.11]. Figure 3-5 shows a representative comparison of 'short-pulse, high heating power' and 'long-pulse, lower heating power' discharges in otherwise similar plasmas: a disruptive ('hard') ideal-MHD β-limit is reached in the short-pulse discharge, whereas the long-pulse discharge with reduced but slowly-increasing heating power eventually encounters a lower 'non-ideal' soft (confinement degradation) β-limit

owing to onset of a saturated m = 2, n = 1 neoclassical island tearing mode (see Section 3.2.3). The different beta-limits obtained in the two cases are respectively ascribed to ideal and non-ideal MHD effects.

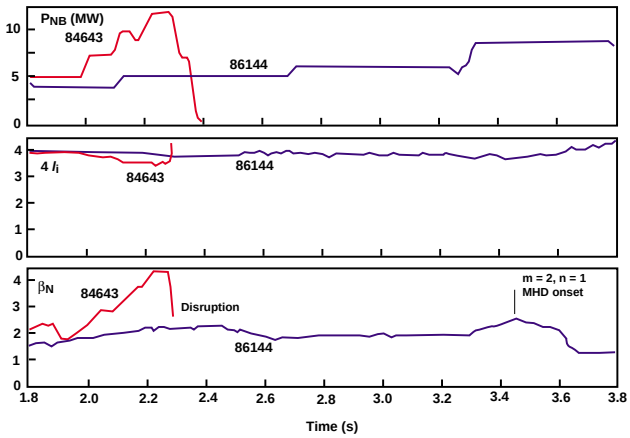

FIG. 3-5. 'Ideal' and 'Non-ideal' beta limits in otherwise similar DIII-D plasmas: the high heating power discharge (84643) reaches a disruptive ideal β-limit at $\beta_N \approx 4l_i \approx 4.4$ after ~0.2 s; the lower-power long-pulse discharge (86144) with otherwise similar parameters has onset of an m = 2, n = 1 'neoclassical tearing mode' and a 'soft' β-limit at $\beta_N \approx 2$ after ~1.5 s (see Section 3.2.3)

The onset of a non-ideal beta limit in long-pulse quasi-stationary discharges is not inevitable: Figure 3-6 shows a long-pulse H-mode plasma obtained in JET where the beta obtained — limited in the example shown by the available heating power — lies only slightly below the ideal MHD limit. At lower toroidal field, similar MHD-stable long-pulse JET discharges with β_N of up to the ideal limit of ~4 have been obtained [3.12]. In these plasmas, the experimentally-measured pressure gradient is found to be near or at the pressure gradient for the onset of ideal ballooning instability (Fig. 3-7). This type of data indicates that these plasmas are well optimized with regard to attainment of maximum beta: the plasma is very close to the onset of ideal MHD ballooning instability over most of the cross-section and the β_N for onset of external kink instability exceeds the β_N for ballooning onset. The attainment of this type of 'optimized' ideal MHD ballooning stability does not always occur automatically (see *e.g.*, the less-than-optimal

ballooning stability characteristics of the high-l_i 'advanced performance' plasmas described in Section 3.2.7).

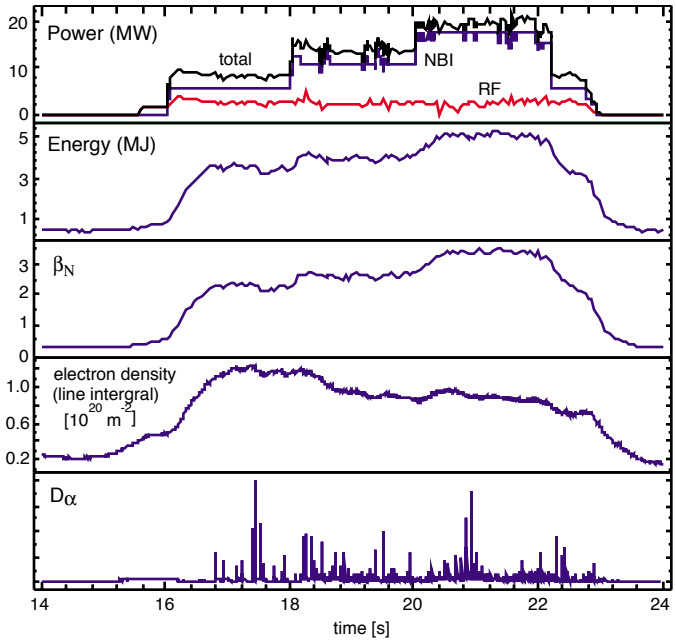

FIG. 3-6. ITER simulation discharge in JET (1.7 T, 1.7 MA, $\beta_{N,max} \approx 3$, limited by available heating power) [3.12]

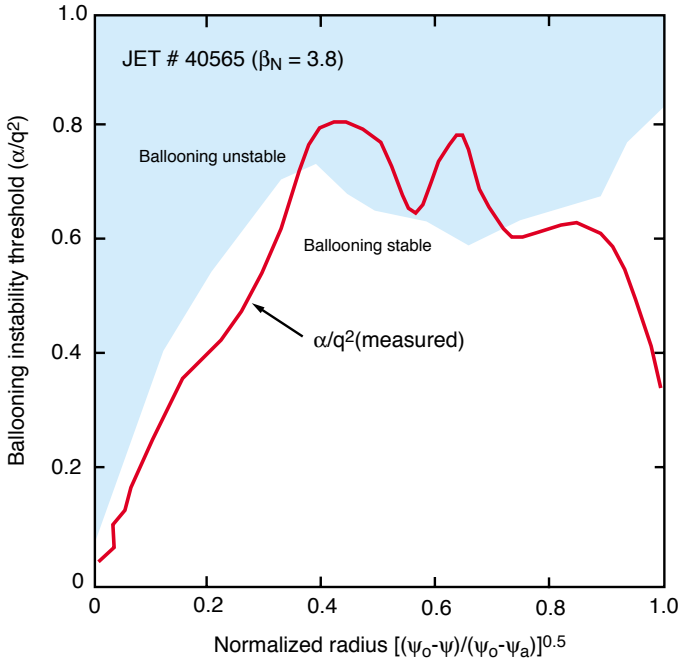

FIG. 3-7. Measured and calculated ideal MHD ballooning onset threshold α/q^2 for a JET 'ITER simulation discharge' with $\beta_N = 3.8$ that operates stably just below the ideal MHD beta limit [3.12]. Here $\alpha = -\nabla p/(B_T^2/2\mu_0 R)$ is the toroidial-field-normalized pressure gradient. The MHD calculation shows that the plasma is close to or at marginal ideal MHD ballooning stability over nearly the whole cross-section. The calculated threshold for external kink instability is $\beta_N \cong 5.2$

Similar long-pulse-stable H-modes with β_N up to at least 3 are also obtained in DIII-D [3.13] and JT-60U [3.14]). The lack of a non-ideal limit in these examples appears to be related to the absence of a large-enough sawtooth amplitude to trigger growth of neoclassical tearing modes. This observation suggests that avoidance of sawteeth or limitation of the magnitude of sawtooth and/or ELM activity may allow reactor tokamak operation up to the ideal beta limit (see Sections 3.2.2 and 3.2.3).

Extrapolation of Experimental Results to ITER. For typical ITER parameters of $q_{95} \approx 3$ and H-mode current density profiles [3.15], the expected internal inductance lies in the range $0.8 \leq l_i \leq 1.0$ and Eq. (3-2) predicts,

$$3 \leq \beta_{N,max}\,(\text{ITER}) \leq 4$$

Given that $\beta_N \approx 3$ already corresponds to attainment in ITER of fusion powers of approximately 3 GW, or more than twice the design basis for the plasma particle and power handling systems, the ideal MHD beta-limit situation for ITER seems quite secure.

ITER Ideal MHD Stability Analyses. The conclusions about ITER ideal MHD limits inferred from extrapolation of experimental results are confirmed by more specific numerical studies of ITER ideal MHD stability [3.15]. Here various ideal MHD stability codes — TORUS, PEST, KINX, GATO and ERATO — were systematically compared against each other and applied for the study of ITER stability for L-mode and H-mode profiles. Agreement among the codes is found to be excellent, with uniform prediction — subject to certain modeling basis caveats about how H-mode profiles are truncated near the plasma edge — of ideal beta limits sufficient for operation of ITER at fusion powers of 2.5 GW or greater. The codes also uniformly predict high-

n ballooning instability rather than low-n kink instability as the more limiting effect, and hence the possibility of a 'soft' (profile modification and confinement degradation) rather than 'hard' (immediately disruptive) manifestation of the ideal beta limit. However, as is often observed in present experiments, onset of a 'soft' ballooning-initiated limit can lead eventually or even promptly to disruption, so either manifestation of ideal MHD instability in ITER may well result in disruption.

The pressure and current density profiles used for the comparison exercise and the various ITER studies were derived either from PRETOR transport code modeling for ITER L- and H-mode plasmas [3.16, 3.17] or from 'experimental profiles' taken from transport analysis and equilibrium inversion of a DIII-D ITER-like H-mode discharge with $\beta_N = 2.1$ [3.18]. The profiles used as the starting basis for the ITER studies corresponded to specific values of β_N: profiles for lower or higher β_N were generated from the original profiles by a multiplying factor for the pressure profiles and maintenance of the current density $\langle \mathbf{j}\cdot\mathbf{B}\rangle\langle \mathbf{B}\cdot\nabla\phi\rangle^{-1}$, where $\langle ... \rangle$ denotes a flux-surface volume average. Current density profiles were also adjusted to keep $q \geq 1.05$ everywhere, leaving the stability assessment complications associated with $q(0) < 1.0$ (see following discussion) for separate consideration. Wall-at-infinity boundary conditions were used for kink modes, and for kink mode stability assessment, the plasma profiles were truncated inside the separatrix at a q-value $q_s \geq 4.0$.

As expected, the predicted beta limits depend somewhat on assumptions about the plasma profiles. For L-mode profiles, where the edge plasma pressure gradient is low, stability up to $\beta_N = 3.4$ for ballooning and up to $\beta_N = 4.4$ for kinks was found [3.16]. For H-mode profiles, assessment of the stability situation is less straight-forward owing to the effect of pressure-gradient driven bootstrap current near the separatrix. This makes the predicted external kink limit sensitive to exactly where the current profile is truncated in the stability assessment. In some of the calculations, the current profile was arbitrarily truncated at 95% flux. However a study of truncation sensitivity with the KINX code, which is capable of extending the profile modeling basis to the separatrix, shows that truncating the profiles just inside $q_s = 4$ yields $\beta_N \approx 2$ as

opposed to an apparently converged value of $\beta_N \approx 4.5$ obtained for truncation at $q_s > 4$ (> ~98% flux) [3.16] (Fig. 3-8). This result shows the importance in kink stability assessments of modeling the current profile out to the separatrix and in incorporating as accurately as possible the profile of the localized bootstrap current associated with the H-mode edge pressure gradient. These considerations make assessment of the kink stability of ITER plasmas somewhat sensitive to detailed prediction of the ITER H-mode edge characteristics, especially the bootstrap current profile near the plasma edge, a matter that is still the subject of on-going experimental and theoretical study and debate with the edge physics community (see Chapter 4).

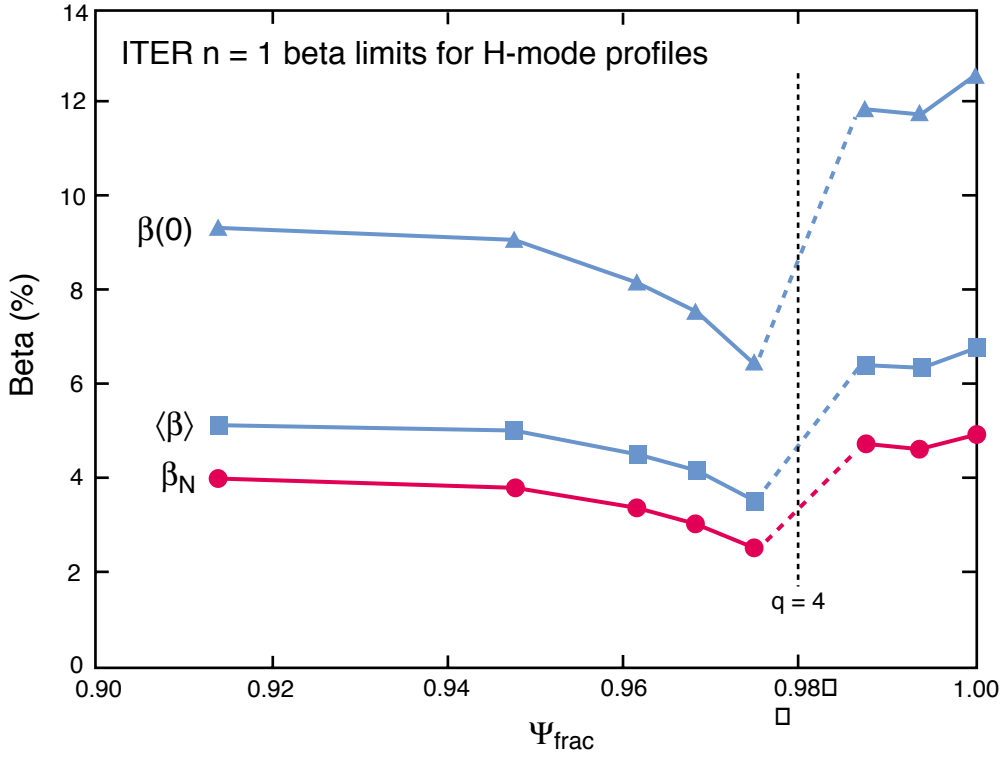

FIG. 3-8. Beta limits for n=1 external kink modes as a function of ψ_{frac}, the poloidal flux fraction associated with truncation for H-mode profiles. Truncation outside of $q \approx 4$ ($\psi_{frac} \approx 0.98$) leads to a converged value of the β limit.

Kink stability predictions for the two basis profiles (PRETOR or DIII-D) also differed somewhat. For KINX calculations based on PRETOR profiles, the stability limit is reached at $\beta_N = 4.9$, whereas GATO results based on the DIII-D profiles found the limit to be $\beta_N = 3.0$.

The KINX calculations further showed almost equivalent limiting β_N values for n = 2 and n = 3 kinks. For ballooning modes, several studies [3.15] showed that the PRETOR profiles were free of ballooning instabilities up to β_N =3.5. The DIII-D profiles, on the other hand, exhibited a very small region in minor radius that was only marginally stable to ballooning at β_N = 2.1 [3.18]. Presumably, minor readjustments of the pressure profile would eliminate this region of potential instability.

The overall conclusion from the various ITER-specific code studies is that the ideal stability limit for ITER plasmas with $q(0) \geq 1.05$ will be $\beta_N \geq 3$. This is sufficient to allow ITER plasma operation with 2.5 GW of fusion power (see e.g., Section 3.1, Fig. 3-1) and a peak neutron wall loading approaching 2 MW/m^2. And as is explained below, these calculations with q(0) = 1.05 are believed to provide an adequate basis for assessing the ideal stability of ITER and other reactor tokamak plasmas with $q(0) \leq 1$.

Ideal MHD Stability for $q(0) \leq 1$. The reference operation mode for ITER is with a sawtoothing ELMy H-mode, so such plasmas will have $q(0) < 1$. Modeling of sawtooth activity (see Section 3.2.2) shows that long-period sawtooth with $q(0) \leq 0.8$ can be expected. All of the ITER-specific code calculations show that when $q(0) < 1$, the onset value of β_N at which the ideal n = 1 kink instability first develops decreases and an additional β_N range of kink instability that lies below the $q(0) \geq 1$ onset β_N threshold value (typically ~4-5) appears. For the PRETOR profiles and q(0) = 0.8, the additional range for kink instability is large: the range $1.0 \leq \beta_N \leq 4.9$ becomes unstable. Similar results were found for the DIII-D profiles: the range $1.0 \leq \beta_N \leq 3.0$ becomes unstable for q(0) = 0.95 ([3.18], see also Fig. 3-9). However, in the course of these studies, it was found that the growth rates and eigenfunctions for the unstable mode in the additional β_N range differ significantly from the growth rates and eigenfunctions for the external kinks that are unstable with $q(0) \geq 1.05$. With $q(0) \geq 1.05$, the growth rate and eigenfunction become insensitive to q(0), and the limiting β_N is interpreted as being a manifestation of the ideal external kink instability. In the additional range of unstable β_N that develops for $q(0) < 0$, growth

rates are lower and the eigenfunction displacements are concentrated in the region $q \leq 1.0$. These modes are interpreted as manifestations of ideal internal kink instability.

Figure 3-8 illustrates these properties. The differences in the mode eigenfunctions with $q(0) > 1$ or $q(0) < 1$ are clearly visible. Beyond these differences in the eigenfunction, analyses with additional kinetic effects incorporated make a profound change in the $q(0) < 1$ growth rates [3.16]. Accordingly, the interpretation is that the additional β_N range associated with $q(0) < 1$ is an element in a more complete, non-ideal-MHD theory of (m,n) = (1,1) modes and sawteeth. Section 3.2.2 discusses these modes and the ITER sawtooth model in detail. For purposes of quantifying the ITER ideal-kink beta limit, the conclusion reached from the ITER ideal MHD studies [3.18] is that β_N-limit corresponding to $q(0) = 1.05$ should be taken as the effective ideal MHD limit. This interpretation is confirmed by DIII-D data, where modification of the q profile to produce $q > 1$ is necessary and sufficient to obtain ideal MHD stability at the experimental β_N.

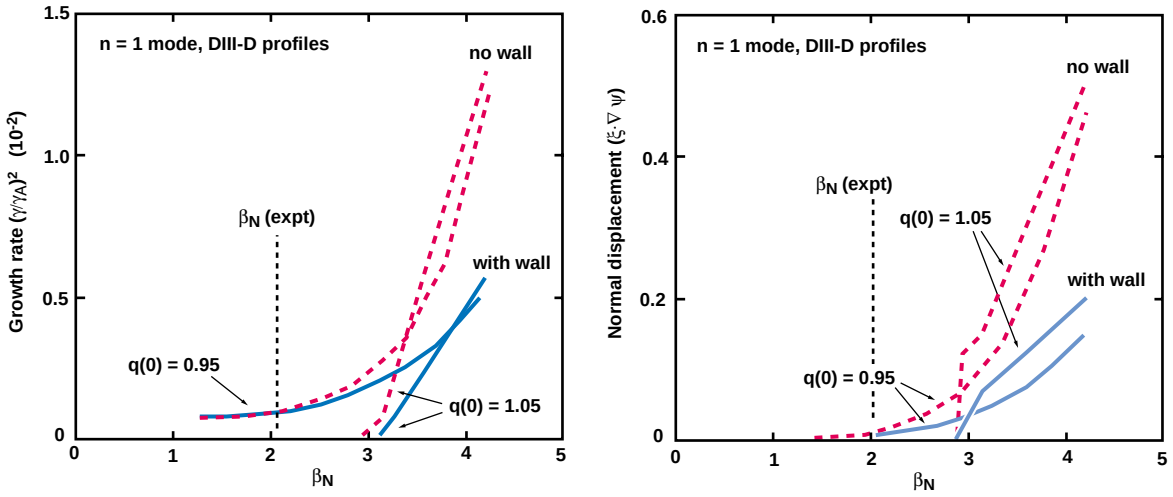

FIG. 3-9. Computed n = 1 mode growth rate and edge normal displacement as a function of increasing β_N, for $q(0) < 1$ and $q(0) > 1$, with and without the presence of a stabilizing conducting wall [3.18]. The pressure profiles and wall position used for this calculation are derived from DIII-D discharge 82205 at 3665 ms. The β_N of the experimental discharge, which was ideal MHD stable, is indicated: other β_N values examined in the calculation were obtained by scaling the experimental profile as explained in the text. The finite growth rate and mode amplitude for $q(0) = 0.95$ and $\beta_N \leq 3$ are ascribed to an internal rather than external mode. The presence of

absence of a wall has no effect on the comparative instability of the $q(0) < 1$ case. The applicable ideal-MHD external kink pressure for instability inferred from this analysis is $\beta_N \approx 3$

As has been noted above, in ITER, the principal effect of sawteeth and $q(0) < 1$ is expected to enter through the role of the sawtooth reconnection acting as a trigger of neoclassical tearing modes, with a consequent reduction in the beta limit. Details of sawtooth characteristics and the expected sawtooth magnitude in ITER are presented in Section 3.2.2. The result presented therein is that owing to the effects of α-particle stabilization of the sawtooth reconnection, relatively long period ($\geq$100 s) sawteeth are expected, and sawtooth triggering of neoclassical tearing mode growth is likely (see Section 3.2.3). Accordingly, it may be necessary to provide localized current drive near the $q = 1$ surface to modify the local magnetic shear so as to destabilize sawtooth reconnection and thus limit sawtooth period and magnitude (see Sections 3.2.2.5 and 3.2.2.6).

3.2.1.5 Other MHD stability considerations

Various other MHD effects and stability considerations that involve both ideal and non-ideal MHD enter into setting limits on plasma current, pressure or pressure gradients. These limits, which tend to apply to localized regions of the plasma (e.g., the plasma edge region just inside the separatrix) and/or to more specific phases of a tokamak discharge (e.g., the H-mode phase or the low-density startup phase) may be more restrictive than the global ideal MHD stability and beta limits addressed above. The specialized considerations that are most directly relevant to ITER are addressed in detail in several following subsections. Here several of the important effects are briefly introduced.

Edge Localized Modes. Edge localized modes (ELMs) are associated with edge pressure gradients near the ballooning limit [3.19] and are thought to involve ideal MHD modes with toroidal mode numbers in the range 5-10. Since the displacement field of the mode eigenfunction is localized to the plasma periphery, these modes have been come to be known as 'peeling modes'.

Experimentally, ELMs do not serve as a major limitation on plasma pressure and current, but take the form of a series of relaxation events which prevent large regions of steep gradients in the H-mode transport barrier (see Chapters 2 and 4) from forming. MHD stability models for peeling modes and ELMs are just now being developed, as are models for the pre-ELM edge equilibrium with self-consistent bootstrap currents. The MHD aspects of ELMs and the role that ideal MHD plays in determining ELM characteristics are discussed in Section 3.2.6

MHD Stability in Reverse Shear Plasmas. The leading candidate for high-bootstrap-fraction, steady-state tokamak operation in ITER is a reverse-shear configuration [3.20] (see also Section 3.2.7). Simultaneous ideal MHD stability with respect to external kink, and ballooning modes and also the so-called 'infernal' mode (a mixed mode localized at intermediate plasma minor radius that combines kink and ballooning characteristics, see Section 3.2.7) requires (in theory) careful optimization of pressure and current density profiles [3.16]. The degree to which adequately stable profiles can be realized and sustained with non-inductive means in reactor or ITER-scale plasmas remains an open R&D issue.

For steady-state reversed-shear scenarios, the ideal MHD external kink mode is a considerable threat owing to the high current densities that such plasmas have near the wall (Section 3.2.4). Reverse shear plasmas have broad current profiles ($l_i \cong 0.5$) and hence, per Eq. (3-2), a low ideal MHD beta limit. Explicit stability modeling and most experimental data to date confirms this (see Section 3.2.7). Without a conducting wall, an ideal limiting β_N of 2.5 is predicted for representative ITER reverse-shear plasmas, as opposed to β_N = 3.5-4 needed for Q = 15 driven burn at 1.5 GW fusion power. The ITER wall would be capable of providing the needed stability were it not for the “resistive wall” mode (Section 3.2.4). The rotation necessary to stabilize this mode is a matter of theoretical controversy and experimental investigation, but it may turn out that MHD feedback control of the resistive wall mode is required. While such control is straightforward in principle, its implementation in ITER could be a significant engineering challenge.

Section 3.2.4 presents a separate discussion the physics of the resistive wall mode, the effects of plasma rotation needed to stabilize it and possible means for feedback stabilization. Such matters are presently the subjects of both experimental and theoretical scrutiny.

Mercier stability of reversed-shear plasmas may also be an issue. In reversed magnetic shear plasmas, the Mercier criterion can be violated from the plasma center to the region with the large pressure gradient due to the internal transport barrier (ITB), when the value of $(q_0\text{-}q_{min})/q_{min}$ is high [3.21]. Here $q_{min} < q_0$ (axial q) is the minimum value of the safety factor. The mechanism of destabilization is that the reversed magnetic shear makes the parallel current term unstable and reduces the magnetic well term. The domain of Mercier instability is characterized by the values of β_p and $(q_0\text{-}q_{min})/q_{min}$. As $(q_0\text{-}q_{min})/q_{min}$ increases, the corresponding value of the stable β_p decreases, so that for strong reverse shear (i.e., for a deeply hollow current profile), the Mercier mode is predicted to be unstable. In reverse-shear-plasmas produced with NBI during current rampup in JT-60U, repetitive pressure-gradient limiting MHD activity localized near the resulting ITB (termed barrier localized modes or BLMs) is observed [3.22]. Analysis shows that the Mercier stability criterion is violated near the ITB and hence Mercier instability may be responsible for the BLMs. If BLMs are to be avoided in future reactor tokamaks and ITER, operation with low $(q_0\text{-}q_{min})/q_{min}$, i.e., with only weak reverse shear appears to be required. This requirement may limit the range of achievable 'advanced performance' plasma operation regimes.

MHD Effects of Non-Axisymmetry. All of the analysis and discussion above is predicated on an assumption of axisymmetry for the initial plasma equilibrium and external tokamak fields. However, there are a number of experimental and theoretical issues that exist with regard to the susceptibility of tokamak discharges to degradation caused by deviations from strict axisymmetry in the structures generating the external, confining magnetic fields. These error fields, which can act to brake and ultimate stop the normal rotation of the saturated internal magnetic islands that are present in most tokamak plasmas, can lead to non-rotating magnetic island structures ('mode locking') which then spontaneously grow to large amplitude, ultimately leading to disruption. The occurrence of this type of disruption (locked mode disruption) is most common during the low-

density 'startup' phase of Ohmic discharges, but mode locking can also affect the feasibility of reliable operation near the ideal or neoclassical-island beta limit and can also play a role in the non-linear mode growth phase that precedes disruption. The mechanism that is responsible for the rapid growth of locked modes is not well understood, but must be non-ideal, as mode topology changes are evident. Section 3.2.5 address the effects and implications locked modes and error field effects for reactor tokamaks and ITER.

3.2.1.6. Summary and application to ITER

The theory of ideal MHD stability has been developed to a high degree of computational sophistication and has been found to accurately describe the circumstances in which external kink and ballooning instabilities develop in tokamak plasmas. Ideal MHD alone constitutes the basis for the experimental observation that kink and/or ballooning instability onset — usually followed by disruption — develops in most cases for $3 \leq \beta_N \leq 4$ (i.e., at the ideal MHD or Troyon beta limit) or for $\beta_N > 4\, l_i$. The only significant exception to the ubiquitous presence of these two equivalent manifestations of the ideal MHD beta limit are in certain cases in present experiments where a combination of sufficient plasma rotation and the presence of a nearby conducting wall make sustained operation above the Troyon limit possible, at least for periods commensurate with present tokamak pulse durations.

Simulation of sustained 'long-pulse' (hardware-limited duration and/or pressure) plasmas with normalized betas approaching the ideal MHD beta limit have been obtained with 'ITER-like' beta-limit demonstration discharges in a number of tokamaks. These ITER demonstration discharges, empirical extrapolation of beta-limit data to ITER conditions and explicit detailed modeling of the MHD stability of candidate ITER plasma profiles all confirm that the limit on attainable plasma pressure in ITER H-mode plasmas is expected to be $\beta_N \geq 3$. Since $\beta_N = 3$ is already sufficient to allow ITER operation with fusion powers of up to 2.5 GW (170% of the design basis fusion power), ideal MHD instability and the corresponding beta limit are not expected to directly restrict ITER operation with respect to attainable fusion power.

Other non-ideal (resistive/neoclassical) aspects of MHD instability may, however, set more restrictive power limits. In addition, the magnitude and period of sawtooth reconnection in $q(0) < 1$ ITER plasmas is expected to have a potentially significant effect on the overall stability and attainable beta in ITER plasmas. While the occurrence of sawtooth reconnection is clearly attributable to internal ideal MHD kink instability, the attainment of ideal MHD beta limits in sawtoothing plasmas that are theoretically expected to be ideal MHD unstable shows that non-ideal resistive and/or kinetic MHD effects must be taken into account to understand the role that sawteeth and internal kink (and also likely Mercier interchange) instabilities play in present and future high-beta plasmas.

3.2.2. Non-Ideal MHD: Sawtooth Oscillations and Central MHD Activity

Non-ideal (resistive and/or kinetic) MHD effects enter in a significant manner in setting further limitations on achievable plasma beta and other core-plasma and edge-plasma operational limits in reactor tokamaks and ITER. This Section and the five following Sections address six of the most important non-ideal MHD considerations: sawtooth oscillations (Section 3.2.2); neoclassical island tearing modes and beta-limits (Section 3.2.3), wall stabilization of external kink modes and resistive wall modes (Section 3.2.4), non-axisymmetric error fields and mode locking effects (Section 3.2.5), ideal and resistive MHD in the plasma edge (Section 3.2.6) and MHD stability of reversed-shear and other 'advanced performance' modes of plasma operation (Section 3.2.7).

3.2.2.1. Sawtooth oscillations

Sawtooth oscillations, the periodic MHD-initiated mixing events that occur in a tokamak plasma in the near-axis region where the safety factor q is less than or equal to unity, are an often-present feature of tokamak plasma operation. The reference plasma operation mode for ITER is

predicated upon the presence of repetitive sawtooth oscillations, and the corresponding near-axis mixing effects of the oscillations are taken into account in making estimates of the plasma energy and particle confinement (see Section 2.5). Figure 3-10 illustrates several of the key observable global features of sawtooth oscillations, including the characteristic sawtooth-like temperature (or soft X-ray emission) waveforms that give the oscillations their common name *(sawteeth)*. The Figure also shows the changes in the plasma temperature and safety factor profiles that occur immediately after the *sawtooth crash* — the internal magnetic reconnection event — that effects the rapid mixing of the axial and peripheral regions of the plasma core that occurs at the end of each sawtooth cycle.

As the waveforms in Fig. 3-10 illustrate, the immediate effect of the mixing is contained within a *sawtooth mixing radius* that lies somewhat outside the nominal q = 1 radius. The exact radial position of the mixing radius depends on the sawtooth parameters (period and pre-crash value of the on-axis q and the degree of internal reconnection, see following discussion) but is typically 25-50% of the minor radius. There is also a *sawtooth inversion radius* located near the radius of the q = 1 flux surface. The phase (sign) of the temperature and safety factor oscillations inverts outside of this radius, showing that the energy and current located inside the q = 1 surface are rapidly transported outwards to the q > 1 portion of the mixing region when the sawtooth crash occurs.

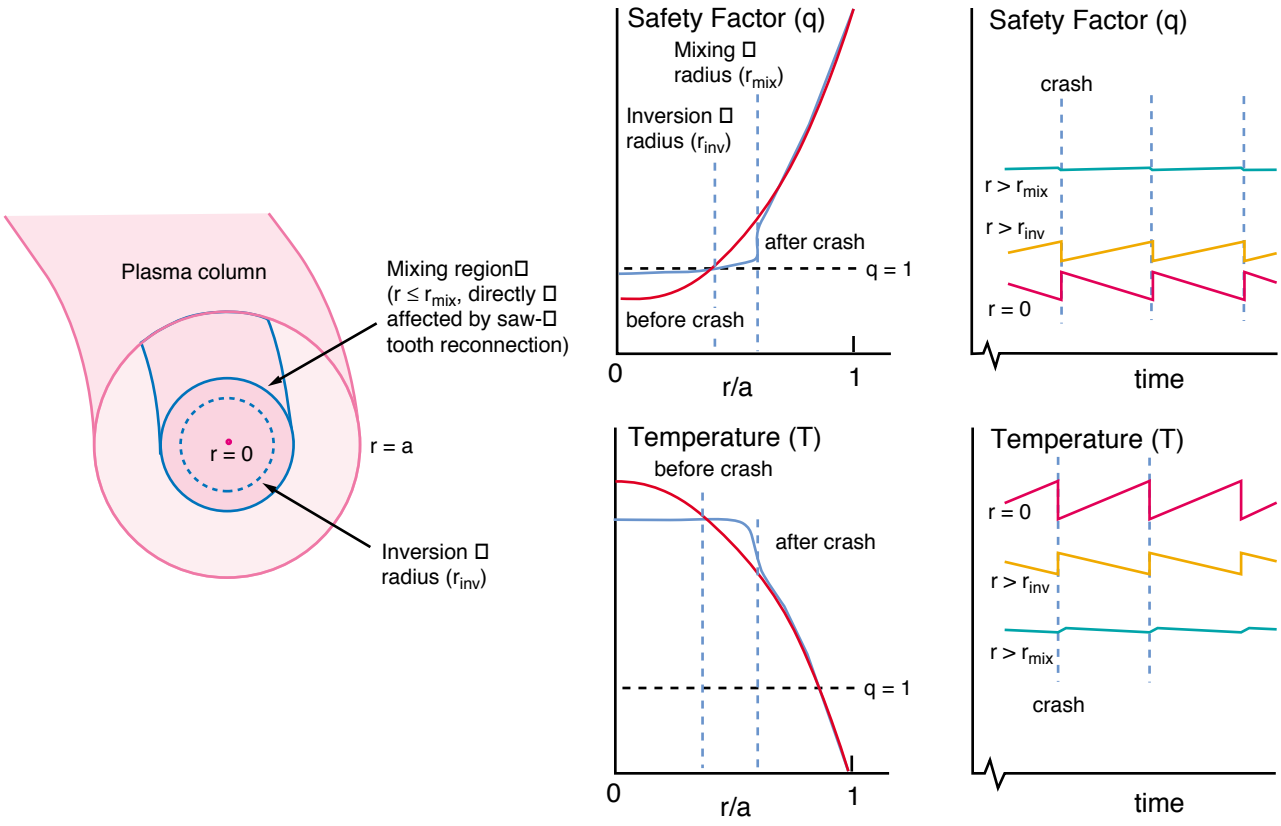

FIG. 3-10. Schematic illustration of sawtooth oscillation features: temperature and safety factor profile waveforms and evolution in an idealized circular cross-section tokamak plasma. See Figures in Section 3.2.2.6 for similar data from simulations of ITER sawteeth.

The mixing effects of sawtooth oscillations are largely confined to a central region of the plasma core, and while the near-axis fluctuations in plasma temperature, local energy content and current density that sawtooth oscillations produce are appreciable, the incremental net transport of energy beyond the sawtooth-affected region is minimal. For this reason, sawtooth oscillations typically have a benign effect on plasma energy confinement (see Section 2.5) and also provide a benefit with respect to particle confinement that comes from their ability to reverse the on-axis accumulation of higher-Z impurities that would otherwise tend to accumulate in the plasma core and cause degradation of energy confinement owing to excessive impurity radiation. Accordingly, selection of plasma operation strategies (initial density, gas injection rate and current rise waveform, see Chapter 8) that result in early onset of sawtoothing is a well-known means for

obtaining optimal performance in Ohmic and auxiliary-heated tokamak plasmas. However, as will be described below, there are exceptions to this preference for early onset of sawtoothing or for the presence of sawteeth at all, and alternate plasma operation strategies wherein sawteeth are either absent or are delayed past the time of optimum plasma performance also exist and may be relevant to ITER.

Sawtooth oscillations are expected to play an important role in ITER, not so much because of their direct impact on confinement (discussed in Section 2.5), but because of the possible couplings between sawteeth and other (non-ideal) MHD activity. For example, recent experimental evidence from DIII-D [3.23] suggests that sawteeth may induce seed islands for the growth of neoclassical tearing modes. Furthermore, sawteeth may couple to locked modes and edge perturbations such as ELMs and external kinks [3.24] and concerns have been raised that these couplings, which can lead to onset of disruption (see Section 3.4.1), may effectively limit the achievable value of beta in ITER. On the other hand, there is considerable evidence that sawteeth do not necessarily have to set restrictive performance- or beta-limits: recent ITER demonstration experiments on JET [3.12] and long-pulse demonstration plasmas in other tokamaks [3.13, 3.14] indicate that sawtooth activity at ITER-relevant dimensionless parameters is either absent or, if present, does not unduly impact plasma performance or lead to disruption. In addition, sawteeth in ITER can potentially be controlled by the current drive and auxiliary heating methods which are to be provided.

The underlying mechanism responsible for the sawtooth crash is MHD instability of an internal kink mode. Within the context of ideal MHD, this instability is predicted to develop whenever the value of the safety factor q in the central plasma region drops below unity. Here it is worth recalling that the theoretical, ideal MHD beta limit, β_{MHD}, assumes optimal profiles where, in particular, $q > 1$ everywhere (see Section 3.2.1). When q drops below unity, a new class of ideal MHD instabilities are predicted to occur for $\beta < \beta_{MHD}$, with internal kinks being one. However, it is clear from experiments that ideal MHD theory alone is not accurate in predicting the threshold for the onset of the sawtooth crash. For instance [3.25], sawtooth crashes can be

suppressed for long periods in discharges where a significant population of high energy ions is present, despite values of $q_0 \equiv q(0) < 1$ and despite values of the thermal plasma poloidal beta, β_p, well in excess of the threshold value for ideal internal kinks [3.26, 3.27]. Consideration of non-ideal MHD effects is necessary to understand sawtooth behavior, particularly the threshold for reconnection and the resulting sawtooth period and amplitude.

In order to address these issues quantitatively, in the following we review briefly present understanding of the ideal and non-ideal MHD aspects of sawtooth phenomenon and summarize the results of a current model for the prediction of the sawtooth period and amplitude in ITER. Possible means of sawtooth control in ITER will also be briefly mentioned.

3.2.2.2. Ideal MHD considerations

The first ideal MHD theoretical investigation of internal kink modes in a *straight* cylindrical tokamak was presented by Shafranov [3.28] in 1970. The conclusion was that ideal internal kinks become unstable in a straight tokamak as soon as q drops below unity, with the instability being an m = 1, n = 1 radial displacement which is nearly constant in the region where $q \leq 1$ and zero outside that region. Here, m and n are the poloidal and toroidal mode numbers, and the internal kink is often referred to as the m = 1 mode. When the experimental observation of sawteeth was first reported [3.29] three years later, internal kinks came to mind as the natural candidate instability causing the rapid temperature collapse (the sawtooth *crash*). However, a nonlinear investigation by Rosenbluth *et al* [3.30] showed that ideal internal kinks would evolve into a kinked neighboring equilibrium with a saturated displacement of amplitude $\xi \sim r/R$ and a singular current sheet on the q = 1 surface. The conclusion here was that while the basic nature of the sawtooth phenomenon could be qualitatively explained within the ideal MHD model, resistive effects would limit the current sheet and therefore need to be taken into account for more detailed understanding.

3.2.2.3. Resistive and non-ideal MHD

In 1975, Bussac *et al* [3.26] found that ideal internal kinks were stable at low-β_p in toroidal equilibria with q below unity, but instability at any β_p and $q \leq 1$ was re-established within the context of the resistive MHD model by Coppi *et al* [3.31]. Against this background, the first consistent picture of the sawtooth phenomenon was formulated by Kadomtsev [3.32]. In essence, the Kadomtsev model assumes that, after the initial growth of a resistive or ideal internal kink mode in the region where q is below unity, the subsequent nonlinear evolution is dominated by the resistive growth of an m = 1 magnetic island on the characteristic time scale $\tau_K \sim (\tau_A \tau_R)^{1/2}$, where $\tau_A = R/v_A$ is the Alfvén time and $\tau_R = 4\pi a^2/\eta c^2$ is the resistive diffusion time. This time scale is typical of a 2-D forced reconnection process as discussed in the pioneering works by Sweet [3.33] and Parker [3.34]. In order to re-establish a stable relaxed state with q above unity everywhere, as was deemed necessary for equilibrium against resistive internal kinks at that time, the m = 1 island has to grow until it fills the entire volume where the pre-crash q is below unity, i.e. until all the helical flux surfaces associated with $q \leq 1$ are reconnected. Hence, the Kadomtsev model is also referred to as the complete reconnection model. Kadomtsev derived a prescription for the relaxed q profile as a function of the pre-crash profile. The *mixing* radius, i.e. the radius of the plasma region involved in the reconnection process, is well defined within the Kadomtsev prescription.

The Kadomtsev model was not borne out of a mathematical solution of the resistive MHD equations, i.e., it was in part conjectural. However, soon after the publication of Kadomtsev's paper, 2-D resistive MHD numerical simulations [3.35, 3.36] basically confirmed Kadomtsev's picture, which emerged as the standard model for the sawtooth phenomenon.

In 1978, Ara *et al* [3.37] investigated the linear theory of m = 1 modes within the context of the two-fluid model, including high temperature effects such as diamagnetic frequency effects. Reference [3.37] gave the first indication of the possibility that resistive internal kinks may become stable at high temperatures even with q below unity. However, possibly because of the success of the Kadomtsev model, this paper went unnoticed for a number of years.

3.2.2.4. Reconnection effects and other considerations

In the 1980s, with the development of new and better plasma diagnostics, a number of experimental findings challenged the Kadomtsev model. The first tomographic reconstruction of the soft-X ray emissivity profile from a sawtoothing plasma [3.38] suggested that the sawtooth crash could occur while the m = 1 magnetic island was still relatively small. Later, tomographic reconstructions of soft-X rays at JET with improved time and space resolution [3.39] were suggestive of a cold bubble penetrating the central plasma region rather then the growth of a large m = 1 island. Measurements of the q profile, on the other hand, indicated that q on axis remained below unity throughout the sawtooth cycle [3.40], with some evidence of the formation of a shoulder of low magnetic shear in the vicinity of the new q = 1 surface after a crash. These findings pointed toward the possibility of partial, as opposed to full, sawtooth reconnection, and raised the question of the existence of stable relaxed equilibria with q on axis below unity. For example, tomographic reconstructions on TFTR are suggestive of partial reconnection initiated by ballooning that develops in a toroidally and poloidally localized region on the bad magnetic curvature side of the plasma [3.41]. This mechanism provides only partial reconnection and is consistent with the finding that q_0 is reported to stay below unity in the same discharges [3.42]. However not all experimental measurements of the q profile find q_0 below unity [3.43]. Thus, the possibility that either partial or full reconnection can occur for different plasma parameters cannot be ruled out.

Another challenge to the Kadomtsev model is represented by measurements of the crash time [3.44], which turns out to be much shorter than Kadomtsev's time, τ_K. A more fundamental problem, raised by Wesson *et al* [3.45], is the absence of any detectable precursor activity in many high temperature plasma discharges. Finally, a wide variety of different sawteeth are observed, ranging from 'compound' [3.44] to 'giant' [3.46] to 'monster' [3.25] sawteeth. The explanation of this variety of sawteeth poses a significant challenge for any theory of the sawtooth phenomenon.

Empirical scaling laws for the sawtooth period and crash time have been attempted: however no scaling law that is able to reproduce the observed variety of sawteeth has been found [3.47].

In 1986, Wesson proposed the quasi-interchange model of the sawtooth crash [3.48], which at first appeared consistent with the observed soft-X ray emissivity profile at JET and with the rapidity of the crash time. However, the quasi-interchange instability requires ultra-flat q profiles with $q \approx 1$ in a wide central region: this requirement is at odds with the actual measurements of q. In addition, the quasi-interchange model fails to provide a prediction for the sawtooth period.

3.2.2.5. More recent understanding and modeling bases

A new theoretical picture of the sawtooth phenomenon is now emerging (see, e.g., the review paper by Migliuolo [3.49]). The cornerstone of this new understanding is the realization of the physical processes that allow stable m = 1 modes in equilibria with $q_0 < 1$. The two-fluid model of the m = 1 instability, first investigated in Ref. [3.37], was fully explored in Refs. [3.50–3.52], which demonstrated the existence of stable equilibria with $q_0 < 1$. Similar results were also obtained in semi-collisional [3.53] and collisionless [3.54, 3.55] models that are more realistic for the high temperature plasmas produced in larger tokamaks. For instance, the collisionless instability threshold appears to be in good agreement with TFTR L-mode and supershot data [3.56] (Fig. 3-11). One of the crucial parameters in these models is the magnetic shear at q = 1, which must exceed a critical threshold value for instability. Thus, a q profile with $q_0 < 1$ and a shoulder of low magnetic shear near the q = 1 surface should be stable according to these models. Conversely, increasing the local magnetic shear around q = 1 (e.g., by localized electron cyclotron current drive) may be a way to trigger the m = 1 instability. This latter factor may be useful in ITER as a sawtooth 'control' mechanism to avoid the occurrence of large-amplitude sawteeth (see below).

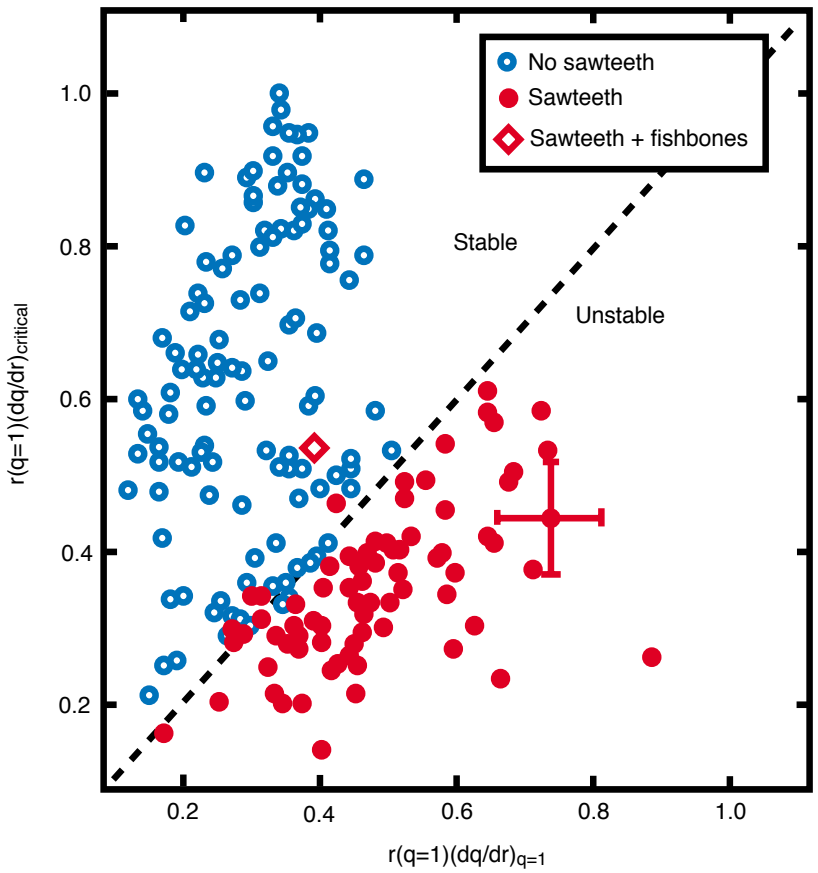

FIG. 3-11. Comparison of predicted critical shear for sawtooth onset with measured shear, both evaluated at the measured q = 1 radius. Data for TFTR L-mode and supershot plasmas, all with q(0) < 1

Another important factor in this emerging picture of the sawtooth phenomenon is the role played by energetic ions. The discovery of sawtooth-free regimes in ICRH-heated JET discharges, to which the somewhat misleading name of 'monster' sawteeth has been given [3.25], is widely believed to be the consequence of fast particle stabilization [3.57]. On the other hand, fast ions can interact resonantly with m = 1 modes, giving rise to so-called 'fishbone oscillation' bursts of MHD activity [3.58] and corresponding increases in fast ion transport. The physics of energetic ions is discussed at length in Chapter 5, and therefore we shall not dwell on this topic in this Section.

The threshold condition for m = 1 modes in relevant regimes and in equilibria with $q_0 < 1$ can be written in the form [3.59] $\delta W = \delta W_{crit}$, where δW is an effective potential energy functional [3.26, 3.27] modified by the (stabilizing) kinetic effects related to the high energy ions [3.57] and to the thermal trapped ions [3.60–3.62], while δW_{crit} is a critical threshold determined by microscopic effects (i.e., non-ideal effects such as resistivity, ion Larmor radius, electron skin depth, diamagnetic frequency, etc.) in a narrow layer around the q = 1 surface, where reconnection of magnetic field lines can occur. Detailed expressions for δW and δW_{crit} can be found in [3.59].

The problem of the rapidity of the sawtooth crash has been partly resolved in recent years. The Kadomtsev time scale for the sawtooth crash is consistent with collisional regimes where the nonlinear reconnection width, $\delta_\eta = (\tau_A/\tau_\eta)^{1/2} r_1$, is wider than the electron inertial skin depth, $d_e = c/\omega_{e.}$, where r_1 is the radius of the q = 1 surface and $\tau_\eta = 4\pi r_1^2/\eta c^2$ is characteristic resistive time scale. In fact, the opposite limit is realized in today's high temperature discharges in large size tokamaks. In this collisionless limit, a better estimate for the sawtooth crash time is [3.63, 3.64] $\tau_{crash} \sim \tau_A r_1/d_e$, which is shorter than τ_K when $\delta_\eta < d_e$. When the ion Larmor radius is larger than the electron skin depth, the theoretical reconnection time can be even shorter [3.54, 3.65–3.67], reaching values comparable with the experimental crash time.

The determination of the relaxed q profile after a sawtooth crash is still an open question. In particular, it is not clear under which circumstances partial rather than full reconnection can occur. Existing 3D toroidal codes [3.68] assume the resistive MHD model and therefore are not capable of reproducing robustly stable relaxed equilibria with $q_0 < 1$, since the existence of these equilibria requires additional physics, as we have seen. Thus these codes always return a relaxed q profile with $q \geq 1$. This partly explains the slowness of progress on this point.

In the absence of conclusive theoretical or experimental evidence on the relaxed state, a phenomenological viewpoint was adopted in Ref. [3.59]. There, it is conjectured that the sawtooth process always starts with the growth of an m = n = 1 magnetic island. However, instead of a *laminar* island growth as in Kadomtsev's model, it is assumed that widespread magnetic turbulence

develops as the island reaches a critical size. Magnetic turbulence may come about because of the coupling of the m=1 mode with the poloidal modulation of the equilibrium [3.69], or possibly because of the secondary instability of modes, such as tearing-parity resistive g-modes [3.70] triggered by the large pressure gradients that form across the separatrix of the quickly growing m=1 island. In this region where chaotic field co-exist with good flux surfaces, the pressure is allowed to nearly flatten up to a mixing radius as observed in all experiments. Based on these premises, a partial reconnection model is proposed in [3.59], which depends on a single free parameter, w_{crit}/r_1, where w_{crit} is a critical island width for the onset of widespread magnetic turbulence. This resulting relaxed q has $q_0 < 1$ (except in the case where $w_{crit}/r_1 \rightarrow 2$, which corresponds to full reconnection) and a shoulder of low shear around q = 1, which ensures stability against m=1 modes.

Using these relaxed q and pressure profiles as the initial condition in a transport code, δW is normally found to increase with time along the sawtooth ramp until the critical threshold value, δW_{crit}, is reached, at which time a crash is imposed and the relaxed state is recomputed. In this way, repetitive sawteeth and a prediction for the sawtooth period can be obtained.

3.2.2.6. ITER sawtooth predictions and control possibilities

The magnetic turbulence model described above has been applied for simulations of ITER sawtooth behavior [3.59] (Fig. 3-12). A sawtooth period ranging between 50 s and 100 s in ignited ITER discharges is obtained. The relatively long sawtooth period predicted for ITER (*c.f.* ~1 s in JET) arises owing to both the larger physical size of ITER and the stabilizing effect of the fast-alpha population present in an ignited or high-Q driven burn plasma. The sawtooth period is longer when Kadomtsev's relaxation is assumed and becomes shorter as the parameter w_{crit}/r_1 of the incomplete reconnection model decreases. In these simulations, the alpha particle and thermal trapped ion effects are found to be important and prevent sawtooth crashes from occurring until the q = 1 radius has reached about 50% of the plasma minor radius (see Fig. 3-12). In this sense, the simulated ITER sawteeth resemble the so-called 'monster sawteeth' (large-amplitude solitary

sawteeth with a large reconnection radius) seen in JET [3.25], and the q profile evolves on the resistive diffusion time. Using this resistive diffusion basis to extrapolate from the monster sawtooth period of a few seconds at JET, one obtains a time scale 0(100 s) for ITER sawteeth. In the absence of the stabilizing effects related to the fusion alpha particles and to the thermal trapped ions, sawtooth crashes are predicted to occur on the pressure peaking time scale, which is 0(1 s) in ITER.

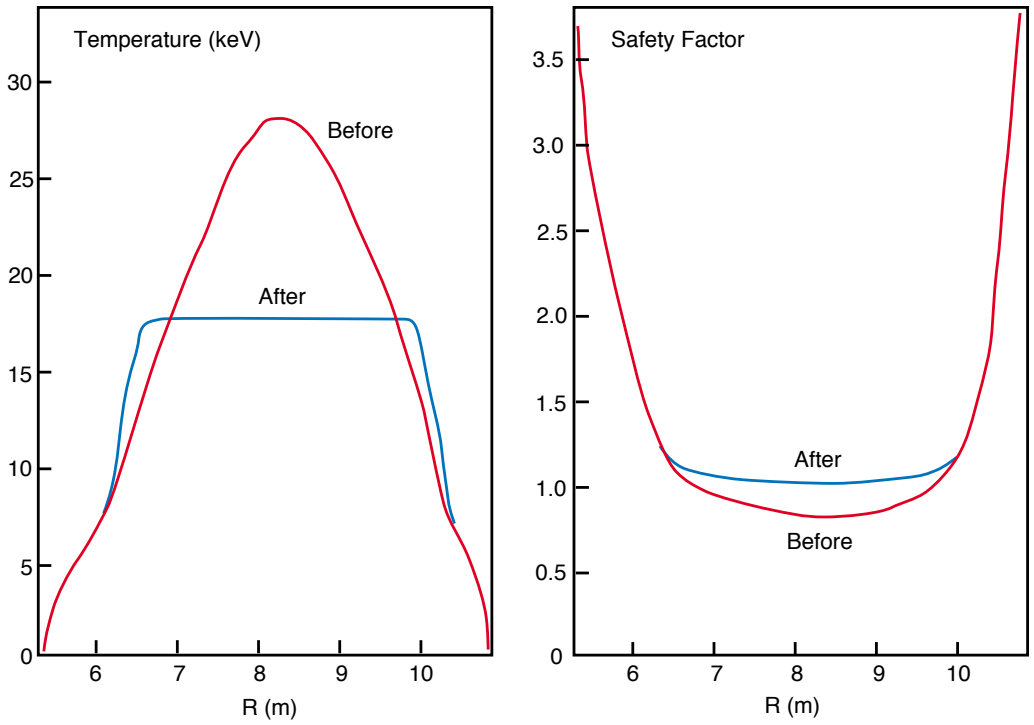

FIG. 3-12. Simulation [3.59] of plasma temperature and safety factor profiles before and after sawtooth reconnection in a 1.5 GW ignited-burn ITER plasma. See Fig. 3-13 for time waveforms for this simulation.

Despite the large mixing radius and dramatic change in the central plasma profiles following reconnection, the simulated global effects of such a sawtooth crash on fusion power, β_p and internal inductance l_i are small (Fig. 3-13) and even such 'monster' sawteeth are anticipated to have negligible effect on plasma magnetic configuration control burn control in ITER (see Chapter 8). However, large sawtooth crashes with a mixing radius exceeding half of the plasma minor radius

are still reason of concern, since, as indicated in the beginning of this Section and as is sometimes seem in present large-size experiments, such crashes can trigger onset of neoclassical modes and/or disruption. Prediction of the precise amplitude threshold for sawtooth triggering neoclassical modes in ITER is still a matter of study and debate (see Section 3.2.2), but avoiding large sawteeth appears to be prudent, and sawtooth-free operation may be needed. In this regard, scenarios in ITER have been found where sawteeth can be avoided for periods long enough to achieve sustained ignition and equilibrium burn, and in addition, sawtooth amplitude/period control by injected rf waves that modify the magnetic shear profile in the vicinity of q = 1 appears to be possible.

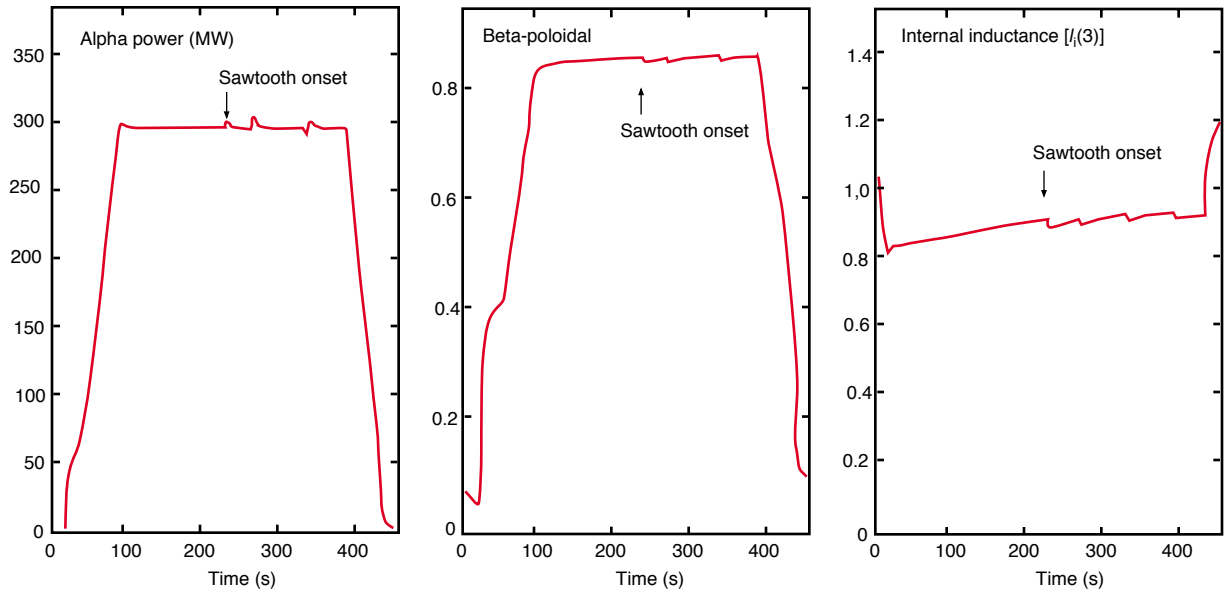

FIG. 3-13. Simulation of ignition and sustained 1.5-GW burn in a 21-MA ITER plasma. The first sawtooth occurs about 200 s after initial heating and a stable 70-s period sawtooth cycle develops by 300 s. This cycle continues indefinitely (the simulation here ends arbitrarily at 400 s). The plasma profiles before and after a sawtooth reconnection are shown in Fig. 3-12. The effect of the reconnection on fusion power, β_p and l_i is barely discernible.

A promising scenario is to delay the onset of sawteeth by applying early heating during the current rampup, in order to (i) increase the plasma electrical conductivity and slow down the current penetration, and (ii) achieve early ignition and exploit alpha particle stabilization before the

onset of the first sawtooth crash. This early-heating scenario was simulated in Ref [3.59], where a sawtooth-free period of about 500 s was obtained. With the application of central current drive, the onset of sawteeth can be delayed for up to 1200 s [3.71].

It may also be possible to control the sawtooth amplitude and period in ITER by applying localized current drive so as to increase the magnetic shear near q = 1. This technique act to trigger low-amplitude short-period sawteeth and has been successfully demonstrated at JET, where minority ion current drive induced by ICRF waves was used [3.72]. In ITER or future reactor tokamaks, similar 'pre-emptive' sawtooth control by ion-cyclotron frequency FWCD or by ECCD should be possible. Here ECCD may ultimately prove to be the most promising control means owing to the high localized current densities that can be achieved and the ability to provide real-time control of the current drive location by changing the launching angle of the injected EC beam [3.73].

Another ideal MHD instability that can occur when q drops below unity is that of localized interchange modes. The threshold condition for these modes is related to the well-known Mercier criterion [3.74], which predicts instability at modest pressure gradients and beta values when q is below unity. Thus, this instability is expected to limit the achievable pressure gradients in the experiments. However, the Mercier stability criterion is often violated with impunity in existing large-size tokamak discharges. In [3.75] it is shown that the same non-ideal physics that explains the improved stability against internal kinks may also account for the absence of localized interchange modes in circumstances when the ideal MHD threshold for these modes is exceeded in experiments.

3.2.3. Non-Ideal MHD: Neoclassical Island Tearing Modes and Beta Limits

The importance of non-ideal MHD effects in determining the ultimate pressure achievable in long-pulse tokamak experiments has become increasingly apparent over the last few years. In particular, the effect of the bootstrap current on tearing mode stability in low-collisionality long-pulse plasmas is now seen to be an important possible limiting factor for the ultimate performance

of reactor tokamaks and ITER. The formation of neoclassical bootstrap-current-driven islands (referred to hereafter as neoclassical islands), with subsequent limitation of achievable plasma pressure or onset of disruption, is the performance-limiting mechanism. The resulting 'soft' (confinement degradation) limit on achievable beta is commonly referred to as the non-ideal or neoclassical-MHD beta limit. When quantified in terms of the normalized beta $\beta_N = \beta(\%)\ a(m)\ I(MA)/B(T)$, the neoclassical (NC) beta limit in an ITER-class reactor and ITER is projected to be $\beta_{N,NC} \approx 2$. For ITER, this beta limit is comparable to what is required for 1.5 GW operation, and hence a non-ideal beta limit may constitute a potential limitation on achievable fusion power in ITER. A non-ideal limit of this magnitude would also restrict neutron wall loadings in future reactor tokamaks based on conventional superconducting technology to relatively modest values (~1 MW/m^2). Understanding the physics of neoclassical island modes and finding means for their avoidance or for limiting their impact on plasma performance are therefore important issues for reactor tokamaks and ITER.

3.2.3.1. Neoclassical islands: observations, theories and issues

Neoclassical islands were first observed on TFTR [3.76]. Subsequently it was observed in many tokamaks that the β-limit at low collisionality (ν*) was determined by low m/n magnetic islands [3.77–3.79] and was often well below the β-limit predicted by ideal MHD stability theory. The MHD modes responsible have since all been identified as neoclassical magnetic islands [3.23, 3.80, 3.81]. Pressure-driven resistive modes have been observed to limit β on JT-60U [3.14]. Recently, the beta-limiting effects of neoclassical islands and details of the island structure have also been observed in JET [3.82] and preliminary MHD analysis of the JT-60U data confirms the neoclassical island origin of the beta-limiting MHD modes [3.83].

The existence of neoclassical islands was anticipated theoretically [3.84, 3.85], but these early theories predicted instability for $\nu^* < 1$ at all rational surfaces and for all values of β_p. In contrast, the experimental data typically show instability only on a few rational surfaces and usually only at moderately high β_p. The observation of a critical island width for instability in

[3.76] has lead to additional theoretical work on other non-ideal effects which tend to stabilize the growth of the neoclassical islands and explain the observed neoclassical mode onset effects. Two effects in particular — the effect of the ion polarization current [3.86, 3.87], and the influence of cross-island transport [3.88] — have been identified that can explain the observed "threshold" island width and the typical need for moderately high β_p before neoclassical modes develop.

The basic mechanism that drives neoclassical islands is simple. If a magnetic island exists, the radial pressure gradient inside that island is absent (assuming the transport along field lines dominates the transport across field lines). The loss of this pressure gradient removes the drive for the bootstrap current in the helical region inside the island separatrix. The loss of the bootstrap current then further increases the size of the island, which removes the pressure gradient over a wider region. This process continues until the drive from the bootstrap current loss is balanced by the stabilizing effects of the equilibrium bootstrap current gradient. The result is a saturated island with appreciable radial width, often large enough to appreciably affect the global energy and particle transport and sometimes large enough to initiate disruption. Figure 3-14 shows a simulation of a hypothetical 'worst-case' saturated 2/1 island in an ITER plasma. The parameters used for the simulation result in an effective island half-width that about 10% of the minor radius. The potential impact that an island of this magnitude near the $q = 2$ surface can have to affect energy transport or initiate disruption is obvious.

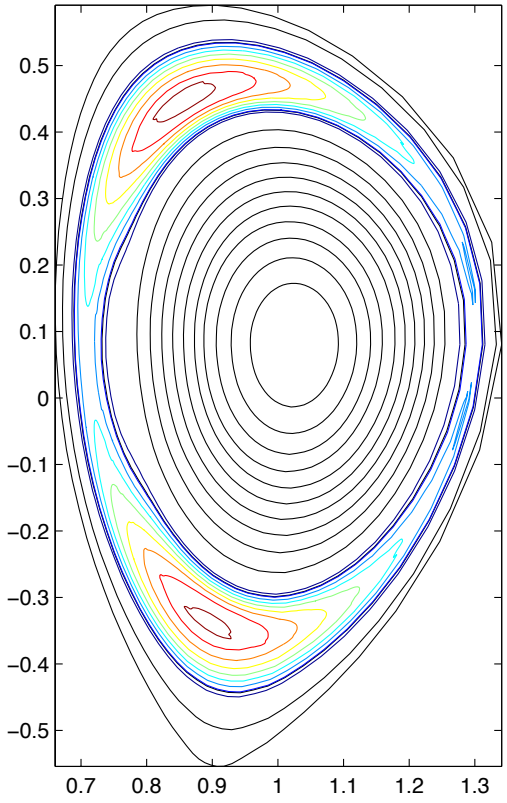

FIG. 3-14. Simulation of a m = 2, n = 1 neoclassical island in an ignited ITER plasma. The low value of the tearing mode parameter $\Delta' = -2.6$ in this simulation produces a large island that can be expected to have a significant impact on energy transport and hence on achievable beta. [Simulation by Alexander Pletzer with the PEST-3 stability code.]

The important issues for ITER, and indeed for any future tokamak power plant, are (1) which neoclassical island modes will be unstable (i.e., what physics determines the scaling of the thresholds and 'seed island' triggering amplitude for neoclassical modes), (2) what will be the saturated radial width of the modes, (3) what effect will these modes have on confinement and the β-limit, and (4) what are the prospects for avoiding the onset of these modes or for controlling their growth?

Neoclassical tearing modes were first experimentally identified on TFTR [3.76]. The modes were identified by fitting the time history of the measured perturbed magnetic field to the predictions of the 'Modified Rutherford Equation' that determines the dynamics of neoclassical tearing mode growth [3.84, 3.85]. The input parameters to the fit were derived from the measured

local plasma parameters. The existence and size of the magnetic islands were confirmed from analysis of electron cyclotron emission data. Similar identification procedures have been repeated on COMPASS-D, DIII-D, and ASDEX-U [3.23, 3.80, 3.81]. Fits of the island width predicted by neoclassical tearing mode theory to the island width calculated from the measured magnetic perturbations ($w^2 \sim \Delta B_{meas}$) are shown in Fig. 3-15 for TFTR, DIII-D, and COMPASS-D data. Agreement between theoretically predicted island width and the magnetic data is excellent. Numerical calculations have also confirmed the destabilizing effect of the bootstrap current in realistic geometry [3.89].

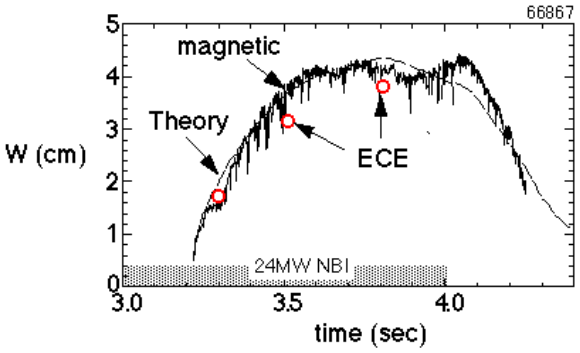

(a) TFTR

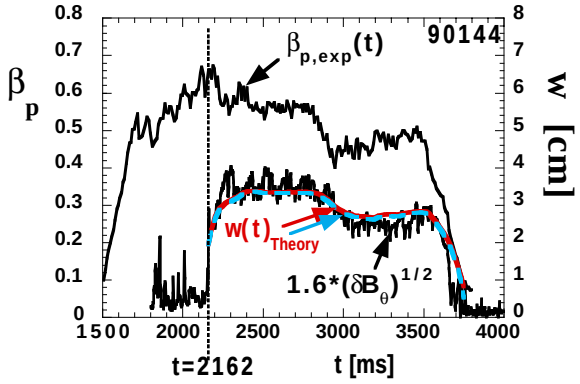

(b) DIII-D

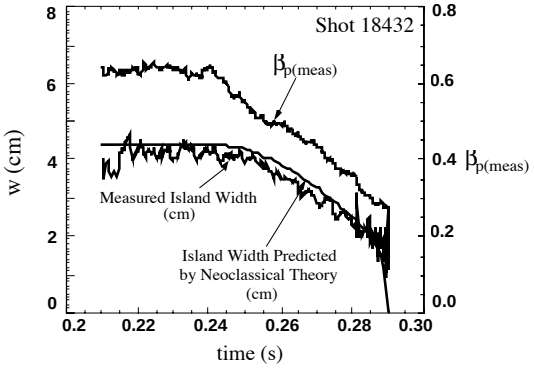

(c) COMPASS-D

FIG. 3-15. Measured island widths in various tokamaks compared with neoclassical tearing mode theory predictions: a) m/n = 4/3 neoclassical tearing mode in TFTR compared with the prediction of the neoclassical island evolution equation from [3.76]. (b) m/n = 3/2 neoclassical tearing mode in DIII-D compared to theoretical predictions (calculated using measured parameters) with either the ion polarization current term included or the cross-island transport term included. Time history

of $\beta_p(t)$ as determined by the equilibrium reconstruction code EFIT is also shown. (c) m/n=2/1 mode during an ECRH power ramp down in COMPASS-D, compared to theoretical predictions [3.80]. Measured $\beta_p(t)$ (from diamagnetic loop) is also shown.

More recently, internal details of the structure of the neoclassical modes obtained in JET at moderate to high values of normalized beta (β_N = 2.4–3.4) have been directly measured by soft X-ray tomography [3.90]. The tomographic reconstruction data (Fig. 3-16) show that the mode structure varies somewhat with normalized beta: at β_N = 2.4 an n = 2 structure with coupled m = 2 and m = 3 poloidal harmonics is seen; at β_N = 3.4, the m = 2 harmonic becomes dominant. At higher $\beta_N \geq 3.5$, a m = 2, n = 1 mode develops that leads either to a plasma-control-system-effected 'soft-stop' (plasma heating and current shutdown) or disruption if shutdown action is not taken.

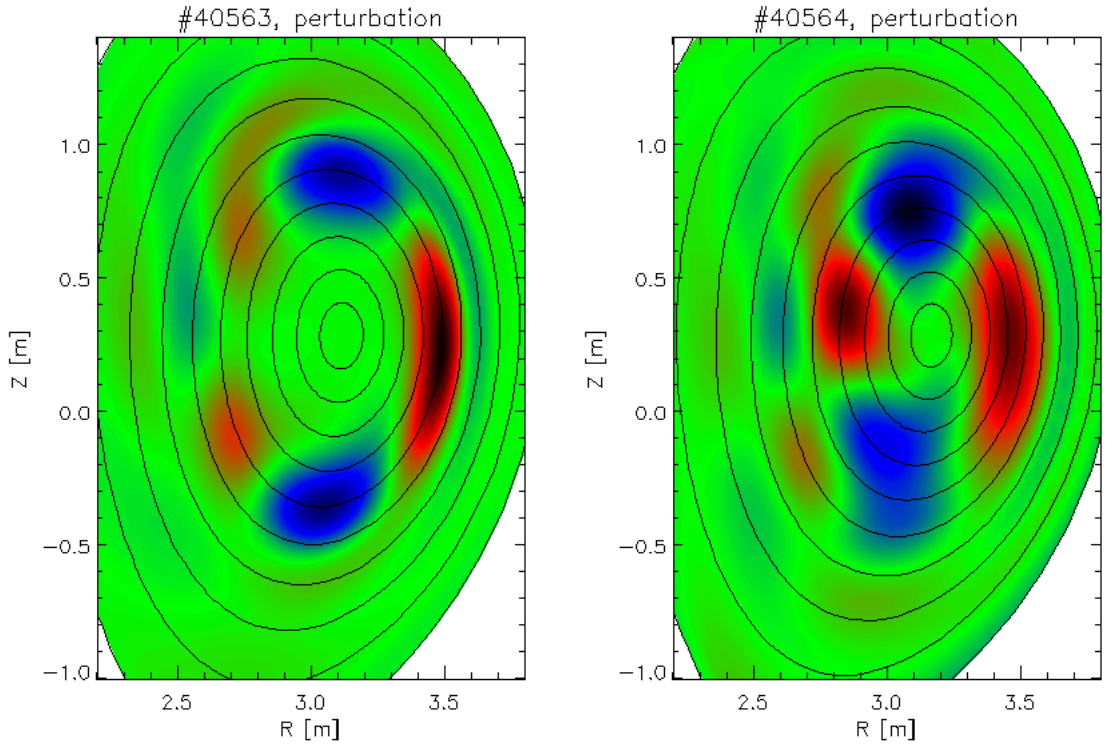

FIG. 3-16. Soft X-ray tomographic reconstructions of saturated n = 2 neoclassical modes in JET at β_N = 2.4 (left) and β_N = 3.4 (right). At the lower β_N, the mode has both m = 2 and m = 3 harmonics; at higher β_N, the m = 2 harmonic dominates. The data plots show the perturbation of

the SXR emission at one toroidal azimuth angle: green = small; blue = positive; red = negative. The axisymmetric equilibrium flux surfaces are superimposed.

The onset of neoclassical mode activity and the resulting limitation on beta depend on the plasma and mode growth dynamics and also upon the presence of other MHD activity (sawteeth or ELMs) with sufficient magnitude to generate a finite size 'seed' island needed to initiate neoclassical island growth. Figure 3-17 (adapted from [3.80]) illustrates the basis for the seed island sensitivity and the corresponding metastability of the pre-onset ideal MHD-stable state. The Figure shows that there is a finite island-width threshold w_{crit} for mode growth. For values of β_p that exceed a threshold value $\beta_{p,crit}$, the neoclassical mode can grow once the seed island size exceeds w_{crit}. Once this threshold is exceeded, the mode grows and eventually saturates with width w_{sat} that increases nearly linearly with β_p and hence with normalized beta. Furthermore, once the mode develops, the Figure shows that the mode will persist until β_p (β_N) is reduced to a value $\beta_{p,crit}$ ($\beta_{N,crit}$) that is typically much less that the onset value of β_p (β_N).

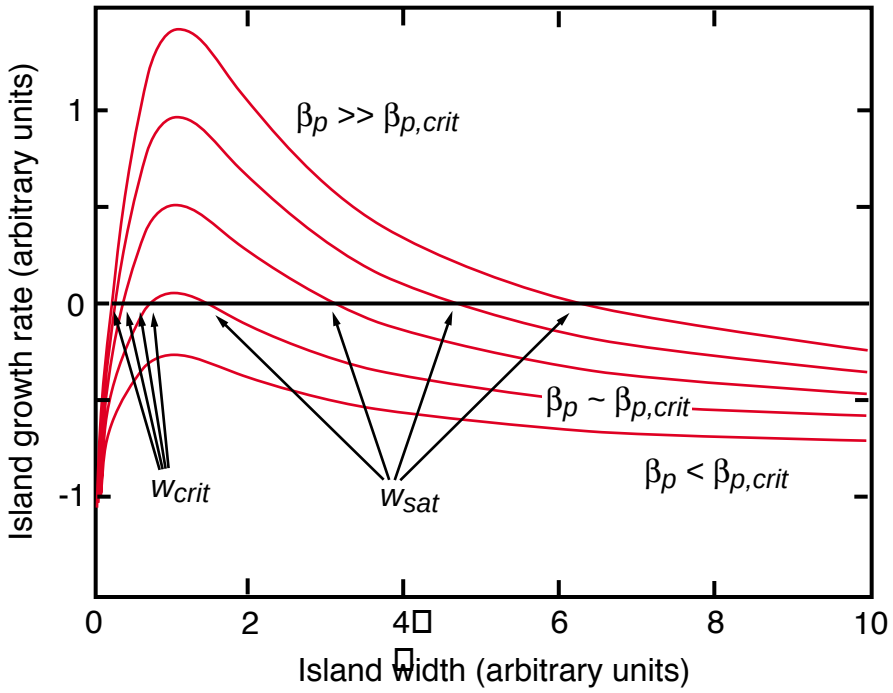

FIG. 3-17. Neoclassical mode growth rate (dw/dt) versus island width w and poloidal beta β_p. There is threshold $\beta_{p,crit}$ for mode growth and for $\beta_p > \beta_{p,crit}$, a critical island width w_{crit} for

mode growth. For $\beta_p > \beta_{p,crit}$, the saturated mode width increases linearly with increasing β_p. For simplicity, details of the sensitivity of w_{crit} to β_p and to the comparative importance of the ion-polarization and cross-island transport effects (and hence plasma collisionality) are omitted here (see [3.80]).

Figure 3-18 shows an example in ASDEX-U of the typical dynamics of neoclassical mode onset and the subsequent effect of the saturated mode on energy confinement and achievable beta [3.81]. The onset of the mode occurs during a quasi-stationary phase of the discharge (with constant NBI power and $\beta_N >> \beta_{N,crit}$), presumably owing to the occurrence of a large-enough MHD 'trigger' event (sawtooth or ELM). The initial ideal MHD-stable plasma is *metastable*, waiting for a critical perturbation that initiates a growing neoclassical island. Once initiated, the neoclassical mode growth is relatively slow (relative to ideal MHD growth rates) and ~100 ms is required for the mode to reach saturation. As the mode grows, confinement deteriorates and increased heating power is required to (nearly) recover the pre-onset β. When heating power is reduced and then removed, the mode persists until β_N falls to $\beta_{N,crit}$, which in this case is a small fraction of the onset β_N.

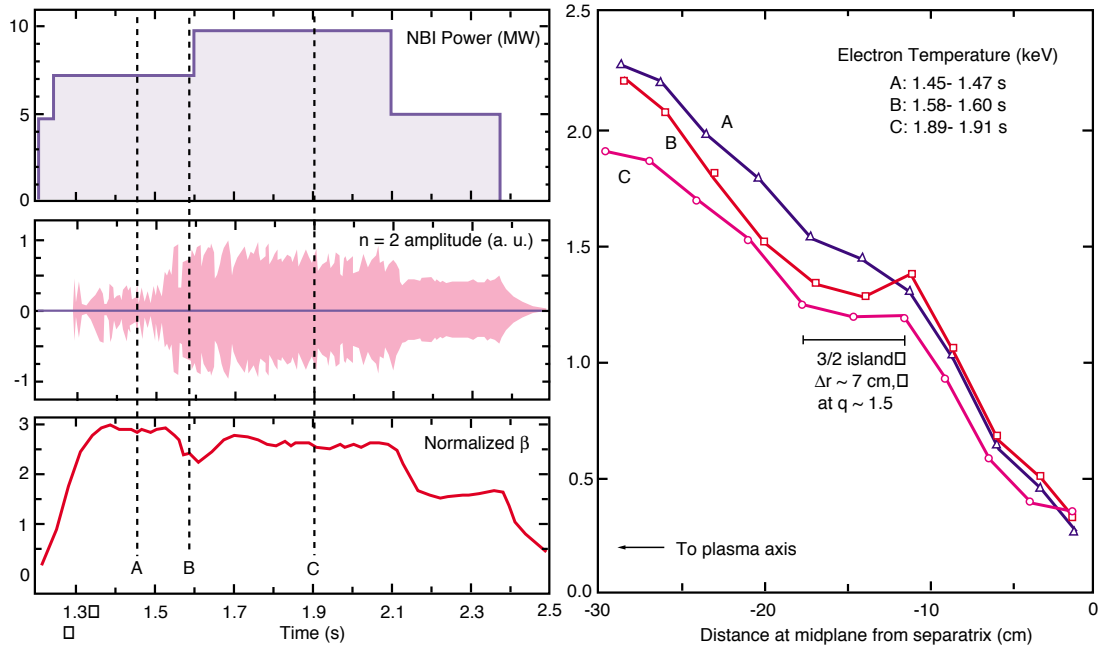

FIG. 3-18. Dynamics of neoclassical mode onset and subsequent confinement and temperature profile effects in ASDEX Upgrade (pulse #8216). An m = 3, n = 2 neoclassical mode develops at t = 1.5 s and persists for the balance of the beam-heated phase of the discharge. Note the drop in β_N at fixed beam power after mode onset and lack of recovery of the full pre-onset beta despite a further ~30% increase in beam power (both indicating confinement deterioration). Thomson scattering electron temperature profile data confirm the presence a 3/2 island and a ~ 7-cm wide profile flattening at q ~ 1.5 when the neoclassical mode is present

The 'flattop' β_N obtained in the quasi-stationary phase of the discharge following mode onset is determined in this example by the amount of heating power applied and is not necessarily the maximum that could be obtained if a further increase in heating were possible. In the example shown, the mode-onset β_N and the attained saturated-mode β_N are nearly equal, albeit with degraded confinement (by ~25%) after mode onset. Similar onset trigger event sensitivity, pre-onset metastability and after-onset mode growth dynamics are seen in all of the tokamaks reporting neoclassical modes. In cases where the plasma safety factor is low ($q_{95} \leq$ ~3), a 2,1 mode can develop that often leads to disruption.

The data above show the dynamic/metastable nature of the beta limit in long-pulse tokamaks and the importance of distinguishing the β_N for mode-onset from the final β_N that is ultimately attainable (in present experiments with possible application of additional heating power) after mode saturation. In this sense, the neoclassical beta limit in future tokamaks is not a single, immediately quantifiable value, and hence its effect on reactor and ITER performance must ultimately be assessed in terms of the mode location and saturated island width and the self-consistent effect of the saturated mode on the plasma pressure profile and confinement. These beta-limit matters are discussed below in Section 3.2.3.3.

Neoclassical mode onset in present experiments is observed to depend on plasma density and also on the presence of MHD triggering activity. On COMPASS-D and DIII-D, the onset of the modes are seen to be dependent on the plasma density (and hence on the collisionality). The lower the density, the lower the plasma β at which the modes appear. On COMPASS-D the measured density scaling of the β at which the mode goes unstable agrees with that predicted by

the ion polarization current model. On DIII-D the scaling for the onset of neoclassical modes with collisionality is consistent with either the ion polarization current model (assuming that the transition from collisionless to collisional is 'slow') or the cross-field transport model (if the parallel transport is conductive, but not if convective). In all cases the onset of the mode is associated with another MHD perturbation (sawteeth, fishbone oscillations, ELMs). Indeed on DIII-D in cases where such perturbations are carefully avoided, and on JET where sawteeth spontaneously disappear with heating, increased stability to neoclassical tearing modes is observed [3.12, 3.23].

3.2.3.2. Island onset thresholds: mechanisms and data

The physical mechanism that determines the size of the island threshold width is an important issue under current examination in the experiments in which neoclassical tearing modes have been observed. Since the critical island threshold determines the onset of the mode and which modes are unstable, it is the key to understanding the likely impact of neoclassical tearing modes on ITER. There is still considerable uncertainty in the theoretical calculations (see [3.91], for example) of the threshold mechanisms as well as in the experimental data. A database of critical plasma parameters at the point of onset of neoclassical tearing modes has been assembled in order to help determine the physical mechanisms responsible for the neoclassical island threshold [3.11]. Figure 6 shows two fits of this database for mode onset. The fits are based on the threshold mechanisms espoused in [3.87] and [3.88]. Figure 3-19(a) shows the scaling expected assuming the threshold island width is determined by the cross field transport model at the critical β_p for instability. The data is generally consistent with the expected $(\nu_e^*)^{0.3}$ scaling that this model implies. The transport models assumed are described in [3.78]. Figure 3-19(b) shows evidence that supports the polarization current model: a generally strong correlation of the onset of neoclassical tearing modes with the collisionality parameter, $\nu_i/\varepsilon\omega_e^*$ — which is predicted to have the strongest effect in the polarization current model — occurs for $\nu_i/\varepsilon\omega_e^* \geq \sim 0.3$. As is explained in the Figure captions, there are certain caveats associated with the experimental data, and both

models in Fig. 3-19 assume that the seed island amplitude does not vary strongly with plasma parameters, an assumption which has only limited experimental justification. The absence of a compelling present basis for choosing between the two threshold models makes the scaling of the seed island amplitude for neoclassical mode stability an issue which requires further experimental and theoretical study.

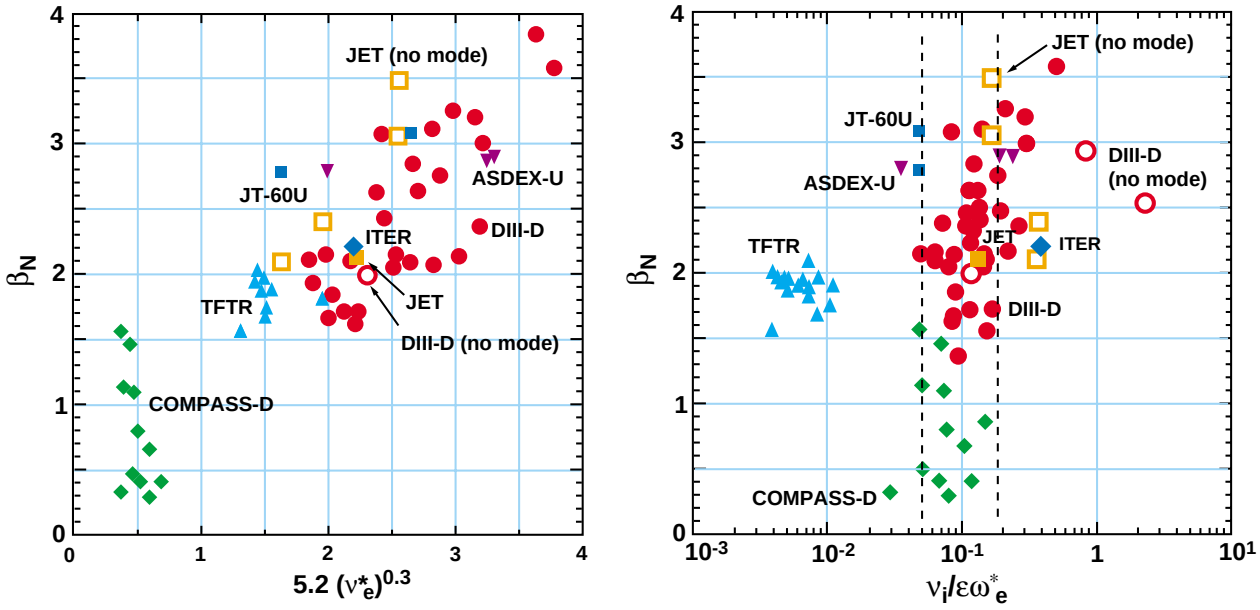

FIG. 3-19. Comparisons of neoclassical mode onset data from the ITER database with the predictions of two threshold model scalings. Left (a): β_N at the point of onset of MHD, plotted vs. $(\nu_e^*)^{0.3}$, a proposed scaling for the onset of MHD from cross-island transport threshold model. Right (b): β_N vs. $\nu_i/\varepsilon\omega^*$, an important parameter in determining the critical island width in the ion polarization current threshold model (large threshold width for $\nu_i/\varepsilon\omega^* > 0.3$, small threshold width for $\nu_i/\varepsilon\omega^* < 0.3$). The dashed vertical lines represent the spread due to a 15% uncertainty in the measured temperature at the rational surface. The following caveats apply to the interpretation of the database: (1) TFTR data have rapid power increases and the value $\nu_i/\varepsilon\omega^*$ goes from above the threshold value to well below in ~200 ms, (2) solid data points for JET and DIII-D are for mode onset; open points are for no mode onset, and (3) The COMPASS-D data is for plasmas with $T_e > T_i$ (ECRH heating), while all other data are with neutral beam heating.

3.2.3.3. Beta limits

If the neoclassical islands grow to sufficient size, they can set the maximum attainable plasma pressure. Beta limits set by neoclassical tearing modes have been observed on COMPASS-D, ASDEX-U, TFTR, DIII-D and JET. The saturated island width and growth time are well predicted by neoclassical theory in all experiments. The size of the saturated island, w_{sat}, on a given rational surface with radius r_s can be expressed by the simple formula:

$$\frac{w_{sat}}{r_s} = \beta_\theta \frac{a_{bs} - a_{GGJ}}{-r_s \Delta'} \tag{3-3}$$

where β_θ is the local poloidal β, a_{bs} and a_{GGJ} are respectively the coefficients that determine the magnitude of the bootstrap current term and the Glasser-Green-Johnson term in the island growth equation and where $\Delta' = [(d\psi/dr)_{+r_s} - (d\psi/dr)_{-r_s}]/\psi(r_s)$ is the usual resistive tearing mode stability parameter that is given by the jump in the logarithmic derivative of the flux ψ across the rational surface. It has been observed from q-scans on COMPASS-D [3.80] that the maximum allowable island width scales with the minimum of either the distance from the rational surface to the plasma edge (hard or disruptive-onset beta limit) or the distance from the rational surface to the q = 1 surface (soft beta limit). This condition can be stated simply:

$$w_{max} = Min\left[\alpha(a - r_s), \gamma(r_s - r_{q=1})\right] \tag{3-4}$$

where α and γ are coefficients of order 1 that determine fractional distance allowed before interaction. The combination of Eqs. (3-3) and (3-4) yields an expression for the maximum achievable β_θ on the rational surface. This combined with knowledge of the profiles (relating the local poloidal β to the global poloidal β) yields an expression for the maximum achievable plasma pressure.

Additionally, tearing modes can degrade the energy confinement time [3.92]. A simple model of the degradation of the energy confinement time, known as the 'belt model', has been proposed [3.93], and is given by:

$$\frac{\Delta\tau_E}{\tau_E} \approx -4\left(\frac{r_s}{a}\right)^4 \frac{w_{sat}}{r_s} \tag{3-5}$$

This model, which is based upon the elementary premise that energy transport is greatly enhanced over the width of the saturated island (see the temperature profile data in Fig. 3-18), gives estimates of the confinement degradation effect that are in reasonably good agreement with the corresponding experimentally-measured island radius and width.

3.2.3.3. Predictions for ITER

Given the uncertainty in the physics behind the threshold mechanisms, it is difficult to extrapolate currently-measured island width thresholds for mode onset to ITER with any confidence. In general, the measured threshold island widths seem to scale with the ion poloidal Larmor radius. The predictions of the threshold island widths for ITER from theoretical considerations give values in the range of 2–7 cm for onset the 2/1 mode [3.11]. It is difficult to imagine how seed island perturbations with this width can reliably be avoided by wholly passive means in a machine the size and pulse length of ITER. Therefore it is prudent to assume that ITER will be unstable to at least some neoclassical tearing modes.

In order to assess the likely impact of these modes on ITER, it is necessary to estimate the expected saturated island width. It is generally observed in experiment that the most deleterious mode is the m=2, n=1 mode, in that it is most likely to lead to disruption. However, higher mode number islands (e.g., 3/2, 4/3, and 5/4), which are observed to reduce confinement times by 10-30%, are also problematic and may not necessarily be tolerable for ITER in terms of the resulting confinement deterioration. Assuming that the 2/1 mode sets the most severe limitation to β, and that the mode has been excited by a perturbation large enough to trigger the growth of the mode, and also that the maximum achievable β is set when the island half-width becomes comparable to the distance between the rational surface and the plasma edge (as in [3.80]), one can then calculate a maximum β for a typical ITER equilibrium. This maximum achievable normalized β ($\beta_{N\max} = \beta_{\max} aB/I$), is $\beta_{N\max} = 2$ - 2.2 [3.11].

A normalized beta of 2.2 is similar to the value required, with 'reference' confinement and impurity content assumptions (see Chapter 2), to achieve 1.5-GW fusion burn in ITER. The present predictions of the beta-limit expected in ITER owing to saturated neoclassical island growth are therefore marginally consistent the achievement of the design basis power. But there is little beta-limit 'head room', and the possible propensity of large-amplitude saturated neoclassical modes to increase the possibility of disruption is a additional concern (see Section 3.4).

The growth time of the 2,1 mode in ITER is quite long due the large plasma cross-section and high plasma temperature. The mode will reach half the saturated size (0.5 w_{sat}) in 30 s and ninety percent of the saturated size (0.9 w_{sat}) in 150 s. Because the growth time is long, it should be technically feasible to employ a feedback scheme to stabilize neoclassical tearing, as long as a stabilizing mechanism can be found. Several tokamaks (DIII-D, ASDEX-U, and COMPASS-D) are currently investigating the possibility of feedback suppression of the 2/1 and/or the 3/2 mode growth using electron cyclotron current drive. The basic principal consideration is to replace the 'missing' bootstrap current inside the island with driven current, and thus remove the island. Localized heating near the rational surface is also predicted to modify or reverse neoclassical mode growth.

Calculations indicate an ECRH power on the order of 30 MW is needed in order to stabilize or at least to control the size of the 2/1 mode on ITER [3.73, 3.81, 3.94]. The required driven current density must equal ~1.5 times the equilibrium bootstrap current. However, the theoretical calculations done to date are not self-consistent and in any case will be necessary to experimentally verify the feasibility of such a feedback scheme.

Additionally, active control of the q-profile, such as $q(0) > 1$, $q(0) > 2$ or negative central shear could avoid the dangerous low-order neoclassical modes, avoid seed islands (such as those produced by sawteeth) large enough to trigger mode growth, or in the case of negative central shear, turn the destabilizing bootstrap current term into a stabilizing term . It has also been proposed that by controlling sawteeth (see Section 3.2.2) to be more frequent and with smaller $m = 1/n = 1$ mode amplitude, the coupling to the $m = 2$ mode might also be made sufficiently

small to avoid triggering neoclassical modes. So sawtooth control, which may be necessary in ITER to avoid 'monster' sawteeth (see Section 3.2.2.6), may also prove to be a means to avoid onset of neoclassical modes. Here, however, the neoclassical mode avoidance requirements are still clouded by the uncertainties about threshold island width.

3.2.3.4. Summary

Neoclassical tearing modes pose a potentially serious challenge to reactor tokamak and ITER high-β operation. If neoclassical tearing modes are triggered and uncontrolled in ITER, they will likely limit the attainable normalized β to values of $\beta_N \sim 2$. High-order MHD modes (e.g., 3/2, 4/3, 5/4) will degrade confinement and may thus not be acceptable owing to the deterioration of confinement and plasma performance (attainable power) that they will produce. In addition, if the 2/1 neoclassical tearing mode grows to its projected saturated size, it may likely cause disruption.

In present tokamaks the onset of neoclassical modes is associated with the presence of an additional MHD activity perturbation (seed island) that pushes the mode over a stability threshold. In the absence of a sufficiently-large seed island trigger, neoclassical modes do not appear and stable long-pulse operation at up to the ideal MHD beta limit is possible. Both sawteeth and ELMs are observed to act a seed-island triggers for neoclassical mode onset in present tokamaks. Theoretical considerations put the size of the threshold seed island width for 2,1 mode onset in ITER in the 2-7 cm range. Given the large size and long pulse length of ITER, it will probably not be possible to avoid perturbations of this size, and so the occurrence of neoclassical modes is likely unless robust preventative measures to limit seed island size from sawteeth and ELMs are taken.

If neoclassical islands are triggered in ITER, estimates of the saturated island width suggest that means to limit their growth will be needed. Schemes for feedback control of the growth of neoclassical tearing modes are currently under investigation. Owing to the long growth time of such modes in ITER, these schemes should be technically feasible, but experimental verification of

their efficacy remains as an important future task for present experiments. Alternatively, neoclassical tearing modes in ITER can perhaps be avoided entirely in a reverse shear mode of operation or perhaps prevented by running with q(0) > 1, or by control of the sawtooth reconnection amplitude. In any case, the provision of sawtooth and MHD island control means in ITER embodied in the form of suite of rf heating and current drive schemes with localized power and current drive capability controllable in the $1 \le q \le 3$ flux surface domain seems highly prudent, if not mandatory. It is likely that such MHD control means will also prove useful in the control of MHD activity associated with error-field-induced locked modes (Section 3.2.5) and perhaps also resistive wall modes (Section 3.2.4).

3.2.4. Wall Stabilization and Resistive Wall Modes

Steady-state operation of a tokamak reactor and ITER is possible if sufficient plasma beta values can be reached with a high bootstrap current fraction. The requirement for a high bootstrap fraction $f_{bs} = I_{bs}/I_p \approx 0.9$ (motivated in turn by the relatively limited efficiency of non-inductive current drive, see Chapter 6) combined with the Troyon beta limit scaling [3.3] leads to a scaling for the beta limit [3.95]

$$\beta\,[\%] \le (0.1/f_{bs})\,(a/R)^{1/2}\,(\beta_{Nmax})^2\,(1+\kappa^2) \qquad (3\text{-}6)$$

This scaling shows that at high f_{bs} and typical inverse aspect ratios, operation at or above the Troyon beta limit ($\beta_N \ge 3.5$) and strong shaping ($\kappa \ge 1.6$) of the plasma cross section are needed to reach reactor-relevant betas. The estimate of the beta limit embodied in Eq. (3-6) is well confirmed by numerical MHD stability studies (see Section 3.2.1). For example, with a full-sized ITER plasma (a = 2.8 m, R = 8.14, B = 5.7 T), Eq. (3-6) yields a beta limit of about 3%, a value that is at best (depending on the plasma profiles and impurity content assumptions) marginally consistent with 1.5 GW fusion power. The corresponding plasma current requirement is 19 MA, and hence about 2 MA of non-inductive current drive, somewhat beyond projected

ITER capabilities with 100 MW of power at the plasma densities required, would needed. These estimates show both the difficulties of achieving steady-state reactor operation and the importance of operation at high bootstrap fractions and normalized betas at or above the Troyon limit.

The Troyon limit assumes '[conducting] wall-at-infinity' boundary conditions (see Section 3.2.1), and more favorable limits result if there is a perfectly-conducting wall close to the plasma. Kessel *et al* [3.96] studied the stability of reversed shear equilibria (see Section 3.2.7). Under the assumption of a perfectly-conducting wall located at 1.3 times the minor radius, they found stable reversed-shear equilibria with a β^* (fusion-reactivity-weighted) limit of over 5%, 92% bootstrap fraction and good alignment (correspondence of radial profile) between the bootstrap and equilibrium currents. In these equilibria, the beta limit is mainly set by low-n external kink modes, in particular $n = 1$ modes, and hence wall stabilization is needed.

The elementary analysis presented above and detailed numerical MHD stability modeling of steady-state relevant plasmas show that wall stabilization (and possibly active feedback stabilization, see Section 3.2.2.4 below) appear to be necessary for the success of a steady-state tokamak reactor and for the achievement of 1–1.5 GW power in steady-state modes in ITER. However, the physics of wall stabilization is not trivial, and until rather recently it was not thought to be effective on a long time-scale. Recent experimental and theoretical results have shown that partial wall stabilization occurs when the plasma is rotating. However, it is not yet clear whether the stabilization by resistive walls and plasma rotation is sufficiently strong and reliable to be used in a reactor and ITER. I what follows we present some of the basic theoretical developments and experimental results and point at issues yet to be resolved.

3.2.4.1. Theoretical considerations and the role of rotation

It is well known that for static plasmas, resistive walls cannot stabilize equilibria that are unstable without a wall [3.97]. A resistive wall merely slows the growth of the instability to the resistive time-scale of the wall ($\tau_{wall} = L/R$). The growing mode that slowly penetrates the wall is called a resistive wall mode (RWM). When plasma rotation is introduced, two types of modes

occur. Some modes rotate with the plasma, and these will be referred to as the plasma modes. If the mode rotation is fast compared with the wall time ($\omega_{rot}\tau_{wall} >> 1$), the magnetic perturbation of such a mode does not have time to penetrate the wall. The wall appears as an ideal conductor, and the plasma modes are wall-stabilized. However, a RWM that rotates slowly with respect to the wall [$\omega_{rot}\tau_{wall} = O(1)$] continues to exist. The magnetic field perturbation of the RWM partly penetrates the wall, and the mode stability involves the dynamics both in the plasma and at the wall. The dynamics inside the plasma is complicated by the fact that the mode rotates relative to the plasma.

Theoretical calculations for *resistive* instabilities in low-beta cylindrical plasmas, taking into account both the dynamics in the plasma and at the resistive wall were made in the 1980s [3.98–3.100]. These calculations showed that if the rotation speed is sufficiently high, resistive tearing modes can be stabilized by a wall that is not too far away from the plasma. The necessary rotation speed is the sum of two contributions: one is the rotation of the mode relative to the plasma, which scales as a resistive tearing growth rate, the other is the rotation of the mode with respect to the wall, which scales inversely to the wall time [3.99, 3.100]. For *ideal* instabilities (e.g., external kinks), Zakharov and Putvinskii [3.101] showed that rotation does not stabilize the RWM if there is no resonant surface inside the plasma.

3.2.4.2. Stabilization of external kink modes

Experiments on DIII-D [3.102–3.105] and PBX-M [3.106, 3.107] showed, however, that plasmas could remain stable for periods of ~100 ms with pressures well above the Troyon limit. The stability of these discharges was hard to explain without invoking wall stabilization, which was typically observed to persist for durations that exceeded the wall resistive time scale. Figure 3-20 shows representative data from a DIII-D discharge that exceeds the Troyon limit for ~100 ms, or about 20 wall time constants [3.103]. The data show the presence of a non-rotating (stationary in the wall frame) RWM in the above-Troyon-limit phase of the discharge. The RWM is stabilized in a quasi-steady-state manner (relative to the ~5 ms RWM growth time) so long as the rotation

frequency of the q = 3 surface is greater than the RWM growth rate. When the q = 3 rotation drops below this threshold, the RWM grows rapidly and the high beta phase of the discharge terminates. The interpretation made in [3.103] is that the high-beta phase of the discharge is sustained owing to rotation-induced stabilization of the RWM. More recent studies of low-inductance wall-stabilized plasmas with weak negative central magnetic shear (produced by current ramping, see Section 3.2.7) in DIII-D have extended the wall-stabilization duration to 200 ms with enhancement factors $\beta_N/\beta_{N,\text{no-wall}}$ of up to 1.4 [3.104]. A rotation rate threshold for wall-stabilization that is consistent with theoretical expectations has also been observed. "Encouraging results" of preliminary 'open-loop' tests of a feedback scheme in which external coils are used to make the resistive wall appear to be ideally conductive (and thus extend the stabilization period) are also reported (see Section 3.2.2.4).

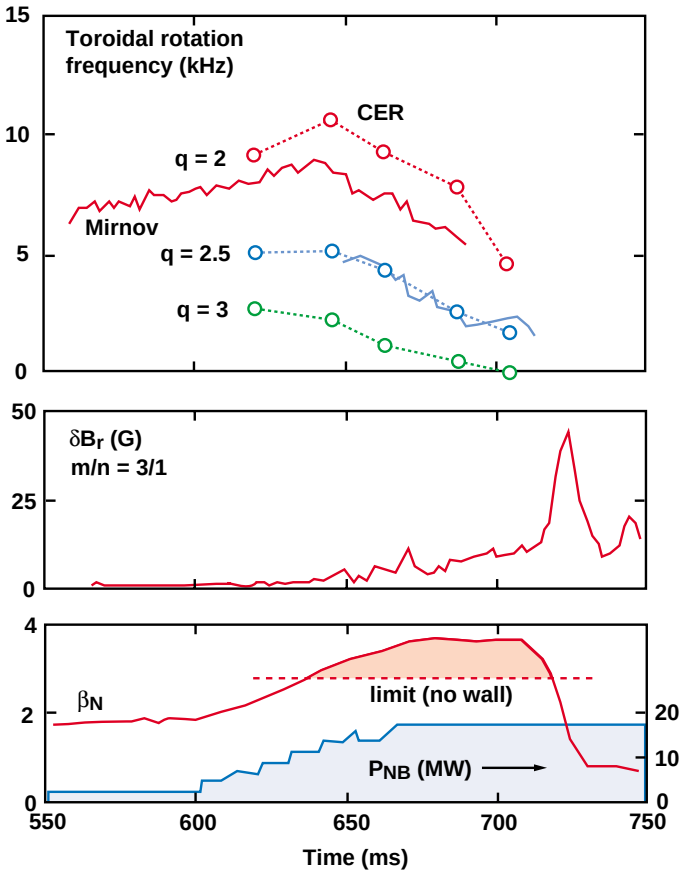

FIG. 3-20. DIII-D discharge #80111 illustrating plasma rotation stabilization of a non-rotating m=3, n=1 RWM (detected by saddle-loop magnetics data, second panel). The RWM develops for

$\beta_N > \beta_{N,ideal}$, but is resistively stabilized (limited in amplitude) by the effect of plasma rotation at the q = 3 surface. As the q = 3 rotation slows, the mode grows in a corresponding manner. When the q = 3 rotation ceases, the wall stabilization ceases to be effective, the RWM grows rapidly on a wall-resistance time scale (~5 ms) and the high-β_N phase terminates owing to severe confinement deterioration. Data reproduced from [3.103].

Bondeson and Ward [3.108, 3.109] showed numerically that pressure-driven ideal external kink modes can be stabilized by relatively modest plasma rotation (ω_{rot}/ω_A ~0.03-0.1) together with resistive walls, and that significant increases of the beta limit are possible. These calculations showed how the stability of the rotating plasma modes and the wall-locked RWM is affected by the plasma-to-wall separation. The basic situation is illustrated in Fig. 3-21, which shows the normalized growth rates for the plasma mode (external n = 1 kink) and the RWM, both as a function of normalized wall position (r_W/a). The pressure in the example shown is about 30% above the ideal MHD 'wall-at-infinity' limit and the normalized rotation rate is $\omega_{rot}/\omega_A = 0.06$. As expected, the plasma mode is unstable, with an ideal-MHD growth rate, when the wall is located outside the marginal ideal-MHD-stability wall position ($r_W/a \approx 1.7$). The RWM is unstable for a close-fitting wall, but becomes stable as the wall is moved away from the plasma. For the example shown, $r_W/a \geq 1.4$ is required for RWM stability. This requirement agrees with simple Δ' calculations.

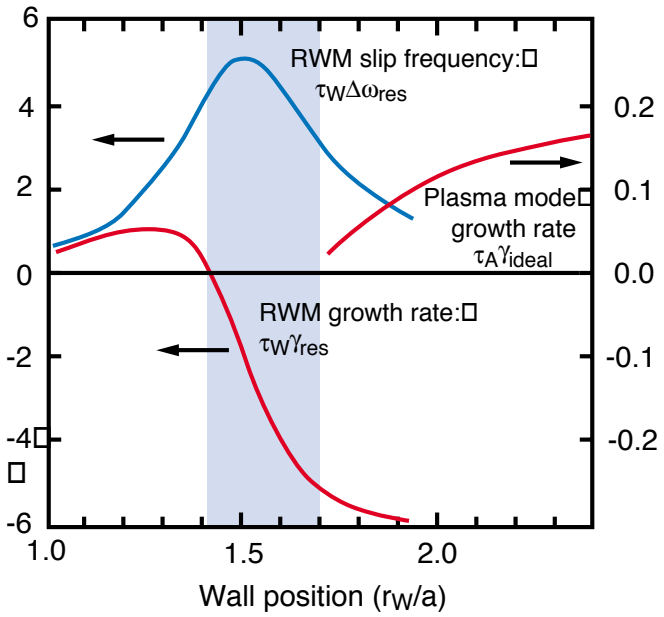

FIG. 3-21. Resistive wall mode growth rate and slip frequency and plasma mode (ideal n = 1 external kink) growth rate versus resistive wall position, for a plasma with pressure 30% above the wall-at-infinity external kink beta limit and $\omega_{rot}/\omega_A = 0.06$. A finite-width wall position window (shaded domain) for simultaneous plasma and RWM stability exists.

For the case shown in Fig. 3-21, there is a window for the wall position $1.4 \le r_W/a \le 1.7$ where both the plasma and the RWM are stable. Figure 3-22 shows how the marginal wall positions for the plasma mode and the RWM depend on the normalized beta for a JET-shaped equilibrium studied in [3.108]. With increasing beta, the stability window for the wall position narrows and eventually closes. Of course, stability is required for modes with all values of the toroidal mode number *n* and the stabilizing effect of the wall decreases with increasing *n*. For the reversed shear equilibria considered for steady state tokamaks, *n* = 1 tends to be the most limiting mode and therefore wall stabilization can significantly raise the beta limit of such equilibria.

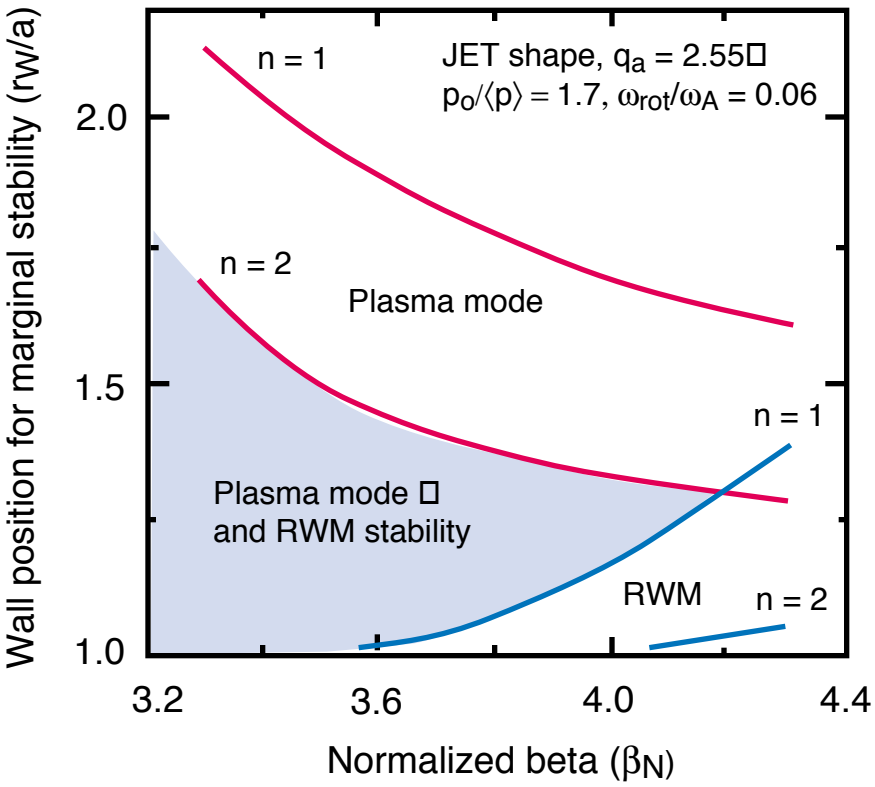

FIG. 3-22. Marginal wall position versus normalized beta for plasma and resistive wall modes. The plasma mode is stable for a wall located inside marginal position and the RWM is stable for a wall located outside the marginal position. A finite wall-position stability window (shaded region) exists in this case for $\beta_N \leq 4.2$. The calculation here is for a relatively broad pressure profile with a central-to-volume-average pressure ratio = 1.7

From Fig. 3-22, it can be seen that the optimal position of the wall is about 1.3 times the minor radius. This is a typical wall position in present-day tokamaks and is also the approximate position of the toroidally-conducting nuclear-shield-module 'backplate' support structure in ITER. Modifications due to incomplete walls have been discussed by Ward [3.110].

Several analytical calculations of wall stabilization have been given in cylindrical geometry. These emphasize the importance of 'dissipation' for the stabilization. Such dissipation may come from resonant absorption (which occurs close to the mode rational surfaces), viscosity and resistivity. The numerical calculations [3.108, 3.109] included dissipation from the resonant absorption as well as from a parallel viscosity that models ion Landau damping and is effective

mainly by coupling to the toroidal side-bands. In a toroidal plasma there are typically many mode-resonant surfaces $q = m/n$, near which the slow plasma rotation frequency resonates with a continuum frequency. Betti and Freidberg [3.111] treat the damping from the sound-wave resonance in MHD and show that this dissipation mechanism gives rise to a window of stability for the wall position. Numerical and analytical work [3.112, 3.113] shows that viscous and resistive dissipation can also give rise to wall stabilization. Fitzpatrick and Aydemir [3.113] analyzed the effects of toroidal coupling of the Alfvénic resonances.

3.2.4.3. Threshold for the rotation speed

The numerical calculations presented in Refs. [3.108, 3.109] showed that the stability of the RWM is sensitive to the assumptions regarding the ion Landau damping. Typically these calculations gave 30-40% increases of the beta limit with rotation speeds of the order of several percent of the Alfvén speed (or about 20% of the sound speed at the $q = 2$ rational surface). This is in agreement with experimental results from DIII-D [3.103, 3.105] and PBX-M [3.107]. However, the experimental threshold rotation speed for wall stabilization appears to be lower than the predictions given in [3.108, 3.109]. In DIII-D, wall stabilization is observed at rotation frequencies below 1% of the Alfvén speed, whereas MHD calculations suggest that several % of the Alfvén speed are needed for a significant effect. It is important to resolve this issue, since rotation speeds in ITER are not expected to exceed 0.5% of the Alfvén speed. A number of possible resolutions to this difficulty have been proposed:

(i) *Ion Landau damping*. One possible resolution may come from consideration of the effect of strong ion Landau damping. Chu *et al*, [3.105] generalized the first toroidal calculations to include sheared flow. These calculations applied a cylindrical model for the ion Landau damping and reproduced the rather low critical rotation velocities observed in DIII-D. It was subsequently pointed out [3.114, 3.115] that the cylindrical results for ion Landau damping typically do not apply to the problem of RWM stability. In toroidal geometry, particle trapping strongly reduces the Landau damping if the mode frequency is below $(r/R)^{1/2}v_{thi}/qR$. For rotation

frequencies substantially below $(r/R)^{1/2}v_{thi}/qR$ (as is usually the case for the wall stabilized discharges), the ion Landau damping becomes negligible. Therefore, the ion Landau damping on the toroidal sidebands is not important in the core of the plasma. One possible explanation of the low experimental rotation thresholds is that ion Landau damping is significant near the edge of the plasma where v_{thi}/qR becomes small. Another possibility [3.115] is that because of a significant Pfirsch-Schlüter-like enhancement of inertia near the edge, the rotation frequency could become large in comparison with the local Alfvén continuum frequency.

(ii) Incomplete poloidal walls. Consideration of the effect of the poloidal incompleteness of the stabilizing wall also appears to be important. Ward [3.110] analyzed the stabilization resulting from a partial poloidal wall using the NOVA-W code. For high-beta equilibria, the wall stabilization from segments on the outboard side is much stronger than that from inboard wall segments. A diminished poloidal extent of the wall can largely be compensated for by moving the wall closer to the plasma. The NOVA-W calculations showed that for a high-beta equilibrium, a small conducting segment on the outboard side, close to the plasma surface, can give complete stability at considerably lower rotation velocities than a complete wall. However, even taking the effect of a partial poloidal wall into account, it seems difficult to explain the stabilization at low rotation speeds observed in DIII-D. An important point [3.110] concerning the possibility of wall stabilization in ITER is that if a conducting wall has to be placed closer to the plasma than the optimum position for a complete wall, it is advantageous for RWM stability to introduce isolating slits in the wall. These slits must, of course, be designed so as not to destroy vertical (n = 0) stability.

(iii) Linear stabilization at resistive rotation frequencies. In a cylindrical stability analysis [3.116], Finn found a parameter region where a plasma that is ideally unstable with the wall at infinity could be completely stabilized by rotation speeds comparable to resistive growth rates. It was later shown [3.117] that, although stabilization of cylindrical zero-pressure equilibria at such low rotation speeds is possible in principle, the stabilization requires extremely careful positioning of the wall and appears not to be experimentally relevant.

Beyond these uncertainties about the basic wall-stabilization processes, it is also not straightforward to translate these cylindrical stability modeling results into predictions for tokamaks. Fully toroidal calculations with the resistive MARS code [3.108, 3.109] showed very little influence of finite resistivity on the linear stability of the RWM. No region was found where an ideal instability could be wall stabilized by a rotation frequency of the order of resistive growth-rates. This is quite natural, because the resistive modes are strongly stabilized by favorable average curvature in MHD and should be irrelevant to RWM stability. Neoclassical effects on RWM stability have not yet been examined. Furthermore, the driving of an external kink mode by pressure in a tokamak depends on toroidal coupling and is fundamentally different than the driving of a resonant mode in a cylinder. This makes it difficult to carry over cylindrical results to tokamaks.

3.2.4.4. Active (feedback) stabilization of RWMs

Obtaining sufficient plasma rotation to robustly stabilize RWMs in reactor tokamaks — even those with continuous NBI — and in ITER appears to be problematical. However, the requirement to have enough plasma rotation to stabilize RWMs can in principle be overcome by employing feedback-controlled external coils to make the resistive wall act as if it is an ideal conductor [3.118]. The basic concept is to use sensors located on the shell to control external coils that counteract the resistive diffusion of the RWM flux through the shell and sensors. The concept is analogous to the well-known use of active feedback to external PF coils to stabilize the n = 0 resistive vertical instability of an elongated plasma in the presence of a resistive wall. Of course, to stabilize kink and/or RW modes, the feedback scheme must be capable of acting upon the specific non-axisysmmetric MHD mode(s) in question, and so proposed concepts for kink and RWM have focused on a modular 'intelligent (or smart) shell' system comprised of a number of independent sensors that are appropriately connected to a multimode feedback system [3.119, 3.120]. These modular systems can — subject to certain limitations imposed by the sensor and coil configuration — autonomously detect and stabilize any combination of modes. Figure 3-23 shows a schematic

of one possible implementation scheme, in which an array of conductors surrounding the plasma surface comprise a virtual shell with multi-mode response that can in principle be controlled by an analogous array of sensors located in the same radial position. More reactor-relevant variants of the scheme in which the active conductors are located outboard of the sensor array are also possible. However, more-or-less complete coverage of the torus by conductors appears to be required. This requirement for complete coverage raises significant access and conductor force support challenges in being able to implement such schemes in a reactor tokamak.

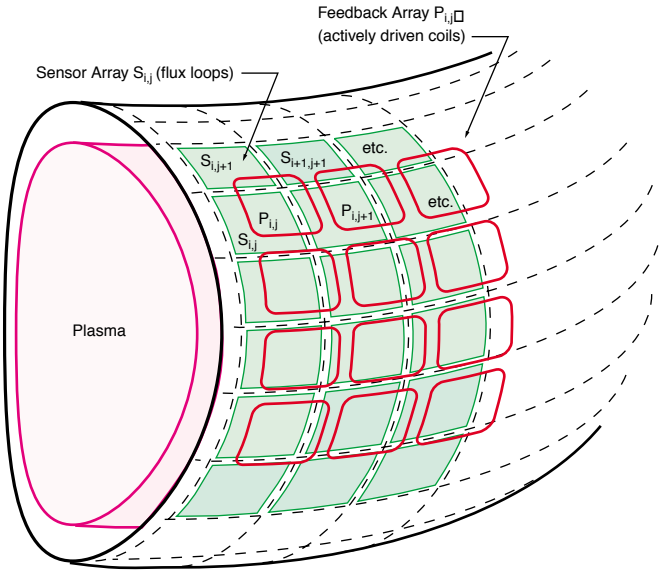

FIG. 3-23. Possible implementation of an 'intelligent shell' scheme for feedback stabilization of RWMs. The system comprises a sensor array S_{ij} electronically coupled to a corresponding actively-driven feedback coil array P_{ij}. With sufficient feedback amplifier gain and bandwidth, the sensor array surface appears to be a resistance-less conductor and the relevant RWM(s) are stabilized.

Studies of the performance and sensor and feedback coil position requirements of such schemes suggest that they could be implemented (in terms of the sensor and feedback coil locations and current-carrying capability and active power) in a reactor [3.121]. Studies of the possibility of a ‘smart shell’ have also shown that the RWM can be stabilized by the alternate artifice of driving

the feedback coils to emulate a 'fake' rotating resistive shell located at the sensor position. The fake rotating shell is found to require lower feedback gain.

Attempts to verify the feasibility of active feedback to affect and ultimately stabilize RWMs are presently in progress in several tokamak experiments. The results reported in [3.104] show initial indications of the ability of actively-driven external coils to affect RWMs. However, definitive demonstration of RWM stabilization and comparison of the merits of 'smart' versus 'fake' shell concepts awaits future experiments. In addition, the details of how the required feedback could actually be implemented in a reactor or ITER remain to be investigated. While the technical (current/voltage) requirements for implementation in ITER or a reactor are in principle achievable, the engineering details of how the sensors, coils and electrical connections can incorporated (and maintained) in ITER or a reactor remain to be evaluated.

3.2.4.5. Summary

Experiments with rotating plasmas and resistive walls show the possibility of stable plasma operation at beta limits well above the wall-at-infinity limit. Increases of the beta limits by 30-50% are observed and wall-stabilized discharges could potentially be used for a steady-state tokamak reactor or ITER. Theory based on toroidal MHD stability can generally explain the observed increases in the beta limit, although the predictions for the rotation speed required tend to be higher than speed observed to be sufficient in experiments for stabilization. Several explanations for this discrepancy between theory and experiment have been suggested, but resolution of the discrepancy still remains open. Furthermore, most examples of wall stabilization at low rotation speeds have only lasted for relatively short times, and hence there is concern that these plasmas may still have been unstable to slowly-growing RWMs. One effect that needs to be better understood is the influence of diamagnetic drifts, which are often comparable to the rotation speeds. This issue and the more general concern that the projected rotation velocities for ITER and reactor plasmas tend to fall below even the-lower-than-theory experimental rotation velocity thresholds remain unresolved.

In this regard, the potential for active feedback stabilization of RWMs without rotation via 'smart' or 'fake' wall schemes also needs to be assessed, as does the engineering feasibility of actually being able to implement such schemes in an ITER/reactor design.

3.2.5. Non-Axisymmetric Error Fields and Locked Modes

Small deviations of tokamak magnetic fields from ideal axisymmetry (hereafter: non-axisymmetric error fields or simply error fields) with amplitudes $B_r/B_T \sim 10^{-4}$ can induce low-m, low-n locked (i.e., non-rotating) MHD modes in the plasma. The induced modes themselves are resistive tearing modes and the physics of mode growth, slowing and locking are governed by resistive MHD. The basic physics mechanism that is responsible for mode locking is the toroidal rotation braking (dissipation) effect of error fields in slowing and ultimately stopping the rotation of m/n MHD modes at the q = m/n rational surface. Once such a locked mode develops, the mode amplitude grows and the resulting high-amplitude saturated mode can degrade confinement quality or result in subsequent or immediate disruption. Saturated locked modes that develop in the early (start up) phase of the discharge can persist and cause subsequent disruption when later changes to the plasma state (heating, proximity to the beta limit, current rampdown, etc.) are introduced. In either case, locked modes can constitute a significant limitation on the operational parameters achievable in present tokamaks, especially at low plasma densities and at high beta.

Since the susceptibility of tokamaks to error-field-induced mode locking is projected to increase with size (major radius) and possibly with toroidal field (see below), large reactor tokamaks are expected to be somewhat more sensitive than present tokamaks to mode locking and small relative levels of error fields. The tolerable levels for error fields and plasma operation strategies for avoiding locked modes are therefore important issues for ITER and future reactor tokamaks. Recent systematic studies of the sensitivity of present tokamaks to the magnitude and harmonic content (m/n spectrum) of error fields and theoretical assessments of the rotation-braking effects of error fields have lead to a semi-empirical understanding, albeit with some outstanding

uncertainties, of the error field correction and control requirements for ITER. There are also theories (see below) that can explain many of the error field magnitude and plasma parameter sensitivities seen in present experiments. On either basis, it appears for ITER that both careful construction and alignment of the toroidal and poloidal field coils before plasma operation and provision of controllable error field correction during plasma operation will be needed to avoid locked mode difficulties during the low-density start up phase of the plasma operation scenario (see Chapter 8) and likely also during the high-beta burn phase.

3.2.5.1. Physics mechanisms and types of locked modes

Locked modes arise from two distinct sources: the first source is the braking of the rotation of inherent MHD instabilities (typically resistive tearing modes) owing to the presence of the nearby conducting structures (torus vacuum vessels, n = 0 stabilizing structures, etc.) that surround the plasma. Most tokamak MHD instabilities rotate toroidally owing to diamagnetic effects, NBI momentum input, etc., and as these rotating modes grow to large amplitude, they drive increasingly large eddy currents in the surrounding conducting structures. These eddy currents in turn exert a torque on the plasma which causes the rotation of the driving MHD instability to slow [3.122]. The braking torque increases with the square of the instability amplitude, so at sufficiently large amplitude instabilities can come almost to rest, at which point interactions with small static external error fields (from toroidal and poloidal coil asymmetries, see below) completely stop, or lock, the modes [3.123]. For reasons discussed in [3.124], this type of resistive tearing mode locking tends to occur preferentially in larger tokamaks such as JET [3.125] and DIII-D [3.78]. In many instances, locking occurs with a well-defined toroidal phase, showing the ultimate role of external error fields.

Figure 3-24 shows a model calculation that illustrates representative aspects of resistive tearing mode growth, slowing and locking in JET. The model reproduces the features seen in the experimental data. The slow decrease in mode rotation frequency followed by sudden disappearance of the usual Mirnov oscillation signal is the typical experimental signature of mode

locking. Note that although the amplitude of the Mirnov signal [derived from ac magnetic measurements of dB_{pol}/dt)] decreases as the mode locks, the actual mode amplitude (experimentally detectable by dc non-axisymmetric radial field or flux difference measurements, see e.g., [3.125]) continues to grow until locking ($\omega = 0$) occurs. At this point, further mode growth (not explicitly shown in Fig. 3-24) often occurs.

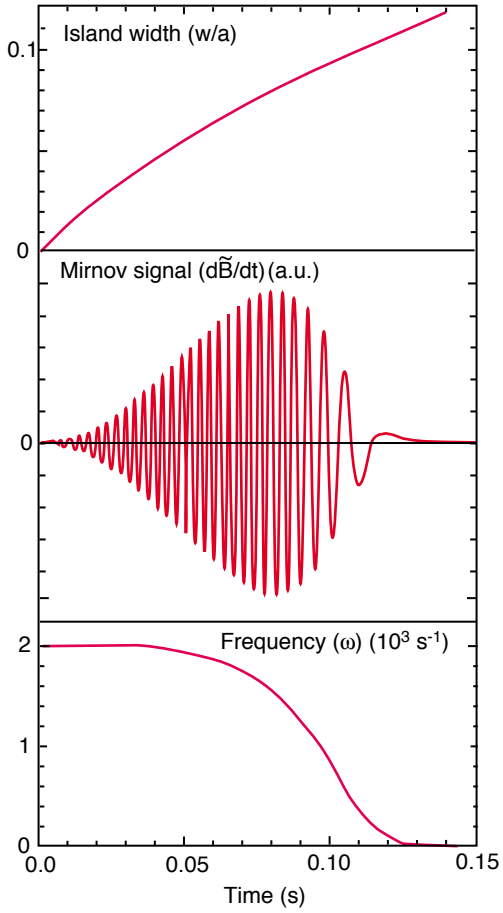

FIG. 3-24. Calculation based on a model described in [3.122] of 2,1 resistive tearing mode slowing and locking in a JET ohmic plasma. An initial plasma rotation velocity $\omega = 2000\ s^{-1}$ is assumed in this example.

The utility of static (dc) flux or field difference measurements in unambiguously detecting the presence of locked modes has made such diagnostics essential additions to the suite of 'plasma operation status' diagnostics implemented on presently-operating tokamaks (see Chapters 7 and 8).

Although occurrence of a locked mode is not always immediately detrimental to subsequent plasma operation, locked modes are usually plasma operation features to be avoided, and detection of a locked mode can be used as an indicator of possible or impending disruption (see Section 3.4.6).

The slowing down and locking of tearing modes occurs on a slow (resistive MHD) time scale that is ~100 ms in present tokamaks. Mode locking is also observed to occur on a much faster time scale during the growth of disruption MHD precursors (see Section 3.4.1), which are typically 1,1 and 2,1 internal kink modes. Here mode growth, slowing and locking with characteristics very similar to tearing-mode locking occurs on a ~1 ms time-scale. External error-field effects and sensitivities are usually not noticeable or immediately relevant to this manifestation of mode locking. But mode locking is clearly an important aspect of the final phase of disruption precursor development.

Resistive tearing mode locking that does not cause immediate disruption can sometimes be reversed, either by decrease of externally-applied error fields (see below) or by the addition or increase of neutral beam injection momentum input. There is appreciable hysteresis before the mode unlocks, so when the mode finally breaks free, the rotation rate increases rapidly and the resulting event, termed *mode spin-up,* produces a characteristic Mirnov oscillation burst of increasing frequency (see Fig. 2 in [3.126]).

The second type of locked mode is directly driven by non-axisymmetric error fields. These error fields inevitably arise in any tokamak from sources such as coil positioning errors, irregularities in the coil shapes, current feeds to the coils, inter-turn connections within the coils, eddy currents and nearby ferro-magnetic materials. 'Resonant' error field harmonics (m, n) that match major plasma MHD instability modes have the greatest effect. Experimentally the resonant (2,1) (m = 2, n = 1) error field component has been observed to act as the seed to induce dominantly (2,1) locked modes in a range of tokamaks [3.126–3.130]. This error-field locking is understood to occur when the torque that the error field exerts on the plasma in the vicinity of q = 2 is sufficient to slow and stop the plasma rotation, overcoming the plasma inertial and viscous torques [3.131]. Error-field locked modes are important because once formed, they can

grow to a large amplitude (for reasons which are not fully understood) and either seriously degrade the confinement quality or cause disruption.

The error-field locked modes are distinguished from natural locked modes in that they can arise in MHD stable plasmas and have no rotating precursor phase. Natural locked modes are simply caused by the instability becoming large, which can often lead to disruption, but the locking generally is of little direct relevance in itself. Error-field locked modes are the more important in so far as their operational effects are concerned, and thus the remainder of this Section concentrates on their characteristics in present tokamaks and their extrapolation to ITER.

3.2.5.2. Theory background

Experiments on error-field locked modes in Ohmic plasmas have been conducted on a number of tokamaks — most notably COMPASS-C (and more recently COMPASS-D) [3.126], DIII-D [3.127] and JET [3.128] — and recently there has been a substantial experimental effort to refine understanding of the error-field sensitivities in these machines [3.132]. These recent experiments use saddle coils external to the plasma to apply known helical 'error fields' (resonant magnetic perturbations, or RMPs) and show that the threshold error field for a locked mode to be induced decreases with decreasing plasma density. Thus error-field locked modes are expected to be most problematic in ITER during the relatively low density phase required for plasma current ramp up and H-mode access. Figure 3-25 illustrates the density sensitivities for Ohmic plasma mode locking and after-mode-locking 'stimulated' disruption seen for an externally-applied 2,1 RMP in COMPASS-C [3.126]. There is an approximately linear correlation between density and applied error field for locked mode onset (penetration). Further increase in error field (or decrease in density) results in disruption.

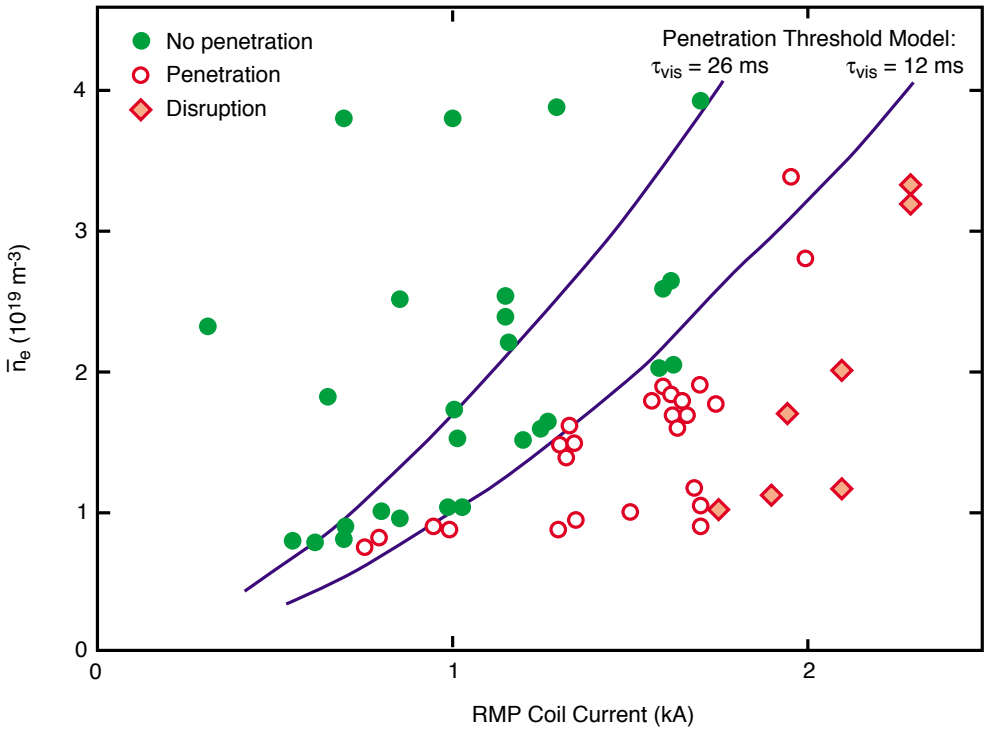

FIG. 3-25. Plasma response to externally-applied 2,1 RMP in COMPASS-C [3.126]. A 1-kA coil current produces a 13 G radial 2,1 field at the plasma surface. Toroidal field is 1.1 T in these experiments. The mode penetration threshold density is well described by a theoretical model (detailed in [3.126]) that includes the effect of strong poloidal flow damping. The viscosity time scale τ_v (see discussion in text) is a parameter in the model: the model curves shown are for the experimentally-measured range of τ_v. A model without poloidal damping fails to describe the data.

A theoretical understanding of the processes involved in the formation of error-field locked modes has been developed and application of this theory allows the various observations noted above to be understood [3.126, 3.131, 3.133]. The basic mechanism responsible for the threshold for mode locking is straight-forward: a resonant error field applies a slowing torque to the plasma in the vicinity of the rational surface, but until a critical perturbation threshold is reached, the plasma effectively shields the applied perturbation and very little internal tearing reconnection (plasma mode growth) occurs. However when the applied perturbation is large enough to slow the plasma to about half its initial rotation frequency ($\omega_0/2$) there is an abrupt transition to a locked mode with significant internal tearing: this process is commonly termed *mode penetration*. The

previously-mentioned appearance of a static (non-rotating) m/n radial field component or flux imbalance provides the most immediate indication of penetration, but there are usually also other indications of penetration — including directly measurable changes in plasma rotation velocity — seen on a wide range of other plasma core viewing diagnostics (see e.g., Fig. 2 in [3.126])

Calculation of the plasma torque balance shows the error field (B_{rmn}) to achieve mode penetration is [3.133]:

$$\frac{B_{rmn}}{B_T} \propto \omega_0 \tau_A \left(\frac{\tau_{rec}}{\tau_v} \right)^{1/2} \tag{3-7}$$

where τ_A, τ_v and τ_{rec} are the Alfven, viscous, and magnetic reconnection times, respectively. Interpretation of this mode penetration formula requires determination of the reconnection and viscous times. For standard models the reconnection time is governed by the plasma resistivity, which in turn can be determined by using an assumed confinement scaling. The viscous time can also be determined by use of empirical observations, obtained in auxiliary-heated tokamaks, that momentum confinement time scales in proportion to the energy confinement time (this scaling is assumed but not proven to be valid in Ohmically heated devices) or by the alternate method of observing the 'spin-up' rate of a locked mode after an externally-applied RMP is removed [3.126].

3.2.5.3. Experimental observations

To determine experimentally the likely error field locked mode thresholds in ITER, and thus the requirements for error field correction, there are 2 basic issues which must be studied in present experiments:

- How the threshold depends on the harmonic spectrum (m,n) of the error field
- The scaling of the threshold with global machine and plasma parameters e.g. q_{95}, B_T, n_e, R, β, etc.

Harmonic Spectrum. The issue of the harmonic spectrum requires consideration of the effect of the m,n spectrum of error-field modes that is present in any real tokamak. The torque applied directly by the error field, in the absence of a natural mode, at a given resonant surface (r_j) is [3.135]

$$T(r_j) = \left| \sum_m I_m C_m^j \right|^2 \tag{3-8}$$

Here I_m are complex numbers arising from the Fourier coefficients of the error field current, which are decomposed into toroidal ring functions [3.135]. The C_m^j are real numbers representing the toroidal coupling of the component resonant at r_j to the error field currents. This is the direct torque at r_j. There are also torques applied at neighboring resonant surfaces, which act by viscous coupling to apply a torque at r_j, this means the total torque at r_j has the form

$$T_{tot}(r_j) = T(r_j) + \sum_{k \neq j} A_k^j T(r_k) \tag{3-9}$$

Experiments have been performed on COMPASS-D and DIII-D to investigate the form of this torque. On COMPASS-D the mixture of Fourier harmonics may be varied by using different combinations of RMP coils external to the plasma. In particular, independently-powered coil combinations with 2 different dominant (m,n) combinations are used. Figure 3-26 shows typical data for how the coil current thresholds for penetration varies as the current ($I_{2,1}$) in the RMP coil set that produces mainly a 2,1 error field is varied against the current ($I_{3,1}$) in the coil set that produces mainly a 3,1 error field. The studies are conduced with single-null plasmas with an ITER-like elongation and shape.

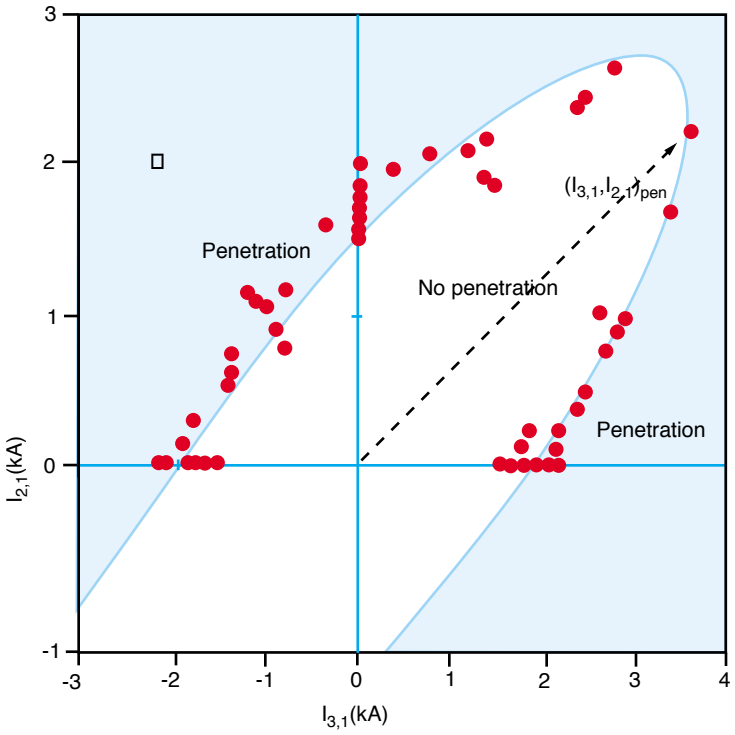

FIG. 3-26. Error-field coil currents for 2,1 mode penetration and locking in low-density Ohmic plasmas (2 x 10^{19} m^{-3}) in COMPASS-D. Mode locking occurs whenever the magnitudes of the currents in the 3,1 and 2,1 coils exceed the boundary indicated by the demarcation between the unshaded and shaded domains. These domains and the boundary presumably extend as shown in an anti-symmetrical fashion for negative $I_{2,1}$

Currents of ~1.6 kA in the 2,1 coil alone or currents of ~±2 kA in the 3,1 coil alone are sufficient to produce mode locking. There is strong interaction between the (2,1) and (3,1) combinations, but the locked mode formed always remains a dominantly (2,1) mode. Similar results are obtained from the interaction of dominantly (1,1) and (2,1) combinations. The Fourier components of the error field current have been evaluated and a general form for the torque fitted to the data [see Eq. (3-9)]: the result is

$$T_{tot}(q=2) \propto B_{pen}^2 \equiv 0.13|B_{1,1}|^2+|(0.21+0.02i)B_{1,1} + B_{2,1}+(0.85-0.17i)B_{3,1}|^2+1.69|B_{3,1}|^2 \quad (3\text{-}10)$$

where the Fourier analysis is performed in straight field line co-ordinates at q = 2 and the results obtained are represented in polar form. The interpretation of Eq.(3-10) is that the principal mode-locking effects are the torque that the (2,1) and (3,1) modes apply at q=2 surface and the viscous drag from the torque applied at q = 3 ($|B_{3,1}|^2$ term). The weighted-sum interaction between 2,1 and 3,1 modes gives rise to the elliptical mode penetration boundary manifested in Fig. 3-26. The (1,1) viscous drag torque and the torque that the 1,1 mode contributes at q = 2 have a smaller effect that results in the same type of (1,1), (2,1) mode interaction behavior shown in Fig. 3-26. The quantity B_{pen} ($\sim [T_{tot}(q=2)]^{0.5}$) can be interpreted as giving the equivalent mode locking threshold for a pure (2,1) field.

The COMPASS-D data is straight-forward to interpret owing to the availability of independently controllable RMP excitation and the fact that the applied error fields needed to produce mode locking are much large than inherent residual error fields. Similar error-field mode sensitivity experiments have been performed on DIII-D in double-null plasmas by ramping down the density until an error-field-induced locked mode forms. Here the harmonic mix was altered by varying the mix of natural (coil construction/alignment) error field and the error fields added by the so-called 'n = 1 coil' and 'C-coil' error-field perturbation coil systems [3.136]. The toroidal field B_t and safety factor q_{95} were also separately varied to elucidate the respective dependencies of the density threshold on these parameters. Empirical analysis in which the error field amplitude and harmonic content is treated in a manner which includes the effect of both viscous and direct coupling, as in COMPASS-D, yields a scaling for the density threshold that is given by

$$\bar{n}_e(10^{19} m^{-3}) = 0.6 \frac{(B_t / 2.1T)^{0.04\pm0.29}}{(q_{95} / 3.3)^{0.8\pm0.58}} B_{pen}(G) \qquad (3\text{-}11a)$$

where (at $q_{95} = 3.3$)

$$B_{pen}^2 = 0.28 B_{r1,1}^2 + (0.25 B_{r11} + B_{r21} - 0.05 B_{r31})^2 + 0.51 B_{r31}^2 \qquad (3\text{-}11b)$$

The equivalent mode locking threshold field derived in this manner [Eq. (3-11b)] is quite similar in magnitude and relative 1,1 and 3,1 harmonic weighting to the equivalent mode-locking field obtained from the COMPASS-D experiments. Although there are some differences in the weighting factors (relative to 2,1) for the 1,1 and 3,1 harmonics, the basic form and magnitude (with typical harmonic content) of the DIII-D and COMPASS-D results agree within about 20%. For example, with the assumption of an 'ITER-like' 2/1/0.67 harmonic mix (1,1, 2,1 and 3,1 modes respectively) and with the out-of-phase terms in Eq. (3-10) omitted, the equivalent fields B_{pen} obtained from Eqs. (3-10) and (3-11b) are respectively 2.3 $B_{2,1}$ and 1.9 $B_{2,1}$.

The limited range in q_{95} of 1.4 and in B_t of 1.4 (at fixed q_{95}) makes the DIII-D best-fit exponents relatively uncertain. However, within the uncertainty, the relative error field (B_{pen}/B_t) does not increase much faster than $1/B_t$. The issue of q and B_t scaling of the error field threshold in other experiments will be addressed below.

The COMPASS-D and DIII-D harmonic mix variation experiments are important for two reasons. First, they show that to understand the locked mode physics in a given machine where the mode mix varies, it is important that harmonic coupling effects be taken into account. Second, these results show that the contributions of the 1,1 and 3,1 harmonics to locking of the 2,1 mode are appreciable and hence that it may be desirable (or necessary) to correct the (1,1), (2,1) and (3,1) error field components independently. The (1,1) correction may be necessary, despite the relatively weak coupling, because (1,1) field errors will typically be larger than (2,1) or (3,1) field errors (the amplitude of the error-field spectra that arise from coil construction and positioning tolerances typically scale approximately as 1/m).

Plasma and Machine Parameter Scalings. We return now to the dependence of the penetration threshold on plasma and machine parameters. We assume that this dependence has a power law form $B_{pen}/B_t \propto n^{\alpha_n} B_t^{\alpha_B} q_{95}^{\alpha_q} R^{\alpha_R}$, which is in line with assuming a power law form for the confinement time in Eq. (3-7). Dimensional scaling considerations (see [3.137] and also Chapter 2) show that for Ohmic plasmas we can expect $8\alpha_n + 5\alpha_B - 4\alpha_R = 0$. Experiments in COMPASS-D and JET with well-determined harmonic content and single parameter (n_e, B_t, or I_p)

variations to determine the α_n and α_B coefficients have been performed. The DIII-D experiments cited above yield similar data, albeit with the need to perform a regression fit to the data set to separate harmonic mix variation effects from plasma parameter variation effects. The result of this fit is given in Eq. (3-11). The various experimentally-determined α-coefficients are summarized in Table 3-II.

Table 3-II. Parameter Dependence of the Penetration Field Threshold Scaling. Values in parentheses are inferred by addition.

	α_n	α_B	α_q	$\alpha_B + \alpha_q$
Parameter(s) varied*	Density	I_p and B_t, with I_p/B_t held fixed	I_p	B_t
JET	0.94	-1.2	(-0.05)	-1.15
DIII-D	0.99	-0.97	0.83	(-0.14)
COMPASS-D	1.0	-2.9	1.6	-1.1

*The second row gives the plasma parameter, which is varied (all others are held fixed) to determine the scaling.

There is very good agreement on the scaling of the density threshold (α_n). The scaling with toroidal field (α_B) agrees within error bars between JET and DIII-D but differs significantly for COMPASS-D. The difference in the field scalings of the three data sets — extrapolated to the same density, q_{95} and effective harmonic amplitude — is explicitly shown in Fig. 3-27. The COMPASS-D and JET scalings are clearly different, while the DIII-D scaling matches the JET scaling, albeit with significant uncertainty owing to the limited range of B_t variation.

The cause of the toroidal field scaling differences between COMPASS-D and JET (and DIII-D) is not yet understood. However, it is found that the variation of measured plasma velocity with toroidal field is stronger in COMPASS-D than in the larger machines, and it is thought that this variation (which can in turn affect the error field threshold) may underlie the stronger toroidal field (α_B) scaling. The differences in α_q seen in Table 3-II may be due to different error field harmonic compositions and their variation as the edge-q changes. While there is present uncertainty as to the q scaling, this uncertainty does not appreciably affect extrapolation to

ITER/reactor conditions, since the differences between safety factors in the present experimental data and proposed ITER/reactor safety factors are small.

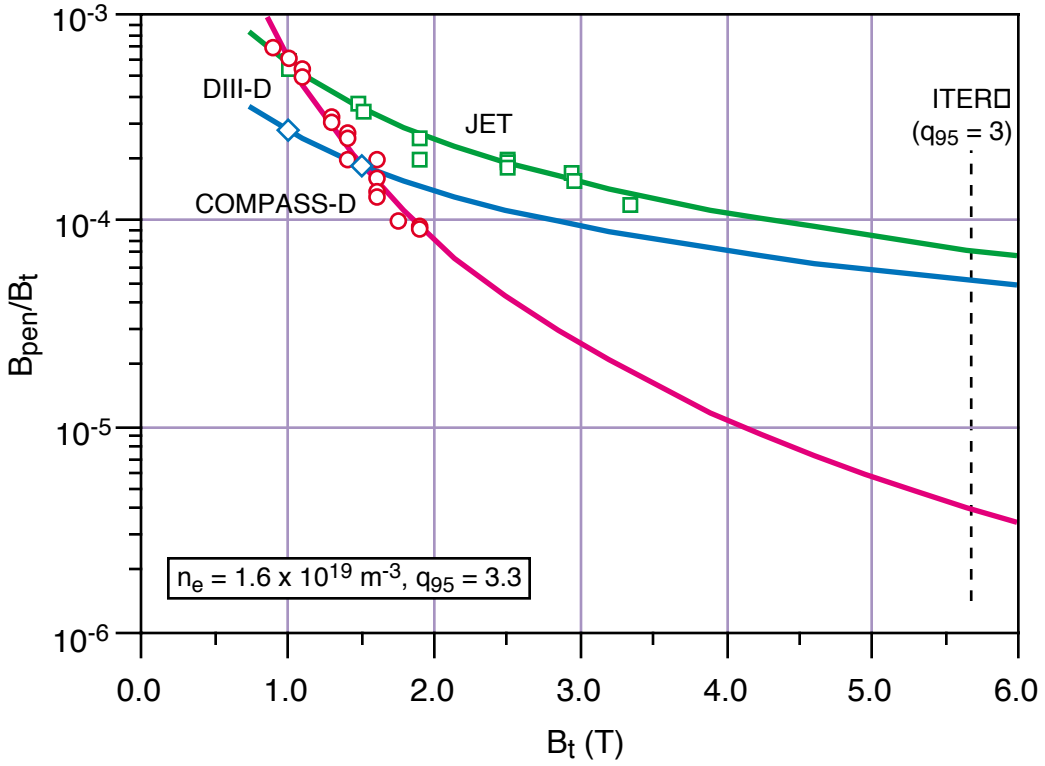

FIG. 3-27. Error-field penetration threshold (B_{pen}/B_t) in COMPASS-D (R = 0.56 m), DIII-D (R = 1.7 m) and JET (R = 2.95 m), scaled for $n_e = 1.6 \times 10^{19}$ m^{-3} and $q_{95} = 3.3$. The error field harmonic mix varies among the three experiments. The data plotted are the equivalent 2,1 field as evaluated using Eq. (3-10) for COMPASS-D and JET and Eq. (3-11b) for DIII-D. The single-experiment toroidal field scalings (α_B) given in Table 3-II are also shown.

High-Beta Effects. The data presented above all address the effect of error fields on low-density, low-beta Ohmically-heated plasmas. There is ample experimental evidence that adding even modest amounts of toroidally-unbalanced neutral beam injection (NBI) significantly improves the tolerance of such 'NBI-driven' plasmas to error-field mode locking, and both 'early' and 'late' application of NBI is a well-known method for locked mode disruption avoidance during the start up and shut down phases of presently-operating tokamaks. However, experimental error-field tolerance results obtained in DIII-D (Fig. 3-28) show that while the initial benefit of NBI-induced

rotation is appreciable, the locked mode tolerance of high-beta, beam-heated plasmas eventually decreases as the beta increases.

For H-mode plasmas, the deterioration of error-field tolerance can be explained in terms of the enhanced tearing mode instability that the strong pressure gradients characteristic of H-mode confinement produce [3.138]. Note in Fig. 3-28 that at high beta (near the ideal MHD or Troyon limit) the error-field tolerance of 2×10^{-4} seen at high density (5×10^{19} m^{-3}) is comparable to the error field tolerance seen for low-density Ohmic startup plasmas at 2×10^{19} m^{-3}.

While projection of this type of high-beta locked mode susceptibility to reactor and ITER plasmas (which have much weaker rotation drive and where NBI may not be present) is a complex matter that has not been pursued in detail, simple extrapolation of the DIII-D data and theoretical model to ITER [3.138] suggest that high-beta error field tolerances may be ~10^{-4}. In this regard, error field sensitivities during the high-beta DT burn phase appear to be similar to those during the low-beta start up phase.

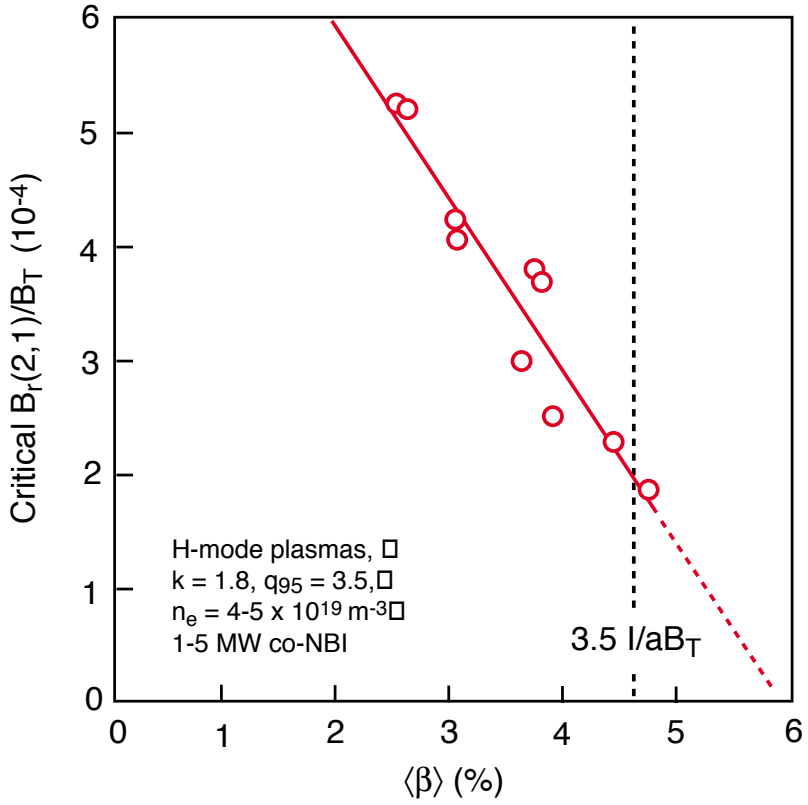

FIG. 3-28. Error field tolerance versus β for DIII-D beam-heated H-mode plasmas

3.2.5.4. Implications for ITER

Error field thresholds have been determined for Ohmic plasmas with the ITER-like shape, q_{95} and density, and so to extrapolate these results to ITER start up plasmas it remains only to take account of the size and B_t scaling. The scaling to the ITER toroidal field using the scalings from COMPASS-D, DIII-D and JET is shown in Fig. 3-27. Determining the size scaling is more problematical.: since the COMPASS-D data is apparently in a different regime (different B_t scaling) it can not be used in an empirical cross-machine extrapolation to ITER. In addition, given the accuracy of the penetration threshold data (due in part to differences in the error field spectra and in part to basic measurement uncertainties) and the limited difference in major radius between DIII-D and JET (1.7 m and 3.0 m), a 'two-machine' empirical extrapolation based on DIII-D and JET is also rather uncertain. Alternatively, the size scaling can be inferred indirectly on a 'single-machine' basis from the dimensional constraint ($\alpha_R = 2\alpha_n + 1.25\alpha_B$). For JET, DIII-D and COMPASS-D this gives $\alpha_R = 0.4\pm0.2$, 0.79 ± 0.3, and -1.65, respectively. Determining the size scaling in this way is again not wholly satisfactory (there is no compelling independent data to demonstrate that the dimensional constraint is actually obeyed) but is the best that can be done at present. Here again, JET and DIII-D results are in approximate agreement and suggest a modestly favorable positive size scaling (allowable normalized error field increases with size, all other factors being equal). In contrast, the COMPASS-D size scaling suggests a strongly unfavorable scaling.

In ITER it is likely that the time of greatest danger for inducing a locked mode will occur during the low density phase ($n_e \sim 2 \times 10^{19} m^{-3}$) required for H-mode access. For ITER at this density and with $q_{95} = 3.3$, the threshold ($B_{2,1}/B_t$) for a pure (2,1) field is 1.25×10^{-4} and 2.0×10^{-4} obtained respectively by using the JET and DIII-D values for α_R and α_B. Given the typical 2/1/0.67 1,1, 2,1, 3,1 harmonic mix expected in ITER, the allowable 2,1 component will respectively be about 6×10^{-5} and 10×10^{-5}. Allowable error field magnitudes arising from

extrapolation of the COMPASS-D results are more than an order of magnitude smaller, but given the apparently different physics regime, these predictions are thought to be less reliable. This is particularly highlighted by extrapolations from COMPASS-D to JET, which differ from the actual JET data by an order of magnitude in error. Finally, we observe that if we disregard the COMPASS-D data and interpret the DIII-D and JET data presented in Fig. 3-27 as showing no discernible (strong) size scaling, a simple field-scaling-only extrapolation of the DIII-D and JET data to ITER field (5.7 T) yields an equivalent (multimode-weighted) normalized allowable error field of $B_{pen}/B_T \approx 7 \times 10^{-5}$.

We also note parenthetically here that most tokamaks built to date have been able to (eventually) achieve inherent 'as-built' or 'as-corrected' error fields ($B_{2,1}/B_t$) in the range of $1\text{-}3 \times 10^{-4}$. Given this achievement, inherent construction-arising error fields normally do not result in appreciable operational limitations in present tokamaks except in the low-density Ohmic plasma regime (several tokamaks encounter *no* error-field-generated locked mode problems). We also note that projections of the construction and alignment accuracies expected for the ITER poloidal field and toroidal field coils suggest that the 'as-built' ITER 2,1 error fields will be $\sim 10^{-4}$. While consideration of the 'engineering' feasibility of achieving 10^{-4} error fields in ITER is beyond the scope of this Section, we believe on the basis of past experience in present tokamaks that it is likely that error fields of this magnitude can (and will) be obtained in ITER and reactor tokamaks and that these error fields will have an appreciable effect upon mode locking in start up plasmas in these tokamaks. Provision of error field correction to ensue robust tolerance to error fields during start up therefore seems prudent. In addition, since simple extrapolation of present high-beta error field tolerance data to ITER suggests that similar (or perhaps higher) sensitivities to error fields may arise during the high-beta burn phase, error field correction, likely with multi-mode capability, appears to be a doubly-prudent addition to the magnetic/plasma control capabilities ITER and reactor tokamaks. The availability of a multi-mode error field variation capability in ITER would also allow the effects of externally-applied RMPs to be definitively investigated in a reactor-regime plasma experiment.

3.2.5.5. Error field correction and other locked mode avoidance means

Given that error fields will likely impose operational limits for ITER startup and DT burn, error-field detection and correction methods need to be considered. Both COMPASS-C and DIII-D have used in-situ detection coil arrays to determine error fields. In the case of DIII-D, a coil array was temporarily installed within the vacuum vessel to measure PF-coil-produced error fields [3.136]. In the case of COMPASS-C, a measuring coil array was permanently installed outside the vacuum vessel and was used to minimize errors during construction [3.139]. JET experiments have determined the error field (though not its detailed sideband structure), with a plasma-based detection method, by making measurements with a range of applied error field phases [3.140]. On DIII-D the contribution to the error field spectrum from the TF coils is determined by multi-variate fits.

Correction of error fields using coils external to the plasma is routinely used on DIII-D where PF coil construction and alignment errors have resulted in 'as-built' error fields of approximately 7 G [$B_r(2,1)$ /2.1 T) $\approx 3 \times 10^{-4}$] [3.127]. These error fields are large enough to cause locked mode difficulties, especially at reduced $B_t \sim 1$ T, for Ohmic plasmas with densities $\leq 2 \times 10^{19}$ m^{-3}. The recent addition of a 'C-coil' correction coil set (six 60° picture-frame coils located external to the TF coil) combined with use of the previously-installed 'n = 1' correction coil (a single off-center coil located above the TF coil which produces a mix of harmonics) [3.127] has made simultaneous correction of the 3,1 and 2,1 modes possible, thereby allowing locked-mode-free plasma operation to be extended to densities below 1×10^{19} m^{-3}. In this regard, previous attempts to correct the as-built errors with the 'n = 1' coil alone were not as successful, apparently owing to the introduction of increased 'sideband' modes (1,1 and 3,1) when the dominant 2,1 error field was corrected. Given a 'multi-mode' sensitivity to sideband harmonics as is embodied in Eqs. (3-10) or (3-11b), some care (sideband mode control) in applying corrections is need to avoid compromising the intent of correcting the 2,1 error field. On COMPASS-D it was shown

that error field correction may be achieved without detailed matching between the spectrum of the error field and correction coil [3.141]. However, higher sensitivity to field errors in ITER may make more detailed matching of the correction spectrum (multi-mode correction, as in DIII-D) more important. The issue here — related to which harmonics can be independently controlled — is affected by the detailed design (including the number of independent coils sets) of the ITER correction coil system.

Measurement of the 'as-built' ITER error fields to the required precision with an in-situ coil array appears technically feasible [3.142], but will require both a relatively elaborate in-torus apparatus and scheduling of the measurement when the toroidal and poloidal field coil systems can be energized to nearly full levels. Development of an efficient plasma-based error field correction assessment means or procedure would obviate what otherwise appears to be a significant cost and schedule time requirement in the ITER device commissioning sequence. The availability of plasma-based system would also eliminate concerns about the difficulties that would be encountered in ITER (or a reactor) if the in-torus apparatus would have to be re-installed to realign coils or check error field characteristics after nuclear (DT-burning) operation commences.

There are also a number of non-magnetic means to avoid locked mode difficulties. Experiments on COMPASS-D have showed that ECRH resonant near $q = 2$ can remove error field locked modes [3.141]. Another possibility to avoid locked modes is to raise the error field threshold by using neutral beam injection to increase the plasma rotation. For start up locked-mode avoidance, counter injection would be the most efficient means to do this, since it adds to the intrinsic Ohmic rotation, which is in the electron drift (counter) direction. Simple calculations [3.142] indicate that 5 to 10 MW of tangential counter-injected 1 MeV beams in ITER would increase the error field threshold by about a factor of 5. Slightly higher power co-injected beams — the present ITER design basis, chosen for reasons of NBI current drive orientation — would have the same effect. The increase in error-field threshold with NBI has been demonstrated experimentally on JET during field ripple experiments [3.143] and on DIII-D in L-mode plasmas [3.138].

3.2.5.6. Summary

Best present extrapolations to ITER based on JET and DIII-D data indicate an error field threshold to induce a locked mode in low-density Ohmic plasmas of $B_{r2,1}/B_t \sim 10^{-4}$, though there is some remaining uncertainty over the size scaling. Given that error fields of the same magnitude are projected to arise from ITER construction tolerances, error field correction appears prudent. Several error field correction methods (correction coils, ECRH and NBI rotation) have been shown to be viable experimentally in present tokamaks. Further work is needed, and planned, to resolve discrepancies over the toroidal field dependence of the locked mode threshold. Also the effects of error fields in high-β regimes, where the critical error field for locking decreases as the β-limit is approached or where error-fields may act as the seed for neoclassical modes (Section 3.2.2) needs to be investigated further. It is also possible (likely) in ITER that the provision of an ECRH or ECCD MHD island control capability to limit the size of saturated neoclassical islands may prove equally useful in avoiding the occurrence of error-field-induced locked modes. However, both the neoclassical island and locked tearing mode mitigation aspects of such rf control methods remain to be demonstrated and carefully studied in present tokamaks.

3.2.6. Edge Localized Modes and MHD in the Plasma Edge

Edge Localized Modes and other MHD instabilities localized in the plasma edge region (defined roughly as comprising the last 5% of the closed flux surfaces) of a tokamak play a key role in mediating the energy and particle transport characteristics of the plasma edge in the regime of enhanced global energy confinement called the high confinement mode (H-mode). The transition from low confinement mode (L-mode) to high confinement mode (H-mode) in magnetic confinement systems is normally accompanied by the appearance in the H-mode phase of a periodic edge instability phenomenon that has come to known as Edge Localized Modes (ELMs)

[3.19]. The underlying causative mechanism for ELMs is the onset of MHD instability in the plasma edge when the edge pressure gradient exceeds a critical threshold. The subsequent loss of edge confinement leads to a temporary reduction of the pressure gradient, and the eventual recovery of the pressure gradient leads to recurrence of the ELM. This cycle, which continues indefinitely in a sustained H-mode discharge, is a ubiquitous feature of such long-pulse H-mode plasmas. The reference plasma operation mode for ITER is projected to be with an ELMing (or ELMy) H-mode.

The study and categorization of ELMs and their effect on plasma energy confinement in the plasma core and on the power and particle flow to the divertor region encompass a subject of considerable richness and scope. This Section of the *ITER Physics Basis* approaches ELMs and related edge instabilities largely from the viewpoint of the ideal and non-ideal MHD stability considerations that apply to their occurrence and characteristics. How these MHD stability aspects extrapolate to reactor tokamaks and ITER is also addressed here. Since much of the present understanding of ELMs derives from their phenomenology, the material that follows here necessarily begins with a brief presentation of this phenomenology and the resulting categorization of ELMs that arises. A more comprehensive presentation of the phenomenology and categorization aspects of ELMs is given in Chapter 4. The effects of ELMs on plasma energy confinement are addressed in detail in Chapter 2.

3.2.6.1. ELMs and other edge MHD instabilities

ELMs were first observed upon discovery of the H-mode in auxiliary-heated divertor plasmas in ASDEX [3.144] and have subsequently been universally observed in all divertor tokamaks and also in limiter tokamaks in certain operational regimes. In all cases, the most immediate manifestations of ELMs are characteristic sharp periodic increases in D_α (or H_α) emission from the divertor or limiter region. These increases are caused by a temporary breakdown of the H-mode edge confinement barrier. As a result, plasma particles and energy are expelled, and the enhanced recycling increases D_α emission. ELMs are also accompanied by

various edge region fluctuations (both magnetic and kinetic) and localized bursts of MHD activity, including magnetic precursors, and there are also directly-observable changes in the edge region plasma temperature and density profiles and energy content. In these regards, the basic phenomenology of ELMs — the periodic MHD-initialed loss of edge confinement and pressure and the subsequent release energy and particles to the plasma-defining surfaces in a tokamak — is well understood.

The cycle of ELM breakdown and profile recovery repeats on a more or less periodic basis, typically with some quasi-stochastic variation in period and D_α magnitude. The relative amplitude of the initial D_α burst and the repetition period and frequency coherency of the ELMs obtained in a given experiment vary, but in a broad sense depend primarily upon the proximity of the plasma operation conditions to the H-mode edge power threshold (see ELM phenomenology below and also Chapters 2 and 4). A number of types of ELMs with different amplitude, frequency and power dependencies can be distinguished: the principal types relevant to ITER are anticipated to be small-amplitude, high-frequency Type III ELMs, which appear when the power flow to the plasma edge is only marginally above the H-mode edge power flow threshold (see Section 2.4) and the higher-amplitude, lower-frequency Type I ELMs, which develop when the edge power flow significantly exceeds the H-mode threshold. Figure 3-29 shows an example of the D_α intensity waveforms for these two types of ELMs in a representative divertor experiment. As will be presented, the occurrence of these two types of ELMs can be ascribed to two distinct MHD instability mechanisms. Since the operation regime for ITER is anticipated to be near the projected operation domain boundaries for both Type I and Type III ELMs (see Fig. 3-31 and associated text below), understanding of both mechanisms is needed for ITER.

Figure 3-29 also shows an ELM-free period between the periods were Type III and Type I ELMs occur. 'ELM-free' H-modes, sometimes without clear indication of preliminary Type III ELMs, are also obtained transiently in many tokamaks, especially under conditions of high power input and rapid L-H transition. The ELM-free period is generally interpreted as being due to the finite time required for the edge pressure gradient to reach the level required for onset of a Type I

ELM, with the discharge then subsequently either lapsing into repetitive Type I ELMing or, if the amplitude of the first ELM is large enough (a 'giant' ELM), terminating disruptively following the first ELM. In other plasma operation regimes, sustained repetitive Type III or Type II ELMs (see below) may develop rather than repetitive Type I ELMs.

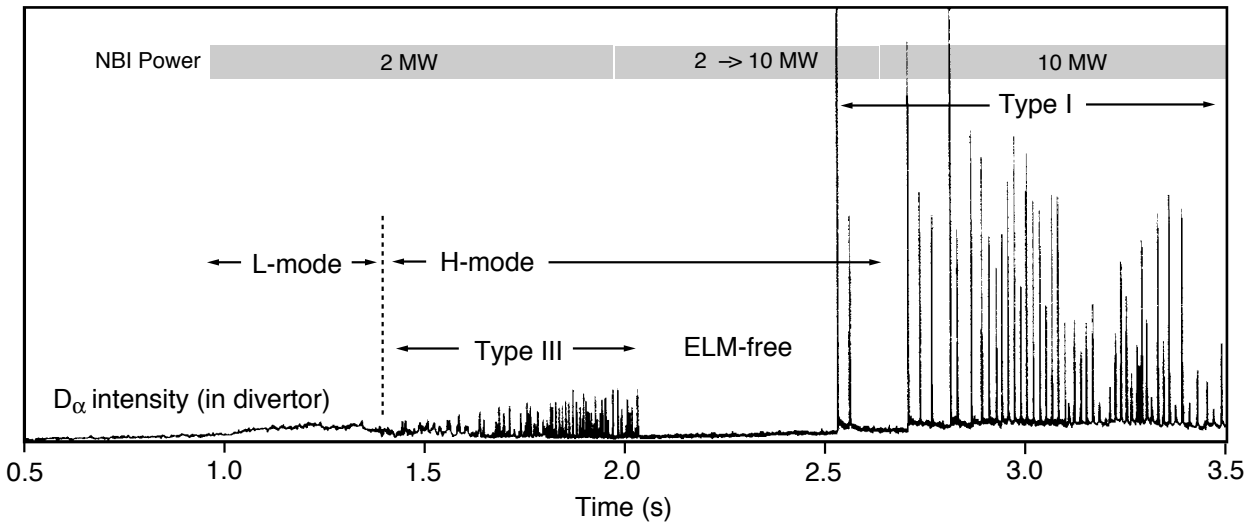

FIG. 3-29. Divertor region D_α intensity in a typical DIII-D plasma with slowly increasing neutral beam injection power. Low-amplitude Type III ELMs appear after the L-H transition when low NBI power is applied and disappear as power is slowly increased. Larger Type I ELMs with increasing frequency appear at high power. Summarized from a more-complete data set presented in [3.19], Fig. 2.

Other types of edge MHD instability are also possible. In hot-ion H-mode plasmas in JET, the ELM-free phase can also be terminated by onset of the so-called *outer mode,* a ~10-kHz n = 1, m = 3-5 sustained MHD oscillation that is typically localized in the outer 20% of the plasma [3.145]. The outer mode, which causes a degradation of central confinement and DD neutron yield (Fig. 3-30), is in some examples followed by a giant ELM that further degrades confinement and DD yield. Edge MHD instabilities with characteristics similar to the JET outer modes have been seen in ASDEX, DIII-D and JT-60U (see [3.145] and references therein). The MHD mechanism responsible for the outer modes appears to be distinct from the mechanism responsible for giant ELMs, but the effects of both types of MHD activity on edge and global confinement

characteristics are somewhat similar, including the enhancement of divertor D_α during mode activity and the sustained effect of an outer mode or ELM on central confinement that continues even after the MHD event that comprises the ELM itself or the outer mode is over.

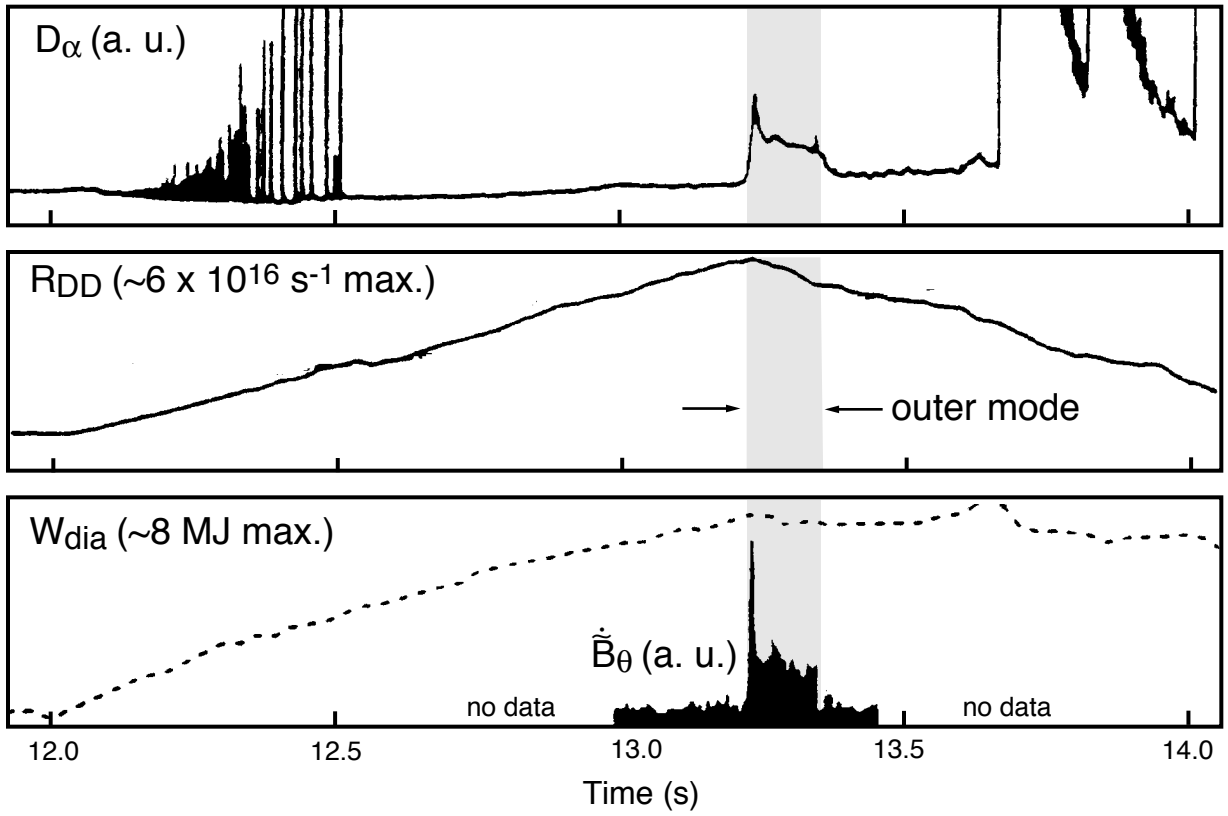

FIG. 3-30. Magnetic fluctuation amplitude and divertor D_α intensity indications of an 'outer mode' MHD event in a JET hot-ion H-mode deuterium discharge (No. 33648). The 100-ms outer mode MHD event results in a corresponding transient increase in divertor D_α and also initiates an prompt and irreversible deterioration of plasma energy confinement and DD neutron yield. Applied NBI power is constant for the full data period (12-14 s) shown. Summarized from a more-complete data set presented in Ref [3.145], Fig. 1.

ELMs have a number of global and local effects on plasma performance and the exhaust of plasma power and particles (hydrogen and impurities) by the divertor. Repetitive Type I or Type III ELMing usually results in some net deterioration of global energy confinement relative to the confinement that can be transiently obtained during the corresponding ELM-free phase of a discharge (see Sections 2.5 and 2.6). Type I ELMs generally have less confinement impact than

Type III ELMs (see Sections 2.5, 2.6 and [3.19]). But ELMs have a beneficial effect with regard to the prevention of density and impurity accumulation by periodically exhausting particles that would otherwise be well-confined within the H-mode edge barrier. It is envisaged that ITER will operate in ELMy-H-mode because the periodic increases in the plasma transport at the edge due to ELMs will avoid impurity accumulation problems and allow control of the plasma density and impurity levels. It is also not possible to see how the onset of ELMs can be avoided for the ~1000-s duration of the ITER discharge flattop.

On the other hand, it is necessary in ITER that the level of ELMs does not seriously compromise the energy confinement properties of the H-mode (see Sections 2.4.2 and 2.5.2). Furthermore, the transient heat loads deposited in the divertor by the ELM must not be too large, in order to avoid thermal damage to the target plates. Finally, there is wide-spread evidence that large-amplitude ELMs can couple to other MHD phenomena (e.g., neoclassical island tearing modes, Section 3.2.3) and thus cause a deterioration in core confinement [Chapter 2] or initiate disruption (Section 3.4.1) or a loss-of-equilibrium-control vertical displacement event (Section 3.4.3). There are therefore many reasons why ELM physics is an important issue for ITER and why optimization and/or control of ELMs will be important for overall plasma optimization in ITER and reactor tokamaks. Understanding and controlling the MHD instability that causes ELMs is an important aspect of the problem.

3.2.6.2. ELM phenomenology and categories

Present understanding of ELMs is largely phenomenological, and while there is progress towards developing first-principles theories of ELMs (see Section 3.2.6.3) and assessing their effect on plasma performance, at present, understanding of ELM effects and how these effects may extrapolate to future devices is largely based upon phenomenology. It is therefore necessary here to go into this phenomenology in some detail and to try to ascertain how it is affected by plasma and operation parameters (size, shape, field, power, etc.). As will become apparent during this presentation, ELM phenomenology contains a considerable richness and significant experiment-

specific features, and ELM theory is still immature, so definitive extrapolation to ITER and reactor tokamaks is still a matter of on-going discussion in the fusion community.

ELM types. At least three major types of ELMs have been defined [3.19]. In a given experiment, the level of the plasma heating power, P, or more directly, the net power reaching the plasma edge $P_{edge} = P - P_{rad}$ (i.e., heating power less radiation losses inside the edge region) is a key factor in determining the ELM type. For heating input or edge power levels at the corresponding threshold for H-mode, P_{th}, so-called 'dithering' ELMs have been identified; these are believed to be transitions back-and-to between L- and H-modes. With increasing power, Type III (or 'small') ELMs are encountered: their frequency decreases with power. As the power increases further, the Type III ELMs tend to disappear and an ELM-free H-mode may be encountered, but at higher power levels, larger amplitude type I (sometimes called 'giant') ELMs appear: their frequency increases with increasing power. A further class of ELMs called Type II (or, sometimes, 'grassy' ELMs) are associated with strongly-shaped tokamaks at high edge pressure when there is access to second stability at the plasma edge. High values of the parameter s/q^2 (magnetic shear/q^2) in the plasma edge appear to be the principal factor in determining the onset of Type II ELMs. Type II ELMs are anticipated to be relevant to ITER only for steady-state operation modes predicated on enhanced plasma performance (see Section 3.2.7) with plasmas that have higher elongation and triangularity than standard ITER plasmas.

Occurrence of ELMs. The circumstances under which ELMs appear provide clues to the underlying phenomena. These conditions can be best characterized in not in terms of the core plasma parameters, but rather in terms of the edge electron density n_e(edge) and temperature, T_e(edge), where the nomenclature 'edge' denotes the parameters at the top of the H-mode edge temperature pedestal. In medium-sized tokamaks (e.g., ASDEX-U), this edge location is typically about 2 cm inside the separatrix as measured at the outboard midplane, at $r/a \cong 0.96$. In ITER, the corresponding edge location would be about 10 cm inside the separatrix. Figure 3-31 illustrates the n_e(edge) – T_e(edge) domains for L-mode and H-mode operation in ASDEX-Upgrade and also

the corresponding domains for Type I and Type III ELMs and also for transient ELM-free operation.

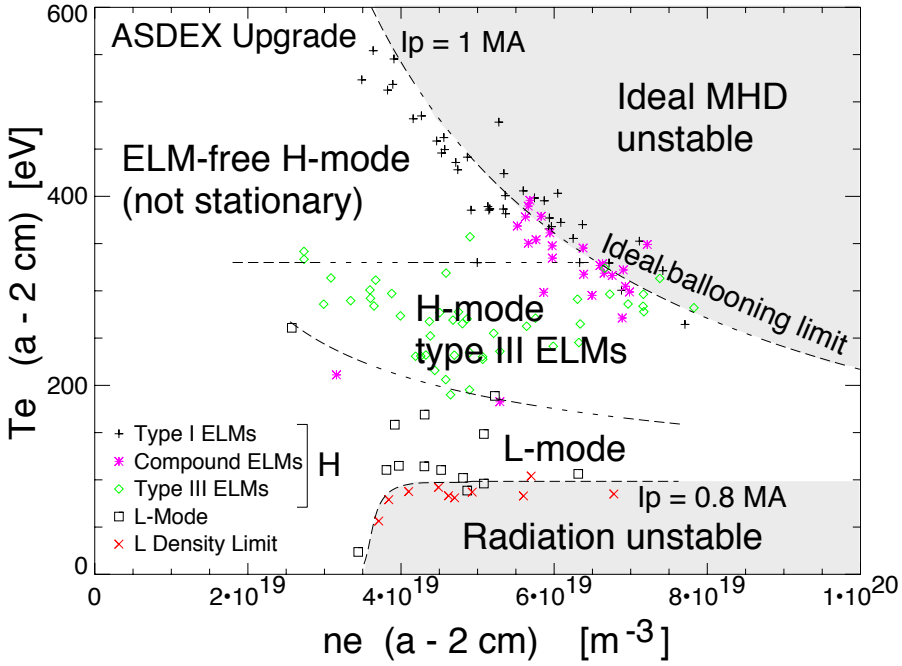

FIG. 3-31. H-mode operational diagram for ASDEX Upgrade presented in terms of the measured electron temperature and density 2 cm inside the separatrix (this location corresponds to the top of the H-mode pedestal). Boundaries indicating different types of confinement regime are marked (Kaufmann et al, 1997). The limiting bound of edge pressure (*nT*) corresponds closely to the predicted pressure gradient for onset of ideal MHD ballooning ('ideal ballooning limit').

Figure 3-30 illustrates the important and widely obtained finding that Type I ELMs appear to be closely connected with normalized local edge pressure gradients α near the ideal MHD ballooning limit α_c [3.19]. Measurements of Type I ELMs in JET that trace the edge pressure gradient trajectories in time show that such ELMs approach this ideal MHD limit [3.146], but some additional trigger event (e.g., an external kink) appears necessary to precipitate the ELM. Scaling studies on ASDEX-Upgrade also show that Type I ELMs are associated with the ideal MHD ballooning limit [3.147], but the discharge can sit at the ballooning limit for some time before an ELM occurs [3.148], again suggesting the need for an additional trigger, such as a low-*n* edge-localized 'peeling' mode, where *n* is the toroidal mode number (see *Ideal MHD* discussion below).

A similar correlation for Type I ELM onset with α_c is seen in JT-60U [3.14, 3.149]; furthermore the triangularity δ ($-0.06 < \delta < 0.4$) has been varied with results in accord with the triangularity dependence of α_c (in particular, as on JET, Type II ELMs are seen at high δ, associated with second stability). Studies in DIII-D [3.150] also show that Type I ELMs occur for $\alpha \sim \alpha_c$; it would appear that these ELMs can occur in ballooning-stable situations, suggesting that while ideal ballooning limits the pressure gradient, some other phenomenon is responsible for the ELM itself, since Type I ELMs can also occur in situations where the $n = 1$ ideal external kink is stable. More recent detailed edge pressure measurements made for Type I ELMs in DIII-D with a high-resolution Thomson scattering system show that $\alpha \sim (2–3)\alpha_c$ is consistently obtained in plasmas with an ITER-similar SND shape and aspect ratio (Fig. 3-32). The data shows no apparent sensitivity to s/q^2. While the scaling clearly that for ideal ballooning, why the magnitude of the pressure gradient substantially exceeds the ideal MHD instability threshold is not yet understood.

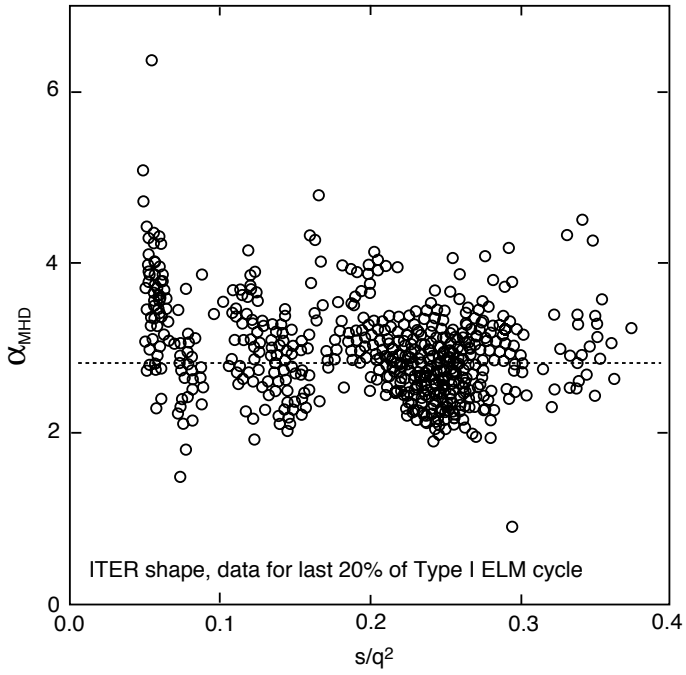

FIG. 3-32. Ideal MHD ballooning stability comparison data for Type I ELMs in DIII-D plasmas with ITER-like shape (q varies). The pressure gradient measured prior to Type I ELM onset consistently exceeds twice the calculated ideal ballooning gradient threshold.

Type II grassy ELMs occur in shaped plasmas at low s/q^2 (where s is the shear parameter $s = d(\ln q) / d(\ln r)$ and q is the safety factor), corresponding to access to second stability. Later studies have shown that α can exceed α_c [3.151] and that calculations taking full account of the equilibria, and the bootstrap current, are necessary for discussing second stability but are sensitive to details [3.152]. H-mode operation in Alcator C-Mod with ICRF heating has to date yielded only preliminary Type III ELMs followed by an ELM-free period, the latter despite pressure gradients with $\alpha \sim \alpha_c$. The lack of Type I ELMs may be associated with the ICRH: ELMs in JET are smaller with ICRH than with equivalent neutral beam heating(NBI) [3.153].Type III ELMs in ASDEX-Upgrade tend to appear below a critical electron temperature $T_e < 300$ eV [3.148]: this suggests a role for resistivity and the possible involvement of resistive ballooning modes. This hypothesis is reinforced by the observation that Type III ELMs can be stabilized by a sawtooth heat pulse and promoted by radiative cooling. Type III ELMs in DIII-D were originally characterized as appearing when $0.3 < \alpha/\alpha_c < 0.5$ [3.150] but recent analysis [3.151] shows that two classes of Type III ELMs exist: low-$\bar{n}_e$ Type III, which disappear above a critical value of α (corresponding to a critical power $P \propto I^{2.4} / \bar{n}_e^2$); and high-$\bar{n}_e$ Type III, which disappear above a critical temperature.

These observations as to the role of factors other than the pressure gradient in determining ELM type and stability are consistent with the observation of what are now recognized to be Type III ELMs in the original ASDEX H-mode experiments (the ASDEX observations were made at a time when distinctions among ELM types were not yet recognized). Only one type of ELM — resembling the Type III ELMs in DIII-D — was seen. Recent experiments in DIII-D that retroactively reproduced the ASDEX plasma configuration and parameters recovered a similar behavior — only Type III rather than Type I ELMs were seen, indicating again that plasma parameters other than ideal ballooning stability, such as T_e, plays an important role in determining ELM characteristics and MHD stability [3.150]. The interpreters of Alcator C-Mod data have suggested that Type III ELMs seen in their experiments are associated with steep edge density gradients which can excite micro-tearing modes [3.154]. The sensitivity of ELM characteristics to

geometrical parameters, such as shaping and plasma-wall separations has been demonstrated on TCV [3.155].

Finally, in COMPASS-D [3.156], ELMs disappear above a critical value of β_N and can be suppressed by edge current ramp-up: this effect was also seen (but less clearly) on PBX-M [3.157]. The ability of externally-applied resonant magnetic perturbations (RMPs) to trigger ELMs is suggestive that some tearing mode involvement in ELMs may be necessary [3.156] (see Section 3.2.5).

ELM Repetition Frequencies. The power dependence of ELM frequencies f_{ELM} has been used as a way of defining ELM types; the frequencies are also significant for estimating transport losses due to ELMs. In the case of giant ELMs in JET, f_{ELM} can be fitted in terms of the heating power P and plasma current I by the expression $f_{ELM} = 8.9(P - P_{rad})/I^{1.84}$ (Hz, MW, MA) where P_{rad} is the radiated power. This result shows that ELM frequency scales linearly with the power crossing the separatrix [3.158]. In JET NBI discharges f_{ELM} decreases with triangularity δ and increases with gas input [3.159]. In JT-60U, a strong link between f_{ELM} and the ballooning stability parameter [3.14, 3.149] is found, i.e., $f_{ELM} \propto P_{net} R q^2 / B^2 l_i$, where P_{net} is the net heating power and l_i is the internal inductance. As in JET, f_{ELM} in JT-60U varies inversely with δ in NBI discharges. Proportionally of ELM frequency to separatrix power is also observed in ASDEX-Upgrade: indeed a scaling law $f_{ELM} \propto P_{sep}/I$ has been proposed, although this scaling is also found to be affected by the use of gas puffs and impurity injection [3.160]. These results are supportive of the idea that f_{ELM} for Type I ELMs is set by the heating time for the pressure gradient to reach α_c. For Type III ELMs in COMPASS-D, f_{ELM} can be reduced by edge heating with ECRH — this observation is consistent with Type III stabilization by increasing T_e,— and f_{ELM} does not seem to depend on I [3.156].

Energy loss from ELMs. Measurements of the edge power losses attributable to the periodic recurrence of Type I ELMs provide further support for the ballooning limit instability origin of such ELMs. For Type I ELMs with $f_{ELM} \propto P_{sep}$ where the pre-ELM edge pressure gradient p' is at the ballooning limit, p_c', over a width Δr, the energy in the edge region scales as

$(\Delta r)^2 p_c'$. If a constant fraction δW of this energy is lost during the ELM and if Δr is independent of power, then the time-average loss fraction $\delta P/P$ should be power- and ELM-frequency independent [3.19]. ELM losses of a constant percentage of input power are frequently observed [3.158, 3.160, 3.161], so such observations are consistent with the hypothesis that Type I ELMs are determined by ideal ballooning with Δr approximately constant. However, detailed analysis of the fate of the lost energy shows that the actual loss process may be more complex than just simple ballooning, and this observation helps to discriminate against some theories. In particular energy loss is *not* always dominantly on the low field side (LFS) as might be expected for ballooning modes [3.151, 3.162]. Furthermore, the identification of non-thermal electron losses suggests that magnetic reconnection is involved in the ELM [3.156, 3.162–3.164]. The energy loss process can be modeled satisfactorily in terms of stochastic magnetic field transport based on the observed magnetic precursors [3.165].

The majority of the energy loss from the ELM ultimately reach the divertor plates, resulting in transient heat loads. For an ITER-class tokamak, large-magnitude Type I ELMs have sufficient energy to cause appreciable divertor surface heating and erosion, and hence avoidance of sustained operation with large-amplitude Type I ELMs is a potentially important issue for ITER. The subject of ELM-produced heat fluxes on the divertor plates is discussed in Chapter 4.

ELM Precursors and Fluctuations. A variety of fluctuations are observed in conjunction with the ELM cycle. Magnetic 'precursors' which may have a causal relationship to, or act as a trigger for, the ELM burst of magnetic fluctuations and transport are of particular interest. These precursors have been seen most clearly for Type III ELMs but there are also in observations in some tokamaks of precursors for Type I or 'large Type III' ELMs. Table 3-III summarizes the various observations. Details are discussed below, but briefly, Type III ELMs have clear magnetic precursors with $n \sim 5$–15, ballooning structures, $f \sim 100$ kHz and resistive growth times. Precursors are less evident for Type I ELMs, when turbulence grows on an ideal MHD time scale, although toroidal asymmetries suggest some other mode acts as a trigger. Precursor frequencies for Type I ELMs often drop just before the D_α burst.

Table 3-III. ELM Precursors in Various Tokamaks for Type I and Type III ELMs

Experiment	n	m	Δr (cm)	f (kHz)	τ (μs)
Type III ELMs					
JET	≥ 8	–	10	50 - 100	250
DIII-D high $\bar{n}_e$, low $\bar{n}_e$,	5 - 10 (6 - 13)	–		(50 - 80)	
ASDEX-Upgrade	10 - 15	15 - 20	4	100 counter; 60 co; (100, 200)	
Alcator C-Mod	> 5	> 10		150	≤ 50
COMPASS-D				70 - 120	≤ 200
TCV	5 - 8			120 -> 70	50
JFT-2M				250 –>	20
Type I ELMs (* denotes possibly 'large Type III')					
JET	0 - 4		5	15	100
ASDEX-Upgrade	5 - 10	10 - 15	1 - 2	(20 counter); 5 co, T_e only	10^3 $<10^3$
COMPASS-D*	3 - 8		1 - 2	70 - 120 Ohmic 140 - 200 ECRH	30
TCV*		16 - 20		50	50

( ) denotes sometimes 2 or more modes; –> denotes that the frequency drops in time

Observations in the various tokamaks vary somewhat at the detailed level. In JET there are clear edge-localized precursors (mode numbers, frequencies, radial localization and growth times are given in the Table) for Type III ELMs [3.166], but only erratic short-lived low-frequency precursors for Type I ELMs [3.167]. Type I ELMs instead exhibit bursts of 25–30 kHz MHD activity, with complex structure not confined to the plasma edge or divertor regions, growing in ≤ 30 μs, i.e., at the ideal MHD growth rate. In JET hot-ion H-modes, Type I ELMs are generally preceded by an outer-mode [3.145]. A low-n coherent mode is detected during the ELM;

observations of toroidal asymmetry of the ELM may be related to coupling to such a low-n mode structure [3.162].

On DIII-D, Type III ELMs typically have precursors with n = 5–10 [3.150], but more complex behavior with multiple modes is observed at low density [3.151]. For Type I ELMs, no coherent precursors are seen: instead broadband MHD activity grows for 30–50 μs before the ELM. In ASDEX-Upgrade [3.148] coherent precursors for both Types I and III, appearing ~1 ms before the D_α rise are seen, but the details differ somewhat for counter- and co-injected neutral beams. For Type III ELMs and counter injection, frequencies are ~100 kHz, measured and estimated mode numbers are respectively n = 10–15 and m = 15–20, and the modes are localized in an edge region with radial width $\Delta r \sim 4$ cm. In the case of Type I ELMs, magnetic precursors (~20 kHz) are only seen for counter-injection; although for co-injection a 5-kHz temperature fluctuation has been detected. The lack of magnetic detection of precursors for co-injection may be due to the low mode rotation frequency or because mode locking tends to occur. Type I precursors typically involve two frequencies, have n = 5–10 and$m$ = 10–15 and are localized with $\Delta r \sim$ 1–2 cm. In the case of the rotating modes, the precursors grow on a ms time scale, suggesting the presence of some wall stabilization, whereas the non-rotating, or locked, precursors grow much faster, on a sub-ms time scale.

Type III precursors are detected in COMPASS-D [3.156, 3.168] at 70–20 kHz with a growth time <200 μs. For Type I (or possibly larger Type III ELMs), the precursors have $f \sim$ 70–120 kHz (Ohmic) or 140 –200 kHz (ECRH). There are often two modes with n = 4 and 5, but there can also be multiple modes, with n = 3–8. Just before the D_α rise, the mode grows on the 30 μs time scale, f drops and the mode evolves into an n = 1 mode, with broadband turbulence during the D_α spike. There is also a further drop in f during the D_α spike. This mode evolution has been interpreted as a sudden interchange of flux tubes which halves m and broadens spatially, suggesting resistive reconnection [3.169].

Type III and either Type I or large Type III ELMs are seen in TCV [3.155]. The Type III ELMs have precursors that develop several 100 μs before the D_α rise. these precursors are

toroidally localized on the low-field-side (LFS) of the plasma, with n = 5–8 [3.170]. These modes grow in amplitude and toroidal extent on a time scale ~50 μs; the D_α rise and growth of magnetic turbulence only begins when the mode has spread toroidally. The poloidal mode numbers m can only be measured in the case of large ELMs. Modes for large ELMs are also localized on the LFS, have $f \sim$ 50 kHz, growth time ~50 μs and m = 16–20. The toroidal localization suggests the involvement of some other mode, e.g., a pressure-gradient-driven tearing mode.

Type I ELMs are not seen in Alcator C-Mod [3.154], despite the edge pressure gradient being near the ballooning pressure limit; this may be due to ICRF heating. Type III precursors are seen and are found to have f ~150 kHz, $m > 10$, $n > 5$ and duration ≤ 50 μs.

3.2.6.3. Theories of ELMs

Theories of ELMs can be divided into three different classes [3.172]. The first class of models are those of a conceptual nature which discuss the conditions for some underlying instability (usually within ideal or resistive MHD) to occur and describe the ELM cycle qualitatively in terms of the periodic build up of the plasma edge conditions to trigger the instability, the consequent loss of plasma edge confinement and finally a recovery phase for the cycle to repeat. The second class of models are those based on limit cycle solutions to models developed to explain the L-H transition and formation of the H-mode edge transport barrier. These models involve coupled equations for transport, turbulence and flow shear and are often electrostatic in nature, and so do not describe the associated MHD fluctuations. The third class of models are limit cycle models in which MHD activity is excited and plays a role in the transport. These three classes of models are summarized briefly below. In all cases, validation and application of the models are matters of on-going discussion within the fusion research community.

MHD Instability Theories. These theories focus upon the effect of MHD instability in initiating ELMs. Theories based upon the effects of both ideal and resistive instability have been developed. Both types of theory have had some success in correlating the predictions of the

theories with the various phenomenology and precursor observations presented above. But as the richness in the observations noted above suggests,

Ideal MHD models. Manickam [3.173] showed numerically that increasing the edge current j_α, particularly with higher p'_α, could lead to $n = 1$ modes, with mixed m, having Alfvénic growth rates. These high-m n = 1 modes can be radially localized at the edge (and hence are typically described as 'peeling' modes owing to the edge-localized loss of plasma that they effect) or global, and can be anti-ballooning, i.e., they have maximum amplitude on the high-field-side (HFS) of the plasma. Huysmans *et al* [3.174] have explored numerically the conditions for low-n external kink stability in JET; in particular an operating diagram in j_α and p'_α has been established. Localized external kink modes are destabilized by a finite j_α, while low values of p'_α ($\alpha << \alpha_c$) have a weak stabilizing effect, particularly on the $n = 1$ mode. For higher values, $\alpha \sim \alpha_c$, the external kink is destabilized by pressure, at first for higher n; the value of the edge bootstrap current is sufficient to cause unstable kink modes in Hot Ion H-modes. At higher β-poloidal and triangularity, access to a second stable regime is possible at lower values of j_α, which do not excite external kinks. Current ramps in these situations can thus allow access to second stability while avoiding peeling modes.

Connor *et al* [3.175] considered localized peeling modes driven by j_α analytically, showing how these can be stabilized by finite pressure through the effect of the 'magnetic well' (i.e. 'Mercier' term) of the Pfirsch-Schlüter currents. Thus, as the plasma is heated, stability depends on a competition between the destabilizing effects of the increase in T_e (which increases the Ohmic current and, if the collisionality is reduced, also the bootstrap current) and the stabilizing effects of p'. If these *p' stabilizing* effects dominate, then with increasing P, the ELMs will die away, like Type III ELMs and f_{ELM} will decrease, since the heating delays the growth of the edge current needed to destabilize peeling modes. If the peeling modes are actually stabilized, an 'ELM-free phase can develop and α can rise to the ballooning limit, whereupon a Type I ELM triggered a coupled peeling/ballooning mode eventually ends the ELM-free phase after the time needed to build up sufficient edge current. These prediction generally fit the generic behavior shown in Fig. 3-29.

Pogutse *et al* [3.176] considered the possibility that ballooning modes in the scrape-off-layer (SOL) can induce a giant ELM by first releasing impurities which subsequently weaken line-tying in the edge of the core region, leading to an interchange instability. These modes grow with a rate $\gamma \sim c_s/(\Delta R)^{1/2}$, where c_s is the sound speed, Δ the SOL width and R is the major radius. They are estimated to remove plasma in a layer $\Delta r \sim (1/nq)a$ and for $n = 1$, $\delta W/W \sim 5\%$, which is typical for Type I ELMs. The ELM frequency is predicted to scale as $f_{ELM} \propto BP/(I^3\Delta^{0.5})$. These results are broadly consistent with observations on JET [3.158].

In fact all theories involving the ideal MHD ballooning limit will predict $f_{ELM} \propto P$, since P controls the heating time to reach the critical gradient. Furthermore, they will remove an amount of plasma energy given by $\delta W \propto (\Delta r)^2 p'$, which results in fractional losses owing to ELMing that will be independent of P to the extent that Δr is a constant.

Resistive MHD models. The ELM model initially developed by the ASDEX Team [3.177], based on ASDEX parameters, predicted the evolution of resistive MHD modes: current-driven peeling modes and resistive ballooning modes. These modes are found to remove a layer $\Delta r \sim a/10$ in a time $\Delta t \sim 20$ μs. Huysmans *et al* [3.178], who only considered JET equilibria, showed resistive ballooning modes with $n \geq 10$ were unstable. Both these theories are able to describe the characteristics of Type III ELMs: Type III ELM stability increases with increasing power since T_e (and hence conductivity) increases, and f_{ELM} decreases since it is necessary to achieve greater values of p'_α to destabilize them at higher T_e.

An explanation of ELM-precursors in terms of an instability due to a relative of the so-called 'micro-tearing' mode has been investigated by Lau [3.179]. The micro-tear mode, which is driven by the electron temperature gradient, is found to be unstable in the steep density gradient region of the H-mode pedestal, but not in the lower density gradient of an L-mode edge density profile. Kinetic effects will limit instability to higher values of m, so $10 < m < 40$. Thus modes with frequencies 100-400 kHz and growth times 80-320 μs are predicted; these are proposed as an explanation of Type III ELMs, e.g. in Ref [3.154].

L-H transition theories. This class of ELM theories is based upon models of the L- to H-mode transition. The theory of Itoh *et al* [3.180] applies to 'dithering' ELMs near the L-H transition: it involves no magnetic fluctuations. The application of this theory, generalized to include density transport, by Zohm [3.181] explains the characteristics of near-transition ELMs in ASDEX. The theory of Vojtsekhovich *et al* [3.182] considers ELM behavior with heating schemes (e.g., lower hybrid) that generate fast electrons. If the electrons are not thermalized, they can escape, possibly along braided magnetic fields. With increasing power P the plasma is predicted to make a transition from L-mode to ELMy H-mode and then to H-mode.

L-H transition theories with MHD activity. The theory of Lebedev *et al* [3.183] involves coupled, local equations for turbulent transport caused by a combination of 'soft' drift wave and 'hard' MHD fluctuations. The theory also considers the stabilizing effects of flow shear generated by Reynolds stress and diamagnetic velocities and the damping effects of parallel viscosity. Two situations in which the theory is applicable arise. At powers near the H-mode onset threshold, with

$P \sim P_{th}$, when poloidal flow dominates, ELMing behavior is possible. However, this ELMing phase follows an ELM-free phase for lower P. In the theory, the ELMs themselves take the form of MHD bursts with duration $\Delta t \sim 1/\gamma_A$ which destroy the region of velocity shear that is responsible for producing the H-mode transport barrier. At low edge power, the theory first predicts $f_{ELM} \propto P^{-1}$ (i.e., Type III ELMs), but with increasing power, $f_{ELM} \propto P$ (Type I ELMs). The second situation in which the theory applies corresponds to a case with greater P, when diamagnetic flows dominate; there is then no intermediate ELM-free phase. But again there are MHD bursts and $f_{ELM} \propto P$ (i.e., Type I ELMing).

The *M*-mode theory of Itoh et al [3.184] is based on the onset of stochastic magnetic field transport in their so-called 'CDBM' transport model at a critical value of α and shows hysteresis in α; the *M*-mode transition occurs at a lower value of α than the ideal ballooning limit α_c, say by 20-50%, while the back transition occurs at an even lower value. The *M*-mode transition is associated with a burst of MHD turbulence and a stochastic magnetic island diffusivity from overlapping islands which is typically 20 times greater than the L-mode diffusivity χ^L. The

growth of the MHD turbulence is on a time scale γ_{Ap}^{-1}, where γ_{Ap} is the poloidal Alfvén frequency. The onset of the *M*-mode at a radial point r_p precipitates an 'avalanche' over a region Δr, removing the pressure gradient. The ELM period is given by the heating time, so f_{ELM} increases with heating power. The theory also provides an estimate of the plasma energy loss δW during an ELM: $\delta W \propto (\Delta r / a) W_{ped}$ where W_{ped} is the pedestal energy. These results are in accord with observations of giant ELMs on JT-60U [3.14, 3.149].

Limit cycle solutions of a transition model based on a *M*-Mode hysteresis diagram, but also allowing for a probabilistic element in the parameters, are presented in [3.185]; ELM cycles for gradients below the critical one can occur with finite probability. This aspect of the model can explain the stochastic range of ELM frequencies that are seen in experiments.

The transition/MHD theory of Pogutse *et al* [3.186] invokes resistive interchange modes in the SOL. When the parameters are far above the instability threshold, the theory predicts quasi-periodical oscillations in time corresponding to spikes of density (or heat) flux at the boundary; these can be interpreted as ELMs. The model exhibits the property that ELMs first appear as β increases and then, in part since the threshold criterion scales as $(T_e)^{-1}$, subsequently disappear as T_e increases. It is therefore expected that f_{ELM} decreases with P. These behaviors mimic those for Type III ELMs.

Finally, the transition/MHD theory of Horton *et al* [3.187] is also associated with electrostatic resistive pressure-gradient-driven turbulence. These authors also develop equations for the evolution of the fluctuation energy, the energy in the sheared flow and the potential energy associated with the pressure gradient. At higher levels of power P, there is a bifurcation from the stable H-mode to a limit cycle solution which can be identified with the ELM. The frequency of the cycles first decreases with P, as is characteristic of f_{ELM} for Type III ELMs, but then f_{ELM} begins to increase with P for $P > 1.6\, P_{th}$ because there is a need to transport more energy out of the system by means of the ELMs.

3.2.6.4. Extrapolation of edge MHD stability results and models to ITER

Although the ideal and resistive MHD instability theories described above and the associated respective correlation of Type I and Type III ELMs with ideal and resistive edge instability provide a modestly satisfactory phenomenological and even semi-quanatative description of ELM characteristics (especially the power scaling) in present tokamaks, present ELM and/or L-H transition theories are not yet mature enough to provide a definitive prediction for ITER ELM types and magnitudes. Accordingly, ITER ELM projects have mainly relied upon empirical predictions of edge plasma characteristics (n-T edge-space operation domain, see Chapter 4 and also Section 3.3 below) and the corresponding ELM characteristics. These empirical projections suggest that ITER will operate in a relatively high-density ($\sim 8 \times 10^{19}$ m^{-3}), high-temperature (~4 keV) edge regime that is simultaneously close to the operational domains wherein Type I and Type III ELMs can be expected.

Figure 3-33, reproduced from Chapter 4, shows one example of how the edge operational space is projected to extrapolate to ITER. However, present edge operational space data and ELM theories are not mature enough to definitively predict the exact outcome with regard to ITER ELM type and magnitude, and there are on-going discussions as to what amplitude and frequency of ELMs can be expected and exactly what the effect of such ELMs (and the resulting high edge densities) on global confinement will be. The plasma edge characteristic issues that are involved are also closely related the need for ITER to operate with high plasma densities (ideally slightly above the Greenwald limit, see Section 3.3) with adequate energy confinement and acceptable ELM type and magnitude. Overall resolution of these matters for ITER (and for future reactors) is presently a matter of on-going discussion that encompasses the full range of effects that ELMs and the plasma edge characteristics are found to have on plasma performance and achievable density.

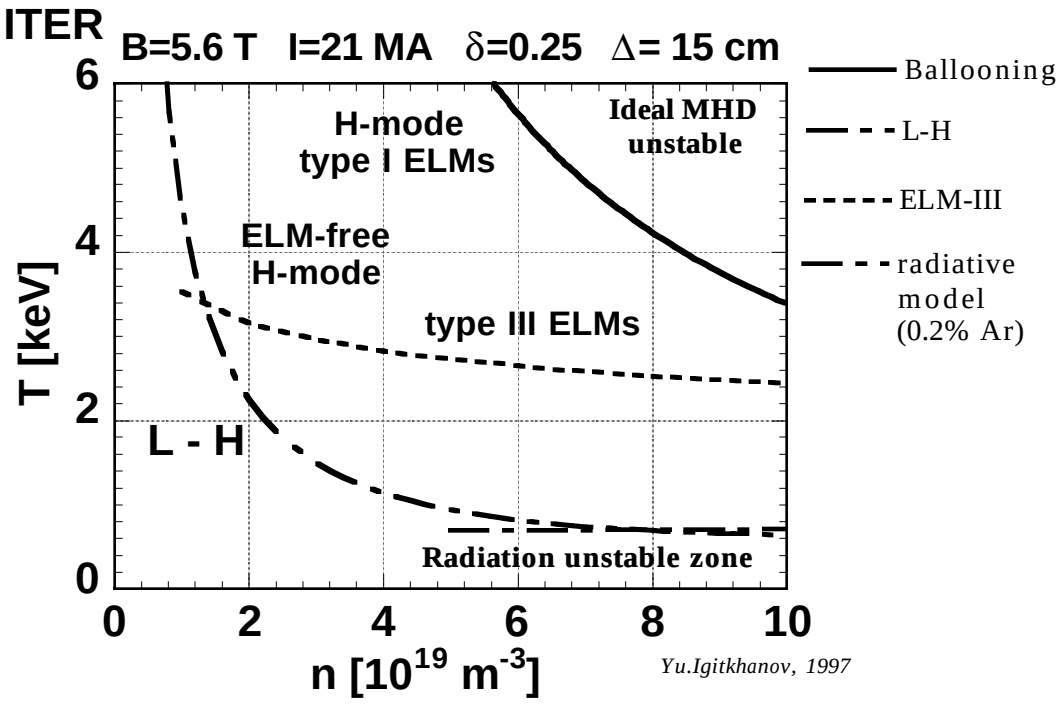

FIG. 3-33. Plasma edge operational space diagram for ITER. The projected ITER edge operation conditions (n, T) lie along the ideal MHD ballooning instability limit contour in the upper right corner of the diagram, at $n \approx 8 \times 10^{19}$ m^{-3}, $T \approx 4$ keV, in the region where Type I ELMs are present, and where Type III ELMs and excessive edge impurity radiation losses are avoided.

In addition, there are uncertainties as to the degree to which it will be possible to exceed the ideal ballooning limit ($\alpha_c = 1$). Better understanding of details of the respective MHD stability conditions and trigger mechanisms are central to bringing these discussions to a definitive conclusion. More wide-spread availability in present experiments of edge density and temperature (and ideally current density) diagnostic measurements with spatial and temporal resolution sufficient to accurately resolve the pressure and safety factor profiles in the edge region will assist in reaching a conclusion.

There is also concern for ITER that Type I ELMs may produce excessive divertor target erosion and the observation has been made that operation with Type II ELMs (as may be possible if the plasma triangularity δ can be increased somewhat) rather than Type I ELMs is desirable. Finally, having one or more 'independent' ELM control means (*e.g.*, edge-localized rf heating or

current drive, or externally-applied edge RMPs or edge-localized pellet injection) available to control ELM type and parameters (e.g., reduce the magnitude of Type I ELMs) is clearly desirable for ITER and reactor tokamaks, where the present principal 'ELM control' means — varying the auxiliary power level and/or changing the plasma shape — will not be available or are incompatible with other plasma operation requirements. Here, as noted above, there have been some successes with independent means in present experiments in being able to modify ELM types or characteristics, but definitive demonstration of an ITER/reactor-relevant ELM optimization and control strategy remains as a future task for the tokamak research community.

3.2.7. MHD Stability of High Internal Inductance and Reverse Shear 'Advanced Performance' Plasma Configurations

Steady-state operation sustained by non-inductive means (heating and/or current drive plus bootstrap current) is an important and arguably essential requirement for the practical implementation of a fusion power reactor. The attainment of steady-state operation is specified as an ultimate objective for ITER. Present understanding of the prospects for such operation in ITER has identified three key enabling requirements: enhanced confinement (see Chapter 2), enhanced MHD stability and normalized beta (addressed here), and plasma profile control by non-inductive means (see Chapters 6 and 8). The attainment of at least partial combinations of these enabling requirements in present tokamak experiments has come to be termed achievement of 'advanced tokamak performance', with the term 'advanced' typically denoting improvement relative to 'standard' tokamak performance, as quantified relative to 'standard' H-mode confinement (i.e., $H_H = 1$, see Chapter 2) and the ideal MHD beta limit $\beta_{N,max} = \beta_{max}(\%)\ a(m)B(T)/I(MA) \leq 3.5$ (see Section 3.2.1). A discussion of the physics considerations that apply to advanced tokamak performance and a comprehensive summary of recent experimental and theoretical work on various advanced tokamak operation modes is given in [3.188].

For steady-state operation in ITER at full fusion power, studies of possible operation modes [3.189] (see also Chapters 8 and 9) show that it will be necessary to simultaneously achieve a certain degree of both enhanced confinement and enhanced β_N in plasma operation modes that are consistent with the heating, current drive and profile control means that can be implemented in ITER. Projected current drive efficiencies mandate operation with ≥80% bootstrap current fraction. The need to have high plasma density (mandated by the fusion power requirement) also means advanced performance in ITER must be compatible with nearly-equilibrated electron and ion temperatures. These operational matters and the related physics basis issues are addressed in Chapters 8 and 9.

This Section addresses the physics basis aspects of MHD stability and beta-limit enhancement, but even here it is difficult to fully isolate these MHD issues from the close interaction that exists among the attainment of enhanced confinement, the attainment of enhanced MHD stability and the use of non-inductive means to establish and control the plasma pressure and current profiles. Modification of the 'natural' tokamak current profile relative to the profile which self-consistently develops in 'standard' L-mode or H-mode plasmas appears to be a central enabling aspect for the attainment of advanced performance and (sometimes) enhanced MHD stability, and hence this Section focuses on the requirements for current profile modification and the MHD stability and beta limit effects of this modification.

3.2.7.1. Effects of current profile modification

Modifications of the current profile shape have been used for many years to increase the achievable normalized beta of tokamaks. The most successful efforts have been those in which the current profile peaking is increased (resulting in increased dimensionless internal inductance, l_i) [3.190–3.193] or those in which the normally-positive magnetic shear s = r/q dq/dr is reversed in the central region of the plasma [3.194–3.201]. The term high-l_i has come to be used to describe plasma operation with increased current peaking. The terms negative-central-shear (NCS) or reversed-central-shear (RCS) or simply reversed-shear (RS) have come to be somewhat interchangeably used to describe plasmas with reversed central shear. There is no scientific distinction among these various terms: in what follows we use reversed-shear. The term enhanced reverse shear (ERS) has also been used to describe the enhancement of confinement attributable to the formation of an internal transport barrier (ITB) that is obtained when centrally-localized neutral beam or other heating is applied to a plasma with pre-existing reversed shear [3.202]. Such heating-induced transport barrier confinement enhancements go beyond the direct effect of shear reversal, but shear reversal ofdr at least weak central shear appears to be a necessary condition for their occurrence (see Section 2.3.4). The 'enhanced' nomenclature is not always consistently used

in the literature, and in some cases plasma operation modes with pronounced ITBs are described simply as RS plasmas.

Figure 3-34 shows representative magnetic and kinetic profiles for a RS plasma produced by current ramping in the DIII-D tokamak. For RS plasmas, the central form of the q profile and the corresponding requirement for a hollow current profile are the key considerations. The radius of the reversal region and degree of shear reversal — strong, weak, marginal (nearly constant q) — can vary.

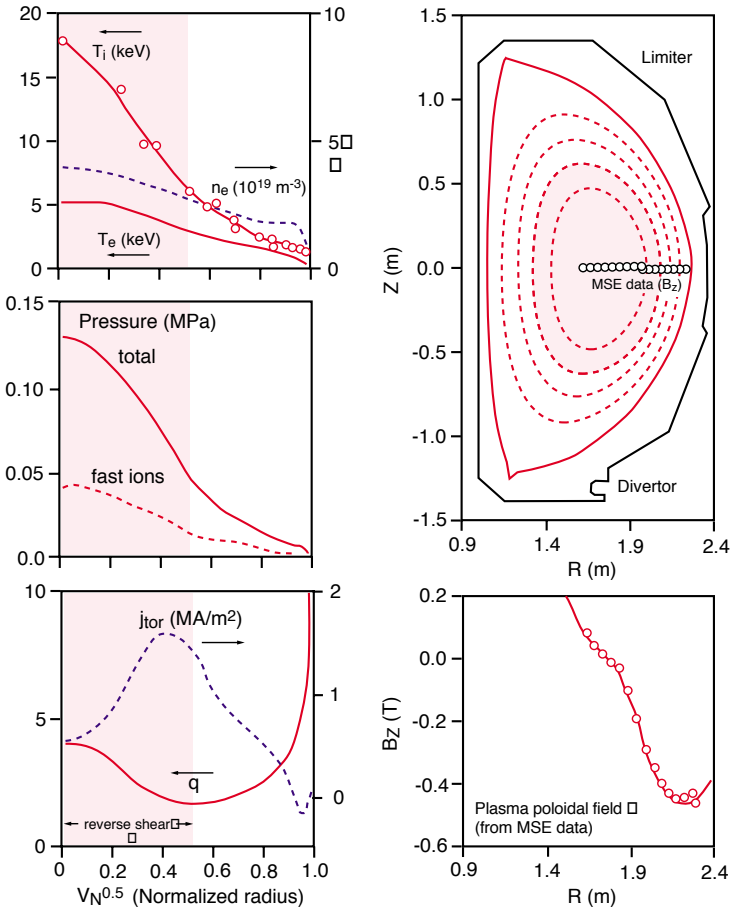

FIG. 3-34. Plasma magnetic configuration reconstruction and profile data for a NBI-heated reversed-shear plasma in DIII-D. The toroidal current density (j_{tor}) and safety factor (q) profile data are derived in this case from MSE measurements of the in-plasma vertical (Z) component of the poloidal field. The radius of the reverse-shear region (shaded) is about half of the minor radius. The pressure gradient steepens within the shear reversal radius. Data reproduced from [3.200].

We note here parenthetically that the recent increased availability of diagnostics [Faraday rotation or motional Stark effect (MSE) spectroscopy] that allow direct measurement of the current density or safety factor profiles (see Chapter 7) has proved instrumental in elucidating the role that current and shear profile modifications play in enhancing plasma performance and in correlating the effects of shear reversal (and heating and current and momentum drive inputs) with the formation of ITBs. Routine use of current-profile/safety-factor diagnostics has become essential for the quantitative study of high-l_i and RS plasmas. A similar diagnostic requirement can be projected for ITER and future reactor tokamaks predicated upon RS/ERS operation. It is also likely that some of the plasmas obtained in early short-pulse 'beta-limit' exploration discharges with rising current waveforms had some degree of shear reversal that went unrecognized owing to the lack of explicit central safety factor profile data [see *e.g.*, the high-β DIII-D plasmas described in [3.203] where marginal evidence derived from magnetic (equilibrium) reconstruction data for reverse shear is shown].

Experiments with transient modifications of the current profile shape, primarily using current ramps, but also using pellets or neutral beams, have demonstrated that good or enhanced confinement can be obtained in both high-l_i and reversed-shear plasmas. In particular, transport coefficients approaching neoclassical values have been obtained in the central reversed shear region of RS plasmas (see Section 2.3.4).

Reversed-shear profiles require a non-monotonic current profile (off-axis peaking of the current density). It has been demonstrated experimentally in Tore Supra [3.194, 3.195] and JT-60U [3.196, 3.197] that reversed magnetic shear can be maintained and controlled by using lower-hybrid-wave current drive (LHCD). Strongly reversed magnetic shear, even stronger than that formed by NBI heating during current ramp-up, with a large region of shear reversal was formed by LHCD alone in Tore Supra [3.195] (Fig. 3-35). A strong gradient was found in the electron temperature profile, suggesting improvement of confinement within the RS region.

Attainable β_N in this discharge was comparable to that of other inductively-created (by ramping) reversed shear discharges.

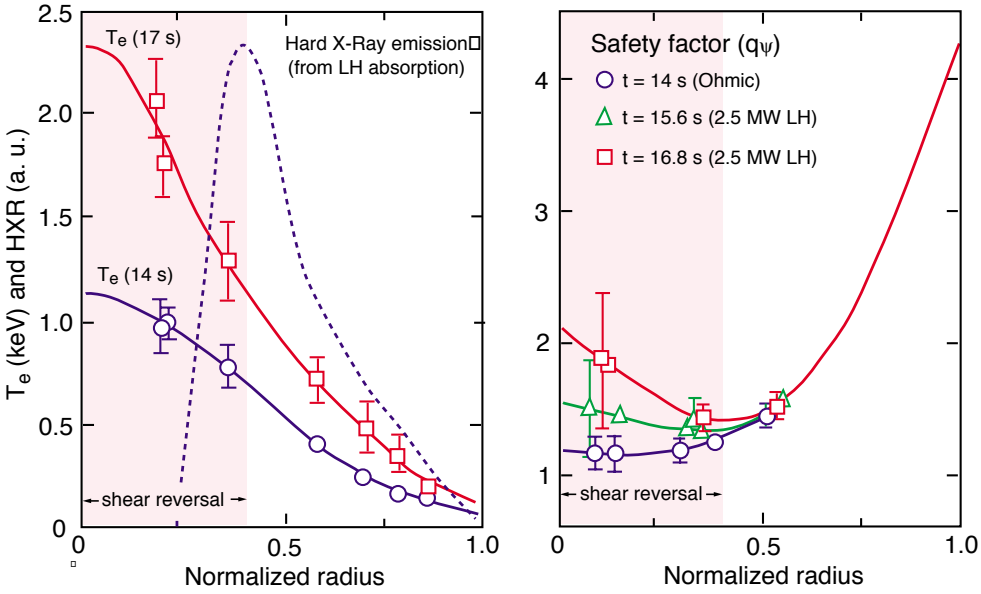

FIG. 3-35. LHCD shear reversal in Tore Supra [R = 2.4 m, a = 0.72 m (circular cross-section), B = 1.3 T, $n_{e0} = 3 \times 10^{19}$ m^{-3}]. A LHCD-sustained quasi-steady-state RS region develops within 3 s of application of 2.5 MW of 3.7 GHz LHCD. T he HXR data shows the approximate LH power deposition profile. Approximately half of the 0.4-MA plasma current is LH-driven. Safety factor profiles are inferred from Faraday rotation measurements of the in-plasma field direction. Data reproduced from [3.195].

Enhanced confinement and/or stability attributed to reversed shear have been obtained in plasmas with near-circular cross-sections (*e.g.*, TFTR and Tore Supra), moderate-elongation, moderate-triangularity cross-sections (JT-60U and JET) and high-elongation, high-triangularity cross-sections (DIII-D). The TFTR and Tore Supra plasmas are limiter-defined; the others are divertor defined, with both single-null (JET and JT-60U) and double-null geometries (DIII-D). The reversed-shear region, not the plasma shape, is the essential enabling factor.

These observations show the importance and potential performance benefits — in both confinement and MHD stability — of control of the plasma current and safety factor profiles. Both requirements are necessary for the achievement of full fusion power in ITER and the achievement

of satisfactory power densities in a reactor that is based upon foreseeable superconducting magnet technology. The balance of this Section focuses on the MHD stability aspects of the two candidate 'advanced performance' plasma operation modes that are relevant to ITER. How these modes may extrapolate to ITER is briefly addressed at the conclusion of this Section. Here we note that since the physics database for advanced performance tokamaks is still very much in a state of development, we discuss the identification and physics basis of such modes for ITER in terms of candidates rather than as already-determined selections. As will be presented in Chapter 9, the demonstration of reactor-relevant 'advanced performance' steady-state operation in a DT-burning tokamak will arguably be a 'first-of-kind' opportunity (and task) for an ITER-class experiment.

3.2.7.2. High l_i plasmas

Experiments in DIII-D, JT-60U and TFTR have demonstrated that increased internal inductance results in a higher β_N limit, and that this enhanced β_N is generally obtained while maintaining H-mode or better levels of confinement. Figure 3-36 shows the procedure typically used to obtain high-l_i plasmas in these tokamaks: the current of a well-equilibrated 'standard' discharge with an edge q of about 3 (usually NBI heated to increase the plasma temperature and thus extend the duration of the transient high-l_i phase) is ramped down rapidly, resulting in on-axis peaking of the remaining current and a transient increase in internal inductance above the 'steady-state' value that is eventually reached when the current profile re-equilibrates. Similar transient increases in l_i can also be obtained by a rapid increase in the plasma elongation [3.193] or by expanding the plasma minor radius [3.202, 3.204]. Since the time scale for current profile relaxation is typically longer than the energy confinement time, it is possible to make energy confinement measurements as l_i and the current profile vary during the relaxation period.

Figure 3-36 shows current profiles at three points in a rampdown L-mode discharge: the highest inductance profile transiently has some reverse current at the inboard (small-R) edge of the

plasma. The pre-ramp and 'steady-state' after-ramp profiles have essentially zero edge current density.

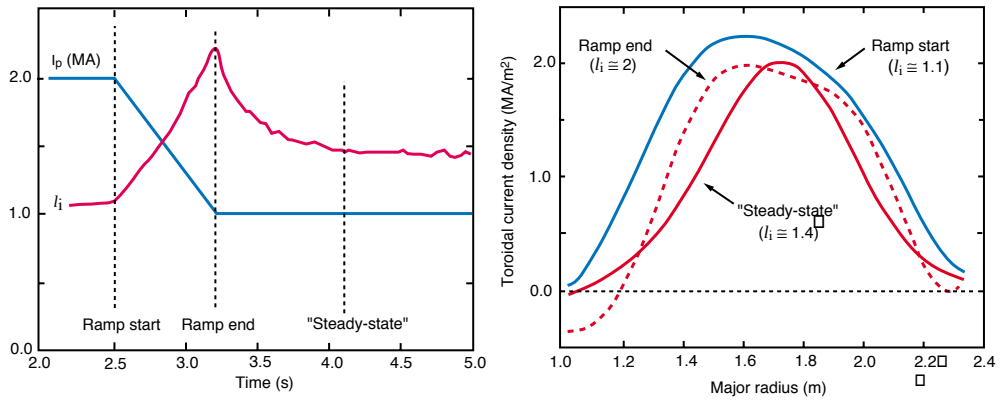

FIG. 3-36. Plasma current and l_i waveforms for a representative DIII-D current rampdown experiment. Current density profiles obtained from equilibrium reconstructions supplemented with MSE data are shown in the right-hand panel. Data reproduced from [3.193]

Figure 3-37 shows representative confinement data obtained in DIII-D experiments in which a current rampdown or an elongation increase is used to increase l_i. Enhanced confinement is obtained for both L-mode and H-mode plasmas. The enhancement increases with increasing l_i and current peaking. High-elongation, high-l_i H-mode plasmas achieve significant (~1.5 ×) confinement enhancement relative to 'standard' ($1.0 \le l_i \le 1.2$) H-mode plasmas.

On DIII-D, $\beta_N = 6$ has been transiently reached in high-l_i plasmas produced by current ramp-down [3.193]. Figure 3-38 shows that in these L-mode plasmas, the attainable β_N increases with increasing l_i and approaches the corresponding ideal-MHD ballooning beta limit. The peak [stably achieved] values of β_N are also close to the $\beta_N = 4l_i$ empirical beta limit scaling (see Section 3.2.1). At the highest inductance, the confinement enhancement in L-mode (now evaluated relative to ITER89P L-mode energy confinement scaling) is approximately 2: i.e., a high-l_i L-mode provides confinement equal to a normal-l_i H-mode of equal current. This 2-× enhancement of L-mode confinement at high-l_i to 'normal' H-mode levels can also be explicitly seen in Fig. 3-37.

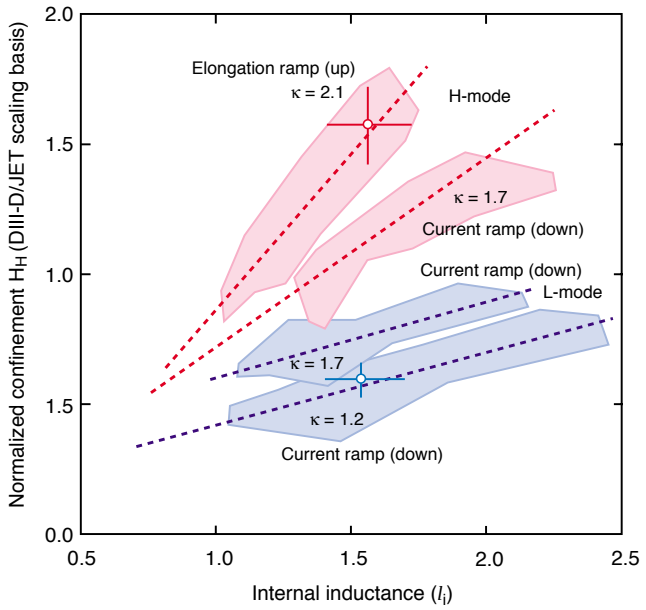

FIG. 3-37. Energy confinement versus l_i in DIII-D. The normalization basis used here is the so-called DIII-D/JET empirical scaling which accurately describes H-mode confinement in both experiments. Reproduced from [3.193] with multiple data indicated by shaded domains (typical data shown to indicate error bars)

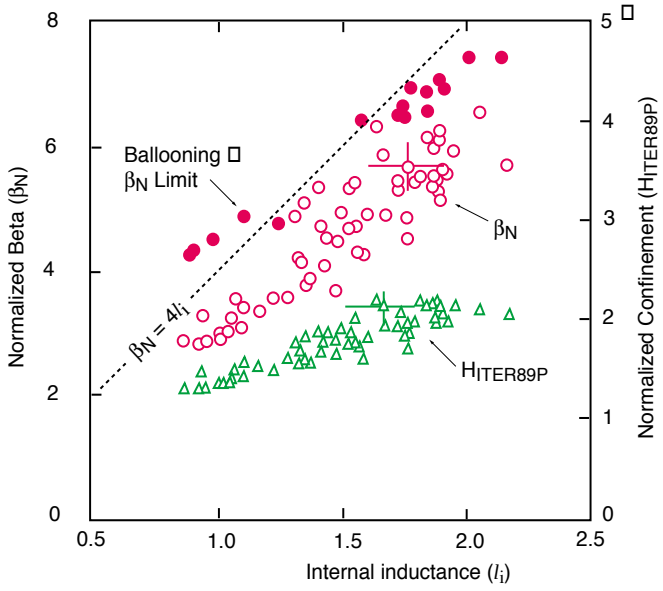

FIG. 3-38. Energy confinement (relative to ITER89P scaling) and peak β_N in DIII-D L-mode current-rampdown plasmas. Explicitly-calculated ideal MHD ballooning limits for various l_i are also shown. Experimental and MHD stability data from [6] with the $\beta_N = 4l_i$ empirical scaling added here for comparison.

On TFTR β_N as high as 4.9 with H_{89P}-factors of 4 have been transiently reached and DT fusion powers of up to 8.7 MW (*cf.* 10.7 MW in a maximum-performance standard-l_i 'supershot') have been produced in discharges wherein $l_i = 1.5$ is transiently obtained by radial expansion of the plasma minor radius [3.204]. In these TFTR high-l_i plasmas, the q(0) is typically well below unity but, as in TFTR supershots, sawteeth are suppressed at high NBI powers owing to fast-ion kinetic stabilization effects (see [3.204] and Section 3.2.2.). The stability of these plasmas at high β_N is in conflict with ideal MHD theory predictions for onset the n=1, m=1 internal kink instability, which is expected (in the absence of fast-ion stabilization) for $q(0) < 1$. However, with the simple artifice of raising q(0) above unity, ideal MHD stability calculations of the resulting 'equivalent' plasmas are then in reasonable agreement with the experimental-observed disruptive beta limits (see Sections 3.2.1 and 3.2.2). Figure 3-39 shows β_N-l_i data for representative TFTR high-l_i high-β_p and standard 'supershot' discharges. As Fig. 3-39 demonstrates, the maximum β_N attained in current rampdown plasmas appears to scale approximately linearly with internal inductance, but lies below the empirical $\beta_N = 4l_i$ ideal MHD stability limit (see Section 3.2.1). Note also that these high β_p plasmas, both static and with current rampdown, reach internal inductances that are approximately twice as large as those obtained in the DIII-D experiments cited above.

Analysis of the MHD stability of a representative TFTR current-ramp-down discharge (Fig. 3-40) shows that the plasma is marginally unstable to high-n ballooning modes in the outer flux surfaces and ballooning instability is identified in [3.190] to be the likely cause for the beta saturation and/or subsequent disruption that limits attainable performance in these plasmas. Similar β-limiting ballooning instability in the outer region is observed in TFTR supershot plasmas (see Section 3.2.1). The MHD stability analysis of the DIII-D high-l_i L-mode plasmas described above also identifies ideal ballooning as the likely β_N limiting instability.

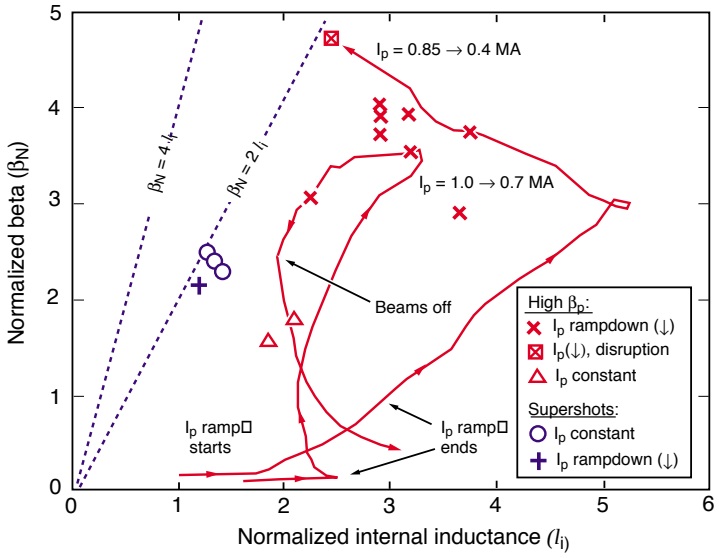

FIG. 3-39. Peak normalized β (from diamagnetic measurements, fast-ion pressure included) as a function of plasma internal inductance l_i as obtained in TFTR NBI-heated plasmas. β_N-l_i trajectories for two current rampdown cases are shown. The highest β_N case ends in disruption. The symbol-coded data show the peak β_N values reached (without disruption) in various current rampdown and constant-current cases. Data for 'standard' TFTR supershot plasmas are also shown. The rampdown plasmas transiently achieve higher β_N and l_i. Reproduced from [3.190], with $\beta_N = 4l_i$ and $2l_i$ empirical scalings added.

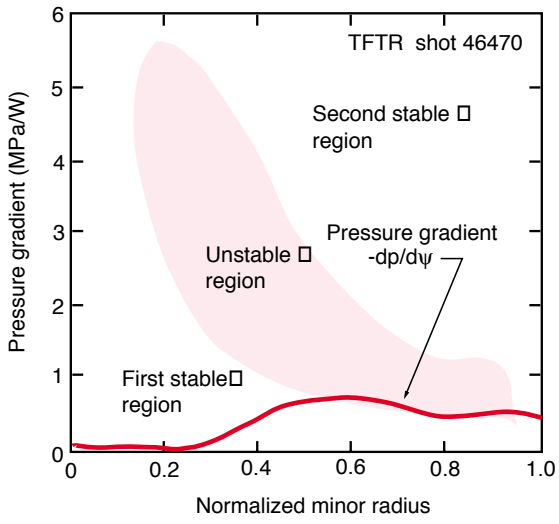

FIG. 3-40. High-n ballooning stability analysis for a TFTR current-rampdown plasma (0.85→0.4 MA). The measured pressure gradient in the outer half of the plasma is found to be close to the calculated first-stable-region pressure gradient limit (first stability boundary).

Table 3-IV summarizes the instability data reported in high-l_i experiments, mostly with current rampdown, in TFTR, DIII-D, JT-60U and Tore Supra. A theoretical 'steady-state' reactor-relevant high-l_i example case with ~60% bootstrap current reported in [3.188] is also included. The data in the Table shows that β_N ~ 4-5 can normally be obtained (the Tore Supra experiments did not explicitly explore the high β and β_N regime), albeit with edge q's ~8. The corresponding relative figure-of-merit for achievable total β (= $\beta_N I/aB \sim \beta_N/q$) is typically about 0.6. The DIII-D L-mode data are an exception: the β_N/q attained at the maximum l_i transient phase that follows the completion of the rampdown reaches 0.9 (note however in Fig. 3-36 that there is some edge current reversal at this point) and the value of β_N/q obtained in the 'steady-state' l_i = 1.4 phase reaches 0.7.

Table 3-IV. Experimental and Theoretical Stability Data for High-l_i Plasmas

Experiment or Model	q (q_{95} or q_{lim})	l_i	β_N	β_N/q
DIII-D (transient, at max l_i) [3.193]	7	2.3	6.3	0.9
DIII-D ('steady-state') [3.193]	7	~1.4	≤ 4.8	≤ 0.7
JT-60U [3.192]	~8	~2.5	4.7	~0.5
TFTR [3.190]	~8	3.5	4.7	0.6
Tore Supra (LHCD, ss) [3.194]*	~8	2.8	0.7*	~0.1*
ITER (theoretical, positive-shear H-mode profiles) [3.15] (see §3.2.1)	3.0	0.9	≥ 3 (*cf.* ~2.2 for P_{fus} = 1.5 GW)	≥ 1 (*cf.* 0.73 needed)
Model (q = 8, f_{bs} = 60%) [3.188]	8	1.2	4	0.5

* The feasibility of higher β_N operation was not explored in these experiments

The values of β_N/q ~0.6 typically achieved in the high-l_i experiments at q = 8 can be compared to the value of $\beta_N/q \sim 1.2$ that can be obtained in 'standard-l_i' plasmas at q = 3 at the ideal MHD beta limit of β_N = 3.5. Explicit estimates of the ideal MHD beta limit in ITER H-mode plasmas show $\beta_N \geq 3$ can be expected (see Section 3.2.1 and [3.15]): the corresponding 'standard-

l_i' figure-of-merit for ITER or a similar reactor tokamak is $\beta_N/q \geq 1$. As noted in the Table, the actual β_N needed for rated fusion power in ITER is about 70% of the ideal MHD limit, so positive shear operation in ITER has ~45% 'headroom' in so far as ideal MHD stability is concerned.

Extrapolation of high-l_i operation to ITER. The extrapolation of steady-state high-l_i plasma operation to a reactor and to ITER is somewhat problematical. There are two difficulties. The first is that given reasonable limits on minimum on-axis q [= q(0)], high-l_i plasmas will have high edge q and hence low β ($\sim \beta_N/q$). This low β tends to limit the fusion power attainable at a given toroidal field. The tendency for high-l_i plasmas to yield β_N/q values that are appreciably lower than 'standard-l_i' plasmas with $q \approx 3$ is evident in Table 3-IV. Generic projections (see *e.g.*, the high-l_i mode presented in [3.188]), suggest that a reactor-relevant steady-state high-l_i mode based on $l_i \approx 1.2$ will have an effective plasma edge $q \sim 8$ and relatively low plasma current (~8 MA in ITER). If such plasmas can reach the ideal MHD beta limit ($\beta_N = 4l_i \approx 5$), the corresponding β will be about 2.5%. While the exact fusion power capability at this beta will depend on the pressure profiles and plasma impurity content, the achievement of full fusion power in high-l_i plasmas in ITER with adequate β-limit headroom appears to be difficult.

The second difficulty in extrapolating high-l_i operation to steady-state ITER operation arises because the bootstrap current profile in such plasmas is not well-aligned with the centrally-peaked current profile needed for the high-l_i mode. This misalignment is inherent owing to the q dependence of the bootstrap current density ($j_{bs} \sim q\, dp/dr$): there is too little bootstrap current near the plasma axis and too much near the edge. Auxiliary current drive is therefore required on axis and negative current drive is needed at the plasma edge. These factors reduce the global current drive efficiency (utilization of current drive power) and hence reduce attainable Q (fusion power gain). However, the practicality of achieving high-l_i profiles on a steady-state basis in an ITER plasma with adequate efficiency remains to be studied in detail, as does the possible benefit of high-l_i operation in achieving a more-centrally-peaked pressure profile (which increases the overall fusion reactivity). The question of how low q(0) can be maintained in a steady-state current-drive-sustained α-heated plasma (where strong α-particle stabilization of the internal sawtooth

reconnection is expected, see Section 3.2.2) also requires further study. If low q(0) and strong axial pressure peaking prove possible in high-l_i ITER plasmas, then such operation may become more attractive for ITER and reactors.

Finally, with regard to utilization of the high-l_i mode in ITER, it is likely that the same type of transient current ramping (and possibly also shape ramping) studies that are conducted in present experiments can be repeated in ITER with auxiliary-heated and ignited or high-Q burning plasmas. The current profile relaxation times for such plasmas approach 500 s, so 'sustained-pulse' explorations of the effect of current profile peaking on time scales much longer than the corresponding energy and particle confinement times appear possible. While the plasma current and configuration control feasibility (PF coil voltage and power requirements) of current and possibly shape ramping experiments in ITER remain to be studied in detail, the nominal PF capacity is likely sufficient to conduct a variety of experiments with inductive current profile modification.

3.2.7.3. Reversed shear plasmas

Plasmas with hollow current profiles (*i.e.* with reversed shear) are predicted and observed to have enhanced stability and confinement under some circumstances. Plasmas with reversed shear are also theoretically predicted to have the additional attractive feature that the alignment of the bootstrap current with the desired current profile shape is relatively good, allowing high bootstrap fraction [3.20, 3.205, 3.206]. Reversed shear plasmas have been transiently created — by current and/or shape ramping — on the TFTR, DIII-D, JT-60U, JET and other tokamaks to allow investigation of their stability and confinement characteristics. Reduced transport of one type or another has been frequently observed. However, the improvements in MHD stability are mixed. On TFTR, JET and JT-60U the highest β_N achieved in reversed shear operation is ~2, not significantly better than what is obtained other high-performance operational regimes. Higher β_N ($\beta_N \approx 4.5$) with $H_{89P} \approx 3.5$ [3.207] has been reached transiently on DIII-D with broader pressure

profiles and weak negative central shear. Some of the highest performance (fusion reactivity) shots in DIII-D are in such reversed shear plasmas, and record DD-neutron yields and equivalent Q_{DT} are achieved (albeit with $\beta_N \sim 2$) in JT-60U RS plasmas with a large-minor-radius ITB (see below).

The maximum β that can be obtained in RS plasmas is found to be limited by both ideal and resistive MHD instabilities. On TFTR, while the reversed-shear plasma core is found — as predicted — to be ideal MHD stable, in the outer, normal-shear region, ideal MHD instability is experimentally found to limit global β. Because of this limitation, TFTR RS plasmas did not provide improved performance over normal 'supershot' operation [3.202, 3.208]. The β-limiting instability on TFTR is driven by the high pressure gradient in a “transport barrier” region which develops in the low shear region near q_{min}. The measured mode growth time of 0.1 to 1 ms shows that the instability is the result of ideal MHD. The instability is modeled as an n=1 'infernal' kink mode [3.209, 3.210], possibly coupled in some instances to a toroidally-localized ballooning mode [3.210] in the low and normal shear region. The so-called infernal mode instability, which is localized in the region of high pressure gradient, combines both kink (low-n) and ballooning (high-n) displacements (hence the description of the mode as being 'infernal': the entire n-spectrum becomes unstable).

With these MHD stability considerations taken into account, good agreement is found between the experimental TFTR RS β limits and the theoretical predictions for instability onset. The infernal mode becomes unstable when q_{min} approaches a low-integer value, generally ~2. Comparisons of the predicted mode structure agree well with experimental measurements (Fig. 3-41).

In the TFTR experiments, the anticipated improvements in stability of reversed-shear plasmas, compared to those with normal (monotonic) shear, were not achieved because of the strong coupling between the magnetic configuration and the plasma transport. Further improvement in the performance of RS plasmas would have required active control of both the pressure and the current profiles. The interaction between the transport and stability aspects of

these TFTR plasmas and the difficulties of obtain a net improvement in plasma performance relative to 'standard' positive-shear operation illustrate some of the challenges and present uncertainties that apply to the extrapolation of such modes to future experiments where, among other uncertainties, how confinement enhancement will extrapolate to a reactor-scale device is not completely clear.

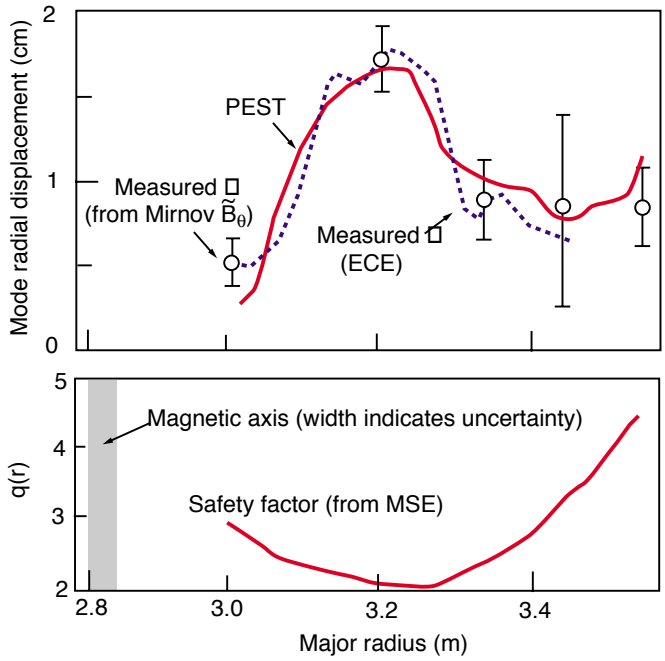

FIG. 3-41. Comparison of calculated (from the PEST stability code) and measured radial displacements for the n = 1 'infernal mode' MHD precursor that precedes disruption in TFTR RS plasmas. The infernal mode is localized near the q_{min} radius and combines kink and ballooning instability features. The precursor growth rates are commensurate with ideal MHD. Data taken from [3.208]

The onset of MHD instability in reverse-shear discharges in present experiments — wherein heating power is continuously applied and the plasma beta or neutron yield rises in a near linear manner — typically results in disruption that occurs near the ideal MHD beta limit. Immediately prior to the disruption, a rapidly-growing ($\gamma^{-1} \sim 0.1$–0.5 ms) n = 1 magnetic precursor is observed, and as it explained above, the onset of the disruption is ascribed in TFTR to an infernal mode that combines the features of kink and ballooning instabilities. Similar mixed kink-ballooning mode instabilities are found to limit JT-60U RS/ITB beta (see below).

In high-performance RS experiments, the plasma current quench that follows ideal MHD instability onset is often very rapid and reverse-shear disruptions are typically among the fastest or hardest disruptions (in terms of current quench rate) observed in a given tokamak (see, e.g., [3.211]), the following discussion of the disruption characteristics of other reverse shear experiments below and also Chapter 8).

Slower-growing non-ideal MHD modes with saturated amplitudes are also possible in reverse-shear plasmas. In the TFTR RS experiments, neoclassical island bootstrap current effects (see Section 3.2.3) are predicted to be stabilizing for tearing modes in the reverse-shear region. This prediction is found to be consistent with experimental observations. Tearing modes with size and growth rate consistent with neoclassical island tearing mode theory have been observed in the high-β phase in the normal-shear region of the plasma. However, islands have not been observed in the reverse-shear region of these plasmas. In the low-β phases before and after high power neutral beam heating, double tearing modes have been commonly observed when q_{min} passes through low-integer rational surfaces. When q_{min} passes through 2, the tearing modes can cause off-axis sawteeth with varying degrees of magnetic reconnection [3.212]. When q_{min} is passes through higher rational numbers, such as 3 or 4, double tearing modes which can trigger major disruptions have been detected with the fast electron temperature profile diagnostics.

The stability of low shear and reversed shear regimes to fusion-alpha driven instabilities has been investigated on TFTR [3.213]. Theoretical calculations predict that TAE modes in low or weakly reversed shear plasmas will have reduced stability, and this is consistent with the experimental observations. Alpha-driven TAE modes have been observed in weak shear plasmas on TFTR with a β_α threshold that is consistent with theoretical estimates. The β_α levels in other TFTR supershot, high-l_i or reversed-shear experiments were theoretically and experimentally below the threshold of excitation for TAE activity. For JT-60U, experiments where a strong internal transport barrier (ITB) is formed in the negative shear discharge find no TAE instability. Stability analyses with the NOVA-K code predicts that TAE modes are stable in these circumstances owing to a lack of gap alignment [3.214].

Various MHD fluctuations including resistive modes and ideal modes are observed in JT-60U RS discharges [3.215]. Profiles for a typical high-performance (high stored energy and DD neutron yield) discharge are shown in Fig. 3-42 [3.216]. In these discharges, the minor radius of the reversed-shear region is relatively large ($r/a \approx 0.6$) and a narrow ITB with very pronounced energy and particle confinement effects develops. Both resistive and ideal MHD activity are observed in these discharges. Resistive modes, which are observed continuously, can be classified by their localization in the minor radius: either at the inside or outside of the ITB or near the plasma surface. Resistive modes localized near the ITB are observed when the pressure gradient and β_N are large enough and when q_{min} is between integer values. Fluctuations with in-out asymmetry and without in-out asymmetry are observed in electron temperatures measured by ECE. Here "in" means within the ITB, and "out" means outside (at larger r/a) of the ITB. Resistive modes without in-out asymmetry seem to be double tearing modes, while the origin of the resistive modes localized near the ITB with in-out asymmetry has not been identified yet.

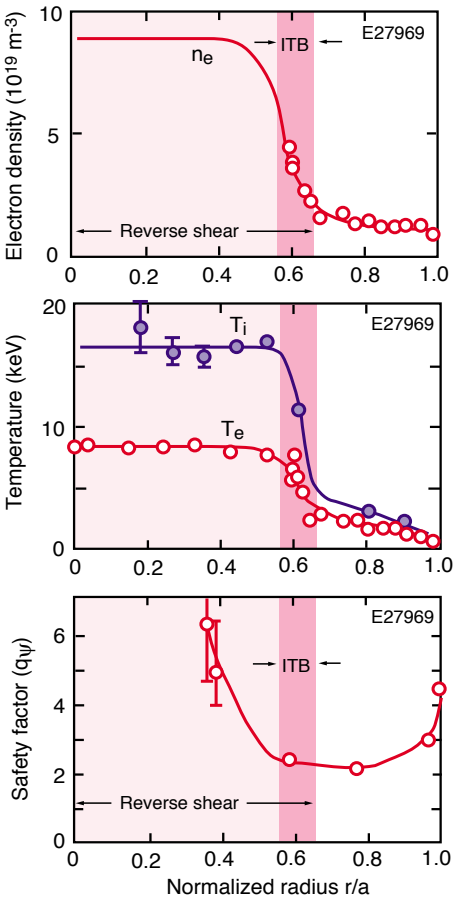

FIG. 3-42. Density, temperature and safety factor profiles for a high-performance JT-60U RS discharge with edge safety factor $q_{95} \approx 3.5$ (from [3.216]). Note the relatively large minor radius of the reversed-shear region and the pronounced effect of the ITB on plasma core energy and particle confinement.

Reversed shear discharges in JT-60U terminate with hard disruptions even for low β_N. The disruptions occur (1) with ideal MHD instability growth time when $q_{min} \sim 4$ or ~ 3 , (2) when the surface q is close to integer values (suggesting the effect of external kink modes), and (3) with mode locking near the plasma surface.

For discharges with $q_{min} \sim 2$, a hard beta/confinement collapse that leads to disruption occurs at $\beta_N \sim 2$. Before the beta collapse begins, precursor oscillations in the electron temperature are observed. These oscillations, which are localized in the ITB region grow on a resistive-MHD instability time scale that is longer than 1.5 ms. The beta/confinement collapse which follows the

growth of these resistive modes then develops explosively from the ITB region on the low field side with a growth time of the order of 10 μs [3.217]. Ideal MHD stability analysis shows that the experimental beta limit ($\beta_N \approx 2$) at $q_{min} \approx 2$ is close to the theoretical calculated threshold for onset of ideal low-n (n = 1) coupled kink and ballooning modes [3.218]. Figure 3-43 illustrates the theoretically-calculated mode structure, which combines low-m internal and ITB-centered kink components with higher-m ballooning component localized outboard of the ITB radius. The propensity of high-performance RS discharges to terminate disruptively is attributed in [3.216] to the profile-wide effect of the coupled low-m and high-m modes. The mode structure is similar to the structure of the infernal mode that terminates high-performance TFTR RS plasmas.

On DIII-D the maximum β achieved with negative central shear is found experimentally to depend on the shape of the pressure profile. Peaked pressure profiles (L-mode edge) result in limiting $\beta_N < 2.5$, whereas with broader pressure profiles — obtained with an H-mode edge — β_N as high as 4-5 has been reached transiently [3.211, 3.219]. An H-mode transition in JET is also found to broaden the pressure profile and allow higher β_N, but DD fusion rate is unaffected or declines owing to a decrease in central ion temperature. DIII-D plasmas with peaked pressure profiles suffer β-limit disruptions similar to those observed in TFTR. The n = 1 disruption precursor mode is localized near or just inside the q_{min} radius. The broader pressure profile (H-mode edge) plasmas are also limited by instabilities in the positive shear region, but the precursors are localized at the plasma edge. The stability limits follow the linear scaling with internal inductance, l_i, seen in normal-shear plasmas. This is interpreted to mean that current density at the plasma edge destabilizes the plasma.

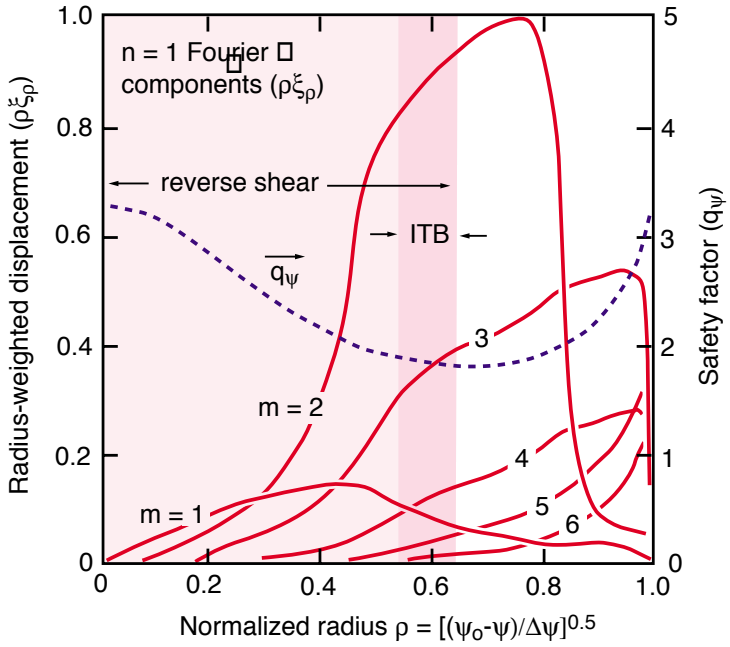

FIG. 3-43. MHD stability analysis for the RS discharge illustrated in Fig. 3-42. Calculations with the ERATO-J code show the presence of a coupled kink-ballooning instability that is localized around the radial position of the ITB (note that the data plotted are for the radius-weighted mode displacement $\rho\xi$, where ρ is the normalized radius derived from the flux surface volume). Reproduced from [3.216] with RS and ITB indications added.

Table 3-V summarizes stability-related parameters for RS plasmas. Theoretical ideal MHD stability projections for candidate ITER and TPX (Tokamak Physics Experiment) and DIII-D RS plasmas are also included. As the data in the Table shows, with the exception of two RS plasmas obtained in DIII-D, the maximum normalized β_N obtained falls in the range of 2–3, and the β_N/q figure-of-merit parameter falls in the range of 0.45–0.65. There are two examples of higher β_N or β_N/q obtained in DIII-D: high β_N (= 4.5) in a weak RS plasma configuration with a broad pressure profile [3.207] and somewhat lower β_N (= 3.7) but higher β_N/q (= 1.4) in what may be a marginal RS plasma with high elongation and low edge safety factor (= 2.6) [3.203]. This latter plasma, which was not explicitly identified in [3.203] as being an RS plasma, shows marginal evidence of shear reversal in the magnetic equilibrium current profile reconstruction data.

Table 3-V. Experimental and Theoretical β_N or MHD Stability Data for RS Plasmas

Experiment or Model	q (q_{95} or q_{lim})	l_i	β_N	β_N/q
DIII-D (weak RS) [3.196]	~6	---	4.5	0.75
DIII-D ¶ [3.104]	4.5	0.7	2.8¶	0.62
DIII-D (possibly RS)# [3.203]	2.6	0.91	3.7	1.42
DIII-D* [3.219]	4.2	---	1.7	0.40
DIII-D (theoretical) [3.206] (I = 1.6 MA, κ = 2.1)	6.5	0.64	5.7	0.88
JET [3.198]	4 (est.)	---	2.6 (est.)	~0.65
JT-60U [3.196]	~4 (q_{eff} ~ 5)	---	2.1	0.53
JT-60U (LHCD, ss) [3.196]	6 (q_{eff} = 7.5)	---	2.2	0.36
JT-60U [3.216]***	~3.5	---	2.2	~0.6
JT-60U [3.220]**	3.46	---	1.84	0.53
TFTR [3.199]	6.2	---	3.5 (β_N*)	≤ 0.5 (est.)
Tore Supra (LHCD, ss) [3.195]	4.2	---	0.9	0.21
ITER (theoretical, for +shear H-mode profiles) (§3.2.1, [3.15])	3.0	0.9	≥ 3 (*cf.* ~2.2 needed for P_{fus} = 1.5 GW)	≥ 1 (*cf.* 0.73 needed)
ITER (theoretical) [3.189] (I = 12 MA, $\kappa_{95} \approx 1.85$, a ≈ 2 m)	5	---	5 (*cf.* ~3.8 needed for P_{fus} = 1.5 GW	1.0 (*cf.* 0.76 needed
TPX (theoretical) [3.20]	3.5	---	1.9 (kink, w at ∞)† 5.2 (kink, w at 1.3)§ 5.5 (ballooning)	0.54 1.49 1.57

¶ 200-ms β_N 'flattop' at ~1.3-x ideal MHD limit (wall at ∞); resistive wall mode instability attributed to edge rotation slowdown (see §3.2.4) ends high-β phase
† for conducting wall at infinity
§ for conducting wall at r/a = 1.3
# with I_p ramp, marginal RS indication in equilibrium reconstruction data, κ = 2.34, β = 11%, sustained for ~50 ms
* Highest Q_{DD}
** Highest Q_{DD}
*** Highest Q_{DD} (multiple data)

Figure 3-44 presents a summary of the experimental and theoretical (ideal MHD) β_N or β_N limit data from Table 1 (for high-l_i plasmas) and Table 3-V. None of the experimental data in Table 3-V attain the full β_N or β_N/q potential of the theoretically predicted ideal MHD stability of

the wall-stabilized TPX low-q RS plasma, and only the DIII-D high-elongation/low-q experimental data [3.203] attains the β_N/q potential predicted for the candidate ITER high-q RS plasma proposed in [3.189]. The weak-RS DIII-D plasma documented in [3.207] has β_N and β_N/q performance similar to the theoretical second-stability VH mode DIII-D candidate plasma described in [3.206]. However the shear profiles for the experimental and theoretical cases are rather different.

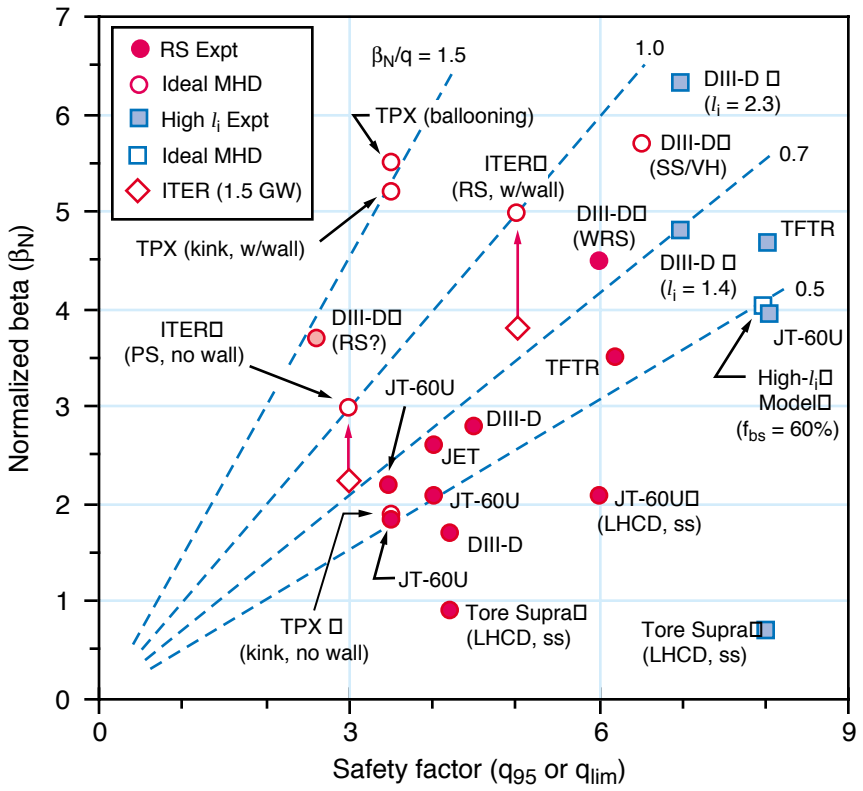

FIG. 3-44. Normalized beta versus edge safety factor for high-l_i and RS plasma experiments (solid data symbols). Theoretical ideal MHD stability limits for proposed ITER, TPX and reactor-candidate plasmas are also shown (open symbols). Calculated beta limits for positive-shear (PS) and RS ITER cases are indicated. The corresponding β_N needed in ITER for 1.5 GW fusion power is also shown: the arrows indicate the β_N 'headroom' relative to the ideal MHD limit.

The conclusion that can be drawn from Table 3-V and Fig. 3-44 is that while there are presently a limited number of experimental results that suggest the potential for RS plasmas to provide 'advanced' reactor-regime MHD stability and (with accompanying confinement

enhancement) $nT\tau$ performance, in most cases ideal MHD instability similar to the infernal mode MHD instability seen in TFTR and the need to operate at reduced plasma current (higher edge q) in order to achieve the RS configuration act to limit attainable plasma β and $nT\tau$ performance to levels that are comparable or somewhat less that the plasma performance that can be obtained in a given experiment in other 'standard' (non-RS) plasma operation modes (e.g. high β_p modes in JT-60U or hot-ion H-modes in JET).

While present assessments of the performance of RS plasmas indicates that the full promise of RS 'advanced MHD stability' has not yet been achieved, we note that there appears to be significant potential for further optimization of RS performance in present experiments. In this regard, better capabilities for direct current and/or pressure profile modification by localized rf heating and current drive are only now becoming available, and it is clear that the interplay among the degree of shear reversal, edge q and the energy and pressure confinement effects of both ITBs and XTBs (i.e., L-mode versus an H-mode edge barrier) is critical to simultaneously optimizing the MHD and confinement performance of present RS plasmas and for determining the basis for optimal RS MHD stability and overall performance in future reactor RS plasmas.

3.2.7.4. Summary and extrapolation to ITER

Experiments in a variety of tokamaks with circular and elongated plasma cross-sections have demonstrated that modification of the current profile relative to the profile obtained with 'standard' magnetically-equilibrated plasmas can result in enhanced confinement and in some cases also in high values of achievable β_N. Beneficial effects of both on-axis and off-axis peaking are respectively seen in high-l_i and reverse-shear plasmas. For high-l_i plasmas, the limit on achievable β_N is typically set by ideal MHD ballooning instability that develops in the outer portions of the plasma, and to date the $\beta_N = 4l_i$ ideal MHD beta limit has been approached but not exceeded. Since high l_i plasmas inherently have higher edge safety factors and lower total current (relative to

normal-l_i plasmas), the total β (and $nT\tau$ performance) of these plasmas are typically not enhanced relative to the β and $nT\tau$ attainable at edge safety factor $q \approx 3$-4.

For reverse-shear plasmas, an ideal MHD stability limit is also found to apply. Because RS plasmas typically have low internal inductance, the corresponding ideal β_N limit is ~2, and the β_N achieved in TFTR, JET and JT-60U plasmas has (so far) been limited to 2-2.5 by the onset or resistive and/or ideal instability. In these plasmas, the limiting MHD mechanism is typically an ideal MHD infernal (or 'infernal-like') mode that is localized near the q_{min} radius. This mode combines internal kink and external ballooning characteristics and leads to disruption. The mode displacement characteristics and β_N threshold calculated from ideal MHD theory are in good agreement with experimental data. Slower-growing resistive instabilities localized near the q_{min} region can also lead to profile changes that in turn can trigger ideal MHD instability and disruption. There is also evidence in certain cases for the presence of resistive neoclassical-island tearing modes in the positive-shear region of RS plasmas, and TAE instabilities have also been observed in TFTR RS plasmas.

The principal exception to the $\beta_N \sim 2$ limit seen in most RS experiments is obtained transiently in DIII-D plasmas with weak reverse shear, wherein β_N as high as 4.5 has been achieved. These plasmas exceed the ideal MHD beta limit by factors ~1.3. In addition to the broad pressure profiles and weak shear reversal that these plasmas exhibit, plasma-rotation-enabled wall stabilization of external kink modes appears to a factor in being able to attain this level of 'advanced' MHD stability, which approaches the β_N predicted to be obtainable on the basis of ideal MHD stability with the effects of a conducting wall located at r/a = 1.3 taken into account. Without wall stabilization, the same ideal MHD calculations predict that the beta limit will be $\beta_N \sim 2$. To date, this $\beta_N \sim 2$ prediction seems to be borne out by the majority of the RS beta-limit data.

While the majority of present RS results are obtained in a transient fashion by current and/or shape ramping, comparable energy confinement enhancement effects are seen in LHCD-sustained RS plasmas in Tore Supra and JT-60U. In both cases, the MHD-stable β_N attained in LHCD-sustained RS plasmas is comparable to the β_N attained by current ramping.

Theoretical extrapolations of RS plasma operation to ITER suggest that $\beta_N \geq 4$ and $\beta_N/q \geq 0.8$ will be needed for 1.5 GW steady-state operation. These requirements lie at the upper limit of the present RS MHD stability/beta-limit experimental data (Fig. 3-44) and also require wall stabilization of external kink instabilities. This requirement is potentially problematic for ITER and for a reactor owing to the low plasma rotation velocities expected in such reactor-scale plasmas. Whether or not the attainable rotation velocity (typically a few percent of the Alfvén velocity) will be sufficient to provide wall stabilization is presently a matter of debate (see Section 3.2.4). If rotation-sustained stabilization of kink modes proves to be inadequate, as Section 3.2.4 explains, active stabilization of the resistive wall mode by external coils will be needed for 'advanced-performance' steady-state RS operation in ITER. In addition to this possible requirement for active wall stabilization, the feasibility of generating and controlling the pressure and current profiles by non-inductive means in an alpha-heating-dominated plasma ($Q \geq 10$) in ITER or a reactor remains to be studied. Here better understanding of what profiles are optimal (or at least adequate) to obtain the desired MHD stability and confinement enhancements is urgently needed.

3.3. DENSITY LIMITS

The ability to operate with adequate energy confinement and MHD stability at plasma densities of about 10^{20} m^{-3} is critical to the achievement of adequate fusion power performance in reactor tokamaks based upon foreseeable superconducting magnet technology. For ITER operation at 21 MA, a plasma density of 10^{20} m^{-3} is about 15% above the Greenwald density $n_{GW}(10^{20}\ \text{m}^{-3}) = I(\text{MA})/\pi a^2(\text{m})$ [3.221]. As is now well known (see discussion of empirical density limit scalings below) the densities achieved in present tokamaks are usually (but not inevitably) constrained by $n_{max} \leq n_{GW}$, and hence achievable density normalized relative to n_{GW} has become a common figure-of-merit—equivalent to β_N—to quantify achievement in obtaining high-density plasma operation. While there are operational scenarios for ITER that produce full or nearly-full fusion power at or slightly below n_{GW}, it is clear that for ITER, an ability to operate

reliably in a density regime with ~0.8 ≤ n /n_{GW} ≤ ~1.2 is very important (see Chapter 2). Accordingly, there has been increased recent emphasis in tokamak research in obtaining a better understanding of the various processes that set limits on the achievable normalized density, especially in 'reactor-regime' plasmas with divertors, and adequate confinement (ELMy H-mode or better). As will be presented below, recent improvement in understanding of the density limits (there is more than one limit) is closely associated with new understanding of the characteristics of the plasma edge region in H-mode. There has also been significant recent progress in developing quasi-steady-state fueling methods that facilitate obtaining stationary above-Greenwald H-mode plasmas with relatively undegraded confinement quality. However, identification of fueling and/or edge optimization methods that can assure above-Greenwald H-mode operation with adequate confinement for reactor tokamaks remains as a topic of on-going experimental and theoretical study.

For ITER two distinct density limiting processes observed in present tokamaks are relevant. In present auxiliary-heated experiments, the highest normalized densities are generally achieved in L-mode plasmas and are almost invariably limited by the occurrence of a major disruption. This *disruptive* limit therefore sets an upper bound on tokamak plasma density. In addition, H-mode experiments have shown that there is a limiting density, somewhat lower than the density at which disruptions occur, above which H-mode confinement cannot be sustained. This limit, which causes a return to L-mode confinement, represents a *performance* limit. It is this density limit than is ultimately important for ITER and reactor operation. The goal for ITER is to obtain operation modes in which this performance limit corresponds to densities ≥ 0.8 n_{GW}, with 1.2 n_{GW} being a highly desirable operational capability goal.

Figure 3-45 shows how the characteristic features of the separate density limits and achievable operational domains for L-mode and H-mode operation are manifested in the ASDEX Upgrade tokamak [3.222]. The Figure shows the achievable domains for stable plasma operation, as depicted in terms of an $\bar{n}_e - P_{sep}$ operation parameter space, where $\bar{n}_e$ is the line-average density and P_{sep} is the power crossing the separatrix. The latter power is inferred from measurements of

the heating power and the profile of the radiated power. As Fig. 3-45 shows, in $\bar{n}_e - P_{sep}$ space, there are well-defined domains for L-mode and H-mode, the L-mode density limit exceeds the H-mode limit and is ultimately disruptive, and the limit for L-mode operation increases with power flow across the separatrix, whereas at high-density, the H-mode density limit is essentially power-independent and an increase in density leads to a transition back to L-mode. Figure 3-45 also shows that at moderate separatrix power, the L-mode limit can (in this example) slightly exceed the Greenwald limit density, and the maximum density for H-mode operation is (again in this example) somewhat less than both the disruptive L-mode limit and the Greenwald limit.

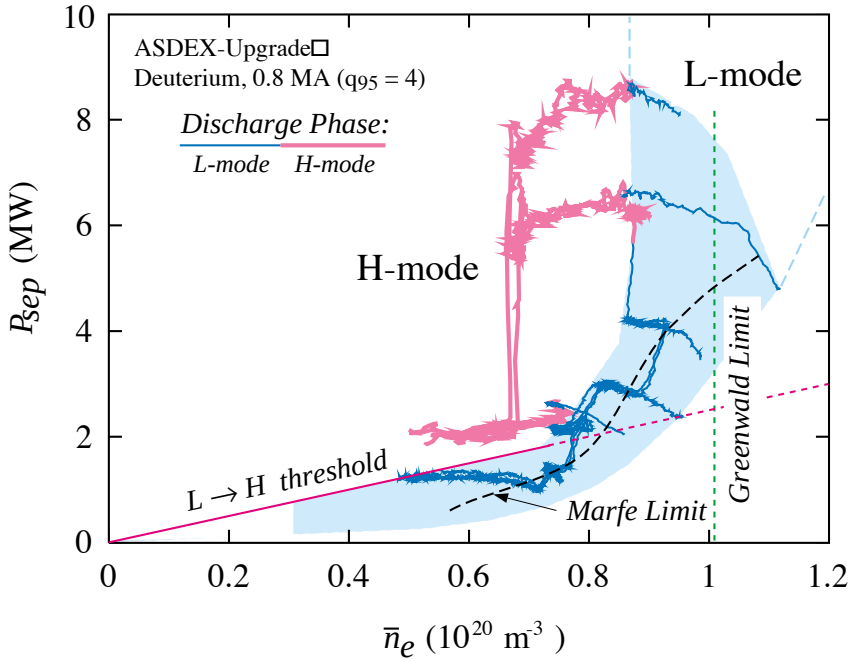

FIG. 3-45. Plasma operation domains and density limits in the ASDEX-Upgrade tokamak. Adapted from Ref. [3.222], Fig. 8. The $\bar{n}_e - P_{sep}$ trajectories for several 0.8-MA discharges with time-varying density and/or heating power are shown. The shaded region encompass the inferred domain for the L-mode phase. The high-density boundary of this domain is disruptive. The 'MARFE limit' curve within the L-mode region shows the onset density at which the divertor MARFE expands into the bulk plasma and full divertor detachment develops.

Figure 3-45 is presented here to illustrate the typical features of the density limits and attainable operation regimes encountered in an H-mode capable divertor tokamak. More detailed

discussion of the physics basis for the features depicted and discussion of the degree to which the various limits manifested in the Figure are affected by plasma parameters and operation attributes (fueling and heating means, wall conditioning and so forth) are presented in the following sub-Sections.

3.3.1. Disruptive Density Limits and Scalings

It has long been recognized that, for given plasma parameters, there is a maximum density which can be sustained, the limit being set by a disruptive instability. Murakami et al., [3.223] showed that in ohmic plasmas the limiting line-averaged density scaled as B_T/R, while Fielding et al. [3.224] demonstrated that the limiting density depended on the plasma current and that the limit could be extended by conditioning the torus wall by titanium gettering. These observations gave rise to the use of the Hugill diagram (see Fig. 3-46), in which the tokamak existence space is plotted in terms of q_c^{-1} vs. $\bar{n}_e B_T / R$, as a tool for describing the accessible density range. It was quickly realized that the density limit could be described in terms of a thermal imbalance between ohmic input power and (predominantly edge localized) impurity radiation losses (Gibson [3.225]; Rebut and Green [3.226]; Ohyabu [3.227]; Ashby and Hughes, [3.228]).

Subsequent, more detailed studies on larger devices (e.g., Campbell et al., [3.229]; Wesson et al., [3.230]; Lowry et al., [3.231]; Stäbler et al., [3.232, 3.233]; Kamada et al., [3.234]; Bell et al., [3.235]; Petrie et al., [3.236]) confirmed the major features associated with this general understanding of the disruptive density limit. Increasing plasma density leads to a rise in the impurity radiation from the plasma edge region, which cools the edge and produces a steepening of the current profile in the vicinity of the $q = 2$ surface. This process destabilizes n = 1 MHD modes (principally those with m = 2) which grow and produce a major disruption (see Section 3.4.1). The resulting plasma current termination, which is inevitably preceded by a relatively slow rise in the radiated power fraction and other indications of increasing radiation from the plasma edge, is commonly described as a 'density-limit' disruption. The rates of current decay

in density-limit disruptions are typically (but not always) slower that the rates of decay encountered in 'beta-limit' disruptions that are initiated by the more-rapidly-growing instabilities associated with the ideal MHD beta limit (see Section 3.2.1).

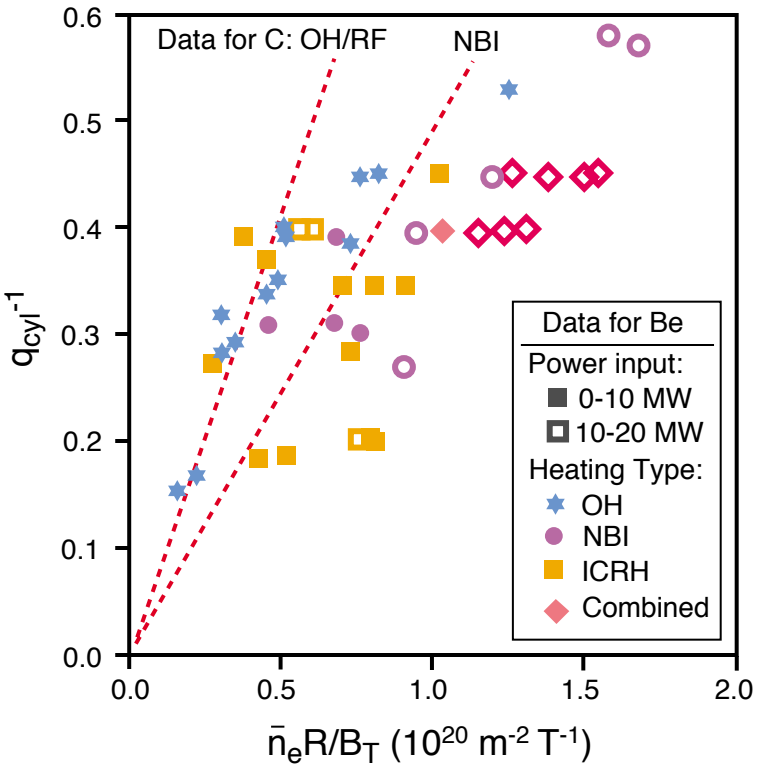

FIG. 3-46. Hugill diagram for JET limiter plasmas following introduction of beryllium evaporation and a beryllium limiter [3.237]. The points show densities normalized by B_T/R achieved in plasmas with various forms of heating. The two dashed lines illustrate the density limits in earlier OH/ICRF and NBI experiments with a mainly-carbon first wall For a given q_{cyl}, the largest values of the Murakami parameter after the introduction of beryllium represent densities 30-50% beyond the Greenwald density. The tendency for the normalized limiting density to increase with power input is also shown in the data.

Other key features identified in the course of these density-limit experiments included the fact that the limiting density should be identified with the edge, rather than the line-averaged density, since the radiated power can be written approximately as $P_{RAD} \approx f_{RAD} n_e n_Z^2 \pi a \Delta_{RAD}$, where $f_{RAD}(T_e, Z_{eff})$ describes the radiated power as a function of T_e and Z_{eff}, n_e is the electron

density characteristic of the (edge localized) radiating region, n_Z the impurity content in the radiating region, and Δ_{RAD} is the width of the radiating shell. This model was confirmed by comparisons between gas- and pellet-fueled plasmas, which showed that the latter achieved significantly (at least a factor of 2) higher line-averaged densities than the former, but had similar edge densities at the disruptive limit.

Support for the proposal that the density limit was determined by the thermal imbalance between input power and radiation losses came from experiments in JET showing that the edge density limited scaled as $P_{IN}^{0.5}$ [3.231] and from ASDEX, where the density limit exhibited a $P_{IN}^{0.25-0.4}$ scaling [3.233]. Finally, the important role played by impurity radiation was emphasized by the increased density limits found in experiments in which the plasma impurity content was reduced by improved conditioning, either by beryllium evaporation (Keilhacker et al., [3.237]) or boronization (Stäbler et al., [3.233]; Bell et al., [3.235]). Both of these wall conditioning methods reduce the plasma oxygen content substantially and hence raise the density at which radiation losses become critical.

An attempt by Greenwald et al. to deduce a generalized scaling for the (line-averaged) density limit, based largely on data from limiter and X-point (largely L-mode) plasmas in Alcator-C, PBX, and DIII-D, concluded that the density limit could be described by $\bar{n}_{\lim} = I_p / \pi a^2$, independent of the additional heating power [3.221]. Moreover, it was proposed that the ultimate limit was set by a degradation of particle confinement. While some experiments have been unable to exceed this 'Greenwald density' (e.g., Petrie et al., [3.236]), other gas-fueled experiments have exceeded it by a factor of 50% or more for certain operation parameters (e.g., Keilhacker et al., [3.237]; Mertens et al., [3.222]) while demonstrating simultaneously an explicit dependence on the additional heating power and no degradation of particle confinement. The RI-Mode of TEXTOR (Messiaen et al., [3.238]) also achieves densities that somewhat exceed the Greenwald value.

3.3.2. Radiation and Scrape-Off Layer Physics

Although the behavior at the disruptive density limit follows the broadest prescriptions of radiation-based models, the detailed behavior as the limit is approached is more complicated. As observed initially in Alcator C, the edge cooling associated with increasing radiation leads to the formation of a MARFE — Multifaceted Asymmetric Radiation From the Edge — (Lipschultz et al., [3.239]). This is a toroidally symmetric but poloidally localized region of cold high density plasma, with intense impurity emission, that is located at the plasma edge, usually on the high toroidal field side of the plasma. The formation of the MARFE is accompanied by a rapid growth in the global radiation fraction, and MARFEs can often raise the radiated power fraction to 100% with little change in the global plasma density. The formation of a MARFE is a common but not necessarily universal precursor to a density-limit disruption (see e.g., Fig. 3-45).

In limiter tokamaks, the MARFE appears to form on the closed flux surfaces, but in divertor devices the MARFE can emerge from the divertor region following the occurrence of divertor detachment (see below). Whether the MARFE ultimately decays into a poloidally symmetric radiation shell or persists for longer periods, the lowering of the flux-surface averaged temperature typically produces the sequence of events leading to a major disruption outlined above [3.230, 3.233]). There are, however, plasma operation strategies that can prevent MARFEs from developing into a disruption: for example, increasing the auxiliary heating power in ASDEX-U can reverse growth of a MARFE that would otherwise lead to disruption [3.240].

Numerous analyses of MARFE formation have been performed for the limiter case, i.e. MARFE formation inside closed flux surfaces (e.g., Stringer [3.241]; Neuhauser et al., [3.242]; Drake [3.243]; Choudhury and Kaw [3.244]; Wesson and Hender [3.245]; De Ploey et al., [3.246]), and there is general agreement on the main elements of the phenomenon. As the electron temperature falls under the influence of radiation cooling to values in the vicinity of 10 eV, power losses due to rising impurity radiation can no longer be balanced by parallel and perpendicular thermal conduction, leading to a growing thermal instability. While various suggestions have been

made for the source of the poloidally asymmetric nature of the instability, this aspect has not been satisfactorily resolved. Moreover, since the analyses are essentially concerned with the linear stability of the MARFE, and are generally restricted to 0-D or 1-D treatments of the plasma equilibrium (but see De Ploey et al., [3.246]) for a 2-D model), they are of limited value for making quantitative predictions.

In diverted plasmas, plasma behavior near the density limit, and in particular the development of a MARFE, is closely intertwined with the phenomena which occur at divertor detachment (Section 4.2-4.4). A complete understanding of the processes influencing the limiting (edge) density in a diverted plasma, therefore, involves an analysis of the relationship between plasma parameters at the midplane separatrix and the corresponding parameters in the divertor plasma in the vicinity of the target plate. This physics is more appropriate to the analysis of divertor behavior presented in Chapter 4 and a detailed discussion is deferred until then. Experimentally, it is observed (e.g., Campbell et al., [3.247]; Lipschultz et al., [3.248]; Asakura et al., [3.249]; Allen et al., [3.250]; Mertens et al., [3.222]) that as the bulk density rises, the plasma density at the divertor target initially rises. With increasing edge density, however, both the density and electron temperature at the target fall. When the temperature at the target drops to the vicinity of several eV, the plasma begins to detach from the target, initially close to the separatrix. At the same time a highly radiating region, denoted an 'X-point MARFE' moves out of the divertor towards the X-point and, if the bulk density continues to rise, the MARFE enters the bulk plasma, precipitating the growth of MHD activity and, ultimately, disruption.

The processes involved in the density limit in diverted plasmas are understood to a large extent and have been modeled analytically (e.g., Lackner et al., [3.251]; Borrass [3.252]; Borrass et al., [3.253]). It can readily be shown that there is a maximum density which can be maintained at the midplane separatrix: this density is essentially determined by classical transport along field lines to the divertor and the recycling and loss mechanisms (radiation, recombination etc.) in the divertor. The maximum density derives from the fact that the separatrix temperature is determined by electron heat conduction from the midplane separatrix to the cooler divertor along the scrape-off

layer. In addition, momentum transfer by charged and neutral particles in the divertor determines the plasma pressure at the separatrix. Thus, for given power flow across the separatrix, scrape-off layer width, and divertor geometry, these mechanisms together set the midplane separatrix density.

While analytic models are useful for assessing trends and parametric sensitivities of the maximum density, the complexity of the competing processes and of geometric effects in the cold divertor region as detachment occurs necessitates the use of 2-D multifluid codes for quantitative predictions (see Section 4.4).

3.3.3. H-Mode Density Limit

While the disruptive density limit bounds the MHD stability of the plasma, sustaining high fusion power in a device such as ITER requires the maintenance of H-mode confinement. Numerous experiments have shown that gas-fueled H-modes exhibit a density limit which manifests itself as a gradual degradation of energy confinement as the limit is approached, and which eventually results in a return to L-mode confinement at densities somewhat lower than the L-mode density limit (e.g., Petrie et al., [3.233]; Campbell et al., [3.254]; Mertens et al., [3.222]). This limiting density for gas fueled H-mode operation appears to be bounded in many present experiments by the Greenwald density, although certain experiments (e.g. Stäbler et al., [3.233]; Campbell et al., [3.247]) have demonstrated H-mode operation at densities 30-50% beyond the Greenwald scaling (Fig. 3-47), albeit typically at high safety factor.

As in L-mode experiments, pellet fueling has been used to extend the density limit somewhat beyond the Greenwald scaling (e.g., Lang et al., [3.255]; Mahdavi et al., [3.256]; Gruber et al., [3.240]), albeit with some penalty in confinement quality or problems with eventual radiative collapse owing to impurity radiation (Fig. 3-48). These results show that loss of H-mode confinement is not inevitable despite $n > n_{GW}$.

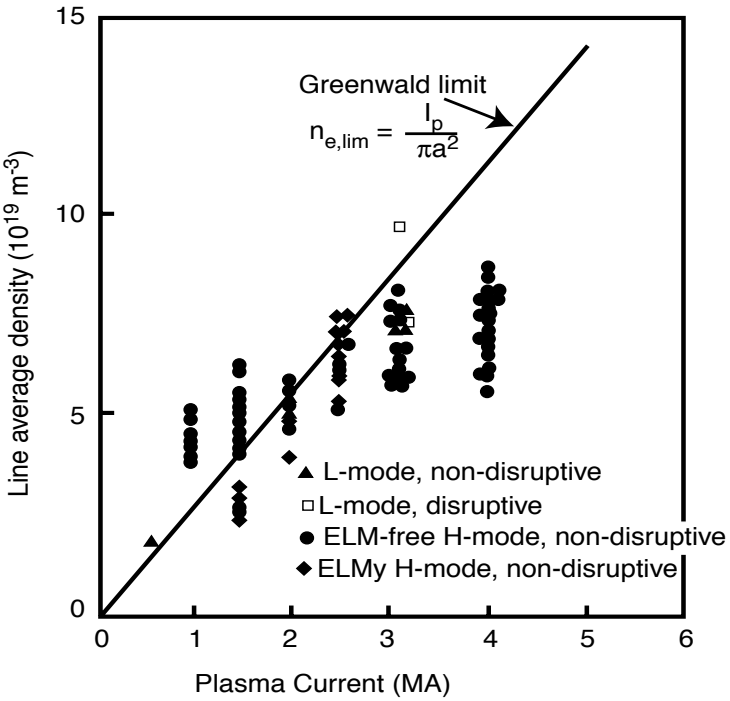

FIG. 3-47. Greenwald diagram for L- and H-mode plasmas in JET. Gas-fueled plasmas attained densities 30% beyond the Greenwald value with little confinement degradation, while pellet fueled plasmas reached higher densities (after [3.233]).

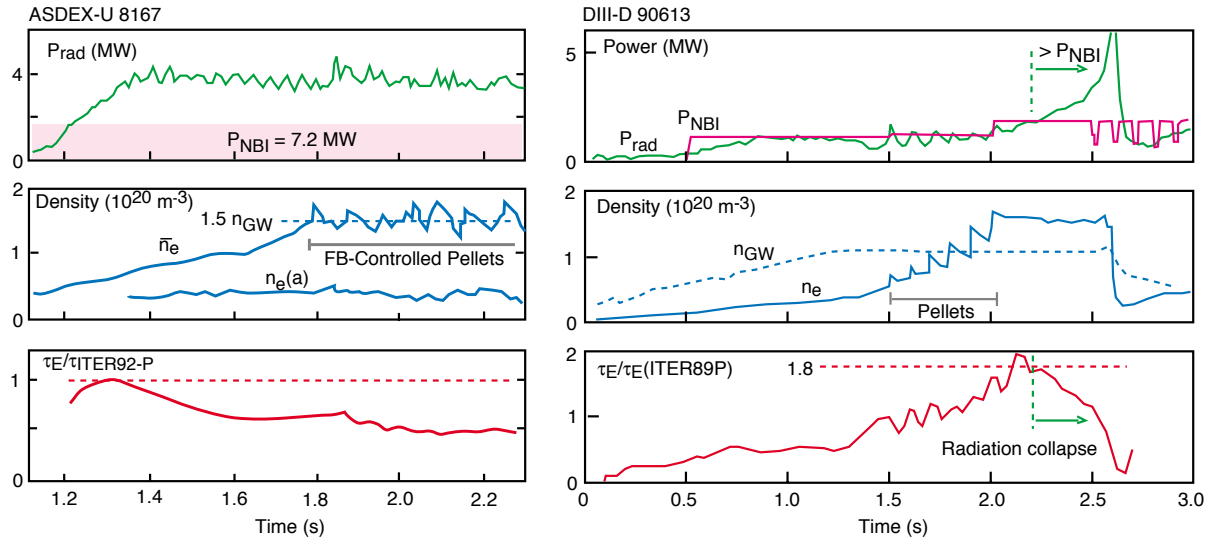

FIG. 3-48. Above-Greenwald pellet-fueling experiments in ASDEX-U and DIII-D.

The processes that limit the density at which H-mode confinement can be maintained differ from those responsible for the L-mode density limit, but are not yet fully understood. A possible explanation has been developed by the ASDEX Upgrade Group in terms of an edge parameter operational diagram for the H-mode (Kaufmann et al., [3.257]). As shown in Fig. 3-49, this diagram indicates the various operational boundaries influencing H-mode behavior in terms of the electron temperature and density at the top of the H-mode edge pedestal.

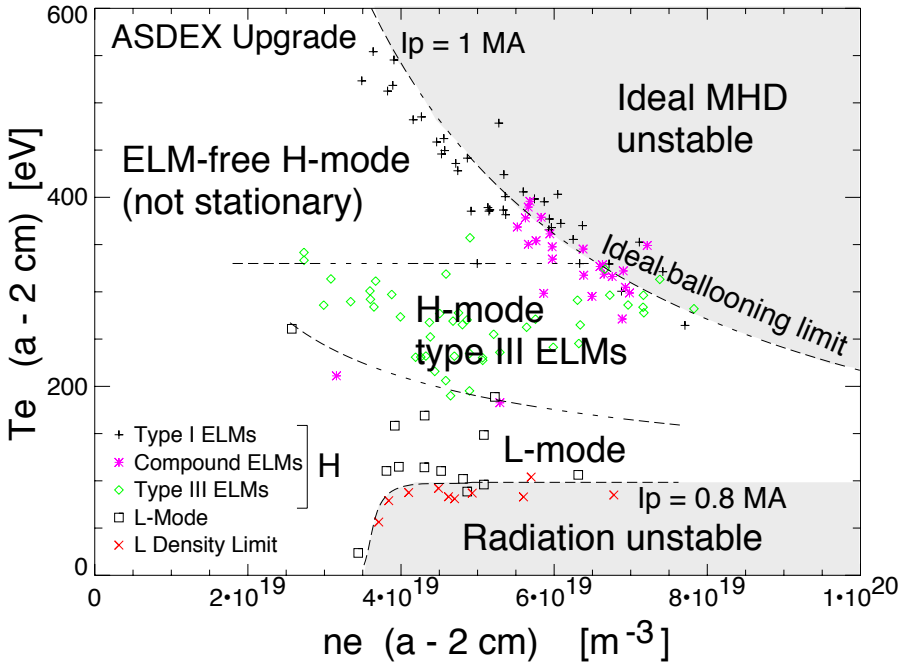

FIG. 3-49. H-mode operational diagram for ASDEX Upgrade presented in terms of the measured electron temperature and density 2 cm inside the separatrix (this location corresponds to the top of the H-mode pedestal). Boundaries indicating different types of confinement regime are indicated [3.257]. The limiting bound of edge pressure (nT) corresponds closely to the pressure gradient for onset of ideal MHD ballooning. The 'limiting density' for H-mode operation is approximately 7×10^{19} m^{-3} (cf. the similar H-mode limit shown in Fig. 3-45). — Same as FIG. 3-21 —

It is proposed [3.257] that the quality of H-mode confinement is influenced by the parameters of the pedestal, and that in gas-fueled discharges, increasing the pedestal density at the expense of the pedestal temperature produces a transition from Type I to Type III ELMs and then

to L-mode (see Fig. 3-49). While the underlying physical processes which determine this behavior have not yet been identified (see further discussion in section 4.3), this nevertheless suggests that, as in L-mode plasmas, the density limit is again an edge density limit. It cannot be excluded, however, that scrape-off layer and divertor processes also play some role in determining the plasma behavior in the vicinity of the limit (Borrass et al., [3.253]).

3.3.4. Means to Obtain High Density in ITER

While the operational diagram in Fig. 3-49 appears to offer a route to high-density, high-confinement operation close to the ideal ballooning limit at the right hand side of the diagram, it has in practice proved difficult to access this regime with gas fueling. Pellet injection from the low field side of the plasma has allowed access to somewhat higher densities, but the low fueling efficiency observed with such injection, which has necessitated additional gas fueling, suggests that this approach may not be an attractive scenario for ITER.

A major challenge at the ITER scale is to achieve pellet injection velocities which permit the pellet to penetrate beyond the pedestal and ELM-affected region. An alternative scenario which has recently been developed is the injection of pellets from the high field side of the plasma (Lang et al., [3.258]). This has allowed steady-state densities above the Greenwald value to be maintained with little loss of confinement quality (Fig. 3-50). The physics processes which influence the evolution of the density perturbation produced by the pellet, and which allow a higher fueling efficiency for high field side as opposed to low field side injection, are under investigation. However, it appears plausible that localized magnetic curvature effects should influence this behavior differently on the inside and outside of the plasma and could account for the improved performance obtained with high-field-side launch.

A further technique which has shown a promising deep fueling capability, though not yet in H-mode plasmas, is the use of compact toroids on Tokamak de Varennes (Raman et al., [3.259]). The possible application of these techniques to ITER is discussed further in Section 4.3.4.

A further operational aspect of obtaining reliable operation at high normalized density is related to the delicate control of the plasma parameters, especially the edge density and radiation fraction, that is needed to access and stay in the relatively small operational domain for high-density, high-radiation fraction H-modes, which typically lie close to a number of operational limit boundaries (see e.g. Figs. 3.3-1 and 3.3-5). Here implementation of feedback control of the fueling and impurity rates that is effected on the basis of core plasma radiation fraction and divertor plasma measurements and implementation of control algorithms that act on the basis of real-time plasma operation state 'cognizance' [3.260, 3.261] have proven to be very helpful in being able to reliably obtain and sustain such 'highly-optimized' plasma operation modes. The basis for such state-cognizant plasma control is further presented in Chapter 8.

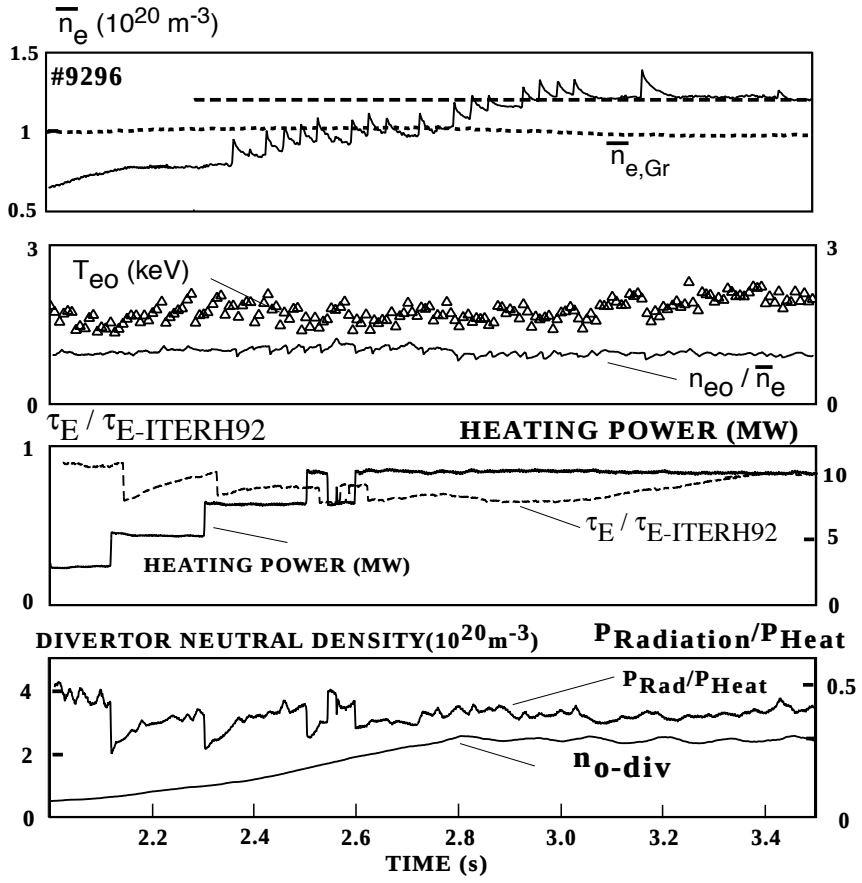

FIG. 3-50. Sustained above-Greenwald H-mode operation in ASDEX-U with feedback-controlled high-field-side pellet injection fueling and 10 MW NBI heating (from [3.258]).

3.4. DISRUPTION AND DISRUPTION-RELATED EFFECTS

Disruptions are an endemic and likely unavoidable (at least on an occasional basis) aspect of tokamak operation. For disruptions in reactor tokamaks, the ratio of plasma thermal energy to the first wall and/or plasma-facing-component surface area is sufficiently high that localized surface melting, vaporization and erosion of the affected areas (*e.g.*, divertor targets or localized portions of the first wall) is inevitable during the thermal quench phase of a disruption. In addition, during the current quench phase of disruption, there are electromagnetic (EM) loads (owing to induced currents) on electrically-conducting first-wall and vacuum vessel structures. In reactor tokamaks, these EM loads typically correspond to pressures of ~0.5 MPa (5 atmospheres) and thus result in structural loadings on the affected components that are typically higher than the loadings that arise in these components owing to their vacuum/pressure containment and gravity/seismic support functions. In addition to producing these immediate thermal and structural loadings, the current quench phase of disruptions in elongated tokamaks is usually vertically unstable (resulting in what is termed a vertical disruption or vertical displacement episode, or VDE). VDEs result in the generation of ex-plasma halo currents — plasma currents that flow helically along the in-plasma field lines that intersect plasma-facing-surfaces — and the poloidal reconnection of these in-plasma currents through the first-wall surfaces produces localized radial and vertical forces on these surfaces and global vertical and radial loadings on the collective in-vessel system and torus vacuum vessel. Finally, in high-current reactor tokamaks, there is theoretical but well-justified concern that the high electric fields inherent in the current quench phase of a disruption and/or VDE (even without a preceding thermal quench) can convert an appreciable fraction of the initial plasma current to ~10 MeV runaway electron current. The ultimate dissipation of this current to in-vessel surfaces can again result in localized surface thermal damage and erosion.

This Section addresses disruptions and their consequential effects, with emphasis on how such effects extrapolate to reactor tokamak conditions. Disruption causes, MHD instability development and frequency are addressed in Section 3.4.1. The thermal and current quench

characteristics of disruptions — the key basis for the electromagnetic and thermal loading design of in-vessel and vessel components — are addressed in Section 3.4.2. The characteristics of VDEs and halo currents and of runaway electron conversion and deposition are respectively covered in Section 3.4.3 and Section 3.4.4. Here is worth noting that these two processes may be at least partially complementary and interrelated — vertical instability typically tends to mitigate substantial runaway conversion, at least in present tokamaks, and so the two subjects must ultimately be considered together. A third aspect, fast plasma power and/or current shutdown by impurity injection — which is also closely related in reactor tokamaks to runaway conversion and the mitigation of VDE loads — is addressed in Section 3.4.5. This discussion is followed by a presentation in Section 3.4.6 of the more general topic of disruption avoidance and effect amelioration. Finally, Section 3.4.7 addresses the need for integrated and self-consistent modeling of the full sequence of disruption effects and ensuing consequences, a capability that is shown to be ultimately necessary to make definitive prediction of the disruption and disruption-effect characteristics in a reactor tokamak and in ITER.

3.4.1. Causative Factors, Development of Instability, and Frequency of Occurrence

It is well known that the achievable domain of stable operation in tokamaks is limited: in plasma current by the safety factor q_ψ, in density by the Greenwald parameter $n/n_{GW} = n_e/(I(MA)/a^2(m)$, and in pressure by the Troyon normalized beta parameter $\beta_N = \langle\beta(\%)\rangle I(MA)/a(m)B(T)$. Each of these 'operational limit' parameters has a nominal limit — minimum q_ψ, maximum n/n_{GW} and maximum β_N — and approach to the respective limiting values ($q_\psi \approx 2$, $n/n_{GW} \approx 1$ and $\beta_N \approx 3.5$) usually initiates an increase in the level of MHD activity and eventually onset of major disruption.

As result of major disruption, plasma energy confinement is lost, the plasma is cooled to sub-keV temperatures in less than 1 ms, and global contamination of the plasma by products of chamber wall desorption and erosion ensues. These factors result in a dramatic increase in plasma

electrical resistance and an ensuing rapid current quench, at rates that can approach 1000 MA/s. The electromagnetic (EM) loadings from the current quench on tokamak torus vacuum vessels and in-vessel components results in structural loadings and forces on these components. These loadings and forces become more significant in high-performance tokamaks operating at fields higher than 2-3 T. For fixed q_ψ and elongation, first-wall magnetic pressures scale as B^2, so ITER and reactor tokamak pressures will be about 4-9 times higher than in present 'low-field' tokamaks.

In addition to these EM loading effects, during the thermal quench there are also impulsive thermal and particle fluxes to the plasma-facing-component surfaces, with corresponding surface heating and erosion and associated thermal stress and fatigue. While the structural and plasma-facing-component surface designs of present tokamaks have generally been sufficient to accommodate the thermal and EM loading effects from disruptions and their associated consequential effects (halo currents and runaway electron formation, see Section 3.4.3 and 3.4.4), instances of in-vessel component damage and unanticipated vessel and in-vessel component forces have occurred in present experiments, in part owing to loading conditions or current-flow patterns that were not fully anticipated in the original design basis. Modification of in-vessel component designs to fully withstand disruption thermal and/or EM loading have been required in many 'modern' tokamaks, including JET, JT-60U and PBX.

3.4.1.1. Disruptions in reactor tokamaks and ITER

Disruptions and their consequential effects pose significant design challenges for reactor-regime tokamaks in general and for ITER in particular. These challenges arise in part owing to the higher magnetic fields (≥ ~6 T) needed to achieve burning plasmas in such devices, and in part owing to the inherently unfavorable size scaling of thermal quench energy loading in large tokamaks, wherein the plasma thermal energy increases as the cube of the device dimension, whereas the surface area for energy deposition increases only as the square of dimension. This size scaling means that, for example, thermal quench energy deposition levels from Ohmic plasma

disruptions in ITER are already capable of producing appreciable divertor target surface vaporization. The combination of higher field and/or larger size make thermal loading effects up to two orders of magnitude higher in ITER than in present sub-ignition experiments and EM loading effects up to one order of magnitude higher.

Modern tokamaks, even the largest operating devices (JET, JT-60U and TFTR) have generally up to now been able to manage the consequences of disruptions with only limited impact on operational schedules, albeit with the need in some cases for application of special first-wall surface reconditioning actions (for example, TFTR required about 400 cleaning pulses to fully recover from a major disruption) and in some cases with the imposition of administrative controls to discourage undue occurrence of disruption, or with implementation special control procedures to avoid impending disruption or to mitigate the consequences of subsequent effects. This relative lack of long-term consequential effect of disruptions in present tokamaks is the main reason why special systems for management and mitigation of disruption consequences have been largely absent in present tokamak praxis. There is, however, a well-known incentive for the operating staff of every tokamak to determine parameters for plasma operation and disruption frequency and recovery that allow an acceptable balance to be obtained between the development of maximum plasma performance and the efficient utilization of the available plasma operation time. The balance that is obtained varies from tokamak to tokamak, but there is a tendency for the larger tokamaks to be somewhat more cautious about producing an undue number of disruptions and to take control and mitigation actions that either prevent the occurrence of disruption or limit the consequential effects of disruption (see Section 3.4.6).

We anticipate for ITER that a systematic approach to disruption avoidance and consequence amelioration will be necessary and prudent, since each disruption will at a minimum consume a finite portion of the divertor target thickness and operational lifetime: for nominal parameters and 10% disruption frequency, disruption and sputtering erosion of the targets in ITER are estimated to be approximately equal in an integral sense and the 'disruption allocation' for a typical target will be of the order of several hundred disruptions. In addition to the anticipated consumption of the

divertor target surface, the combination of a hot-plasma VDE (Section 3.4.3) or runaway conversion event (section 3.4.4) combined with the geometrical localization inherent in the achievable limitations on the first-wall to toroidal-field alignment can cause localized surface damage to the first wall that will require surface repair or module replacement. It will be highly desirable to avoid this latter degree of intervention.

It is therefore reasonable to suppose that the ITER plasma control system (see Chapter 8) will incorporate a number of means to predict and avoid the occurrence of major disruptions and hot-plasma VDEs (see Section 3.4.3) and to mitigate or ameliorate the effects of the disruptions and VDEs that cannot be avoided (see Section 3.4.6). However, the concept development and testing of such disruption prediction, avoidance and amelioration means are presently the subject of R&D studies in present tokamaks, and there are a number of physics issues involved in the extrapolation of such means to a reactor tokamak, and hence final definition of the disruption avoidance and amelioration means that will be implemented in ITER awaits progress in this reactor-critical aspect of plasma control R&D.

3.4.1.2. The physical nature of major disruptions

The basic physical nature of disruptions in tokamaks is well understood and hinges upon the fact that the tokamak magnetic configuration can become unstable to helical perturbations of the form

$$\xi(r,t) = \xi(r) \exp i(\omega t + m\theta - n\varphi)$$

where θ and φ are the poloidal and toroidal angles and m and n are the corresponding poloidal and toroidal integer mode numbers. The rapid and ultimately non-linear explosive growth of such instabilities, especially in a multi-mode combination, gives rise to the rapid loss of thermal energy confinement that starts the disruption sequence.

Two distinct physical phenomena have been proposed as disruption mechanisms:

1. The magnetic reconnection (overlapping) of plasma areas with different helicity [3.262]. This reconnection is possible under the nonlinear development of helical instabilities (nonlinear tearing mode). The resulting plasma-wide region of chaotic magnetic field provides a conductive transport mechanism for the rapid loss of thermal energy in the onset phase of disruption.

2. The nonlinear development of the ideal helical instability in conditions of low magnetic shear. This development can result in capturing and macroscopic transportation of "vacuum bubbles" (helical flux tubes with cold peripheral plasma) from the boundary into the center of the plasma column [3.263]. The net result of this process is again a rapid loss of thermal energy, this time largely by macroscopic mixing, with subsequent final conduction to the plasma-affected surfaces.

Consideration of the observable details of disruption instability development and thermal energy loss tends to suggest that the second mechanism is more likely to be ultimately responsible for the development of major disruption. There is, however, clear evidence for an important role for mechanism (1), particularly in the precursor growth phase that occurs before the thermal quench begins, and both mechanisms may be operative in some disruptions. In any case, numerous experiments [3.230, 3.264–3.268] show that the major disruption thermal quench develops after an initial fast flattening of $T_e(r)$ profile in the center, a behavior essentially like the flattening that occurs (without disruption) in a sawtooth oscillation (see Section 3.2.2). This pre-thermal-quench 'sawtooth' behavior points indirectly to loss of the magnetic shear in the plasma center as being the instability enabling mechanism. Direct magnetic measurements that confirm shear loss during a major disruption have not been carried out yet, however, they have been done during softer internal disruptions — in normal sawteeth — using Faraday rotation and MSE [3.269] (JET).

These measurements demonstrate the apparent rise of Δq in the center after sawtooth: the current profile flattening and magnetic shear decrease. With the increase of the disruption energy, Δq rises to 0.2. We can expect that this value will reach close to 0.5-1 in a 'giant' sawtooth (see Section 3.2.2) and the penetration of m = 2 perturbations into the plasma center will become possible.

Soft X-ray measurements (Fig. 3-51) made just before a major disruption in T-10 demonstrate both the precursor growth phase, the coalescence of the m = 1 and m = 2 magnetic islands and the eventual entrance of a cold 'bubble' into the plasma core. A generally similar sequence of instability growth and disruption data is obtained in a wide variety of tokamaks, but there are variations in the details of the sequence and data both within a given tokamak (owing to variations in the pre-disruption plasma parameters) and from tokamak to tokamak. Presentation of the richness of this detail and its correlation with various interpretations of non-linear MHD instability theory are beyond the scope of this Section. But here it suffices to say that a great deal of magnetic and plasma soft X-ray and electron cyclotron emission data on disruptions is available and that discussions of sometimes complementary models of detailed MHD evolution of the after-precursor instability growth phase of a disruption continue within the disruption/MHD community. Representative examples of the mode growth data and MHD interpretation and further references to the extensive literature on instability growth can be found in Refs. [3.24, 3.267–271].

Finally, as was manifested in 'advanced performance' JET plasma operation regimes with small magnetic shear in the center, the development of major disruption is very possible [11]. The same tendency is typical for all regimes with negative shear in the center. The destruction of hollow current profile (near q_{min}) in this regime results in a major disruptions (see the discussion of MHD stability of reverse-shear plasmas in Section 3.2.7).

The obtained experimental experience proves the suggestion that the key event proceeding the major disruption is the weakening of the magnet shear in the core. The reasons of this weakening could be different: instabilities in the center (minor disruptions), locked mode development, impurity accumulation, neoclassical tearing mode development and so on. The

threshold for each instability corresponds to an MHD limit on current, density, pressure, periphery perturbations and so on.

The most common form of this type of event is a minor disruption.

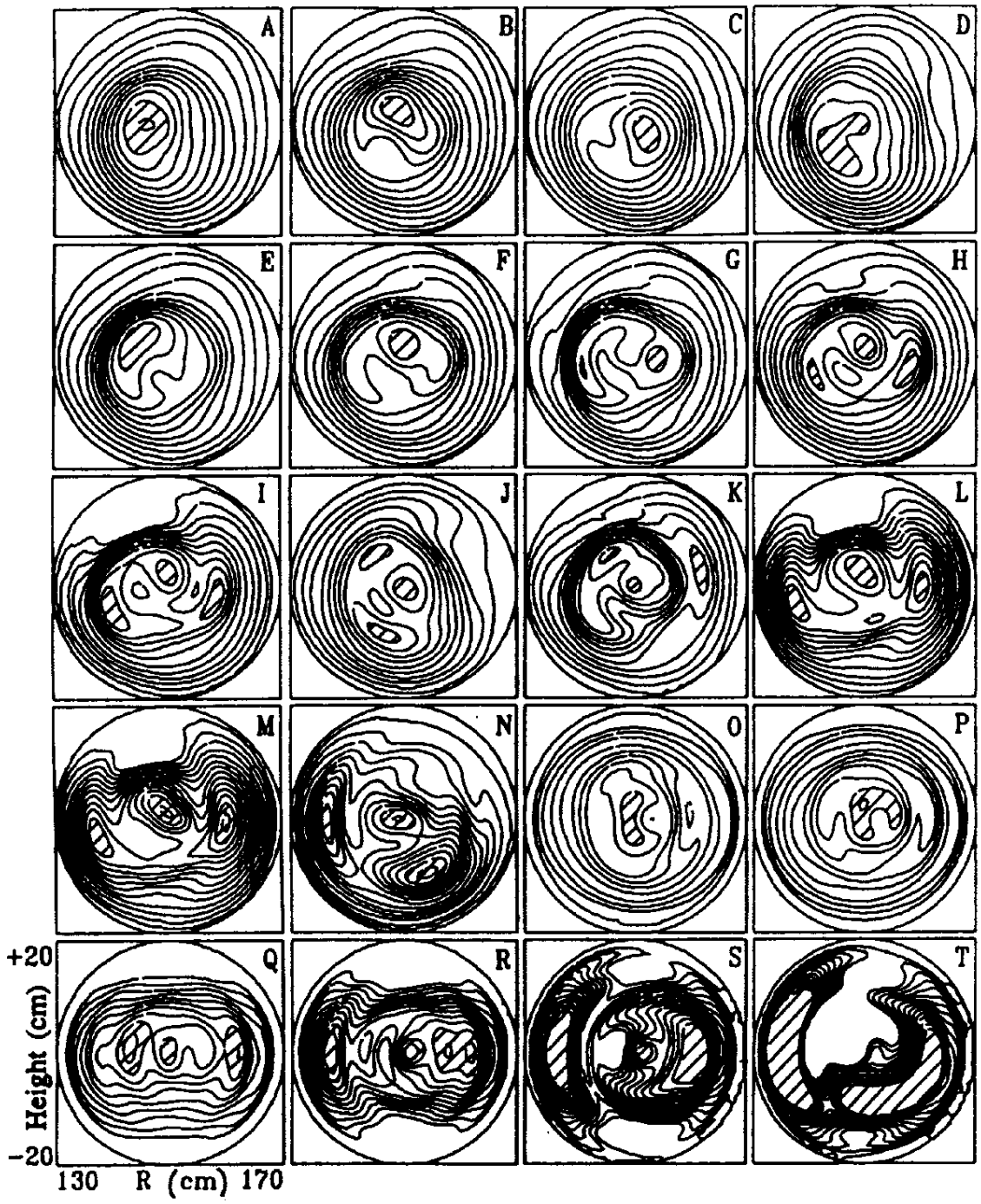

FIG. 3-51. Soft X-ray tomographic reconstruction of the development of a major disruption in T-10. Contours of equal SXR emission; high-emission region diagonally shaded. Frames A-F (at 60 μs intervals): m = 1 precursor growth; frames G-L (Δt = 830 μs total, interval varies): m = 2 mode growth; frames M-T (Δt = 230 μs total, interval varies somewhat): m = 1 and m = 2 modes coalesce and 'cold' bubble enters plasma column (frame T).

3.4.1.3. Minor disruption

The notion of minor disruption (earlier called "pre-disruption") [3.264] is used to define phenomena with fast local reconnection of magnetic field lines and corresponding plasma losses, but which do not lead to large energy fluxes onto walls and current quench.

The energy coming into divertor in a major disruption is comparable with the total plasma thermal energy (JT-60, [3.272]), whereas during a minor disruption the thermal energy loss is only about 5-20%. This loss is due to local character of overlapping of neighbor magnetic islands with m and m±1, forming as a result of nonlinear tearing or neoclassical tearing mode development. The overlapping process is manifested as a fast turbulent mixing on a time scale τ = 10-100 μs. Simultaneously, the main losses of plasma energy and T(r) local profile flattening occur, likely owing to magnetic stochastization.

Internal disruptions — the sawtooth instability with m = 1 and n = 1 — are very similar to minor disruptions. The giant sawtooth is usually accompanied by island overlap for the m = 1 and m = 2 modes and looks much like a minor disruption. Owing to its local character, the minor disruption can develop in the plasma center and also, under tdouble tearing mode development in the negative-shear regime [3.210, 3.211], in the ring area near the column boundary.

3.4.1.4. Edge local modes (ELMs)

MHD events localized in the plasma edge called ELMs, share certain similarities with minor disruptions. ELMs develop near the column boundary in conditions of large pressure gradient in H-mode regimes. ELMs are believed to some sort of pressure-driven modes with a wide spectrum

n = 1-15, while for usual minor disruptions n = 1-3. Discussion of the MHD basis for ELMs and a brief review of ELM phenomenology will be found in Section 3.2.

Two main types ELMs are observed — Type I ELMs and Type III ELMs. For Type I ELMs, the recurrence period increases with increasing plasma heating power till a transition into single (solitary) ELMs — called 'giant' ELMs [3.19] occurs. In contrast, for Type III ELMs, the period decreases with increasing heating power and or stabilization with the rise of electron temperature near the boundary: this behavior points on the resistive origin of this type of ELM.

Giant ELMs can have effects on plasma-facing-surfaces similar to minor disruptions. Experience in JET [3.162], shows that the maximum energy output in this type of ELM can reach ~10% of the total thermal energy, and the typical time of the process is about 100 μs. The resulting local thermal loads to the divertor can reach the value of 5 GW/m^2. Evaluations for ITER give divertor target power loadings of about 30 GW/m^2 (~3 MJ/m^2 deposited energy): this level will be high enough to produce divertor target sublimation and erosion.

Overlap between a giant ELM and a giant sawtooth can be especially dangerous: the resulting thermal disturbance that develops can span the width of the entire plasma column and initiate a major disruption. Giant ELMs or giant sawteeth alone may also act as triggers for neoclassical island tearing mode growth (Section 3.2.2) and can thus also lead to eventual disruption.

3.4.1.5. Dynamics of major disruption

In Fig. 3-52 we can see a typical n_e (or β)-limit major disruption in JET [3.230]. This kind of disruption will likely be most dangerous for ITER.

The three characteristic steps in major disruption development are shown in this example (Fig. 3-52): a phase of slow thermal quench, a phase of fast thermal quench with follow-up short positive current pulse $\delta I_p \approx 0.1 \times I_p$ generation and finally, a phase of current quench.

Analysis shows that origin of slow thermal quench phase is a locked (non-rotating) n = 1 helical mode. This slow initial thermal quench onset is followed by a second more rapid and

nearly complete cooling of plasma column. The sudden initiation of a locked (non-rotating) mode (see Section 3.2.5), which frequently occurs as the result of minor disruption or sawtooth fast development in the plasma center, is believed to be responsible of the thermal quench onset. If rotation is only braked, but not stopped completely (TFTR), a major disruption does not occur. This points on a possible way to avoid major disruptions of this kind in ITER by the forced rotating the column. This can possibly be done by using neutral beam injection.

The origin of main fast thermal quench is believed to be m = 1 / n = 1 mode development (giant sawtooth, TFTR [3.267]), as was originally seen in small tokamak experiments [3.266].

The direct cause for the ensuing major disruption (marked by the l_i drop and positive current spike) is believed to be the loss of magnetic shear and “bubble capture”, as has been mentioned above. Here the precise details of shear loss, bubble capture and subsequent partial or full plasma cooling are complex and can vary from tokamak to tokamak and from plasma to plasma in a given tokamak. This variation gives rise to the range of thermal quench behavior details (i.e., thermal content decay waveforms) that are observed. But despite these variations, the effective consequences are similar: there is a rapid rapid loss of thermal energy followed by initiation of a current quench. The characteristics of these phases are addressed in Section 3.4.2.

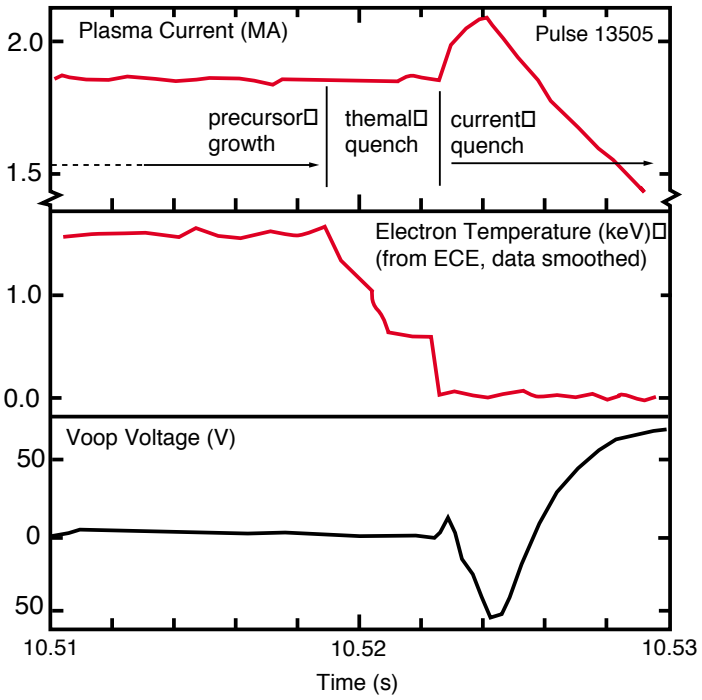

FIG. 3-52. Typical disruption in JET (ohmic plasma). The slow and fast phases of the thermal quench, the ensuing positive current rise and negative voltage spike and the subsequent onset of the current quench are shown. Precursor growth occurs during a period that may extended from up to 100 ms before thermal quench [3.230]. Note that the zero of the plasma current axis is suppressed: only the first part of the current quench is shown

3.4.1.6. Disruption frequency

The frequency of occurrence of disruptions in present experiments on a per pulse basis falls in the range of 1 to 100%, with the low end of this range corresponding to plasma operation with reliable hardware and well-documented 'reference' or 'setup' discharges with conservative operational parameters (q_{95}, n/n_{GW} and β_N and easily controlled plasma shape). There are also examples of high-performance 'reference' discharges that operate quite near the ideal MHD beta limit with disruption frequencies ≤ 1% (see e.g., TFTR 'supershots' [3.273]). The high end of the disruption frequency range is obtained in plasma operation development campaigns with parameters close to or exceeding key plasma operation limits (low q_{95}, high normalized density,

high edge radiation fraction and/or high normalized beta) or to operational situations where disruptions in a secondary phase of the plasma operation scenario (e.g., during current rampdown) have no deleterious impact and are accepted as a routine operation consequence. When such 'don't care' disruptions and obvious hardware-failure-initiated disruptions are eliminated from consideration, the disruptivity during current flattop (disruptions per pulse) typically falls in the range of 3-to-40%, with the upper end of this range again being characteristic of exploratory operation close to operational limits.

While attempts have been made to correlate disruption frequency with plasma shape, edge safety factor, proximity to theoretical or empirical beta limits, density limits (radiation or H-mode threshold limits, see Section 3.3) and so forth, no overall understanding of the relationship of disruption frequency to these parameters and proximity (as opposed to transgression) of well-defined operational limits has so far emerged. While there are examples of broadly-collected data sets that show a tendency for disruption likelihood to increase in a gradual manner as various operational limit parameters are approached (see *e.g.*, the TFTR data in [3.273]), there are counterexamples from the same experiment that show that for a given discharge, it is possible to predict the β threshold for onset of disruption arising from ideal MHD instability to within a few percent (see Section 3.4.6, Fig. 3-53) and to avoid disruption by staying just below this threshold. Under these conditions, the 'physics' reliability of this type of high-performance 'developed' discharge can be 99% or higher.

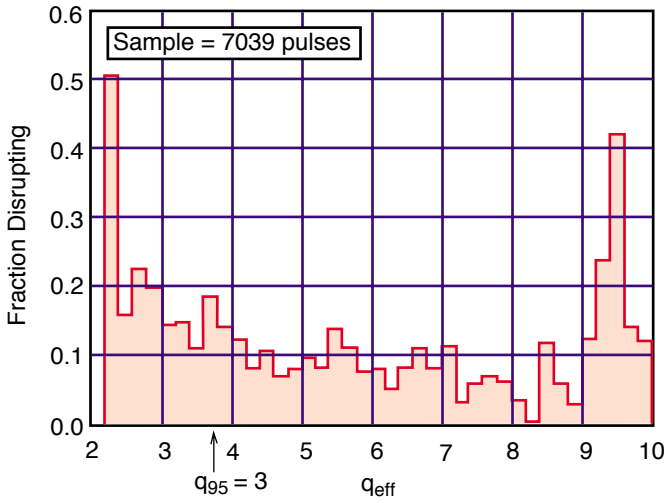

FIG. 3-53. Disruption frequency versus effective safety factor ($q_{eff} \approx 1.25\ q_{95}$) in JT-60U. Only disruptions during current flattop are included. A wide range of experiments and plasma parameters are included in the data set. Data and analysis courtesy of R. Yoshino on behalf of the JT-60 Team

Figure 3-53 shows representative disruption-likelihood data summarizing the per-pulse disruption frequency obtained in JT-60U over a prolonged campaign of plasma operation with a wide range of plasma currents and fields and some shape variation. Overall disruption frequency per shot for current flattop is 9.6% (average for 7039 shots with $q_{eff} \approx 1.25\ q_{95} = 2.2$-10). The average frequency versus q_{eff} rises gradually to about 15% with decreasing q_{eff} from 5 to 3 (q_{95} = 4 to 2.4), with local maxima of ~20% at $q_{95} \approx 3.8$ and 2.8. Disruptivity as a function of q_{95} evaluated on a per-second basis (disruptions per second of plasma operation duration) in Alcator C-Mod and TCV for similar 'wide ranging campaign' periods show a similar nearly q-independent frequency distribution. The data tends to shows a gradual rise in disruption frequency in the $q \leq 4$ regime, but the details of the rise vary from machine to machine and the statistics of the frequency distribution in the $2 \leq q \leq 3$ domain are poor. There is also anecdotal evidence that it is possible to improve the reliability of low-q operation if plasma operation goals mandate and if adequate operation time (and disruption budget) for optimization of such low-q plasmas is provided.

3.4.1.6. Extrapolation to ITER

The design basis assumption for ITER disruption frequency in a developed full-performance operation mode with $q_{95} = 3$ and $\beta_N = 2.2$ is 10%. The design basis assumption for overall disruption frequency during the commissioning and operations development phase that leads up to this phase of ITER operation is 30%. While these frequencies are consistent with present experimental achievements, final detailed justification for them will require continuing studies of the sensitivity of inherent disruptivity to the proximity to operational limits (especially density and non-ideal MHD beta limits) and careful analysis of data to separate the effects of administrative limits on disruptions and plasma operational objectives, procedures and operator experience from the underlying physics aspects of disruptivity. The effect of having a sophisticated suite of plasma and machine status diagnostics available to provide a basis for disruption avoidance and onset warning in aggressive operation regime experiments also needs to be quantified.

As is presented in Section 3.4.6, there are potentially promising methods for the early (well before precursor growth onset) prediction of impending disruption and a number of 'active' intervention means (including rf current drive control of mode growth) that may make it possible to intervene during the precursor growth phase to avoid disruption occurrence. However, the degree that such methods can be applied in ITER and their effectiveness in reducing disruption frequency remains a matter for R&D studies in present tokamak experiments.

Given that the frequency of disruptions in ITER will be ~10% (say 1500 disruptions during a ~15,000-pulse Basic Performance Phase operation campaign, see Chapter 9), it is essential that the ITER vessel and in-vessel structures be designed to accommodate the EM and structural loading consequences of at least this number of disruptions (plus the additional disruptions that would occur in the follow-on Extended Performance Phase). It is also essential that the at-risk plasma facing and first-wall surfaces be designed to accommodate the thermal and erosion effects of the total number of disruptions expected during their respective service lifetimes. As noted

above, there are also structural and/or thermal consequences of the VDEs that will follow disruption and thermal and erosion consequences of the runaway electron conversion that may follow disruption. The thermal and current quench characteristics of ITER disruptions, and the expected characters of ITER VDEs and runaway conversion are respectively developed in the following three Sections.

3.4.2 Disruption Characterization: Thermal and Current Quench

Disruptions terminate plasma operation by a thermal quench in which most of the plasma thermal energy is rapidly lost, primarily by conduction to the plasma-defining surfaces (limiter or divertor targets). During a thermal quench, the core plasma temperature typically falls, first to less than several hundred eV and subsequently to less than 100 eV. In the ensuing rapid current decay (current quench phase) that this cooling precipitates, the plasma magnetic energy is also dissipated, mostly by more-or-less-uniform impurity radiation to the torus vessel or first-wall surface.

The rapid loss of thermal energy during the thermal quench has important design consequences for the plasma in-vessel and torus vessel components, and the rapid change in the plasma poloidal magnetic field that occurs during the current quench generates significant induced electrical currents and corresponding electromagnetic (EM) forces in electrically-conducting in-vessel components and the torus vacuum vessel. In a vertically-elongated divertor tokamak, coupling of the current decay to the vertical position instability also results in a vertical displacement of the plasma column (a VDE) that occurs on the same time scale as the time of the current decay.

For in-vessel component and torus vessel design purposes in reactor tokamaks, the most important design parameters are the durations of the thermal and current quenches and the parameters that characterize the localization and magnitude of the resulting thermal energy deposition on divertor targets. There are theories that attempt to model the non-linear MHD instability development that is responsible for the onset of the thermal quench and to then subsequently model the effects of the thermal energy loss, the resulting influx of wall-generated

impurities and the vertical instability and halo currents that follow in the current quench phase. However, the resulting complexities of instability development and the plasma mixing that it produces (see Section 3.4.1), experiment-to-experiment variance in the details of thermal and current quench and VDE phenomena in present tokamaks and the onset of new physics effects in reactor-scale tokamaks (e.g., divertor surface vaporization and impurity generation and avalanche multiplication of runaway electrons) make theoretical prediction of disruption characteristics and consequences in future high-current, high-specific-energy reactor tokamaks a matter of on-going discussion and model development. The present status and validation of the 'integrated' modeling capability that will be needed to make such predictions for ITER are discussed in Section 3.4.7.

In the meantime, an empirical basis is needed to predict disruption characteristics for future reactor tokamaks and to this end, ITER Expert Group on Disruptions, Plasma Control and MHD has made efforts since 1994 to establish a multi-machine database, the ITER Disruption Database (IDDB) that can be used for characterization of disruptions and disruption-related effects. A discussion of disruption phenomenology and references and a preliminary account of the Expert Group characterization effort through 1995 is given in [3.271]. The IDDB has since been substantially expanded and now comprises three types of data: (1) a global disruption database from 14 tokamaks that contains 'typical' data relating to disruptions, (2) a halo current database from 6 vertically-elongated divertor tokamaks, and (3) a thermal and current quench database from 7 tokamaks. This latter database is presently limited to current quench data, but work to add systematic thermal quench data is in progress. This Section presents the characterization of the thermal and current quench aspects of disruptions based on the first and third components of the IDDB. Characterization of VDEs and halo currents derived from the second IDDB component is presented in Section 3.4.3. More recent accounts of the ITER disruption design basis specifications and of the halo current characterization derived from the IDDB can be found in [3.274, 3.275].

It has not yet been possible to employ the IDDB for runaway electron characterization. Discussion of data on runaway generation in present experiments and of the mostly theoretical

basis for extrapolation of these data to the reactor regime will be found in Section 3.4.4. Prior discussion of the runaway electron design basis specifications for ITER will also be found in [3.275].

3.4.2.1. Thermal quench characteristics

In the sequence of events that comprises disruption in a tokamak, thermal quench follows the initial MHD precursor growth phase (see e.g., [3.230] and Section 3.4.1). From a global viewpoint, the ultimate result of the thermal quench is a rapid loss of the plasma thermal energy to the same plasma-defining surfaces (limiter or divertor) that were active in defining the plasma (receiving conducted power) prior to disruption. However, on detailed inspection, the thermal quench process exhibits complexities in exactly how and in what time sequence the energy loss proceeds, there are clearly discernible non-axisymmetric MHD effects (e.g. toroidal asymmetries) visible in where thermal energy is deposited on the affected plasma-defining components, radiation effects are sometimes appreciable and there are significant differences among the quench dynamic behaviors seen in various experiments and even among different discharges and types of disruptions in the same experiment [3.230]. These variances are seemingly the result of the complexity of the underlying MHD process that culminates the precursor growth phase and the presence of the two MHD mixing mechanisms — mode overlap and 'cold bubble' entrance (see Section 3.4.1) — that contribute to thermal energy transport in the thermal quench phase of disruption.

In this latter regard, evidence for the presence of two mechanisms can be found in the fact that thermal quenches are often observed to take place in two stages (see *e.g.* [3.230] and [3.268]), as shown schematically in the inset of Fig. 3-54 and explicitly in Fig. 3-52, Section 3.4.1. However, single-stage thermal quenches, sometimes on a somewhat slower time-scale, are also often observed (see *e.g.*, [3.268]), presumably owing to overlap of the two stages. During the first stage of two-stage thermal quenches, an m = 1/n = 1 erosion of central temperature takes

place and the temperature profile inside the q = 2 surface flattens. The plasma outside the q = 2 surface seems to still act as a thermal barrier, although a fraction (~10-30%) of the total thermal energy is spilled out to the wall. In the second stage, the edge thermal barrier breaks down completely and most or all of the remaining thermal energy is rapidly lost to the wall. However, sometimes the second stage itself exhibits a further staging of energy loss, resulting in a multi-step thermal energy decay waveform.

The first stage of two-stage thermal quenches can be understood by modeling of non-linear interactions of 1/1, 3/2, and 2/1 magnetic islands [3.271]. The time scale of the nonlinear interaction is in agreement with the prediction made in [3.276], which is $\tau_s = [(\tau_\eta)^3(\tau_{A\theta})^2]^{1/5}$, where τ_η is the magnetic diffusion time and $\tau_{A\theta}$ is the Alfvén time with respect to the poloidal magnetic field. The theoretical basis for the time scale of the fast quench — believed to be determined at least in part by the macroscopic convective transport that arises from 'bubble entrance' — is not as well understood or predictable on an *a priori* basis, but the relevant time scale is clearly Alfvénic. Data for time scales of both time-scales of thermal quenches from the IDDB are plotted against plasma minor radius in Fig. 3-54. Although the data are quite scattered, the initial delay time $\tau_{1\text{-}2}$ and the final fast quench time τ_2 both increase roughly in proportion to plasma minor radius (with respective size scaling scalings $\sim a^{1.5}$ and $\sim a^1$), and the ratio $\tau_{1\text{-}2}/\tau_2$ is typically about 10. As shown in Fig. 3-54, extrapolation of the two quench times to ITER minor radius yields $\tau_{1\text{-}2} \approx 20$ ms and $\tau_2 \approx 1$ ms. The scatter and error bars of the data in Fig. 3-54 show that these values have considerable uncertainty, and the ranges of possible values that may occur in ITER are estimated to be 6-60 ms and 0.3-3 ms respectively.

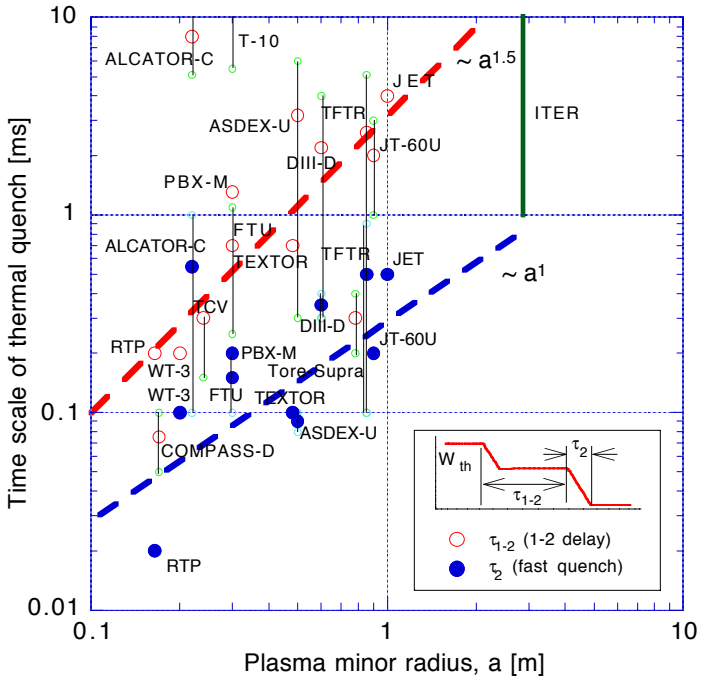

FIG. 3-54. Thermal quench times $\tau_{1\text{-}2}$ (delay between initial and final quench) and τ_2 (fast quench) for various tokamaks, plotted as a function of plasma minor radius. Extrapolation to ITER (a = 2.8 m) yields $\tau_{1\text{-}2} \approx 20$ ms and $\tau_2 \approx 1$ ms

The thermal quench duration measurements presented above are derived from plasma temperature or pressure or soft X-ray emission measurements. There are also corresponding measurements of the thermal energy deposition on limiter and divertor surfaces (*e.g.*, [3.277]). Here the thermal energy lost from the plasma core is found to be deposited on the same plasma-defining-surface — limiter or divertor target — that was active in receiving the pre-disruption power flow from the plasma scrape-off layer (SOL). The thermal quench produces a readily observable surface temperature excursion whose onset and rise time is well-correlated with the corresponding loss of thermal energy in the plasma core. Figure 3-55 shows a representative set of plasma and target power/energy data for a disruption in the ASDEX-U tokamak.

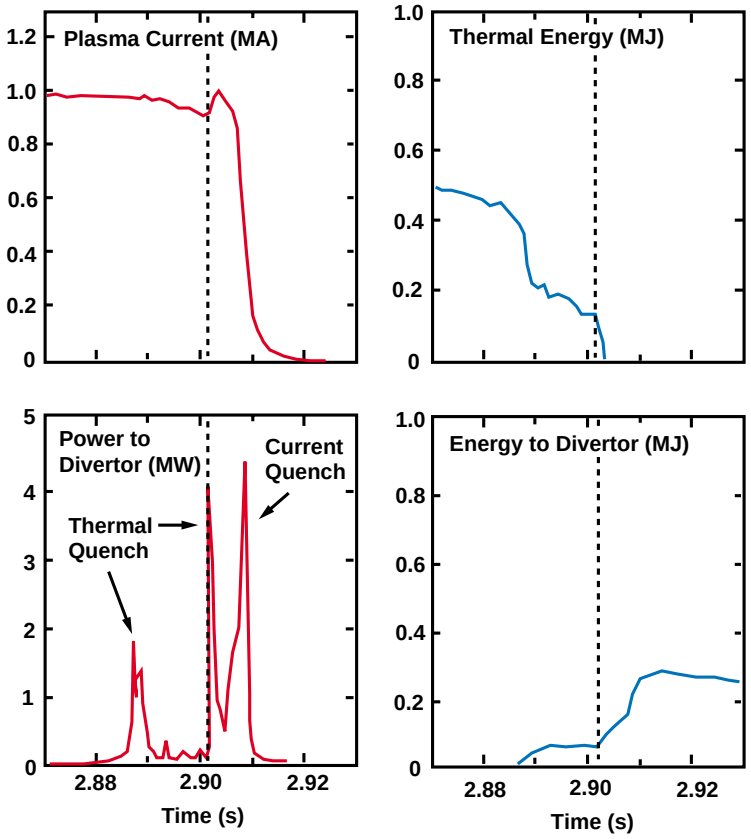

FIG. 3-55. Plasma current and thermal energy and inner divertor target power and cumulative thermal energy during a disruption (pulse 6134) in ASDEX-U. In this example, about 20% of the initial plasma thermal energy reaches the inner target at the end of the thermal quench. The remainder of the target energy comes from the dissipation of magnetic energy in the current quench, which is accompanied by a VDE (vertical motion toward the divertor). The authors conclude in this example that there is significant loss of plasma thermal energy by radiation upstream of the divertor. Data courtesy of O. Gruber for the ASDEX-U Team.

Estimates derived from such data of the energy accountability during a thermal quench show that the fraction of the initial plasma thermal energy that reaches the limiter or divertor can range between 20% and 100% of the initial plasma thermal energy. Energy depositions in the range of 50-100% are typical (see Fig. 3-56 below). The lack of full accountability for the plasma thermal energy can be explained in several ways, including (1) radiative diversion of what would otherwise be power conducted to the limiter or targets, (2) toroidal asymmetries and the lack of full toroidal monitoring of the limiter or target and other plasma-heated surfaces, and (3) uncertainty in

the limiter and target temperature rise data and in the resulting calculation of deposited energy. In the latter regard, the accuracy of total energy accountability measurements is limited (±20% accuracy is considered quite good) and systematic thermal quench energy accountability data on a multi-machine and/or multi-discharge basis is not yet available. Typical energy accountability data for several types of disruptions and VDEs in DIII-D are shown in Fig. 3-56. The design basis recommended for ITER is 80-100% of the initial plasma thermal energy [3.278]. The possibility of up to 30% thermal energy deposition on the surfaces of the ITER divertor entrance baffle is also recommended.

Measurements of the spatial profile of the surface temperature rise show that the conducted power is deposited in a radially-localized region that corresponds (in a divertor tokamak) to the approximate position of the pre-disruption SOL. There is, however, usually an expansion of the poloidal width of the SOL width during the thermal quench and there may also be some lateral (poloidal) shift in the deposition centroid. The expansion is typically about 3 relative to the pre-disruption width, but expansion factors of 1-10 have been reported and there is significant evidence in many cases for fast dynamic changes — attributed to the effects of MHD fluctuations in the SOL — in the surface heat flux and profile within the duration of the heat pulse. There are also changes in the ratio of deposited energy on the inboard and outboard divertor targets in single-null divertor plasmas relative to the pre-disruption ratio for normal conducted power: an inboard/outboard energy ratio of 2:1 is typical during disruption versus a 1:2 ratio for power during normal operation. Figure 3-56 shows data for toroidal asymmetry, in-out ratio and total accountability in various DIII-D disruptions and VDEs. This data is representative of what is reported by other experiments, but systematic multi-machine data on SOL expansion and inboard/outboard deposition ratios and on the effects of MHD fluctuations are presently lacking. The recommended nominal design basis for ITER is a 3-x SOL width expansion (to 3 cm), a inboard/outboard divertor energy ratio that may vary between 2:1 and 1:2 and the possibility of a nominal toroidal energy peaking factor (peak/average ratio) of up to 1.5 [3.278].

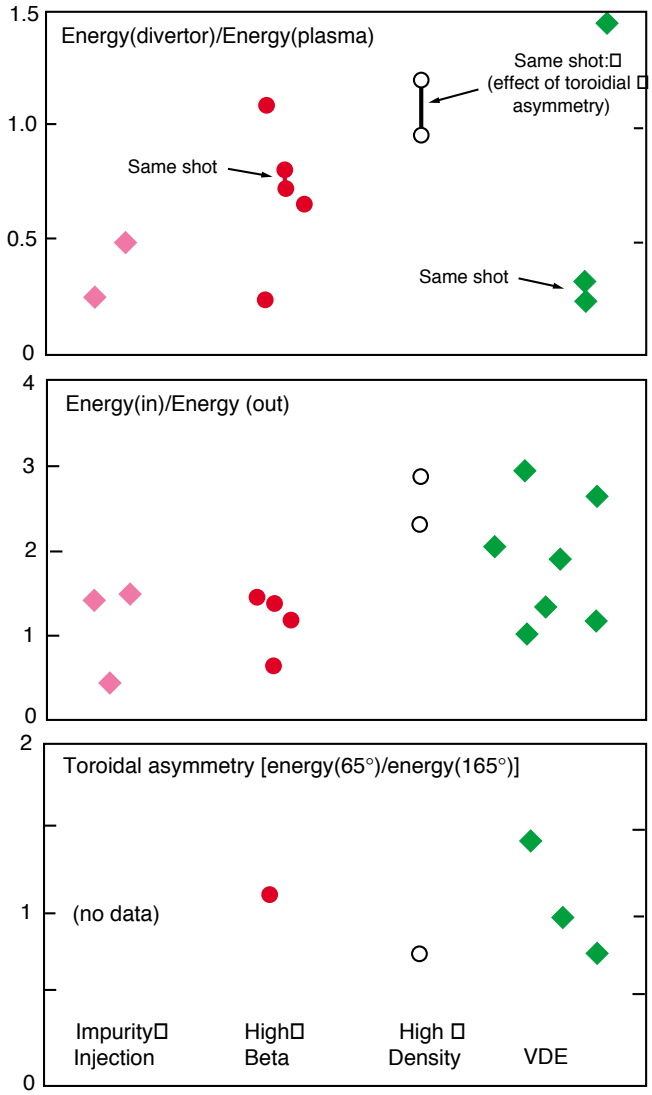

FIG. 3-56. Toroidal asymmetry ratio, inboard/outboard divertor target ratio and total energy accountability (referenced to plasma thermal energy) in various DIII-D single-null divertor disruptions and VDEs. The horizontal arrangement of the data within the four groups is for presentation purposes only and has no significance. Data and analysis by A. Hyatt, C. L. Lasnier, R. L. Lee, A. Kellman

Consideration of the effects of disruption thermal energy deposition on the affected plasma-facing-surfaces in present experiments and in ITER falls outside the scope of this Chapter and the IDDB data collection activity. Here we note only that in present divertor experiments, while the time scale of energy deposition is short (~100 μs), the specific plasma energy content (energy/torus

surface area) is low and the resulting energy loading on the divertor surfaces is typically less than the ~0.3 MJ/m^2 threshold required to produce appreciable surface melting and vaporization or sublimation. Accordingly, target erosion owing to thermal quenches and 'plasma shielding' effects — defined below — are both generally negligible in present tokamaks. In contrast, in ITER, elementary estimates show that while the expected thermal quench will be somewhat slower (~1 ms), the 'raw' incident energy loading on the divertor targets — calculated without consideration of the redistribution effect of plasma shielding but with a 3-x SOL expansion and toroidal peaking factor assumed — will be in the range of 30-60 MJ/m^2. This is well above the surface vaporization threshold, which is ~1 MJ/m^2. Consequently, in the ITER divertor, the incident thermal quench energy is expected to quickly lead to formation of a localized high-density plasma shielding layer near the surface of the affected component. This layer will in turn shield the underlying surface and radiatively redistribute most of the remaining incoming incident plasma thermal energy to nearby surfaces. This 'plasma shielding' redistribution mechanism will limit the target surface power flux and surface erosion but will also produce energy loadings in other nearby regions of the divertor channel that are high enough to initiate vaporization and further propagation of plasma shielding. The resulting in-divertor energy redistribution effect is analogous to the redistribution of incident energy inside an inertial fusion hohlraum target and is expected in ITER to spread the incident thermal quench energy over an appreciable fraction of the total in-divertor surface area (~400 m^2).

Estimates of the thermal quench energy effects expected in ITER, especially the predicted divertor target surface erosion — which must be inferred on the basis of simulations of the plasma shielding and energy redistribution effect — will be found in Chapter 4. Here we note only that owing to the present uncertainties in both the time duration of the incident energy deposition and the area ('footprint') of the disruption-affected portion of the target surface, the sensitivity of the predicted erosion to variations in the time scale and energy loading magnitude (including the effects of uncertainties in the inboard/outboard partitioning, MHD fluctuation effects and toroidal asymmetries) and also to the possibility of two or more separated thermal quenches in a single

disruption or a 'slow' quasi-linear thermal quench will need to be examined with detailed and self-consistent models of the target surface response and in-divertor redistribution of incident energy.

We also note here parenthetically that both the present quantity and quality of the plasma thermal energy loss time scale and magnitude data in the present IDDB are not as good as can be desired, and that there is very little systematic data in general on the surface energy deposition area and effective scrape-off layer width and asymmetries during disruption. Consequently, future efforts to improve data quality in these regards and to better validate models for extrapolation to reactor-scale experiments are required. A summary discussion of the basis for extrapolation of present thermal quench data to ITER and of the need for future research needs follows in Section 3.4.2.3 below.

3.4.2.2. Current quench characterization

The principal direct effects of the current quench phase of a disruption are the EM forces that arise in the electrically-conducting structures that typically comprise the torus vacuum vessel and — in an ITER-class tokamak — the modular structures that make up the plasma-facing-surface (first-wall) and nuclear shield. In addition, in a vertically-elongated tokamak, residual or inherent up-down asymmetries (e.g., a SN divertor) in the first-wall/vessel configuration and plasma geometry result in coupling of the m = 1 vertical position instability to the current quench, and so current quenches in elongated tokamaks are usually manifested as 'vertical disruptions' or VDEs, in which vertical instability and current decay occur simultaneously and on essentially the same time scale. The resulting plasma motion generates both toroidal and poloidal currents the in-vessel and vessel structures. In either case, the first design consideration is the rate of current decay, which not only determines the direct EM loading (induced toroidal currents) but also enters into determining the magnitude of the 'ex-plasma' halo currents that produce local forces on in-vessel structures and global vertical forces on the collective in-vessel/torus-vessel structure (see Section 3.4.3).

For quantifying the anticipated current quench characteristics of reactor tokamaks and ITER, it is important to understand that while fast quenches result in the highest direct EM loads, slower current quenches are predicted — owing to the close thermal coupling that exists between the closed-flux-surface plasma core region and the open (wall-intersecting) halo region in which halo current flow develops — to produce higher halo current magnitudes and vertical forces on the in-vessel and vessel system (see Section 3.4.3). Accordingly, the worst-case design basis situations are complementary and it is important for design purposes to understand the possible range of current quench durations, from minimum to maximum. In addition, the conversion of plasma current to runaway electron current via the knock-on avalanche is theoretically predicted to depend (at least in some marginal situations, see Section 3.4.4.) on current quench rate. So again, understanding of the range of possible quench rates is needed.

To provide for these ITER design basis needs and to help develop a better understanding of the mechanism(s) that determine current quench rates in tokamaks and of how these mechanisms extrapolate to an ITER-class tokamak, a comprehensive set of current quench data have recently been added to the IDDB from Tore-Supra (192 shots), ASDEX-U (206 shots), JET (755 shots), JT-60U (220 shots), Alcator C-Mod (2907 shots), TFTR (239 shots), and DIII-D (1802 shots). Figure 5 shows the results of analysis of the resulting multi-machine set of current quench data, in which the current quench time $\Delta t_{\rm cq}$ divided by the plasma cross-section area S is plotted as a function of the before-disruption average current density $\langle j_{p0} \rangle = I_{\rm p0}/S$. Here $I_{\rm p0}$ is the pre-disruption plasma current, $S = \kappa \pi a^2$ is the before-disruption plasma cross-section area and the current decay time $\Delta t_{\rm cq}$ is uniformly corrected to represent the '60% linear decay' time (the time required for a 60% drop in the plasma current), as inferred from the time-average or maximum current quench rate data provided by the various tokamaks. As the Figure legend shows, the basis for the current decay rate or decay times provided by the various machines differs somewhat (80% to 20% current for ASDEX-U and Alcator C-Mod; 90%-10% for DIII-D and TFTR; 100%-40% for JET, maximum $dI_{\rm p}/dt$ for Tore Supra and JT-60U). Using the '60% linear decay' equivalent

time (i.e., $\Delta t_{80\text{-}20}$ for ASDEX-U and C-Mod, $\Delta t_{100\text{-}40}$ for JET, $0.75\Delta t_{90\text{-}10}$ for DIII-D and TFTR, etc.) allows the data from all machines to be combined.

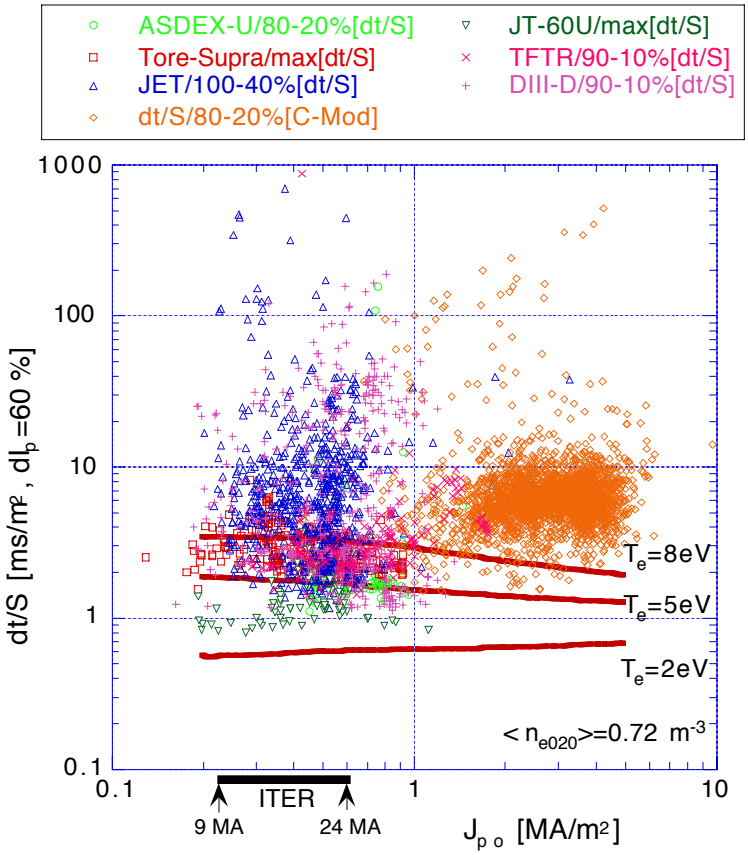

FIG. 3-57. Time-average current quench times (for $\Delta I_p = 60$ %) divided by plasma cross section area versus plasma current density before disruption. The normalized quench times for three electron temperatures as inferred from a simple radiative power balance model are compared with the experimental data.

Detailed evaluation of the data from those machines (e.g.,. Alcator C-Mod) in which both maximum and average (80%-20% or 90%-10%) data are available shows that the systematic differences among the four definitions for decay rate are, after correction for the explicit differences in measurement basis, not appreciable relative to the data scatter and the other machine-to-machine differences that enter into the multi-machine assessment of the data. For example, the linear decay time inferred from 90%-10% data in C-Mod is typically about twice the time inferred from 80%-

20% data (Fig. 3-58). The rate inferred from 80%-20% data is similar to the maximum rate. These statistical observations extracted from the database are consistent with the well-known tendency of current decay waveforms to have an 'S-shape', with highest decay rate at roughly 50% current and slower initial and final decay rate (see inset in Fig. 3-58). This type of waveform analysis suggests that a linear decay time inferred on the basis of a 60% change in plasma current provides a good measure of both the average and peak instantaneous current decay rate.

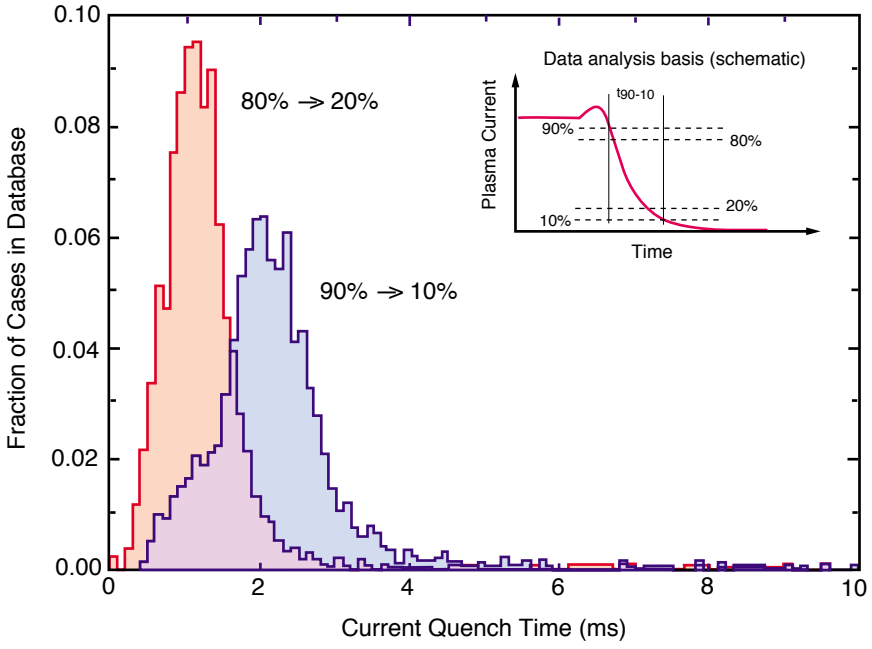

FIG. 3-58. Histogram of current quench times (100% linear decay) derived from 80%-20% and 90%-10% current thresholds in Alcator C-Mod. Current magnitudes are measured relative to the initial before-disruption plasma current. Data and analysis by R. Granetz

The data presented in Fig. 3-57 demonstrate that while a wide range of area-normalized quench times are obtained in a given experiment, the mean normalized quench times are essentially independent of (1) device configuration (limiter/circular or divertor/elongated) (2) the presence or absence of vertical instability during the current quench (there is no difference evident between limiter/stable data and divertor/unstable data), (3) machine size and toroidal strength and (4) before-disruption plasma current density. Furthermore, the minimum value of $\Delta t_{cq}/S$ in the database is

bounded by 0.8 MA/ms*m^2, again independent of initial current density: this bound implies that the time in ITER for 60% current decay will be about 32 ms, or 53 ms for 100% decay. These values are minimum decay times: if disruptions in ITER prove to have the same type of decay time variance as present experiments, the fastest 'typical' decay times in ITER will be about 100 ms, and much longer decay times, exceeding 1000 ms are possible. As is noted above, such 'slow' current decays are predicted to result in higher halo currents and vertical forces during the VDE phase of the current decay.

The basis for both the wide variation seen in the normalized quench time within a given experiment and the existence of a lower bound on the normalized quench time for all experiments can be understood in terms of a model for the quench phase in which the characteristic current decay time $t_{cq} = L_p^{eff}/R_p$ can be rewritten in terms of the normalized quench time as

$$\frac{t_{cq}}{S} = \frac{L_p^{eff}/2\pi R_0}{\eta_p} \tag{3-12}$$

where L_p^{eff} is effective plasma inductance (as determined by the poloidal flux within the torus vessel or first-wall), R_p is plasma resistance, R_0 is the major radius and $\eta_p = R_p S/2\pi R_0$. For the relatively fast current quench times that comprise most of the database entries, only the plasma inductive energy internal to the torus vacuum vessel enters into determining the current decay rate and $1.2\, L_p^{int} = 1.2\, \mu_0 R_0 l_i/2$ (l_i is the usual internal inductance) is a good estimate for the effective plasma inductance. Given this estimate and the well-known fact that the internal inductance of typical tokamak plasmas is essentially constant, the ratio t_{cq}/S is determined only by the plasma resistivity, which in turn depends mainly upon the decay phase electron temperature T_e and only weakly, especially at low temperatures, on plasma density and impurity species. The normalized decay times predicted by Eq. (3-12) can be compared with the experimental data by means of a simple calculation of the average plasma resistivity in the current decay phase, wherein T_e and η_p are determined through the power balance between joule heating from the decaying plasma current

and impurity radiation loss, the impurity content being adjusted to self-consistently obtain the desired temperature. This calculation gives

$$\eta_p = \left(\frac{n_e}{j_p}\right)^2 f_z L_z(T_e) \tag{3-13}$$

where n_e, f_z, and L_z are respectively the electron density, impurity fraction, and the impurity radiation rate assuming coronal equilibrium. Using Eqs. (3-12) and (3-13), $L_p^{eff}/2\pi R_0$ = 0.084 μH/m (l_i = 0.7 plus 20% flux between plasma surface and first wall), assuming a carbon impurity and taking the corresponding coronal equilibrium ionization state (Z_{eff}) and radiation rates into account yields the normalized decay times versus T_e and $\langle j_{p0} \rangle$ shown in Fig. 3-57. The $\langle j_{p0} \rangle$ dependence is very weak. The lower bound on the normalized current quench times corresponds to an average plasma temperature between 5 eV and 3 eV. This average temperature in turn corresponds to the lower limit on plasma temperature that is consistent with the expected effects of impurity radiation cooling from low-Z impurities, where radiation rates fall dramatically at temperatures less than about 3 eV.

The lower limit on normalized quench rate is obtained only when there are sufficient impurities present in the quench phase to bring T_e down to ~3 eV. In contrast, in a situation where impurity influx (after the thermal quench) is insufficient to cool the plasma to this minimum temperature, the resulting normalized quench times increase, and the 'mean' of the experimental data, which corresponds to higher average temperature, is consistent with quench temperatures in the 10-20 eV range. We note here, however, that the indications of temperature presented in Fig. 3-57 and the temperatures discussed herein are indirect: future work to correlate these inferred temperatures with direct measurements of T_e and Z_{eff} during the quench phase of representative plasmas would confirm our modeling.

Table 3-VI summarizes key machine and plasma parameters and results from the database for current quench analysis. The final column shows the estimated wall L/R time and demonstrates that the lower range of the current quench times obtained in a given experiment are less than the

characteristic times of surrounding structure. Therefore the approximation made above about the effective plasma inductance is well-justified for these data. On the other hand, the high end of the quench time range in a given experiment is often greater than the wall time, and the corresponding increase in the effective inductance (plus possible attempted corrective action by the plasma current regulating system or the presence of some runaway conversion) may account for some of the very large normalized decay times that are present in the database.

Table 3-VI. Machine and Plasma Parameters and Analysis Results for Current Quench Database

Tokamak	R_0 (m)	a (m)	κ	S (m^2)	Min. t_{cq}/S (ms/m^2)	Min. t_{cq} (ms)	t_{wall} (ms)
Tore-Supra	2.3	0.75	1.0	1.77	2	3.5	7.5
JET	3.0	1.0	1.5	4.71	1.5	7.1	5
C-Mod	0.68	0.22	1.6	0.243	1.7	0.4	6
ASDEX-U	1.65	0.5	1.6	1.26	1.1	1.4	13
JT-60U	3.3	0.9	1.4	3.56	0.8	2.8	20
TFTR	2.5	0.9	1.0	2.54	1.2	3.0	10
DIII-D	1.7	0.6	1.8	2.04	1.0	2.0	10
ITER	8.14	2.8	1.6	39.4	0.8*	32*	~1000

Extrapolation for ITER based on $S^{-1}dI/dt = 0.8$ MAm^{-2}/ms

3.4.2.3. Application to ITER and future needs

Straight-forward application of thermal and current quench data assembled in the IDDB yields estimated thermal quench times in ITER of about 1 ms, delays between the first and second thermal quench of up to about 20 ms and minimum current quench times of 50 ms (maximum dI/dt ≤ 450 MA/s). This maximum current quench rate corresponds to an average plasma temperature of about 3 eV, which is the minimum average plasma temperature consistent with impurity radiation cooling. 'Typical' fast current quenches in ITER with somewhat higher plasma temperature are probably more likely and can be expected to have at least 100 ms duration. Much slower current

quenches, with durations of up to 1 s (dI/dt ≅ 20 MA/s) are possible and need to be considered with respect to the more-severe VDE and halo current loading effects that a slower current decay and higher halo temperature can be expected to produce.

The theoretical basis for the essential linear extrapolation with plasma minor radius of thermal quench times from present experiments to ITER seems to be in reasonably good agreement with the experimental data, but the quality and more systematic compilation of the thermal quench data could merit future attention. Systematic data on the localization of thermal quench energy loss to divertor targets and/or other in-vessel surfaces is presently sparse and it is not yet possible to make very definitive predictions of how thermal energy deposition in an ITER-class experiment will be localized on the divertor targets and what the possible toroidal peaking or other asymmetry factors will be. While provisional estimates for these quantities based on the limited existing data have been developed for ITER, these estimates are accompanied by a recommendation that the effects of the significant uncertainties that presently exist should be carefully examined.

The basis for prediction of the minimum current quench duration in an ITER-class experiment and the corresponding worst-case estimates for the maximum expected direct EM loads on the in-vessel components seems to be sound and consistent with the predictions of a simple radiation cooling model. In contrast, prediction of the maximum, as opposed to minimum, current quench duration is less certain and will, at a minimum, have to await development of self-consistent predictive models for impurity generation and influx, for VDE and halo current effects and for possible runaway electron conversion. Discussion of the considerations involved follows in Section 3.4.4, Section 3.4.6 and Section 3.4.7 of this Chapter.

3.4.3. Vertical Instability and Halo Currents

Vertical instability plays an important role in the current quench phase of disruptions in vertically-elongated tokamaks, and the resulting generation of poloidal current flow ('in-vessel halo currents') in electrically-conducting in-vessel components gives rise to significant local and global

forces on the in-vessel and torus vessel systems of such tokamaks. In a reactor-scale experiment such as ITER, the estimated maximum magnitudes of the in-vessel current and total vertical force are respectively about 8 MA and 150 MN. Accommodation of this current flow and the resulting EM forces become important design considerations. Systematic documentation of the effects of vertical instability in present tokamaks is essential to develop an understanding of how such effects will extrapolate to an ITER-class experiment. Vertical instability and the MHD fluctuations that are apparently associated with it also seem to play a pivotal role in determining whether runaway electrons generated during the disruption current quench are well enough confined that appreciable runaway current conversion develops. This effect of vertical instability is separately addressed in Section 3.4.4.

3.4.3.1. Vertical instability: causes and consequences

Since elongated plasmas are vertically unstable, a sufficiently large and fast change in plasma parameters (I_p, β, l_i, and/or elongation, for example) can cause a loss of vertical position control, leading to an uncontrolled upward or downward displacement of the plasma column and eventually to plasma contact with structures at the top or bottom of the chamber/first wall/divertor. Such a scenario is a common outcome of a major disruption in an elongated-cross-section tokamak. Figure 3-59 shows an example of a typical elongated-plasma disruption in Alcator C-Mod [3-279]. Vertically-unstable disruptions with similar characteristics are observed in all presently-operating elongated-cross-section divertor tokamaks, including ASDEX-Upgrade, COMPASS-D, DIII-D, JET and JT-60U.

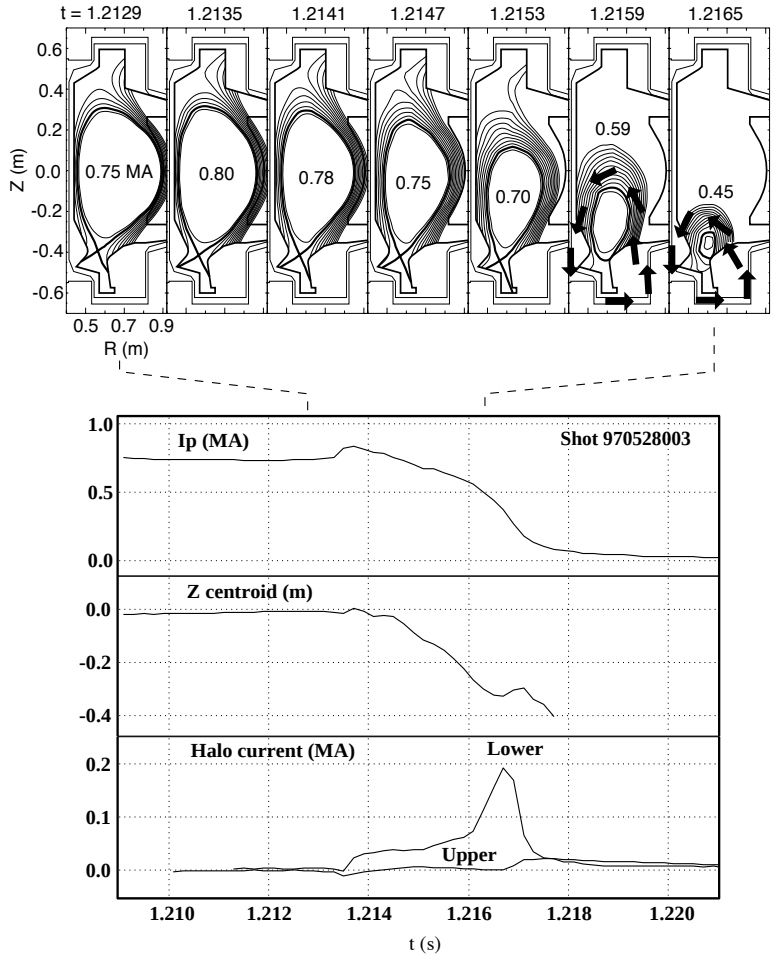

FIG. 3-59. (a) Upper figure: Magnetic flux reconstructions at 0.6-ms intervals during a disruption and subsequent vertical displacement in Alcator C-Mod. The arrows show the poloidal projection of halo current flow. The halo circuit in the plasma scrape-off actually follows a helical path, in order to be force-free. (b) Lower figure: Plasma current, vertical motion, and in-vessel halo currents in the upper and lower portions of the vacuum vessel wall. In this example of a downward-going displacement, halo current in the upper portion of the vessel is essentially zero.

The disruption process begins with a thermal quench, in which most of the plasma thermal energy is rapidly lost through radiation and/or conduction to the divertor strike points (Section 3.4.2). The fast changes in β, l_i, etc. which accompany the thermal quench lead to a loss of vertical position control. In the ensuing vertical displacement phase of the disruption, the plasma elongates (owing to the current profile broadening and decrease in l_i that follows the onset of the

thermal quench) and moves rapidly downwards, and eventually comes into full poloidal contact with the lower portion of the plasma-facing first-wall and divertor entrance baffle structures. Significant poloidal current flow in these structures occurs in this displacement termination phase. Peak poloidal currents in the example shown are about 200 kA, or roughly 25% of the initial before-disruption plasma current. This peak normalized current magnitude is both representative of what is typically seen in present tokamaks and what extrapolation of present halo current data predicts as the likely upper bound on halo current magnitude for an ITER-class tokamak.

The magnetic energy stored in the poloidal field of the plasma current decays on a slower time scale than that of the vertical motion, and usually the magnetic energy is not dissipated until the plasma contacts and terminates at the top or bottom of the chamber. Note in Fig. 3-59 that more than one-half of the initial plasma current still remains in the last frame, where the plasma core (region of closed flux surfaces) is localized almost within the divertor entrance and where most of the plasma current flow is now in the wall-intersecting halo-current scrape-off-layer which surrounds the core.

In addition to the preceding disruption-produced VDE scenario, it is also possible to lose vertical position control without a disruption thermal quench. Faults in the vertical position feedback control system (power supply failures, sensor failures, power supply voltage/current limitations), running plasmas with excessive elongations, or even large ELMs can result in initiation of an uncontrolled vertical displacement. The main difference between this type of VDE and a thermal-quench-initiated 'vertical disruption' is that the thermal quench and current quench occur simultaneously. This type of VDE can be termed a 'hot-plasma' VDE to distinguish it from a 'cold plasma' VDE or vertical disruption in which thermal energy loss is essentially complete before appreciable vertical motion develops. Since modeling predicts that higher plasma edge temperature will lead to higher halo current fractions (see Section 3.4.7), hot plasma VDEs are expected to have higher halo current fractions (see discussion below) and halo current EM loadings. Hot-plasma VDEs in a reactor plasma will also have plasma-wall interaction

consequences (impurity release and wall melting and vaporization) that are not present or appreciable in hot-plasma VDEs in present experiments.

The direction of vertical disruptions in present single-null tokamaks is typically but not universally downwards, towards the divertor. Upwards (away from the divertor) displacements after disruption are sometimes observed, particularly in disruptions in which full current profile broadening ($l_i \rightarrow \sim 0.5$) is not obtained. Simulations of the initial dynamics of disruptions with axisymmetric equilibrium models (see, e.g., the model described in [3.280] and also in Section 3.4.7 and the modeling described in [3.281]) show that the direction of initial motion is determined by the competition of the equilibrium-modifying effects of current profile broadening and pressure loss with the separate effect of the induced toroidal eddy currents in in-vessel and vessel structures that arise from the initial current decay. For loss-of-control VDEs, the initial direction is usually random.

Vertical control loss after disruption is not inevitable. In rare instances (typically with lower elongation plasmas and very fast current quenches), the after-disruption plasma in Alcator C-Mod remains in approximate vertical equilibrium and the plasma motion is radially inward [3.279]. In these passively-stable cases, halo currents appear mainly in the inboard wall. A similar passive 'neutral-point' behavior is obtained — with careful selection of the initial pre-disruption vertical position — for more-elongated plasmas in JT-60U, and with optimization of the vertical position control algorithm, active control of the plasma position after a thermal quench can be maintained for a wider range of plasma configurations and current decay rates [3.281]. In these vertically-stabilized disruptions, the halo currents seen in the lower portion of the vessel in vertically unstable disruptions are avoided. Plasma operation near the neutral point and with adequate vertical position control is a potential means for VDE and halo current avoidance in reactor tokamaks (see [3.281] and Section 3.4.6).

3.4.3.2. Halo currents

During a vertical disruption or a VDE, both the plasma current and cross-sectional area (which encloses toroidal flux) decay to zero. Both decays generate an electric field which can drive current flow along the helical field lines in the wall-connected scrape-off-layer (SOL) region of the plasma. This so-called 'halo' current was first explicitly observed on JET [3.282] and DIII-D [3.283]. Indirect but compelling evidence for the existence of halo currents was also obtained for vertically-unstable disruptions in PBX-M [3.284] and halo-currents are now retrospectively understood to have been responsible for what at the time were inexplicable incidents of mechanical or attachment-heating damage to in-vessel components in early tokamak experiments.

The halo current flowing helically on wall-intersecting plasma flux surfaces makes a complete circuit by flowing from the strike points at one end of the open SOL field lines, through the conducting first wall structures, and out onto the other end of the SOL field lines. The poloidal projection of the halo current flow is shown in the last frames of Fig. 3-59a. Measurements in Alcator C-Mod show that for downward-going disruptions, halo currents flow only in the bottom portion of the chamber, as shown in Fig. 3-59b, and vice versa for upward-going disruptions. In the rare instances when a disrupting plasma remains at the midplane (usually for near-circular plasmas), halo currents are observed at the vessel midplane. Figure 3-59b shows that the time of maximum halo current occurs around the time of maximum current quench rate, and that the plasma is still carrying about 60% of the initial plasma current even though it has shrunk dramatically in size. The value of q_{edge} at or near the last closed flux surface is low and is typically (within the approximations inherent in the magnetic reconstructions shown in Fig. 3-59a) equal or less than unity. Similar localization of the terminating plasma and near-unity values of the core safety factor obtained with a full Grad-Shafranov equilibrium reconstruction are found for the DIII-D VDE described in [3.283].

The poloidal halo current flowing in the wall, when crossed with the toroidal magnetic field, gives rise to additional structural forces above and beyond the well-understood toroidal or

saddle eddy current forces induced during disruptions. Experimental measurements and numerical simulations on ASDEX-U [3.285] and DIII-D [3.282] have shown that the forces associated with halo currents are a major contributor to the vertical force acting on the torus vessel during a disruption. Representative data from ASDEX-U are shown in Fig. 3-60. Estimates of the effective radial width Δr_{eff} for the in-vessel halo current flow path derived from such data show that the effective width is comparable to the initial plasma minor radius. These width estimates confirm the localization and estimated width at maximum displacement derived from magnetic reconstructions of the type shown in Fig. 3-59a.

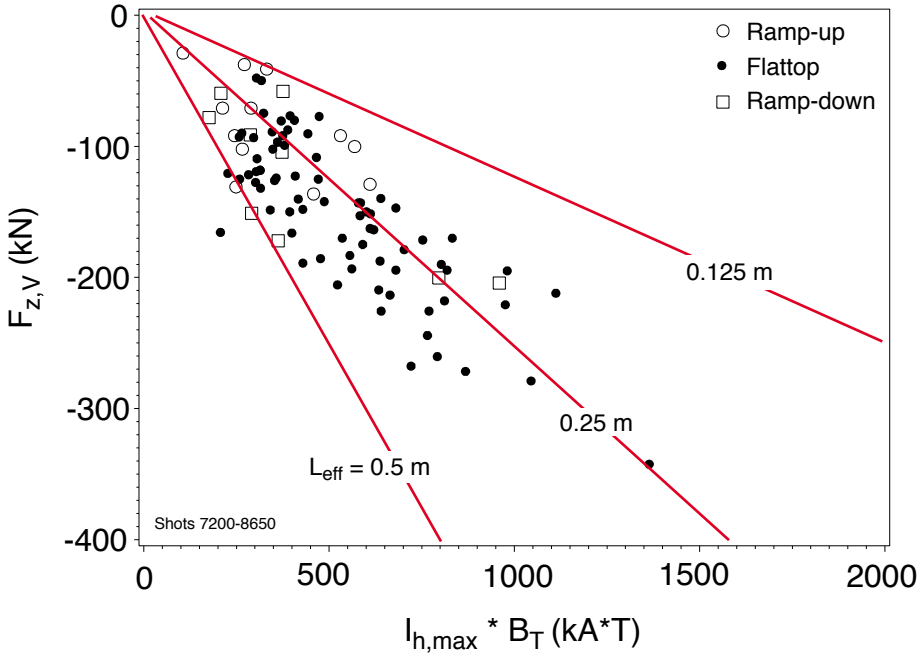

FIG. 3-60. Measured vertical disruption forces in ASDEX-U compared with the product of maximum halo current (measured) and toroidal field. The mean slope of the data implies an effective in-vessel halo current flow length of about 0.4 m (~$0.8a_o$). The toroidal conductivity of nearby in-vessel components is negligible, so in this case, halo current provides the entire vertical stabilizing force on the plasma.

3.4.3.3. Vertical forces

The global magnitude of the total vertical force produced during a vertical disruption or a VDE can be estimated on a very simple basis from the plasma destabilizing force

$$F_{Z,max} \approx 0.7\, I_0\, \Delta Z_{max}\, \partial B_{r,eq}(\Delta Z_{max})/\partial Z \qquad (3\text{-}14)$$

where I_0 is the pre-disruption or pre-VDE plasma current, $\partial B_{r,eq}/\partial Z$ is the radial equilibrium field gradient evaluated at the location ΔZ_{max} of maximum plasma column displacement (typically near the top or bottom of the in-vessel structure) and the numerical factor of ~0.7 is chosen to reflect the experimental observation that the plasma current at maximum displacement is typically about two-thirds of the initial current. Applying Eq. (3-14) for typical ITER parameters with I_{p0} = 21 MA gives a maximum vertical force of about 150 MN (15,000 tonnes). Since the plasma must be in force balance, the total vertical force developed on the in-vessel and vessel systems by toroidal and poloidal eddy currents and by in-vessel halo currents cannot exceed this value. Comparison of the force estimated by Eq. (3-14) with either mechanical measurements of the actual vertical force or estimates of the $I_{h,max}B_T\Delta r_{eff}$ force derived from in-vessel halo current measurements and knowledge of the halo current flow geometry confirms that the expected in-vessel/vessel vertical forces are obtained and are in good agreement with corresponding plasma destabilizing force.

While estimates of the maximum vertical force derived from Eq. (3-14) can provide a good basis for the design of the vessel support system in future tokamaks, in order to specify the engineering design constraints on the first wall for reactor tokamaks, the magnitude and in-vessel distribution of the halo current needs to be specified. To this end, the ITER Expert Group on Disruptions, Plasma Control and MHD has compiled a database of disruption information, including halo current measurements, from a number of present-day tokamaks (see Section 3.4.2 and [3.275, 3.278]). The magnitude of the maximum halo current is the first design consideration. As shown in Fig. 3-61, for ITER-relevant elongations in the range of 1.5–2.0, the peak halo

current ($I_{h,max}$) seen in present tokamaks can range between about 1% and 50% of the pre-disruption plasma current (I_{p0}).

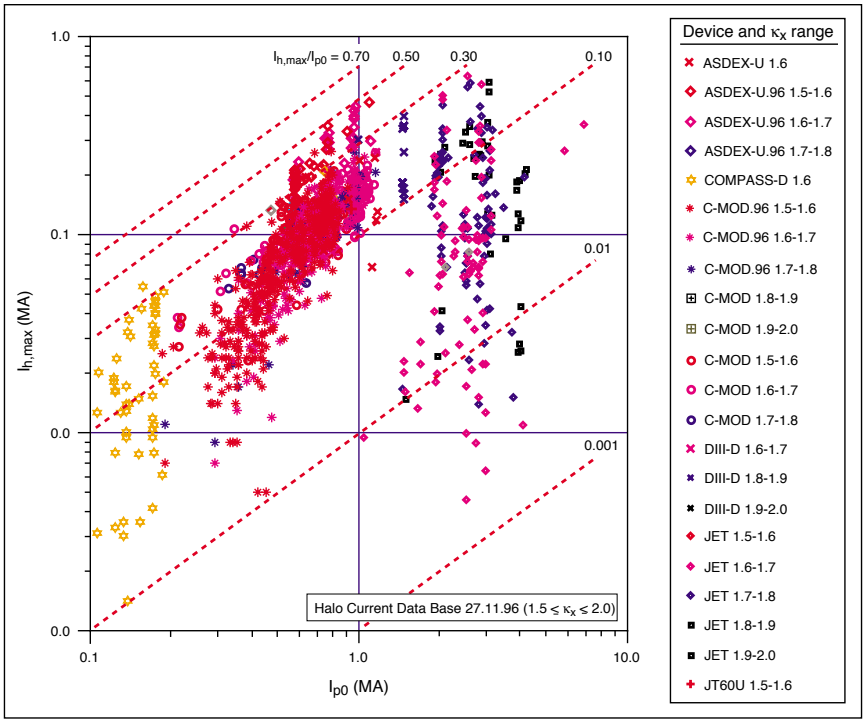

FIG. 3-61. Peak total halo current ($I_{h,max}$) versus pre-disruption plasma current (I_{p0}) for disruptions in various elongated tokamaks. The data is for plasmas with vertical elongation $1.5 \leq \kappa_X \leq 2.0$, where κ_X is the elongation at the separatrix.

The large amount of scatter in the maximum halo current data within a single experiment and within the database as a whole suggests that there are one or more underlying 'hidden variables' in the data set. However, systematic analysis [3.275] of the database in terms of the elongation and/or q_{95} sensitivity has failed to show any clear systematic multi-machine dependence on these parameters or on plasma size of current or on after-disruption 'cold-plasma' VDEs versus comparable loss-of-control 'hot-plasma' VDEs. While there are clearly discernible systematic I/q_{95} and/or I_p/B_T dependencies in the Alcator C-Mod data [3.279] these same dependencies are not as clearly evident in the remainder of the database. For the database contributions in which a significant range of elongations is present there is also no explicit elongation (κ_X) dependence for

normalized halo current magnitude except for obvious cases where the elongation is insufficient to result in vertical instability. Selecting $\kappa_x \geq 1.5$ removes these vertically-stable cases from the database.

The higher maximum halo current fraction observed in ASDEX-U (up to 50% as contrasted with 30-40% in other experiments) stands out in the overall database and is likely the result of the lack of appreciable vertical stabilizing effect from induced toroidal currents (the saddle-connected vertical stabilizing structure in ASDEX-U is ineffective for vertically-displaced plasmas). If this aspect of the ASDEX-U data is taken into account, the maximum normalized halo current fraction that can be inferred from Fig. 3-61 is about 40%, and the majority of the data lies below about 30%. The upper bound of the halo current fraction recommended for ITER design is 40% (8 MA for I_{p0} = 21 MA) [3.278].

The measurements in Fig. 3-61 have been assembled from tokamaks of many different minor radii (0.16 m to 1.25 m). At the present time, understanding of the variance in the data is not yet adequate to determine whether or not halo current fraction depends on machine size, but the JET and JT-60U data in Fig. 3-61 and more-recently-reported measurements of halo current magnitude in JET [3.286–3.288] and further magnitude data from JT-60U [3.289] increasingly suggest that larger machines have a normalized maximum halo current fraction ($I_{h,max}/I_{p0}$) that does not exceed about 25%.

If this lower bound on maximum current fraction continues to ITER, it will have modestly favorable design implications. There is some support from the modeling of ITER halo currents in dynamic axisymmetric equilibrium simulations (developed with the model described in [3.280], see Section 3.4.7 for a further presentation) that show that the normalized current fraction for credible plasma edge (halo) temperatures will not exceed about 25%. We also note that for ITER that taking 25% normalized halo current and $\Delta r_{eff} \approx 0.8 a_o$ = 2 m yields $F_{Z,halo} \approx$ 80 MN, or only about half the expected total maximum vertical force. Simulations of ITER VDEs developed by R. Sayer and S. Jardin, which the modeling parameters are adjusted to produce 25% maximum halo current, indicate that the total vertical force generated (including the force from toroidal eddy

currents, which are appreciable for ITER) will be about 120 MN. Our point here is not to introduce the use of simulations for design (this is discussed in Section 3.4.7) but rather to demonstrate that the presently-estimated 'large tokamak' halo current magnitude bound of 25% I_{p0}, the expected plasma localization and vertical position for a downward-going VDE inferred from the reconstruction data of the type presented in Fig. 3-59a and the estimated maximum vertical force inferred from Eq. (3-14) all lead to a self-consistent picture of the maximum forces and axisymmetric halo current effects that can be expected for a typical 'worst-case' downward-going VDE in ITER or comparable reactor tokamak.

3.4.3.4. Halo current distribution, toroidal asymmetries, and lateral loads

While the upper bound on the expected collective vertical force on in-vessel and vessel systems can (subject to some uncertainty about the magnitude of the plasma current at maximum displacement) be estimated from the elementary considerations embodied in Eq. (3-14), and the expected magnitude of the maximum expected halo current can be derived from empirical analysis of the halo current database, evaluation of local forces and stresses in the vessel chamber/first wall/divertor requires knowledge of the toroidal and poloidal distribution of in-vessel halo currents. Here in-vessel measurements and magnetic reconstructions in a number of tokamaks have shown that (1) the poloidal width of the halo region is relatively narrow ($0.2a_o$–$0.3a_o$) and remains approximately constant as the vertical displacement proceeds and the closed-flux-surface plasma core radius decreases, and (2) there are significant toroidal asymmetries present. These asymmetries have important design implications, since they result in toroidal peaking of the in-vessel halo current flow and $\mathbf{j} \times \mathbf{B}$ force, and as elementary analysis shows, a net radially-directed sideways or lateral loading on the in-vessel/vessel system. Lateral displacement of the JET vacuum vessel has been observed in certain JET VDEs [3.286, 3.288]. Lateral loadings are an important design issue for reactor tokamaks, since most previously-proposed solutions for support of in-vessel and vessel systems have not explicitly addressed the possibility of such loads. The mechanical problem is significant in both present and future tokamaks: the lateral loads

inferred for a 3.5-MA JET VDE are ~2 MN and a simple I_p*B_T*R scaling of this value to ITER yields lateral loads of ~50 MN.

Measurements of the toroidal symmetry of halo currents in the six tokamaks contributing to the IDDB give typical toroidal peaking factors (TPF, defined as ratio of maximum halo current density to toroidally-averaged halo current density) in the range of 1.2–2, although there are also some data with TPF greater than 3. An example of the toroidal distribution and temporal behavior of halo currents in a typical Alcator C-Mod vertical disruption [3.279] is shown in Figs. 3-62a and 3-62b. A basic n = 1 structure of the toroidal distribution is clearly seen. There is also evidence of higher-n modes and dynamic variation of the fine structure of the current distribution within the time-scale of the halo current pulse. Furthermore, in C-Mod this structure is usually seen to rotate toroidally at frequencies of order 1 kHz. This rotation rules out first-wall non-uniformities as the cause of the asymmetry.

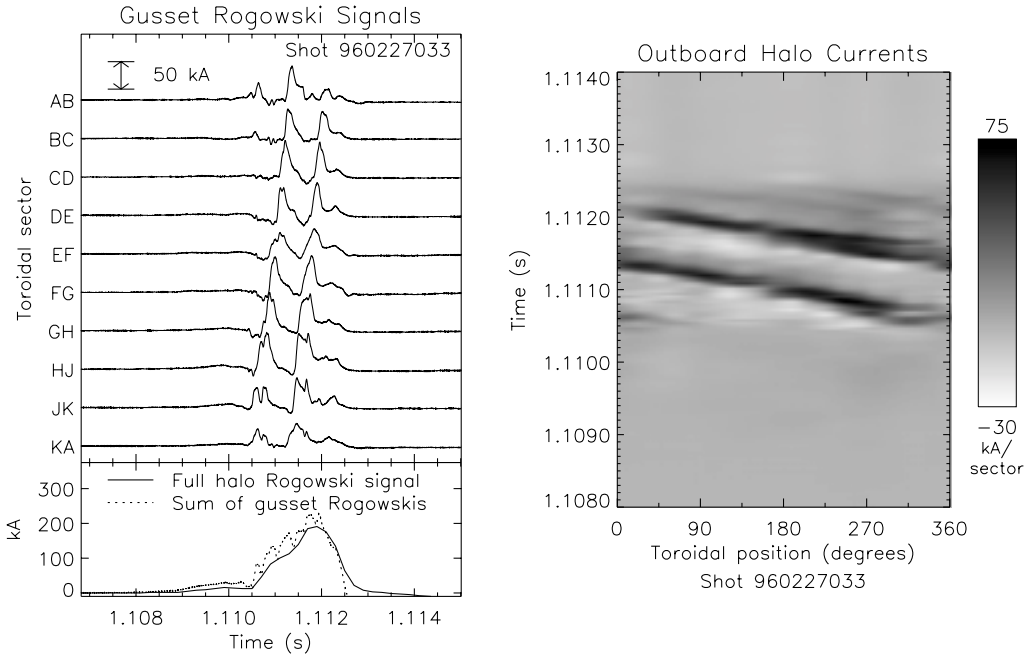

FIG 3-62. Halo current density measured at 10 toroidal locations around the Alcator C-Mod divertor: (a) A relatively peaked `filament' of halo current is seen to rotate twice around the torus. (b) The same data plotted in a different manner, showing the predominantly n = 1 structure of the toroidal asymmetry.

Detailed measurements of the spatial structure in C-Mod show that the halo current flow in the vessel structure is purely poloidal. This implies that the wall-intersecting field lines carrying the halo current must make an integer number of toroidal transits in going from the entrance strike point to the exit strike point (typically one toroidal transit in C-Mod [3.279]). This suggests that there may be a resonance condition for halo current flow which involves the field line helicity. Depending upon the geometry of contact, this also implies that q_{edge} has to be between 1 and 2. This is consistent with the previous observation derived from magnetic reconstruction concerning the low (~ 1) plasma core safety factor in the last frame of Fig. 3-59a.

Rotation of the halo current asymmetry is not observed on all machines, or even on all disruptions in a single machine. In general, non-rotating asymmetries are observed in larger machines. The observation of low (near-unity) edge-q in the final maximum-displacement phase of the current decay is, however universal, as is the presence of some degree of an n = 1 structure. For moderate asymmetries, $1 \leq TPF \leq 2$, the resulting azimuthal dependence of the toroidal distribution can be described to a reasonable approximation as $j \sim j_o(1 + \delta \sin \phi_{tor})$ where ϕ_{tor} is the toroidal coordinate.

For cases with $TPF \geq \sim 2$, the n = 1 structure is increasingly modified by higher-n harmonics that reflect localization of the in-vessel halo current in a relatively small fraction of the full torus circumference. The resulting distribution of halo current approaches a toroidally-localized peak or 'filament' with low or zero current elsewhere. Figure 3-63 shows an example of a high-TPF halo current distribution obtained in an Alcator C-Mod disruption at times near the halo current magnitude peak [3.279]. The calculated TPF for the three times varies between 2.5 and 3.8 and the halo current is localized within approximately three of the ten equally-spaced divertor support structure modules. While detailed evidence for the exact degree of toroidal localization in present tokamaks is somewhat limited by the finite toroidal number and resolution of in-vessel halo current measurements, the possibility of a relatively-high toroidal localization of in-vessel halo current in reactor tokamak VDEs is a design aspect that must be taken into consideration.

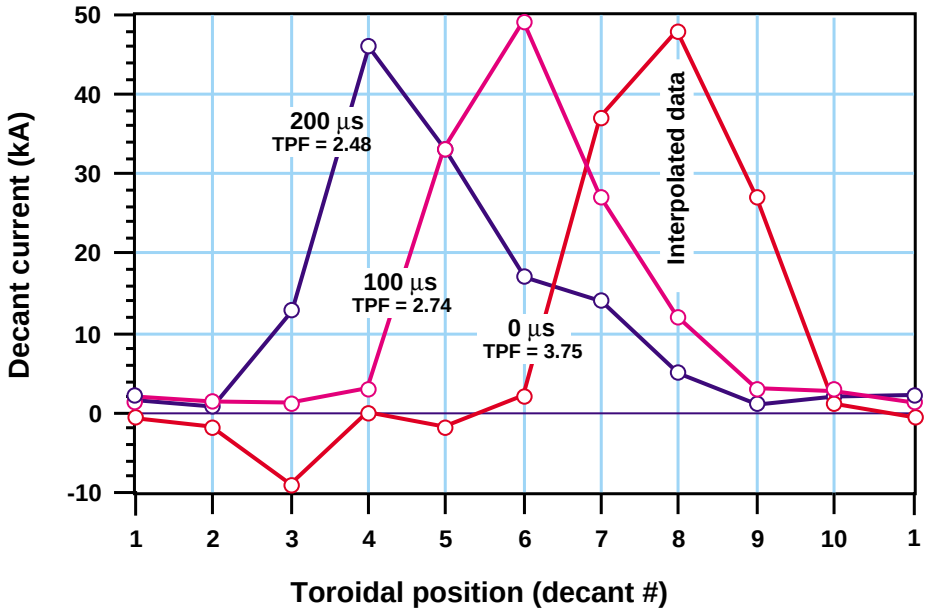

FIG. 3-63. Halo currents in the Alcator C-Mod divertor structure (ten electrically-isolated decants) at three 100-μs intervals near the time of maximum halo current. Halo current at a given time is largely localized within 4 of the 10 decants. The TPF varies between 2.5 and 3.8. The distribution rotates toroidally at a frequency of 1.4 kHz

3.4.3.5. Toroidal peaking factor

Information on the toroidal peaking of halo currents in a number of tokamaks has been assembled as part of the ITER Disruption Database (see Section 3.4.2) as shown in Fig. 3-64. It is apparent that the higher peaking factors tend to be seen only at lower normalized halo currents. A hyperbolic relationship can be used to define a bounding curve, which can then be used for engineering design guidance. The curves shown in the Figure for $(I_{h,max}/I_{p0})$*TPF = 0.75 and $(I_{h,max}/I_{p0})$*TPF = 0.50 have respectively been recommended as 'worst-case' and 'typical maximum' bounds for ITER halo current magnitude [3.285].

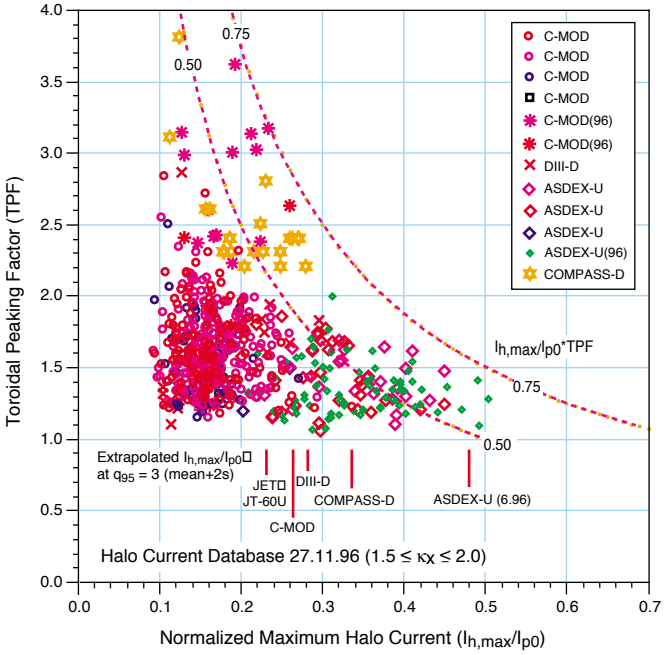

FIG. 3-64. Toroidal peaking of halo currents in various tokamaks, for plasmas with $1.5 \le \kappa_X \le 2$. High peaking factors occur only at low halo current fraction. The hyperbolic curves show limiting bounds for the data. The bounds in the various tokamaks on the normalized maximum halo current at $q_{95} = 3$ derived from the data in Fig. 3-61 are also shown.

There is some theoretical justification for this hyperbolic bound that derives from semi-empirical models that explain the n = 1 character of the in-vessel current asymmetry on the basis of the interaction of an n = 1, m = 1 helically-deformed plasma column with an axisymmetric conducting shell [3.290]. Toroidally non-uniform contact of the halo region of the deformed plasma gives rise to the n = 1 variation of the shell halo current and variation in the degree of contact during the VDE evolution gives rise to an inverse correlation of halo current magnitude and TPF that is qualitatively similar to the bounds of the data in Fig. 3-64. The addition of higher order n/m modes to the deformation could explain both the toroidal localization that occurs at higher TPF and the dynamic fine structures that are visible in the data in Fig. 3-62.

A similar explanation of the n = 1 character of the asymmetry and an estimate of the lateral vessel force measured in JET can be obtained for a plasma that is tilted and/or radially displaced with respect to the JET vessel shell [3.287, 3.288]. Measurements of the axial and radial position

of the plasma cross-section in JET at various toroidal locations during toroidally-asymmetric VDEs confirm the existence of a non-rotating tilted and/or deformed plasma in cases where appreciable sideways displacement of the vessel system is observed. The measured maximum tilt displacements (difference in plasma axis height on opposite sides of the torus) are about ±0.15 m, or ±15% of the nominal minor radius. There is also an ~0.02 m off-center shift of the plasma torus axis relative to the vessel torus axis. There are also indications that higher-n or higher-m plasma deformations are present. Finally, analysis of the electromechanical loading expected for this type of tilted plasma and the measured mechanical response of the torus and torus support system are found to be in reasonably good agreement.

The development of an n = 1 m = 1 'external' kink instability at the q = 1 termination phase of a vertical disruption or VDE is an obvious candidate for explanation of the toroidal asymmetries seen in present experiments, and modeling of such a deformed plasma with a three-dimensional MHD equilibrium code would provide a quantitative basis for both interpretation of present plasma displacement and halo current data and for the prediction of halo current asymmetries and vessel forces in future tokamaks. However, clear measurements of a helically-deformed or tilted plasma in experiments other than JET remain to be obtained, and modeling of a helically-deformed plasma with halo currents in self-consistent equilibrium with an axisymmetric conducting shell remains as a future challenge to the MHD equilibrium and stability modeling community.

3.4.3.4. Extrapolation to ITER and open issues

The halo current and VDE design basis recommended for ITER are maximum vertical and lateral forces of 150 MN and 50 MN respectively, $I_{h,max}/I_{p0} \leq 0.4$ (≤ 0.25 typical), $1.2 \leq TPF \leq 4$ and $(I_{h,max}/I_{p0})(TPF) \leq 0.75$ (≤ 0.50 typical) [3.278]. These guidelines have intentionally been set to define worst-case limits and there is a possibility that they can be relaxed in the future if the present hints of an advantageous scaling of halo current magnitude and/or asymmetry with machine size turn out to be well supported. We note parenthetically here that while these halo current

design requirements appear formidable, assessments of the ability of the ITER design to accommodate the resulting worst-case structural loadings show that these requirements can in fact be satisfied with adequate engineering margins. However, there is obvious future benefit in being able to refine and relax these requirements and to improve understanding of the degree to which disruptions and VDEs in ITER will lead to a distribution of loading conditions rather than worst-case limits. Better specification of such 'statistical' aspects of disruption and VDE loading may become relevant to future regulatory assessments of reactor tokamak functional and structural integrity in normal and 'off-normal' operation conditions.

The question of the possible tokamak size scaling of the maximum halo current fraction is one of the principal remaining uncertainties. In addition, the reasons for why there is such a wide range of maximum halo current and asymmetry for a given equilibrium are not well understood, nor is the possible dependence of such parameters on vessel/divertor structural geometry in the contact region and other machine-specific parameters. Recommendations for resolving these issues are to expand upon the integrated modeling, both axisymmetric and non-axisymmetric, that has been carried out so far (see Section 3.4.7), and to continue with experimental measurements of halo currents, particularly in the larger tokamaks. In this latter regard it will be important to have as extensive an array of in-vessel halo current diagnostics as possible (full poloidal and toroidal coverage of first-wall currents in existing experiments is limited to at least some degree and in-vessel component halo current flow paths are not always fully instrumented) and to attempt to make more definitive correlations among non-axisymmetric plasma displacement measurements, halo current asymmetries and in-situ measurements of forces and/or stresses in in-vessel components. This recommendation extends to ITER itself: a comprehensive set of plasma configuration, in-vessel halo current and in-vessel and vessel structural response diagnostics is recommended (see Chapter 7).

3.4.4. Runaway Electron Formation, Loss, and Wall Interaction

The generation of significant levels of superthermal multi-MeV runaway electrons following onset of plasma disruption is a well-known effect in tokamaks, and persistent after-disruption runaway currents with magnitudes up to about half of the pre-disruption plasma current are seen in certain circumstances, usually at low plasma densities, in many present experiments, including TFTR [3.291], Tore-Supra [3.292], JET [3.293] and JT-60U [3.294]. The subsequent loss of these initially-well-confined runaway currents to plasma-facing-surfaces (typically the limiter) leads to intense hard X-ray generation, photo-neutron activation of the impacted surfaces and, in some cases, localized surface damage, erosion or component failure. Figure 3-65 shows representative data for runaway conversion following a low-density disruption in JET. Approximately half of the initial plasma current converts to runaway current. High-current reactor tokamaks such as ITER are theoretically expected to be susceptible to similar runaway current conversion even at high density following disruption [3.295, 3.296], onset of the current-collapse phase of a loss-of-control VDE (see Section 3.4.3), or use of pellet-injection fast plasma power and current shutdown (see Section 3.4.5 and [3.297]).

Wholesale runaway conversion is a potentially-important design issue for reactor tokamaks, since present understanding of runaway loss and wall interaction shows that the plasma-facing-surface energy deposition levels that arise when the runaways ultimately reach the first wall can be very high (see below), and hence questions of the long-term endurance and integrity of the at-risk surfaces arise. For this reason, it is important to understand both the physics basis of runaway formation, loss and wall-interaction in both present and reactor-scale tokamaks and to quantify the possibilities for runaway conversion avoidance and/or deposition effect amelioration in reactor tokamaks. Furthermore, since the dominant mechanism by which runaways are generated in reactor tokamaks is not significant in present experiments, physics understanding of the underlying loss and wall-interaction mechanisms — particularly the effects of MHD fluctuations —

is critical to being able to project runaway formation and loss, interaction and damage effects to the reactor/ITER regime.

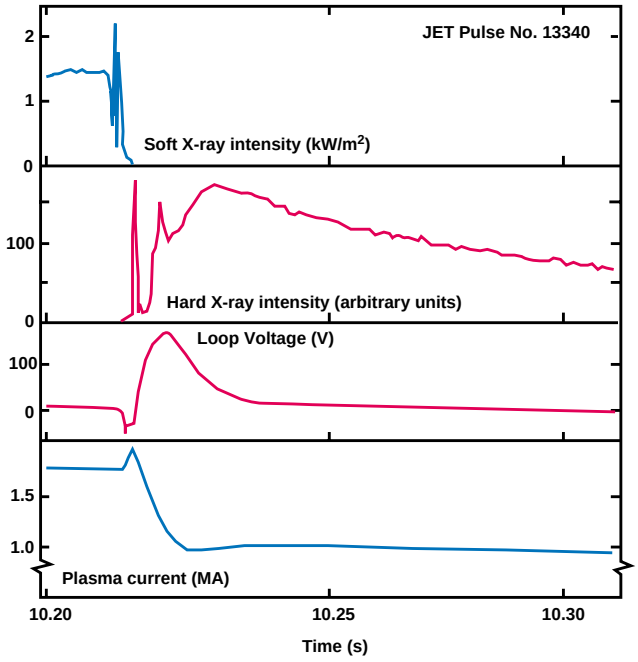

FIG. 3-65. Plasma disruption leading to runaway conversion in JET [3.293]). Loss of plasma thermal energy (fall in soft X-ray emission), onset of runaway conversion (current plateau at 1 MA) and subsequent onset of quasi-continuous runaway losses (indicated by sustained hard X-ray emission) are shown. Equilibrium control is maintained following conversion and the 1-MA runaway discharge persists for several seconds. Note suppression of the current waveform zero.

3.4.4.1. Knock-on avalanche production of runaways

High current tokamaks such as ITER may be subject to the production of large numbers of runaway electrons during disruptions. The basic issue for runaway production in large tokamaks is that knock-on secondary electrons which can also run away lead to an exponential buildup of runaway current j_{RA} [3.295–3.297] with growth rate γ_{RA} given to good accuracy by [3.298]:

$$\frac{1}{j_{RA}}\frac{\partial j_{RA}}{\partial t} = \frac{1}{\tau_{RA}\ln\Lambda}\sqrt{\frac{\pi\gamma}{3(Z+5)}}\left(\frac{E}{E_c}-1\right)\left(1-\frac{E_c}{E}+\frac{4\pi(Z+1)^2}{3\gamma(Z+5)(E^2/E_c^2+4/\gamma^2-1)}\right)^{-1/2} \qquad (3\text{-}15)$$

Here E is the toroidal electric field, $\gamma = (1 + 1.46\sqrt{r/R} + 1.72r/R)^{-1}$ is the neoclassical conductivity factor, $\ln\Lambda$ is the Coulomb logarithm, Z is effective charge of the main plasma, $\tau_{RA} = mc/eE_c$,

$$E_c = \frac{4\pi e^3 n_e}{mc^2} \ln\Lambda \cong 0.12 \cdot n_{e,20} [V/m] \tag{3-16}$$

is the electric field necessary to balance the drag at the electron energy ~mc^2 [3.299, 3.300] and $n_{e,20}$ is electron density in units of 10^{20} m^{-3}. Growth rates projected using Eq. (3-15) for typical ITER parameters during the current decay phase — where densities are projected to be a few times 10^{20} m^{-3} and where $E >> E_c$ — are in the range $100 \le \gamma_{RA}(s^{-1}) \le 1000$.

Equation (3-15) describes the growth rate given by a fit to Fokker-Planck theory that is valid in the region of positive growth rate. For fields smaller than the critical value given in Eq. (3-16), i.e., for $E < E_c$, there are no new runaways and existing runaways gradually slow down. This classical slowing down process is, however, relatively slow (1-10 s) in a reactor tokamak and hence cannot be depended upon (without enhancement) to provide benign (without wall contact) runaway current dissipation.

Equation (3-16) implies that if runaways are to be unconditionally avoided during the current quench phase of a disruption, the electron density must be quite high,

$$n_{e,20} > \frac{10}{2\pi R} \frac{\Psi}{\tau}$$

where Ψ is the poloidal flux available during the current quench (≈100 Wb in ITER), and τ is the current quench time. For the 100-1000 ms range of disruption-initiated current quench times expected in ITER (see Section 3.4.2) an after-disruption density $n_{e,20} \ge 20$–200 is required for unconditional runaway avoidance. It is unlikely that densities in this range will be occur naturally during disruptions. If densities of this magnitude are obtainable at all, the most likely means for attaining them appears to be injection of massive amounts (~0.1 kg) of deuterium in the form of

multiple solid pellets or as a liquid jet [3.297]. These aspects of the unconditional runaway-avoidance issue for ITER are further discussed below and also in Section 3.4.5.

At present, evidence for the importance of the knock-on avalanche process in reactor tokamaks is based largely upon the avalanche theory embodied in Eq. (3-15) and the underlying premise that the runaways are well-confined during the avalanching process. With regard to verifying the predictions of Eq. (3-15) by means of data obtained in present tokamaks, it is not easy to compare present experimental results on runaway production with the theory, since the corresponding avalanche growth rates are small ($\sim$1 s^{-1}), there may be competing MHD fluctuation or other loss mechanisms present (see discussion below), and the Dreicer source of runaways — the dominant source in present tokamaks — depends exponentially on parameters such as plasma temperature and electric field. Thus meaningful comparisons require at a minimum careful measurements with high-time-resolution temperature and density profile diagnostics during disruptions and also ideally direct measurement of the evolution of the actual runaway content of the plasma.

Such in-plasma runaway measurements are only now becoming possible, and present data on the details of runaway formation are still sparse. Nonetheless qualitative and quantitative trends are in agreement with prediction, with modest avalanching being seen in the current flattop phase of low-density TEXTOR discharges (Fig. 3-66) [3.301] and also following disruption in TEXTOR [3.302]. More recently the anticipated effect of Z_{eff} on avalanche growth rate [3.303] has been explicitly confirmed during current flattop in TEXTOR. We note here parenthetically that synchrotron radiation emission measurements (made at infra-red wavelengths) of the in-plasma runaway content of TEXTOR discharges have been instrumental in being able to assess runaway production in a quantitative manner. Infra-red indications of in-plasma runaways have also been seen in JT-60U [3.304]. The need to have this type of diagnostic to monitor runaway content in future reactor tokamaks and ITER is very clear.

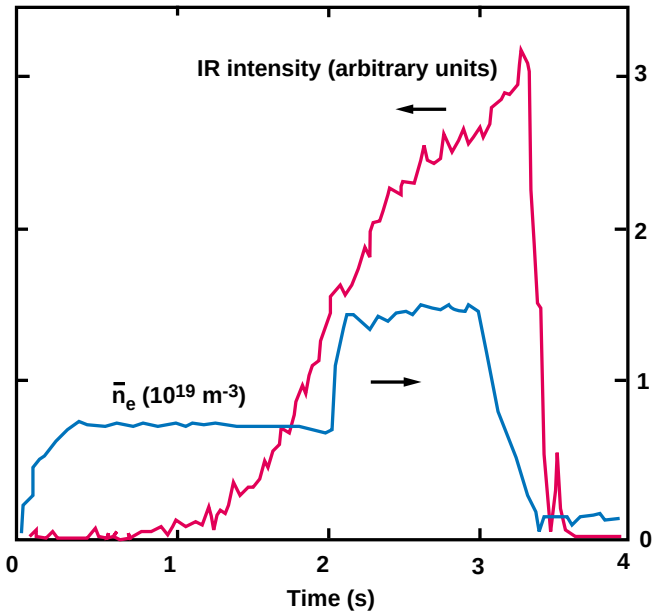

FIG. 3-66. Avalanche production of runaways during the flattop phase of a low-density TEXTOR discharge (from [3.301]): synchrotron emission intensity (infra-red wavelengths, λ = 3-8 μm) and plasma line-average density. The initial quasi-exponential growth of runaway content (indicated by the IR intensity) and subsequent reduction in growth rate following a plasma density increase are evident. The synchrotron radiation spectrum shows that the maximum runaway energy is about 20 MeV

If the no-runaway condition is violated and $E >> E_c$, it can be seen from Eq. (3-15) that the number of e-foldings of runaway current, N, is proportional to the available magnetic flux and hence the initial plasma current. The number of e-foldings is roughly $N \approx 2.5\ I_p$(MA): this result shows both the limited role that avalanching has in present tokamaks (and hence the need for careful experiments to observe the avalanche effect) and the critical point that it is larger future tokamaks which are primarily at risk, as was first pointed out in [3.296]. For ITER, the exponentiation predicted by Eq. (3-15) is sufficiently high that even such minute seed sources for initial runaways such as Compton electrons produced by X-ray emission from walls or electrons from tritium decay can multiply to convert the initial 21 MA of thermal current to ~15 MA of runaway current (Fig. 3-67). At the same time the fast growth of runaway limits their average energy. The energy spectrum of the runaway electrons produced by avalanche is close to

exponential, $f(E) \propto \exp(-E/E_0)$ with a relatively-low average electron energy of E ≈ 10–15 MeV. This low energy has been confirmed in TEXTOR [3.301].

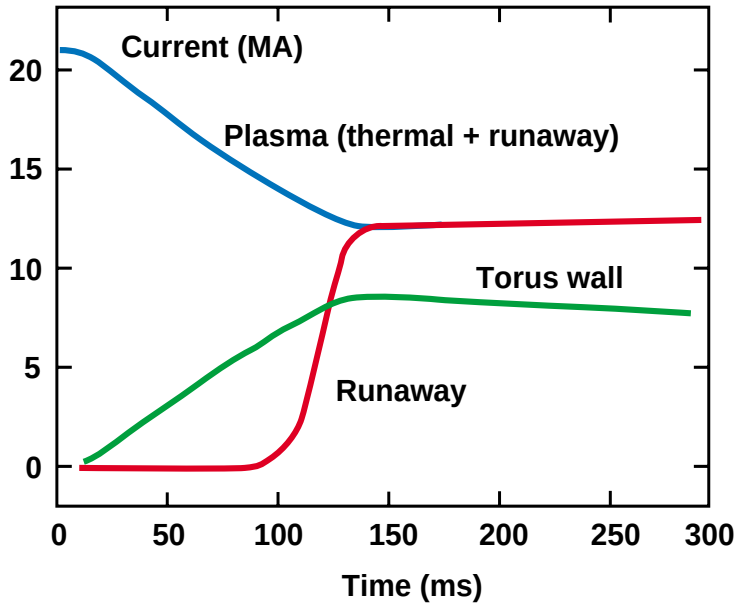

FIG. 3-67. Runaway conversion in a simulated ITER "disruption" (actually a fast plasma shutdown obtained with 1% Xe injection, [3.297]). The initial rate of thermal current decay corresponds to ~300 ms decay time. Onset of appreciable avalanche growth at 100 ms (I ~12 MA) results in the prompt conversion of the remaining plasma current to runaway current. The final magnitude of current conversion is only weakly sensitive to assumptions about the initial seed runaway number, initial current quench rate and so forth

3.4.4.2. Magnetic fluctuation losses

Equation (3-15) has been well verified by Fokker-Planck and Monte-Carlo simulations and is supported by the TEXTOR experimental data, and on this basis we can claim that the theory of runaway formation is fairly secure as long as good flux surfaces are present. However, the extent to which good (or sufficiently-good) flux surfaces are present during disruption is an open question and an issue that assumes critical importance for predicting runaway production in reactor tokamaks. Here the experience in present experiments with regard to flux surface integrity and the effects of MHD fluctuations during disruption varies depending on both the disruption phase and

the details of the current quench. It is clear that plasma core flux surfaces are globally destroyed during the thermal quench phase, but apparently re-heal to some degree following the ensuing onset of current profile broadening and the start of current quench (see Section 3.4.1). A positive plasma current spike is normally observed at the start of the current quench, and high-frequency magnetic perturbations that indicate the presence of global chaotic internal MHD activity (with corresponding degradation of flux surfaces) have maximum amplitude at this time.

Depending on the current quench details, these fluctuations can persist or decay away, and the level of fluctuations is found to affect runaway generation in present experiments. In JT-60U, immediate rise of runaway electron content is observed at the start of current quench only for low magnetic fluctuations [3.294]. For runaways generated at the later phase of the current quench, the threshold amplitude of magnetic fluctuations (normalized by the toroidal magnetic field) for runaway generation increases with increasing current quench rate [3.304, 3.305] (Fig. 3-68), and a runaway current tail is not observed for low toroidal magnetic field (e.g., $B \leq 2.2$ T). A similar toroidal field effect is seen in Tore Supra: photoneutrons (evidence of high-energy runaway losses) are only rarely detected below 2 T [3.292]. In order to understand this behavior, more detailed measurements and understanding of the causes and magnitude of magnetic fluctuations during the current quench under ITER conditions (especially with VDEs, see Sections 3.4.3 and 3.4.5) are needed to provide input to runaway modeling.

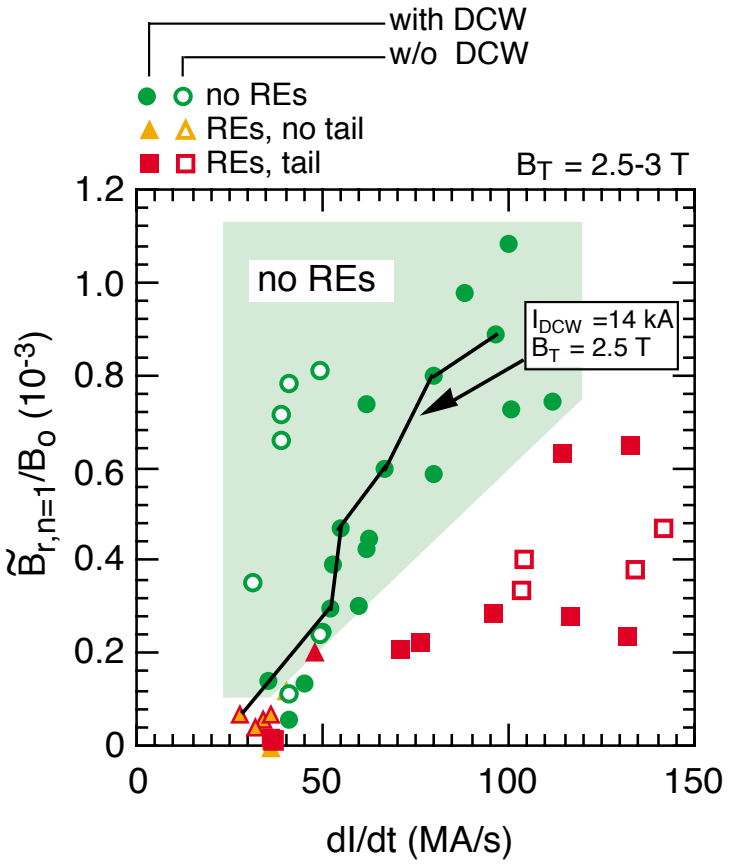

FIG. 3-68. Runaway generation in JT-60U versus normalized fluctuation amplitude $\widetilde{B}_{r\ n=1}/B_t$ and current quench rate (from [3.304]). In the shaded region no runaways are observed either with or without excitation of the DCW (external helical field) coil. Use of the DCW expands the runaway-free domain (see mitigation discussion in text below)

In present experiments, fast plasma shutdown ('killer') pellet injection experiments frequently produce transient runaway bursts (see Section 3.4.5) during the time of the pellet ablation. Such bursts are obtained in experimental situations where otherwise similar normal (non-injection) disruptions do not produce detectable runaways. The direct correlation of such runaway generation with pellet injection suggests that local effects associated with the pellet ablation may play a role. Recent DIIID experiments [3.306] suggest that mixing of the high energy thermal electron tails from the hot region in front of the pellet with the cold (and high electric field) region behind the pellet could provide a strong seed source of runaways. Disruptions provide a similar mixing, but also bring with them an accompanying MHD fluctuation loss mechanism that can

mitigate subsequent runaway acceleration. Hence these experimental results suggest that runaway electrons are generated for adequate flux surfaces during the current quench, and the ergodization of the flux has the possibility to avoid and/or mitigate the runaway electron generation.

Present understanding of the effect of fluctuations is largely empirical and how to extrapolate the data to the reactor knock-on avalanche regime is open to question. Here there is urgent need for a full 3-D MHD code which can calculate non-axisymmetric field structures and the consequent effect on runaway buildup. As yet such a code does not exist. However a new code [3.307] has been developed which can calculate runaway orbits for a given perturbed field. This code is capable of calculating the 3-D collisionless electron motion in a plasma with stochastic magnetic fields generated by perturbations (islands) with different poloidal and toroidal mode numbers. Preliminary results show that 3-D chaotic magnetic perturbations cause collisionless loss even for low-energy electrons (~100 eV) owing to the violation of the momentum conservation in the toroidal direction. These results suggest that magnetic perturbations can provide an effective mechanism to avoid runaway electron generation just after the energy quench at the major disruption and the sudden drop of the electron temperature at the killer pellet injection [3.294] (see Section 3.4.5). However, it will be necessary to confirm this premise by a self-consistent 3-D MHD calculation of the expected perturbed fields. Optimally, fluctuations will occur early enough and with sufficient magnitude to prevent runaway buildup. However the MHD and tearing stability of a runaway discharge needs to be studied further. A somewhat different rational surface inner-layer structure is to be expected.

3.4.4.3. Other runaway loss mechanisms

Once runaway electrons are generated, their loss will not be enhanced by small-scale magnetic perturbations owing to the phase averaging effect [3.308]. There are, however, additional mechanisms that can produce loss or slowing down of otherwise well-confined runaways. These mechanisms are in addition to the 'classical' frictional drag slowing down of

runaways for $E < E_c$. We will return to this classical loss process shortly. Mechanisms which can potentially contribute to additional runaway loss include:

Synchrotron Radiation. Once the runaways are established they lose energy by synchrotron radiation owing to their motion around the torus in an orbit with a radius R. This is a very slow process, with a long energy loss time. It becomes a significant loss mechanism only for runaway energies of several hundred MeV and hence will not be important in the knock-on avalanche regime.

Toroidal Field Ripple. Runways can be scattered by the toroidal field ripple [3.309] and this scattering leads to a small fraction of the runaways being continuously lost to the vessel wall. A resonance between the electron gyrofrequency and the fundamental ripple frequency can also lead to larger synchrotron radiation losses and thus create an upper bound on runaway energy. Calculations of this process show that runaway interaction with the higher harmonics of the ripple field can lead to a further limitation on runaway energy. However the magnitude this effect is very sensitive to the ripple amplitude, which for higher ripple harmonics decays exponentially with distance from the toroidal field coils. An energy limit of 270 MeV was predicted for scattering from the second-harmonic ripple in the ITER CDA design [3.310]. A similarly-high limiting energy is expected for the present ITER design. Here again however, the energy-limiting effect of the knock-on avalanche should make this loss mechanism unimportant.

Synchrotron Radiation Owing to Scattering on Ions. When runaway electrons are scattered, they rapidly lose their energy by synchrotron radiation. This mechanism has been considered in JET as a possible mechanism to explain the observed 2-s runaway current decay [3.293]. The characteristic loss time may be expressed for electrons moving at an angle α to a parallel magnetic field as $\tau_{ES} = 3\times10^8/\gamma^* B^4\beta^2\sin^2\alpha$ [in seconds]. Here B is the field in kG, β is v/c, and γ^* is the relativistic factor $[(1-(v/c)^2]^{-1/2}$. Estimate of this effect for JET (γ^* ~70, 2.7 T) showed that only modest scattering (~0.05 radian) would be required to explain the observed loss time. However, we note that estimates developed herein (below) suggest that a ~2-s decay may be consistent with purely 'classical' slowing down, so that the evidence for the presence of ion-

scattering synchrotron losses in these JET experiments can be debated. Estimates for ion-scattering losses in ITER ($\gamma^* \sim 20$, 6 T) for the same scattering angle was estimated for JET yield loss times of about 0.1 s. The corresponding is losses are not significant relative to the projected avalanche growth rates, but the ion-scattering synchrotron loss process could be important in ITER in the after-conversion phase.

Instabilities. Beam-plasma instabilities are not expected in the cold post-thermal-quench plasma due to collisional stabilization of the relevant hybrid mode [3.311]. However, recent computational and theoretical studies [3.312, 3.313] have shown that owing to the neoclassical modification of the growth rate shown in Eq. (3-15), a natural peaking of the runaway current occurs. This concentration generates perhaps 1-2 MA in a 20-cm radius and might produce runaway current channel sawtoothing (or a radial filamentation owing to the beam-plasma mode) whose effect on the field structure needs to be considered.

When a large toroidal electric field is present, the loss mechanisms noted above can have some effect during the acceleration of runaways. However, once all of the current tail is driven by runaway electrons and an externally-applied electric field is absent, the in-plasma toroidal electric field decreases to a magnitude that is $\approx E_c$, as may be seen from consideration of the electron momentum balance equation. In the absence of additional loss mechanisms, using Eq. 3-16 to relate E_c to the plasma density yields a runaway current plateau phase loop voltage for a pure hydrogen plasma that is given by

$$V_{RA} \approx 0.75\, R(\mathrm{m})\, n_{e,20} \tag{3-17}$$

and a characteristic runaway current decay time of

$$\tau_{RA} \approx 0.9\, I_{RA}(\mathrm{MA})/n_{e,20} \tag{3-18}$$

In Eq. (3-18), we have taken the effective inductance of the runaway plasma to be 1/2 the free-space inductance ($\approx \mu_o R$) that would apply in the absence of the PF coil system. This approximation introduces an uncertainty of about a factor of 2 in Eq. (3-18).

For the 1-MA JET runaway example from illustrated in Fig. 3-65, where the after-conversion plasma electron density is estimated to be 2×10^{19} m^{-3} [3.293], Eqs. (3-17) and (3-18) respectively predict a runaway plateau loop voltage of about 0.5 V and a decay time of about 4 s. The plateau-phase loop voltage data reported in [3.293] is not precise enough to make a comparison between predicted and measured voltage, but the reported 2-s runaway current decay time is within a factor of two of the pure-plasma prediction from Eq. (3-18). If we take the additional drag effect of the bound electrons in the impure but weakly ionized low-temperature plasma that is likely present in the after-conversion phase into account, the predicted and measured runaway decay times can be brought into agreement. It thus appears to us that the data in [3.293] is consistent with more-or-less 'classical' frictional drag decay of the runaway current. This conclusion about frictional drag being the dominant slowing mechanism in well-confined runaway discharges is reinforced by recent observations in JT-60U experiments that the steady-state measured loop voltage for the constant-current plateau phase of an after-Ne-pellet-injection runaway discharge (#E27507) is approximately 3 V [3.314]. While this voltage seems initially to be too high to agree with the prediction of Eq. (3-17), when the effect of the appreciable numbers of bound electrons that are present in this Ne-dominated plasma is taken into account, the measured and predicted loop voltages in the plateau phase are again found to be in good agreement.

For ITER parameters in a 15-MA runaway discharge with an after-conversion electron density of 10^{20} m^{-3}, Eqs. (3-17) and (3-18) predict a loop voltage of ~6 V and a corresponding decay time of about 12 s. If there are appreciable impurities present, or if the after-conversion density is artificially increased by massive gas or pellet injection, runaway decay times ≤ 1 s seem conceivable. While these decay times are still somewhat longer than the ITER vertical instability growth time (see below), the possibility of using injected gas or impurities to accelerate dissipation of after-conversion runaway current appears to have enough merit to warrant future study.

3.4.4.4. Wall interaction

If runaways in ITER are well-enough confined such that an appreciable runaway current develops, then the resulting runaway current channel, which is predicted to be centrally localized, will have high internal inductance and low toroidal beta and will be vertically unstable. The resulting evolution will be a VDE in which the runaway current channel ultimately strikes the first wall, typically within about 0.5 s of runaway current conversion. An example of this type of evolution for an upward-going VDE is shown below: the resulting deposition of the runaway current is poloidally localized at the top of the first wall in a location that is largely pre-determined by the vacuum equilibrium field configuration. This means that runaway strikes in ITER or a similar elongated reactor tokamak will tend to be localized and repeated. The critical issue is then the nature of the interaction to be expected if 15 MA of 15 MeV electrons hits the wall. The kinetic energy of the runaway electrons in such a discharge is not very high. For example, to support the 500 MJ of stored poloidal field energy in ITER requires only 30 MJ of fast electrons. If these electrons are uniformly deposited toroidally, and if there is a vertical motion of 0.5 m during the period of loss, then the resulting surface energy loading is only about 1-2 MJ/m^2. This energy level can readily be accommodated by the first wall. However, these assumptions, while plausible are certainly arbitrary, and the premise of good toroidal uniformity — which depends on being able to achieve millimeter-tolerance first-wall-surface to toroidal-field alignment — may not be mechanically attainable in future reactor designs or ITER. This concern about toroidal localization is reinforced by observations in present experiments — e.g., in Tore-Supra [3.315] — that the runaway scrape-off length is about 1 mm and that runaway deposition has been found to be very sensitive to toroidal alignment.

Self-consistent studies of ITER runaway conversion and wall-interaction using the axisymmetric 2-D DINA equilibrium code illustrate the nature and potential magnitude of the runaway deposition problem. The dynamic equilibrium evolution model used for these studies includes a detailed model of the ITER vacuum vessel and in-vessel component support structures

plus plasma halo currents, runaway evolution, MHD equilibrium and vertical and horizontal equilibrium motion. The plasma model is axisymmetric and does not allow for stochastic loss of runaways. It is found that for a typical 21-MA disruption with an initial magnetic energy of 1 GJ, and with the further assumption that runaway currents with $q < 1$ are inhibited, the estimated first-wall runaway energy deposition is about 75 MJ and the poloidal motion of the plasma-wall contact point during runaway current loss is only about 0.1 m (Fig. 3-69). The corresponding axisymmetric deposition is about 15 MJ/m^2.

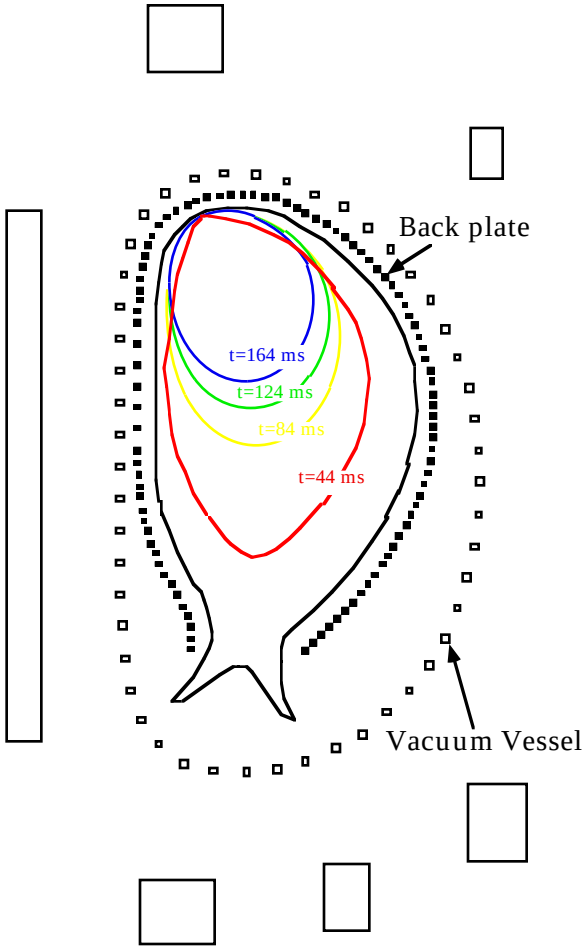

FIG. 3-69. Plasma equilibrium evolution during an ITER VDE with runaway conversion, as simulated with DINA dynamic equilibrium code. The well-known tendency for upward-going VDEs to impact on a limited portion of the upper-inboard first wall is clearly shown. In this case, the termination phase of the VDE is a 10-MA runaway current channel. Simulation data courtesy of V. Lukash and R. Khayrudinov

If, as the present Tore-Supra observations suggest, the ITER runaway radial scrape-off length is ~2 mm, toroidal peaking owing to projected ITER first-wall misalignment is estimated to increase local deposition by a factor of ~5, to ~75 MJ/m^2. These levels would be high enough to cause surface damage to the affected region and repetitive runaway strikes would likely mandate repair or replacement of the affected surface. However, there is need to validate these very preliminary simulation model results, and to incorporate the effects of natural and enhanced stochastic loss of runaways into the calculations. In addition, as noted above, massive gas injection may provide a means to restively dissipate at least part of the runaway current as the VDE phase progresses.

If the interaction time with the wall is rapid compared to the halo plasma skin time (~0.1 s for an assumed halo temperature of 5 eV), then the lost runaway current is replaced with halo current. For slower interactions, new runaways are produced as a skin current by avalanching and the total runaway energy may be an order of magnitude higher. However even a low negative surface electric field might avoid this re-generation of runaways, because the electric field for a 100% runaway discharge is very small. If, furthermore, there are secondary disruptions during the current quench phase, sufficient to destroy the flux surfaces, this could prevent or at least partially forestall runaway buildup. Thus the runaway electron generation and MHD dynamics during the plasma wall interaction (including VDE) need to be investigated further. To create a self-consistent picture, a considerable modeling effort is needed and new experiments to validate the details of the modeling will likely also be needed. Self-consistent runaway electron production and loss during a disruption and/or VDE is a critical aspect of the integrated modeling development need addressed in Section 3.4.7.

3.4.4.5. Mitigation

In view of the apparent risk of large energy deposition on a localized area of the first wall in reactor tokamaks, it will be important to develop mitigation procedures and scenarios which avoid runaway production and which are practical and reliable to implement in the ITER/reactor

environment. Possible approaches for direct (no runaway formation) or indirect (increase of prompt losses) mitigation include:

Injection of massive quantities of hydrogen. A current quench on the time scale of the wall time constant ($\tau < 0.5$ s) is desirable to mitigate plasma wall electromagnetic interactions, and this implies that electron densities for ITER greater than about 10^{22} m^{-3} — about 100-x normal — are required if runaways are to be avoided. Of course the current quench time depends also on the plasma temperature determined by a balance between Ohmic heating and radiation. It appears from 1-D numerical modeling (see Section 3.4.5 and [3.297, 3.310]) that only high-density deuterium (or hydrogen) is able to maintain a high enough temperature to allow an adequately rapid current quench with $E << E_c$. As mentioned above, an increase in density by about a factor 50 is predicted to provide for a rapid enough current quench, limiting VDEs, without production of runaways. Higher Z materials are predicted to generate low temperatures, high voltages and runaways. The technical problems and physics uncertainties about massive hydrogen injection are considerable: multiple pellets, liquid jets, and massive gas puffing are candidates which need to be studied experimentally (see [3.297, 3.311] and Section 3.4.5). There is also encouraging evidence in recent JT-60U [3.316] and DIII-D [3.317] shutdown experiments that massive gaseous He injection can effect a benign rapid plasma current shutdown in a manner that is similar to the predicted effects of massive solid or liquid H (or D) injection (see Section 3.4.5). However, there are again uncertainties as to how this type of massive He gas shutdown will extrapolate to larger-scale reactor plasmas.

Enhancement of prompt losses by pellet-injection-excited MHD. This may be an alternative to direct high-density-injection runaway suppression. Spontaneously-generated magnetic fluctuations produced by pellet injection have been demonstrated in JT-60U [3.294] and TFTR [3.318]. Here the injected pellet enhanced the magnetic fluctuations in the plasma (see Section 3.4.5). Control of the penetration of pellets to produce enhanced deposition near integer surfaces ($q = 1, 2$) can in principle generate intense magnetic fluctuations. A single large pellet can penetrate to the plasma center ($q < 1$) but could generate mechanical damage to the first wall if the

plasma is absent. Thus many small pellets at the same time (like shotgun pellets) or a train of multiple pellets may be better and needs to be assessed. In addition, the concept of pellet-induced disruptions to break up the runaway avalanche needs to be analyzed. A 3-D resistive MHD simulation model coupled to pellet ablation modeling with self-consistent inclusion of the resulting local particle transport effects will ultimately be needed for this assessment (see Section 3.4.7).

External imposition of helical fields sufficient to ergodize the flux surfaces. This technique has been demonstrated on JT-60U to prevent runaways [3.294, 3.304, 3.305] (see also DCW data shown in Fig. 3-68). However to avoid perturbing other before-disruption attributes of the plasma, the helical fields must be pulsed on in a time short compared to the plasma current decay time. Such rapid pulsing is feasible in present experiments, but a suitable design concept for a fast-acting coil system for a reactor-sized tokamak such as ITER has yet to be developed. The technical problems of incorporating the required high-voltage modular coil system within the nuclear-shield or breeding-blanket structures appear to be formidable.

External imposition of a negative voltage. This method has the possibility to shorten the runaway current decay. This effect is observed in many tokamaks. However the possible application to ITER seems unpromising owing to engineering limits on poloidal coil voltage and power: the required one-turn coil voltages exceed 1 kV. However, zero or small positive loop voltage can still shorten the runaway current decay appreciably, as demonstrated in JT-60U [3.314], and the results obtainable with a comparable method in ITER need to be explored. Here the minimum requirement for appreciable effect will be to apply a plasma loop voltage that is comparable to the 6 V 'resistive' after-conversion loop voltage predicted by Eq. (3-17). An applied voltage of ~ 20 V is in principle possible in terms of PF coil capabilities (similar voltages are developed during plasma startup, see Chapter 8), but would require a special 'on-demand' power supply system to be available after disruption occurrence.

Mechanical intervention. As a last defense, there is the option of inserting mechanical barriers (e.g. control rods or jets) or using laser blow-off from a sacrificial target to create a high-density protective plasma in front of the runaway-impacted region of the first wall. These types of

mechanical interventions may be possible because the induced toroidal eddy currents will keep the runaway discharge off the wall for approximately 0.5 s, which is conceptually long enough for mechanical devices to be inserted. A laser blow-off system could be much faster, but it is not clear whether the energetics of producing enough blow-off plasma are workable and whether the plasma can be sustained long enough to fully dissipate the runaway current.

3.4.4.6. Conclusions and recommendation for future research

The high currents and strong avalanche growth predicted in reactor-scale tokamaks makes localized energy deposition by runaway electrons a potentially-serious problem for all such devices and for ITER. The concerns apply to the generation of runaways by disruptions, loss-of-control VDEs and fast plasma current shutdown. In all of these cases, the theory of axisymmetric (good-flux-surface) evolution of runaways seems to be well-understood and the localized wall-loading consequences of axisymmetric disruptions/VDEs with runaway conversion appear to be unacceptably large. However, there are a number of possible mitigating factors that need to be assessed. Anomalous loss of runaways are observed in present experiments and need to be explained, especially in regard to the effect of MHD fluctuations in enhancing losses in the runaway formation phase. Here 3-D MHD simulations are needed to understand the effect of magnetic perturbations on the runaway electron generation in present experiments and to make predictions for ITER. Beyond taking the effects of inherent MHD fluctuations into account, a number of possible runaway prevention and mitigation schemes are identified, but they all require further theoretical and experimental development before their efficacy in a reactor situation can be ascertained. Issues that relate to runaway avoidance and/or mitigation during/by fast plasma shutdown are further addressed in Section 3.4.5.

3.4.5. Fast Plasma Power, Energy, and Current Shutdown

A means for effecting fast fusion power and thermal energy shutdown on a time scale of a few seconds is foreseen as being needed for tokamak reactors in general and for ITER in particular. The reasons for having a fast plasma power and energy shutdown capability in ITER are many and include the 'machine-protection' need to thermally protect actively-cooled divertor surfaces if a loss-of-coolant-flow or loss-of-coolant event occurs, the need to be able to radiatively dissipate the plasma thermal energy before a first-wall-contact event occurs and the possibility that safety-related licensing requirements may call for the availability of one or more fast plasma power shutdown systems. For ITER, thermal protection of the divertor surfaces requires that the fusion burn be terminated within about 3 s. Power shutdown on a similar time scale would also seen to be adequate for foreseeable licensing requirements. A somewhat faster thermal energy shutdown, in ≤1 s, is needed for unequivocal wall-contact-damage avoidance.

3.4.5.1. Requirements and means for fast shutdown

The time-scales for a normal well-controlled plasma power and current termination in ITER are respectively projected be about 100 s and 200 s [3.8]. The termination time scales for normal shutdown are set both by the physics considerations involved—energy and particle confinement times for power termination, current profile equilibration times for current termination—and by practical design considerations—particle exhaust capability (pumping capability), PF power and voltage limits, time-constants of the vacuum-vessel and in-vessel component support structures and so forth. These 'practical' matters are discussed in Chapter 8. These physics and practical considerations collectively make obtaining a fast shutdown by normal control means without disruption unlikely, so schemes for ITER shutdown have focused on the use of impurity injection to first rapidly terminate fusion reactivity (easily obtained by the immediate adiabatic cooling that injected impurities provide) and then (ideally) to subsequently radiate the plasma thermal and magnetic energies in a more-or-less uniform and benign manner to the first wall (see e.g.,

[3.319]). Reactivity termination in ITER is sufficient to achieve the divertor target thermal protection goal; radiative energy dissipation is desirable to minimize divertor target erosion and is necessary to avoid wall-contact damage. A variety of impurity injection schemes (details below) are theoretically capable of achieving these primary fast-shutdown objectives in ITER [3.297].

In addition, the parameters of the fast current termination in ITER should also ideally be such that the magnitude and toroidal asymmetries of the in-vessel halo currents produced during the VDE phase of the current decay are minimized (see Section 3.4.3), and also such that appreciable runaway electron conversion (see Section 3.4.4) is avoided. These objectives for fast current shutdown, which are secondary to the more-essential power and thermal energy shutdown objectives, pose a contradictory set of shutdown considerations and there are presently substantial physics uncertainties in being able to define fast shutdown concepts that unequivocally satisfy all primary and secondary fast shutdown objectives for reactor scale plasmas [3.278].

The options proposed for ITER fast shutdown are (1) impurity pellet injection and (2) other very-low-Z injection methods (massive deuterium pellet injection, intense D or He gas-puffing, and injection of a liquid hydrogen jet). Present understanding of the physics basis for these options and of related considerations that affect their implementation in ITER are presented below. Conclusions about the overall extrapolation of present understanding to ITER follow in Section 3.4.5.5.

3.4.5.2. Impurity pellet injection

The injection of a solid impurity pellet (commonly termed a ‘killer pellet’), typically comprised of moderate-Z or high-Z material, into a tokamak plasma is capable — provided that the pellet size and velocity are chosen such that the pellet can penetrate deeply into the plasma core — of effecting a non-disruptive fast plasma energy and current shutdown. Impurity pellet shutdown experiments demonstrating non-disruptive dissipation of the plasma thermal and/or magnetic energies have been performed in JT-60U [3.130, 3.294], ASDEX-U [3.320], DIII-D [3.321], Alcator C-MOD [3.322], JET [3.323] and TFTR [3.324]. Figure 3-70 shows an example of fast

shutdown of a neutral-beam-heated plasma in JT-60U. In this example, obtained with injection of a solid neon pellet (~3-mm diameter, ~5×10^{20} Ne atoms, injection velocity ~0.8 km/s), the adiabatic and radiative cooling that follows injection is very effective: the central plasma temperature drops in ~0.5 ms and the 1.6 MA plasma current subsequently decays in ~20 ms. Energy deposition on the divertor targets is low relative to disruption thermal quench levels and is correlated with the current quench: the intense thermal energy pulse associated with a disruption thermal quench is absent. There is also evidence from hard X-ray data that the current shutdown produces an appreciable number of runaway electrons.

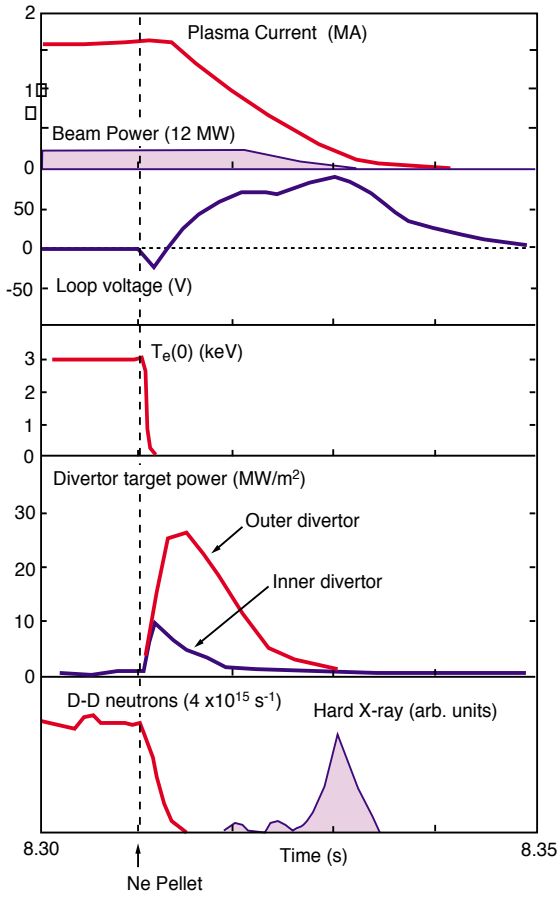

FIG. 3-70. Fast plasma shutdown in a beam-heated JT-60U plasma [3.130]. Ne pellet injection produces rapid radiation of the plasma thermal energy and a non-disruptive current quench. The hard X-ray emission indicates that runaway electrons are produced during the current quench (see Section 3.4.4).

The relatively benign discharge termination by impurity pellet injection shown in Fig. 3-70 is typical of the other experimental results cited above and differs significantly from a density-limit-disruption produced by gas-puffing. When a discharge is terminated by a deeply-penetrating impurity pellet, thermal energy deposition on the divertor is reduced or absent and the thermal energy is instead radiated more-or-less uniformly to the first wall. The usual positive plasma current and negative loop voltage spikes typically seen after disruption are also small or absent. These characteristics are observed in cases in which sufficient pellet penetration to cool the plasma center is obtained: shallow penetration that fails to reduce the central electron temperature generates instead a disruptive thermal energy quench energy and a positive plasma-current spike, exactly as observed for a normal density limit disruption or for gas-injection-initiated plasma shutdown.

Pellet Penetration and Species. The efficacy of killer pellet shutdown clearly depends on having sufficient penetration of the pellet into the plasma such that the resulting impurities are deposited more-or-less uniformly throughout the plasma cross-section. Effective shutdown also depends on selecting an impurity that radiates strongly at the moderate plasma temperatures (typically a few hundred eV) that arise following the initial adiabatic cooling that injection produces. In present experiments, these features are obtained by tailoring of the pellet species and mass (see e.g. [3.320]) and to a more limited extent, injection velocity. Plasma and pellet injection parameters for the various injection experiments are summarized in Table 3-VII. Data from a unique massive D_2 pellet injection experiment in Alcator C-Mod are also included, as are data from two ITER pellet shutdown simulations. The interpretation that can be drawn from the Table is that medium-Z or high-Z impurity pellet injection with injection velocity ~1 km/s can effect non-disruptive thermal and current shutdown in present tokamaks, albeit often with at least some runaway generation.

Table 3-VII. Plasma and Pellet-Injection Parameters for Present Fast Shutdown Experiments and for Simulations of ITER Fast Shutdown

Tokamak	n_e[(a)] (10^{20} m^{-3})	$T_e(0)$ (keV)	Pellet	Size[(b)] or Mass (mm or mg)	Atoms (10^{20})	v_{pellet} (km/s)	τ_{tq} (ms)	τ_{cq} (ms)	HXR or runaways
Alcator C-Mod	1–2	1.5	Ag+poly-ethylene	2.5 mg (Ag)	0.14 (Ag)	~1	≤0.5	2	HXR burst at injection
Alcator C-Mod	2	1.5	D	20 pellets	30 total	0.8	≤0.5	5 (same as dis-ruption)	no indication
ASDEX Upgrade			Ne	1.7 × 1.7 × 1.8	1.7	0.56	~1	6	no indication
DIII-D	~5 (?)	~ 2	Ar or Ne	1.8 Ø × ~1.8 or 2.8 Ø × ~2.8	~3 (Ne)	0.5	~0.1	3-5	HXR burst at injection; also during I_p decay
JET	3.9 (central)	3.8	Polypro-pylene	6 Ø × 3 ; 70 mg	40 (C), 7 (H)	1.2	1-2	20	HXR, etc. at VDE max
JT-60U	0.06-0.08	~2	Ne	4 Ø × 4 (x0.2–0.7)[(c)]	2–7	0.6–0.95	---		HXR at I_p termination
TFTR	0.4–0.5	4–5	D+0.01–0.1% Kr	3.8 Ø × ~3.8 (?) 2 sequential pellets, 2 ms separation		1.2	5	none, 400 or 20-30[(d)]	no evidence
ITER	1.1	18 ⟨T⟩ = 11	Kr	10 Ø	~80	3.7	~80	~80	No runaways: (Drecier source insufficient)
ITER	1.0	⟨T⟩ = 11	Xe	~7.5 Ø	~20	NA	~40	~300	~12 MA

(a) Line-average or volume-average (indicated by ⟨ ⟩) unless otherwise noted

(b) Diameter (sphere) or diameter x length (cylinder) or H x W x D; ? denotes uncertainty

(c) 20-70% of nominal pellet mass is estimated to be delivered to plasma

(d) Current quench effect varies depending on Kr content (% Kr)

Extrapolation of the penetration characteristics of impurity pellets to reactor-regime plasmas with higher temperatures and densities shows that the method is viable for ITER, albeit with a need

for higher pellet velocities and larger pellet sizes. Calculations of the ablation of solid noble-gas pellets in a burn-phase ITER plasma show that a solid krypton pellet with 10-mm diameter and 3.7 km/s velocity (as can be marginally achieved with a two-stage gas gun launcher, see [3.325]) can penetrate to about 2/3 of the ITER plasma minor radius (Fig. 3-71) [3.319]. This penetration, which is well inside the sawtooth radius, is likely sufficient for a non-disruptive shutdown, although the modeling subsequently developed in [3.297] suggests that with this type of Kr (or other high-Z species) injection, major runaway electron conversion will occur in the subsequent current quench (see discussion of runaway avoidance below). If the lack of full penetration in ITER proves to be a problem (velocities for full penetration are probably beyond gas gun limits), sequentially-injected lower-velocity pellets would allow impurities to be delivered to the plasma axis. Here the cooling produced by the first pellet allows deeper penetration by a following pellet. The use of two sequential pellets to obtain deeper penetration has been successfully demonstrated in experiments in TFTR [3.324]. Extension of the technique to multiple sequential pellets, perhaps with species/size/velocity tailored to achieve optimal distribution of impurities throughout the plasma cross-section is in principle straight-forward, but has not yet been attempted.

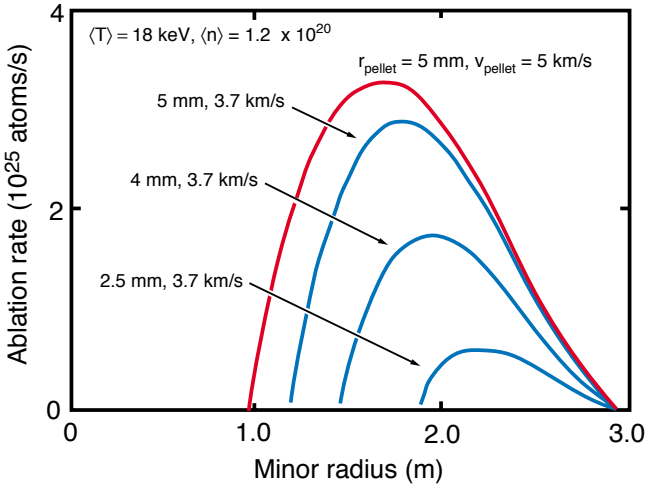

FIG. 3-71. Calculated penetration of solid krypton pellets into a high-temperature (ignited burn) ITER plasma (a = 3.0 m, reproduced from [3.319]).

3.4.5.3. Effects of impurity pellet injection

In addition to the basic adiabatic cooling, thermal energy radiation and current shutdown effects addressed above, a number of additional physics considerations are relevant to application of impurity pellet injection for fast plasma shutdown. The principal considerations discussed below are (1) distribution of the deposited impurities, (2) radiative mitigation of divertor thermal quench heat loads, (3) vertical stability of the plasma during the current shutdown, (4) reduction of halo currents and halo current asymmetries, (5) runaway electron generation, and (6) effect of fast shutdown on energetic (α) particle losses.

Distribution of impurities. Adequate distribution of injected impurities within the plasma cross-section is need for successful fast shutdown. Here comparisons of the predicted versus measured pellet penetration in present experiments show that penetration is reasonably well described by standard pellet ablation models that are suitably adjusted from the applicable pellet species (see [3.325, 3.326]). However, the resulting in-plasma distribution of ablated impurities and the electron density that arises from the ablation are not adequately described by a simple model in which the ablated and then ionized impurities stay localized on the flux surfaces near where they were born. Instead, the resulting distribution of impurities is better described by a 'back-averaging' mixing model in which the particles produced at a given point in the pellet ablation are spread more-or-less uniformly over the flux-surfaces outboard of the ablation location [3.327]. The degree of back-averaging required to match the results of TFTR fast shutdown experiments is ~100% (added impurities uniformly distributed along the pellet penetration chord). Incorporation of back-averaging in simulations of the DIII-D Ne pellet injection also seems to be needed to explain the details of radiative shutdown observed in these experiments. The net effect of back averaging is to reduce the effective penetration of the pellet relative to ablation model predictions of the type shown in Fig. 3-71. This penetration reduction effect is not particularly serious in present experiments, where deep penetration is readily achievable, but may be more serious for an ITER-class plasma.

A similar rapid outward transport of injected particles is seen in hydrogen pellet injection experiments intended for plasma fueling: net fueling efficiency is much lower than what a static pellet ablation model would predict. This is for pellets injected from the low-magnetic-field-side (LFS) of the plasma column; much higher injection efficiencies (near unity) are seen with otherwise similar injection from the high-magnetic-field-side of the plasma column [3.258]. The difference in efficiency and the origin of the back-averaging effect in present LFS impurity injection is ascribed in [3.258] to the effect of toroidal curvature in expelling the diamagnetic ablation cloud. The diamagnetic effect would aid (or at least not degrade) impurity penetration for HFS injection, but it is not clear that the curved pellet guide tube techniques used for HFS hydrogen pellet fueling can be extended to the larger/heavier impurity pellets required for ITER shutdown. If HFS impurity pellet injection is not possible for ITER, injection will have to be from the low-field side and the effects of outward diamagnetic drift of the injected impurities will have to be taken into account in choosing the pellet parameters.

Radiation of Thermal Energy and Divertor Energy Deposition Mitigation. With a suitable choice of pellet injection parameters, there is no thermal quench in the classic sense and efficient radiation of the plasma thermal energy (which is conserved in the initial adiabatic fast cooling phase) is possible. The heat load on the divertor targets has been drastically reduced by neon pellet injection in JT-60U [3.130, 3.294] (see Fig. 3-70). Neon injection into an ASDEX-U Ohmic plasma [3.321] results in a similar reduction of thermal energy deposition on the divertor and a ~10-× increase in power radiated from the plasma (300 MW peak, or ~20 MW/m^3 if the radiation power is volumetrically uniform). These radiation levels are consistent with radiative dissipation of the total thermal and magnetic energy (0.6 MJ) during the 5-ms current decay. In DIII-D experiments, analysis of the radiative cooling effect of a 1.8-mm diameter Ne pellet (2×10^{20} atoms) injected with moderate velocity (390 m/s) show that the measured radiation is consistent with the expected multi-step impurity ionization process, and also with the observation that the divertor energy deposition was reduced by about 50% rather than 100% [3.328]. In the JET pellet experiments, divertor target energy deposition (which may include some magnetic

energy) was ~20% of the 2.6-MJ thermal energy and multi-chord bolometer data showed more-or-less uniform radiation from the full plasma cross-section with peak intensity 7×10^6 W/m^3 [3.323]. The estimated total radiation is, with an assumption of toroidal symmetry, consistent with the dissipation of 2.6 MJ thermal energy in ~10 ms and with dissipation of 13 MJ of combined thermal and magnetic energy in the 35-ms current decay. The overall self-consistency of the plasma energy balance in present experiments and the premise that ~100% radiative dissipation can be obtained in a reactor plasma shutdown therefore seem to be well-founded.

Too-rapid radiation of either the ITER plasma thermal energy or the plasma magnetic energy (both ~1 GJ) can lead to first-wall surface melting and hence is undesirable. This concern is noted in [3.319]. Elementary analysis shows that for present ITER parameters and moderate radiation peaking factors (~2), the quench duration threshold for melting of a beryllium first wall surface will be ~10 ms. As simulation data for ITER shutdown shows (see Fig. 3-75 below), most candidate scenarios stay comfortably clear of this 10-ms wall-melting-onset threshold.

Vertical Instability, Halo Currents and Halo Current Mitigation. For elongated plasmas, the rapid plasma pressure (β_p) loss and current decay that pellet injection shutdown produces can initiate vertical instability of the plasma column (a vertical instability event or VDE, see Section 3.4.3), and fast shutdown in Alcator C- Mod, ASDEX-U, DIII-D, and JET typically produces vertical instability with the generation of plasma and in-vessel halo currents that in turn produce substantial vertical forces on the respective in-vessel or vessel structures. In this regard, the effects of fast shutdown is qualitatively similar to the effects of a disruption. However, comparison of the measured halo currents and the measured or inferred vertical forces for pellet-shutdown VDEs versus comparable disruption-initiated VDEs in ASDEX-Upgrade show that pellet shutdown can produce reduced halo current magnitude and vertical force [3.320] (see Section 3.4.3). Figure 3-72 shows the substantial halo current magnitude and force reduction obtained in ASDEX-U by pellet shutdown compared to disruption. A 4-× estimated peak force reduction is typical and the reduction in total vertical impulse ($\int F_Z dt$) is even greater owing to the faster overall current decay.

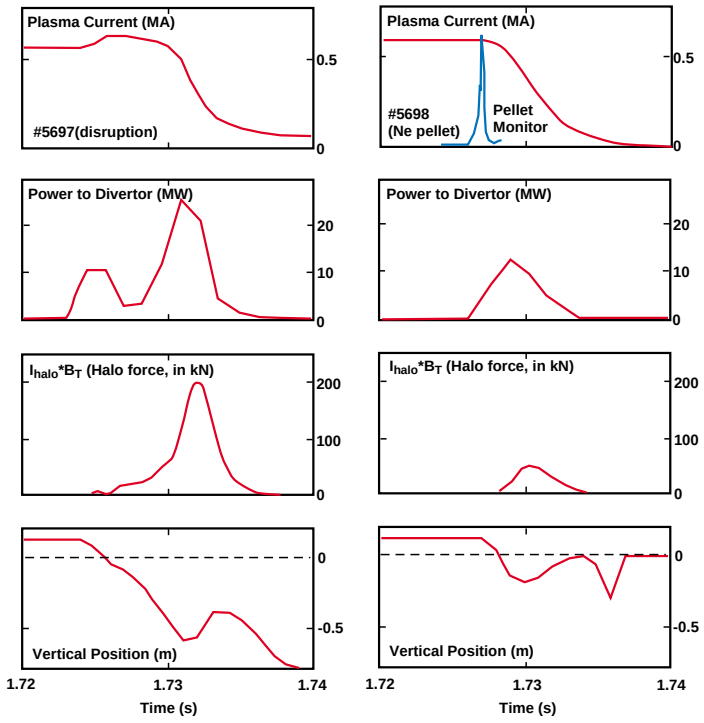

FIG. 3-72. Disruption and pellet-injection fast shutdown in ASDEX Upgrade. Fast shutdown (Ne pellet) results in reduced vessel vertical force (inferred from the measured halo current) and absence of significant thermal quench loading on the divertor. Note also the absence of a positive plasma current spike and reduction of the divertor target heating associated with the current quench.

Similar halo-current reduction benefits of pellet shutdown are seen in DIII-D experiments in which the halo current characteristics of loss-of-control VDEs (initiated by disabling the vertical position control) are compared with and without pellet injection (Fig. 3-73). Pellet-injected VDEs have substantially reduced halo current magnitude and toroidal peaking factor (peak/average current density, see Section 3.4.3) [3.321]. Halo current magnitude reductions in Alcator C-Mod pellet experiments are similar, and are typically about 50% [3.322]. The reduction in halo current magnitude in the various experiments cited is consistent with the predicted dependence of halo current fraction on halo temperature (lower temperature results in lower peak halo current, or alternately, the acceleration of the plasma current decay relative to the vertical instability growth

time). The cause for the reduced toroidal asymmetry is not as obvious, but may also be due to lower plasma and halo temperature.

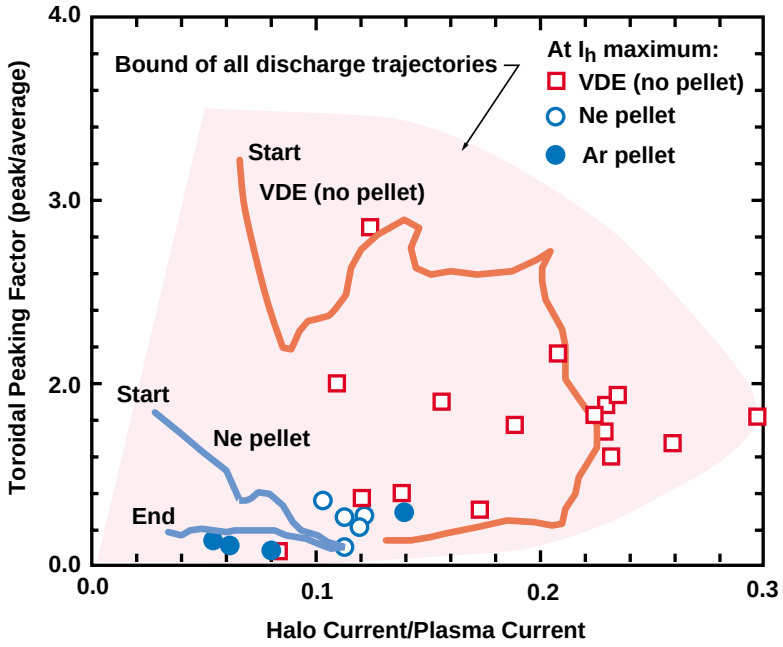

FIG. 3-73. Halo current data for DIII-D VDEs (vertical control disabled) and pellet shutdown (also with control disabled). Datum points show peak normalized halo current magnitude and TPF (see Section 3.4.3) at time of maximum halo current; typical trajectories (versus time during the current decay) of I_h/I_{p0} and TPF for VDE and Ne pellet VDE are also shown. Pellet-injected VDEs have lower halo current magnitude and toroidal asymmetry.

Avoidance of Vertical Instability and Halo Currents. The onset of vertical instability following fast shutdown in a vertically-elongated plasma can be avoided if the initial plasma position is chosen to be close to the so-called passive-stability 'neutral point', where the initial vertical displacement of the plasma magnetic axis or current centroid that occurs after disruption or fast shutdown β_p loss is small or zero [3.281]. If the ensuing current quench is rapid enough with respect to the vertical instability growth time, then the resulting plasma motion is predominantly radially inward (Fig. 3-74) and a major vertical excursion and the associated halo currents in the upper or lower in-vessel and vessel structures are absent. This type of passive neutral-point

instability avoidance is observed for fast current quenches in JT-60U [3.281] and Alcator C-Mod [3.279], and comparison of VDEs in DIII-D with faster versus slower quench rates show that faster VDEs have lower halo currents and correspondingly lower vessel forces [3.322].

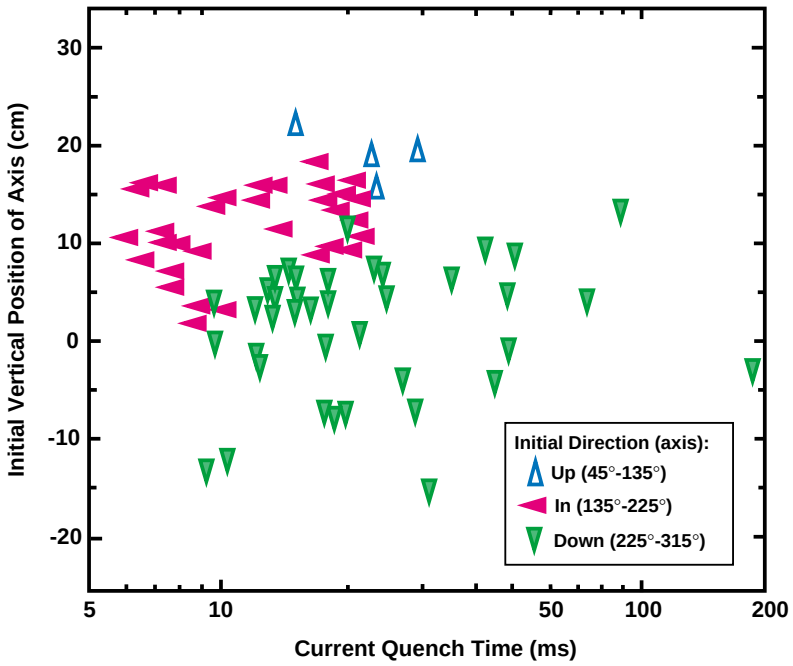

FIG. 3-74. Direction of plasma axis motion in after-disruption VDEs in JT-60U versus initial vertical position of the magnetic axis and current quench time (from [3.323]). The angles referred to in the Figure legend give the direction of the initial axis motion: 0° = radially outward, 90° = vertically upwards, etc. Plasmas with initial position ~10 cm above the midplane exhibit passive neutral stability for quench times in the 5-25 ms range. Compare with Fig. 3-75.

In JT-60U, it has been possible to extend the neutral point VDE/halo-current avoidance technique to slower current quenches with active control of the plasma position [3.329]. Such control is made possible by a plasma-axis vertical position magnetic diagnostic signal that includes compensation for the effect of the toroidal vacuum-vessel eddy currents that develop during the current quench [3.330]. The resulting actively stabilized single-null divertor plasmas can be controlled vertically down to low plasma current (≤10% I_{p0}) and halo currents in the divertor region are avoided [3.331].

The location of the JT-60U neutral point ~15 cm above the device midplane, the sensitivity of the neutral point height to current quench rate apparent in Fig. 3-74 and the key observation noted in [3.281] that the growth rate for vertical instability depends on current quench rate can be all be explained in terms of the destabilizing effect that up/down asymmetry in the toroidal eddy currents induced in the JT-60U vacuum vessel has on the vertical position instability [3.332]. Here modeling of the initial plasma equilibrium modification that changes in β_p and/or current profile produce and of the separate vertically-destabilizing effect that asymmetric induced vessel currents produce shows that the passive neutral point for JT-60U disruptions should be about 10 cm above the device midplane (Fig. 3-75). This estimate is in reasonable agreement with the passive neutral stability data shown in Fig. 3-74. However, the fact that there are two separate mechanisms responsible for the initial vertical motion makes the precise position of the neutral point dependent on both the magnitude of the profile changes that arise during the disruption or fast shutdown thermal quench and on internal inductance change and rate of current quench that follow in the current decay phase. This means that the neutral point in a single-null tokamak with an up/down asymmetric vacuum vessel and/or an asymmetric initial plasma position will be somewhat sensitive to both the disruption or fast shutdown profile parameter variations (especially to variation in l_i) and to initial dI_p/dt. Such sensitivities are in fact observed in JT-60U plasma equilibrium control transients (response to ELMs, sawteeth, etc.) [3.333] and similar neutral point sensitivities can be expected in ITER.

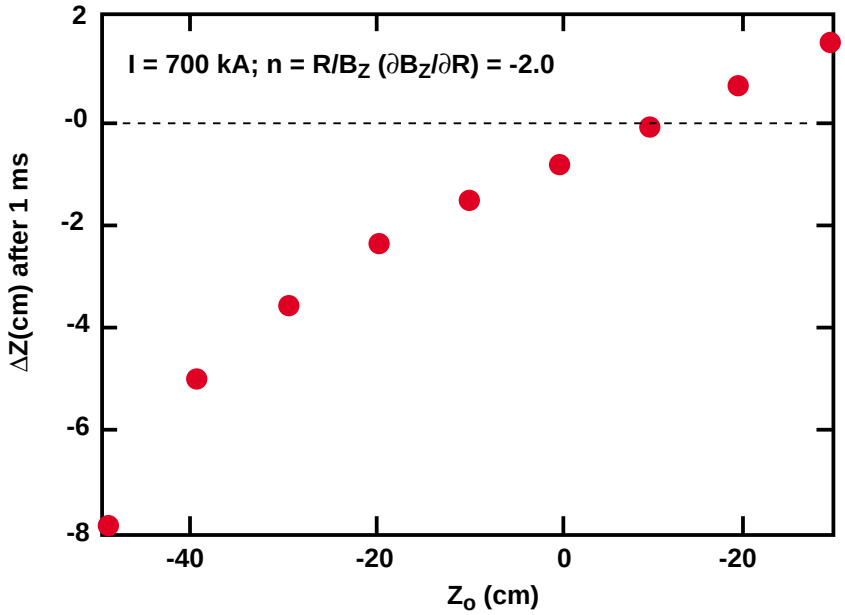

FIG. 3-75. Calculation with a TSC model of the initial displacement of the JT-60U plasma magnetic axis 1 ms after a simulated thermal quench [3.332]. The initial position Z_o of the plasma magnetic axis before the quench is varied relative to the machine midplane (Z = 0). The field index parameter n chosen for the modeling results in a plasma with an initial elongation of about 1.6. The neutral point is about 10 cm above the midplane (*cf.* data in Fig. 3-74)

Studies of the neutral point location and sensitivities for an ITER-like model tokamak show that the neutral point for JT-60U-like profile variation parameters ($\beta_p \rightarrow 0$, $\delta l_i \geq 0$) lies about 20 cm below the as-designed position of the plasma magnetic axis [3.334]. This suggests that the ITER plasma will exhibit close-to-neutral initial vertical stability characteristics for disruptions or fast shutdowns in which the change in internal inductance is small or positive. For these conditions, representative of pellet-injection shutdown, a relatively slow upward initial motion of the plasma will occur and it may be possible to maintain active control of the current decay, especially if the decay rate is not too high. However, detailed study of the poloidal field system feasibility of maintaining vertical control in ITER after fast shutdown or disruption remains to be performed.

Runaway Electron Generation. Pellet injection shutdown in present experiments has a clear tendency to produce runaway electrons. In some cases, substantial runaway conversion is

obtained. In JT-60U, when the n = 1 and n = 2 mode fluctuation levels were small at the time of impurity pellet injection, decrease of the central electron temperature is always followed by a full-current runaway discharge [3.278]. However, in cases where intense magnetic fluctuations are present, this fast generation of runaway electrons is avoided, although runaway generation is observed in the later phase of current quench when the level of magnetic fluctuations becomes low. The fluctuation amplitude threshold for avoiding runaway electron generation increases with higher current-quench rate [3.305] (see Section 3.4.5, Fig. 3-73 and related text). Avoidance of runaway generation has been demonstrated in JT-60U for low B_{tor}, $\leq$ 2.2 T [3.278] and for enhanced magnetic perturbations generated spontaneously or by an external helical magnetic field at $B_{tor} > 2.2$ T [3.304]. Further discussion of the effects of magnetic fluctuations on runaway production and how these effects may extrapolate to reactor plasmas can be found in Section 3.4.5.

Transient runaway production indicated by a HXR or non-thermal ECE burst is seen in pellet shutdown experiments in other tokamaks. Bursts correlated with pellet ablation are seen in DIII-D and can be explained by an 'electron interchange' mechanism identified in [3.328] in which localized MHD instabilities driven by the large pressure gradients produced by pellet injection lead to an interchange of hot electrons from the plasma interior with cold electrons in the high E-field region behind the pellet. Subsequent acceleration of the hot electrons produces runaways and the observed HXR burst.

Runaway generation in present shutdown experiments appears to be qualitatively consistent, with the addition of the interchange mechanism note above, with the usual Dreicer-source production mechanism. However, in future higher-current reactor plasmas such as ITER the knock-on avalanche mechanism (see Section 3.4.4) is expected to dominate runaway production and this difference in mechanism leads to preference for shutdown scenarios based upon massive deuterium injection. This aspect of the pellet-shutdown runaway avoidance issue is discussed below.

Loss of High Energy Alpha-particles. For fast shutdown in a reactor plasmas, the fast drop of plasma temperature and increase in density will reduce the slowing-down time of α-

particles to ~1 ms, so that the pre-shutdown α-particles will be thermalized very rapidly relative to the current quench. However the magnetic fluctuations that impurity injection produces and which are of benefit for mitigating runaway electron generation may enhance the loss of α-particles. Thus the optimum level of magnetic fluctuation is not clear and both the runaway and α-loss effects of injection need to be considered.

There is experimental evidence for MHD fluctuation enhancement of fast alpha loss. In TFTR α-particle loss before and during high-beta disruptions was detected with escaping fast ion detectors [3.335]. Detectable alpha losses started during the disruption precursor phase, which was dominated by the explosive growth of a ballooning mode, and a large bust of escaping α-particles occurred at the thermal quench. Approximately 20% of the stored α-particles were released during the disruption, and the remaining alphas were either thermalized or lost in places not predicted by models for the alpha losses in the steady-state (pre-disruption) phase. Alpha losses owing to other types of MHD activity included sawteeth and locked modes (see Section 3.2.2 and Section 3.2.5) were also seen. Further consideration of the TFTR results and study of comparable situations for disruptions and/or fast shutdown in future DT experiments (e.g., JET) is needed.

3.4.5.4. Other fast shutdown methods

The exponential multiplication of minute levels of initial runaway electrons following disruption or fast shutdown in high-current reactor tokamaks by the 'knock-on' avalanche process is theoretically expected to be the dominant mechanism for runaway electron current conversion in such tokamaks [3.297, 3.311, 3.319] (see also Section 3.4.4). According to the theory of the knock-on avalanche process, shutdown schemes based upon very-low-Z injection that produce high after-injection density are favored to avoid or reduce runaway electron generation. Figure 3-76 shows data from simulations for ITER of the thermal and current quench duration and runaway conversion characteristics (predicated on an assumption of no MHD fluctuation losses)

for candidate injected impurities [3.297]. The Figure demonstrates that only injection of massive quantities (~50 g) of deuterium (or hydrogen) produces a current quench that is rapid enough to appreciably mitigate halo currents while simultaneously avoiding significant runaway conversion. High-Z (Xe) or even nominal low-Z (Be) injection produces substantial runaway conversion.

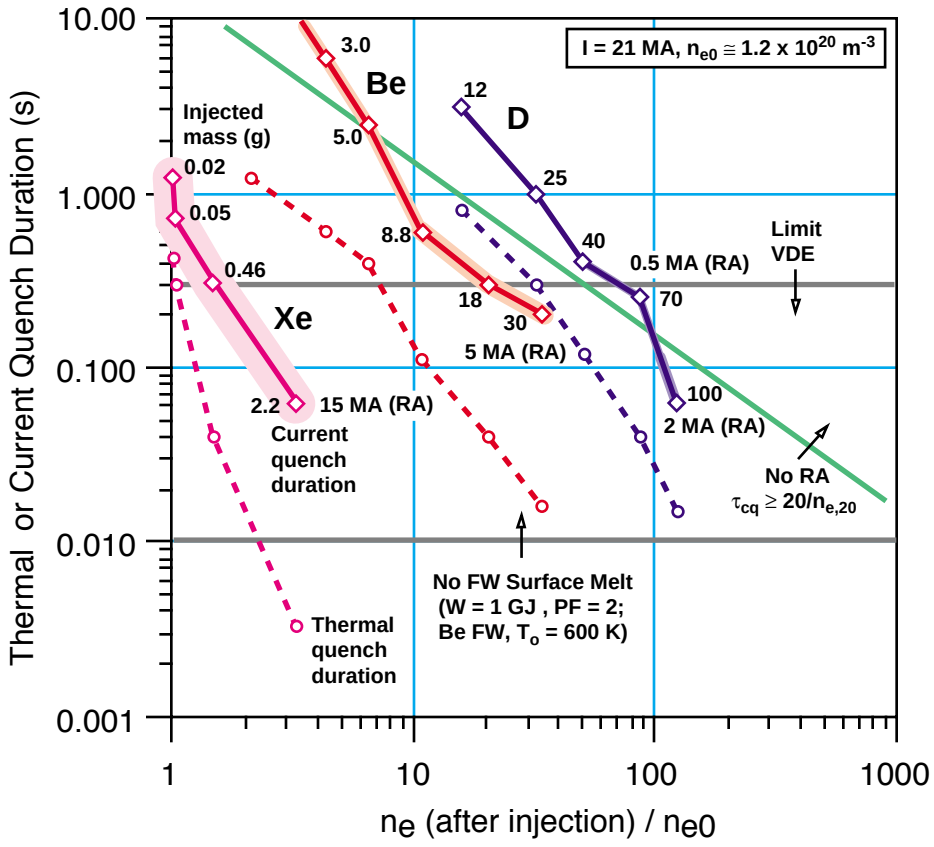

FIG. 3-76. Thermal and current quench durations for fast plasma shutdown in ITER with various quantities (masses in g) and species (xenon, beryllium and deuterium) of injected impurity. From simulation data in [3.297], presented to show the effect of after-injection density increase. The relative magnitude of the resulting runaway (RA) conversion is shown by the width of the shaded umbra that surrounds the lines joining the datum points for each species. The predicted density enhancement threshold for unconditional runaway avoidance ('No RA', see §3.4.4), the limit on maximum current quench duration set by VDE/halo-current mitigation (see §3.4.4) and the limit on minimum thermal quench time set by first-wall surface melting(see text above) are indicated.

The quantity of injected deuterium required for unconditional runaway avoidance in ITER is large (10^{25} atoms or a 0.1-m diameter pellet) relative to normal refueling pellet injection practice and the resulting after-injection plasma density of 10^{22} m^{-3} is more than a factor of ten higher than the highest densities obtained in present tokamaks and more than 100 times the Greenwald 'density limit' for ITER (see Section 3.3). There are therefore major physics questions associated with the feasibility of high-density shutdown, including how such massive quantities of deuterium can be delivered to the plasma and whether the resulting plasma densities can be sustained for long enough to effect a disruption-free shutdown. The candidate options for runaway-free shutdown appear to be limited to D_2 or He injection (H injection is undesirable owing to the subsequent contamination of D-T plasmas that in-vessel-retained H would produce), with injection effected in gaseous, solid (D_2) or liquid (D_2 or He) form. These options are examined below. As the discussion shows, physics understanding of the high-density shutdown regime is incomplete and experimental studies are extremely preliminary and so future R&D is needed.

Intense Gas Puff. The quantities of D or He needed to effect a fast plasma shutdown in ITER can be delivered to the torus by high-pressure gas injection. What the plasma response to such massive injection will be is, however, an open question, and extrapolation of present experience suggests that gas injection will produce a disruption rather than a radiative shutdown. In JT-60U, intense helium gas injection has been used to generate a fast current quench [3.316]. This injection typically produces several minor disruptions during the resulting current quench and the current quench rate is observed to increase at each minor disruption. Runaway electrons are not produced. However, with the maximum injection rates available (90 Pa m^3/s at 2 atmosphere) it was not possible to greatly enhance the average current-quench rate even for the relatively favorable conditions of low flattop plasma current and toroidal magnetic field (400 kA, 1.5 T) chosen for the experiments.

The limitation on quench rate observed in the JT-60U can be ascribed to the shrinkage of the plasma current channel that occurs just before each minor disruption. This shrinkage raises the joule heating power density, so the reduction in central electron temperature need for a more-rapid

current quench is not obtained. Furthermore, the minor disruption also expels particles in the central region and so tends to counteract the desired effect of gas injection. Similar limitations are expected for reactor/ITER shutdown, so the technique may be more suitable for shutdown scenarios (e.g., safety) where concerns about reliability of action outweigh concerns about producing a disruption.

Liquid Jet Injection. Injection of a high-velocity (~600 m/s) jet of liquid deuterium with a diameter of ~1 cm has been proposed as a means to deliver the massive density increase need to avoid runaway electron generation in an ITER-class tokamak [3.336]. The method bears a considerable similarity to injection of a closely-spaced train of solid pellets (see following discussion), and in fact calculations of the plasma penetration and ablation of a jet into an ITER plasma show that breakup of the continuous jet into a train of droplets owing an ablation pressure instability is likely [3.336]. Theoretical analyses of other hydrodynamic and thermodynamic stability considerations that apply to jet penetration into a plasma and to the preceding vacuum propagation phase where 'vacuum flashing' (jet surface boiling) is a potential issue suggest that the method can be successfully applied (subject to questions about the plasma response to the deposited deuterons) for shutdown of an ITER-class tokamak [3.336]. Testing these theoretical predictions in present experiments and with more sophisticated simulations is needed. More modest jet velocities (100-300 m/s) and diameters (~ 1 mm) are sufficient for present tokamaks.

Solid Deuterium Pellet Injection. The density increase necessary to provide a runaway-free shutdown in ITER can in principle be obtained by injection of a single ~10-cm diameter deuterium pellet with an initial velocity of 1 km/s. However the technological problems of making and accelerating a pellet of this size and the virtual certainty that a large pellet will fragment upon initial penetration into the plasma make sequential injection of multiple smaller pellets a more credible alternative, and the injection of a sequential train of relatively small (~1 cm^3) solid deuterium pellets has been proposed as a possible means for ITER deuterium pellet shutdown [3.297]. The use of two sequential pellets to facilitate deeper penetration has been demonstrated in TFTR with Kr-dropped D_2 pellets and the anticipated benefit of deeper penetration of the second pellet has been

verified [3.324]. The central plasma density increases (mainly from the deuterons) obtained in these experiments were substantial: about 5-fold on an initial basis of 5×10^{19} m^{-3}.

An exploratory experiment to study the effects of massive deuterium injection with a multiple-pellet injector has been carried out on Alcator C-Mod [3.337]. Up to 20 pellets (3×10^{21} deuterons) were injected within 1.5 ms. The injection geometry and velocity dispersion among the pellets resulted in a pellet 'barrage' rather than a well-organized sequential train. Approximately half of the pellets were seen to ablate within the plasma. The after-injection density and temperature were respectively about 1.6×10^{21} m^{-3} (~10-× the initial density) and 200 eV (consistent with adiabatic cooling of the initial 2 keV plasma). The after-injection density corresponded to approximately one-half of the injected deuterons being retained. Injection produced a disruption with a thermal quench followed by a positive current spike. However, the resulting current quench was not any faster than a naturally-occurring disruption, and halo currents were also not reduced. These current quench and halo current behaviors are consistent with earlier high-Z pellet experiments on C-Mod, which showed that T_e had to be reduced to 20 eV or less in order to accelerate the current quench and reduce halo current [3.323]. Future experiments with a better injection technique and/or the addition of higher-Z impurities to facilitate more rapid plasma cooling are indicated.

Theoretical modeling of the radiation opacity and resistive MHD stability characteristics of very high density hydrogen and other low-Z plasmas is also needed. The radiation opacity issue [3.338] for such plasmas is important for reactor applications, since it can significantly degrade the plasma radiation efficiency (absorption of line radiation within the plasma core limits radiation to the plasma surface rather than from the full volume, as is assumed in the data presented in Fig. 3-76).

3.4.5.5. Summary and extrapolation to ITER

Injection of solid medium-Z and high-Z 'killer' pellets into present tokamaks shows that such injection can provide the plasma reactivity termination and rapid radiative cooling functions that are needed for pellet-injection fast shutdown of reactor plasmas. The penetration of pellets into the target plasma and the effects of the resulting enhancement of impurity radiation are found to be consistent with expectations, and full mitigation of divertor thermal loads and substantial mitigation of halo current magnitudes and vessel vertical forces in after-injection VDEs are observed. In some cases it has also been possible to avoid VDEs and halo currents completely by a combination of passive and active vertical stabilization.

The principal discrepancy between theoretical expectations and observed results in present experiments lies in the impurity distribution that is obtained after pellet ablation is complete: the resulting profile of impurities and added plasma density is more localized in the outboard portion of the plasma than the ablation source alone would indicate. The outward redistribution effect is, however, consistent with the expected diamagnetic expulsion of deposited particles and is expected to be absent if shutdown pellets can be injected from the high-magnetic-field side of the plasma.

Present experiments also confirm the predicted tendency of fast shutdown to generate runaway electrons. While runaway generation in present experiments has not been a serious problem, perhaps in part owing to the effect of MHD fluctuations that frequently accompany injection, projections of runaway growth to ITER show that pellet-injection-induced runaway conversion may be a more serious concern. Here runaway avoidance appears to favor massive deuterium or helium injection as a shutdown means, but there are presently great uncertainties about the plasma response to the ~100-x increase in density that such injection would produce. There is also estimates that more modest ~10-x deuterium or helium gas injection could enhance resistive dissipation of runaway current after conversion occurs (see Section 3.4.4). Both demonstration-of-concept experiments to provide data about high-density plasma behavior and better understanding of the interaction that appears to exist among runaway production, MHD

fluctuation losses of runaways and vertical instability after-conversion interaction with a high-density background plasma are needed to be able to project the need for and the feasibility of high-density runaway-free shutdown to the reactor plasma regime.

3.4.6. Disruption Avoidance, Softening, and Amelioration of Consequences

Disruptions are presently an unavoidable consequence of tokamak operation, and although implementation of disruption avoidance and/or mitigation measures (to be described below) are highly desirable ITER design and operation goals, the present design basis assumption for ITER is that the success of such methods cannot yet be guaranteed, and hence that major disruptions will occur during an appreciable fraction (~10%) of ITER pulses (Section 3.4.1). Consequently, ITER components are designed to withstand the EM and thermal loading stress and erosion consequences of these disruptions (Section 3.4.2) and provision is made for replacement of eroded divertor surface components on a regular basis (see Chapters 1 and 4). However, given that the usable lifetime of the plasma facing surfaces is finite and given further that disruption erosion may consume approximately 50% of the overall component lifetime, and also given that reconditioning of plasma facing surfaces after disruptions will be required before normal plasma operation can be resumed, there are clear incentives in ITER to avoid the occurrence of disruptions whenever possible and to reduce or mitigate the direct and consequential effects of such disruptions that do occur. This Section describes the possible means for such avoidance and mitigation of effects. Additional details of the means by which fast plasma shutdown — one of the key means for mitigation — can be effected are presented in Section 3.4.5. Discussion of integrated disruption effects modeling — which contributes centrally to assessment of mitigation efficacy — is given in Section 3.4.7.

Broadly speaking, the subjects of disruption avoidance and effect amelioration or mitigation can be divided to three considerations: (1) prediction of the impending occurrence of disruption and/or avoidance of disruptions by *a priori* avoidance of the operation conditions that lead to

disruption , (2) intervention, either before disruption precursors occur or before precursor growth leads to irreversible onset of thermal quench, to actively effect avoidance, and (3) amelioration or mitigation of effects, in which after-onset actions are taken to reduce the severity or consequential effects of a disruption. All of these methods have been tested and/or demonstrated with some degree of success and reactor relevancy in present tokamaks. However, to date a completely successful single method or combination of methods that allows reliable avoidance or mitigation of disruptions has not been demonstrated, and the subjects of disruption prediction, avoidance and effect mitigation remain as important subjects of on-going tokamak R&D.

3.4.6.1. Disruption avoidance

Disruptions can in principle be avoided during tokamak operation by the provision of an operation scenario that skirts the various operational limits and conditions that cause disruptions and by the provision of adequately reliable plasma operation systems (hardware) and control systems (hardware and control algorithms) such that all critical parameters of the prescribed scenario (including suitable pre-pulse conditioning of the plasma facing surfaces, see Chapter 8) can be reliably obtained and repeated. Selection of a scenario that maintains a relatively wide margin against known disruption-initiating conditions is an obvious benefit in the development of such 'disruption-free' scenarios. Under such conditions, often embodied in present so-called "setup" or "reference pulse" discharges but also in standard operation mode discharges that can produce high plasma performance (for example the standard TFTR 'supershot' used for DT experiments), per pulse disruption rates can be low (e.g., ≤1% for TFTR supershots) [3.339] and can in principle approach zero if hardware reliability and control of wall conditions (see Section 8.1) can be made sufficiently high.

Setup scenarios are often based upon conservative plasma operation parameters that do not press close to known disruption-initiating limits or plasma configuration control limits. The same type of 'passive' or *a priori* disruption avoidance procedures can in principle be extended to operation scenarios that come closer to several operational limits: in these cases (representative of

the regime needed for ITER burning plasma operation) cognizance of the various operational limits involved must be taken into account, and provision of real-time disruption prediction (onset warning) capability becomes an important consideration. Here monitoring of various plasma performance indicators, including edge safety factor (q_{95}), internal inductance (to quantify position in the q–l_i tearing mode stability domain), plasma density relative to the Greenwald value, radiated power fraction, and status of MHD activity become essential operation scenario development tools. Monitoring of such indicators can provide both indirect (via the cognizance of operation staff, typically employed on a next-shot basis) and immediate (on-line, by electronic means) during-pulse warning of impending or potentially-impending onset of disruption. Using a proximity or warning indicator to effect feedback-controlled intervention (i.e., feedback from β_N to control P_{aux} [3.273] can lead to improved ability to operate reliably near an operational limit that can initiate disruption (see Section 8.x). In the same vein, provision of plasma control systems incorporating feedback algorithms to control sensitive scenario parameters (plasma density, radiation fraction, etc.) makes reliable achievement of the desired scenario parameters without occurrence of disruption a matter of closed-loop control rather than open-loop setting of parameters on a before-the-pulse basis [3.340].

3.4.6.2. Disruption-onset prediction

Basing disruption prediction on single parameter proximity or the confluence of several single parameter limits may not necessarily provide complete certainty for disruption avoidance, or conversely, may unduly restrict the accessible operation domain. A possible improvement here can be made by implementation of a neural network disruption predictor [3.341], wherein multiple disruption-related indicators or diagnostic signals are combined via a neural network to provide a composite impending-disruption warning indicator that is more robust and reliable than simple single- or multiple-parameter indicators. There has been recent successes (Fig. 3-77) in demonstrating both enhanced disruption predicting capabilities of the method and the procedures to be used for the on-line 'training' of the network [3.342]. However, how to directly apply training

obtained in a present experiment to ITER or how to shorten the period required for network training in ITER (will which require producing disruptions) remains to be assessed.

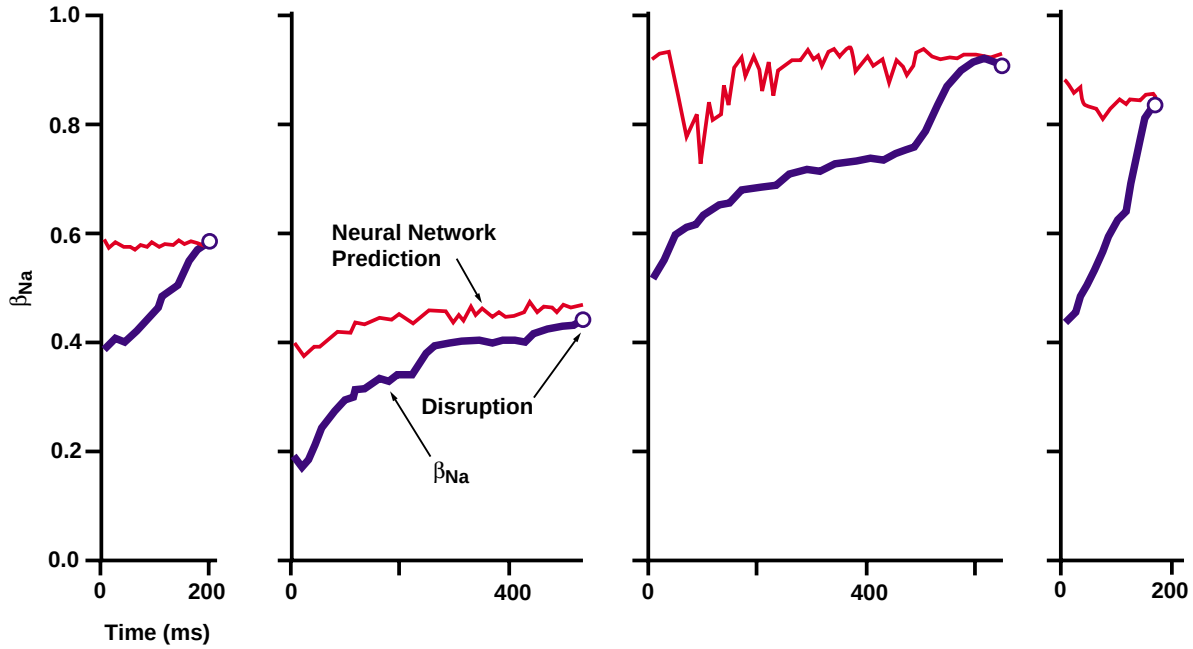

FIG. 3-77. Neural-net disruption prediction in DIII-D. After training, the neutral net successfully predicts the β_{Na} at which disruption occurs in plasmas in which the disruption threshold is not well-described by β_{Na} = constant. Here β_{Na} is an on-line signal that provides a relative measure of the normalized total beta (Troyon coefficient). Depending on the threshold basis chosen, a 'look-ahead' time ≥ 100 ms for prediction of an impending disruption is achieved.

Finally, since disruption onset is ultimately determined by exceeding MHD stability boundaries (Section 3.4.1 and Section 3.2), real-time evaluation of plasma MHD stability (done either via a real-time stability code or look-up application of a pre-compiled stability database) can in principle be used as a disruption-onset predictor, and there are many cases in which occurrence of disruption has been closely correlated (on an after-the-fact basis) with a corresponding prediction of MHD instability onset. Figure 3-78 shows an example of the success of MHD modeling in predicting the β_N for onset of disruption owing to internal balloon modes in high-performance DT 'supershots' in TFTR. The β_N at which disruption occurs can be predicted to an accuracy of a few percent. Provision of adequate and sufficiently-accurate diagnostic data (e.g.,

plasma flux configuration, pressure and current density) is however required for application of this method, and the effect of measurement accuracy on the degree of achievable disruption predictive reliability remains to be fully quantified.

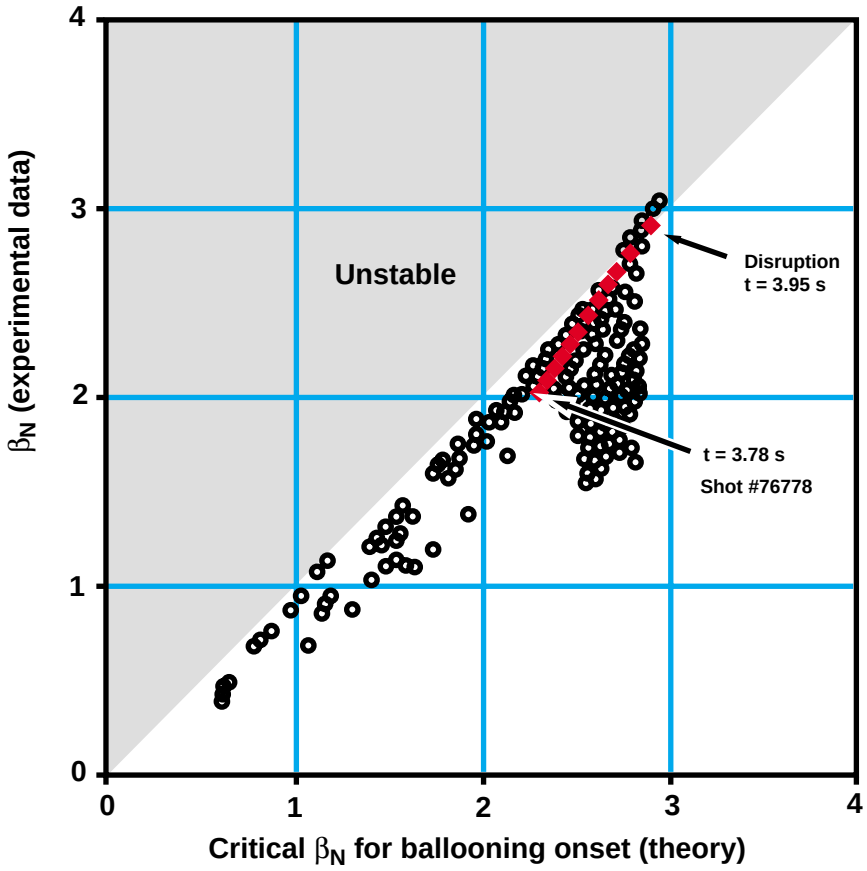

FIG. 3-78. 'Prediction' of a beta-limit disruption in TFTR. Actual β_N and calculated MHD stability limit critical β_N (defined at r/a = 0.33) for a selection of non-disrupting TFTR supershots (open data symbols, time and pressure profile vary over the data set, critical β_N obtained by off-line MHD stability calculation) and comparison of the calculated and actual β_N for Shot #76778, a high-performance DT pulse, which disrupted upon reaching the 'predicted' stability limit.

The result of any of these prediction methods or of the more traditional approach of detection of disruption MHD precursor growth is *a priori* indication of the possible or likely occurrence of a disruption. Such indication can the basis for initiating the avoidance and/or mitigation procedures described below. The time needed for the implementation of such procedure

determines the 'look-ahead' time-horizon capability needed for the predictor. Reliability of the predictor is a second key consideration: simultaneous achievement of highly reliable prediction of disruption and low (ideally zero) occurrence of 'false alarms' is important. Identification of a suitable predictor that satisfies both of these requirements remains a subject of on-going R&D.

3.4.6.3. Avoidance methods

Avoidance methods fall into two categories: passive and active. Passive measures involve direct intervention to mitigate the underlying cause of the disruption, for example, by reducing the plasma density if approach to a density-limit threshold occurs, or by the addition of auxiliary power if an edge power balance condition develops. Preset operation of the feedback control loops provided in the plasma control system for 'control' of such operation parameters (see Section 8.2) constitutes a first level of implementation of such avoidance techniques [3.340]: with the further addition of making the set points of such control loops plasma state [3.342] or event (e.g., disruption-onset predictor) dependent (e.g., Fig. 3-79), a disruption-avoidance scheme is implemented.

The achievable time response of such indirect avoidance schemes is determined by the physics considerations involved: for most variants of the schemes, the characteristic time is the plasma energy or particle confinement time, or for measures that involve modification of the current profile, even the plasma resistive diffusion time. Such methods are therefore usually relatively slow (≥ few s to few × 10 s in ITER), and hence their application is limited to situations in which a predictor with a sufficient 'look-ahead' time horizon is available. For example, owing to the expected short growth time of traditional MHD precursors (~ 100 ms, see Section 3.4.1), coupling of such detection to slow intervention schemes is not a useful option for disruption avoidance in ITER. The method may be useful in preventing disruptions with more-slowly-growing neoclassical-island tearing modes, where the expected growth times in ITER are predicted to be long enough (≥10 s) to make slow indirect intervention possible (see Section 3.2.3).

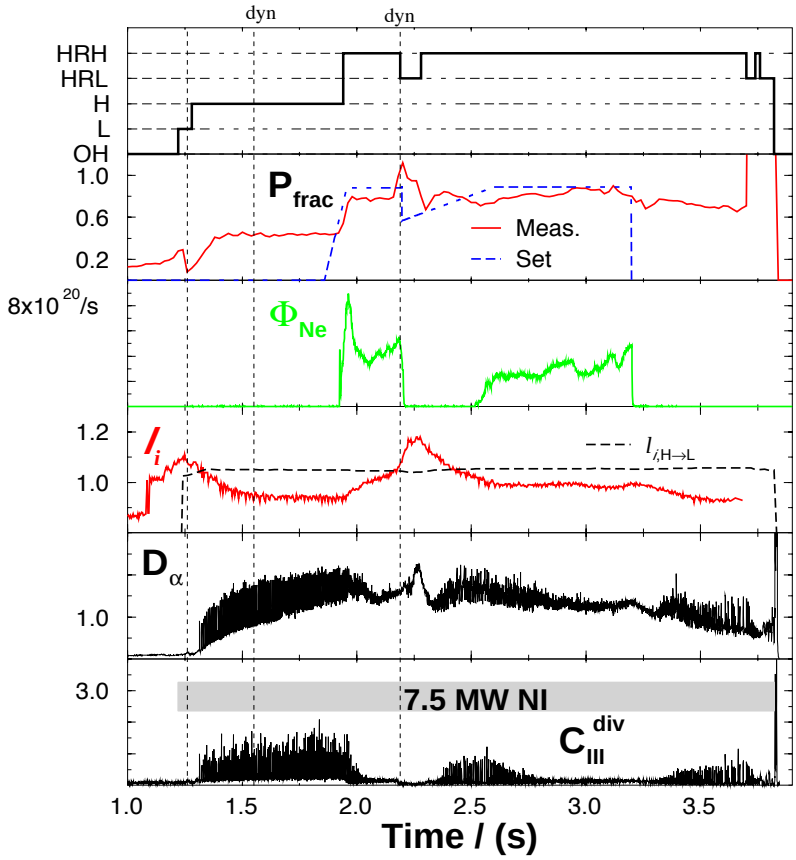

FIG. 3-79. Plasma control autonomy and disruption avoidance during an ASDEX-U discharge. Corrective actions ('repair procedures', in this case reduction of the injected neon) taken by the control system upon detection of loss of HRH mode (high-radiation H-mode) allow the mode to be recovered. The disruption that would have otherwise occurred is avoided.

The second category of intervention schemes are 'direct' schemes that act on a fast (≤ 1 s) time-scale with active heating or current-drive means to locally modify pressure and/or current density gradients or plasma rotation profiles so as to slow or prevent growth of the MHD instability (see Section 3.4.1) that leads to thermal quench onset. Owing to the highly localized current drive capability that it can provide, ECCD is the primary means envisioned for such intervention (see Chapter 6 and Section 3.2.3) and there have been some preliminary successes in using ECRH to modify disruption precursor growth (see e.g. [3.343] and [3.344]). However, ICCD and LHCD may also have potential fast-intervention capabilities, as may the application of

NBI momentum drive in situations where modification of the plasma rotation profile can forestall locked-mode-initiated disruption.

3.4.6.4. Softening and amelioration of consequences

If a disruption can not be avoided or if insufficient warning is available for taking intervention action, other measures can be taken to soften or ameliorate the resulting sequence of consequential effects that include the thermal quench, the current quench, vertical instability and in-vessel halo current and conversion to runaway electron current. In present experiments where relatively fast-acting equilibrium control systems are available, it is possible to take control action to reduce elongation and or plasma current fast enough to at least minimize the vertical instability consequences of disruption. For example, the JET plasma control system is now configured to implement a rapid reduction in plasma elongation upon detection of disruption precursors or actual disruption. This reduction serves to limit the severity of VDEs and the resulting torus vessel vertical and radial forces (see Section 3.4.3). However, for ITER such direct mitigation by PF control will not be possible (owing to power limitations), and hence injection of impurity or hydrogenic species in the form of 'killer pellets' is proposed as the most benign 'fast-shutdown' amelioration means. As is presented in Section 3.4.5, in present experiments impurity pellet injection has proven to be effective for key aspects of disruption amelioration: divertor thermal load reduction and VDE and halo current magnitude reduction have been successfully demonstrated. However, application of such methods in ITER is complicated by the predicted tendency of such methods to promote wholesale runaway conversion, and identification of an amelioration method that balances overall minimization of loading on ITER systems, reliability and certainty of action remains an open R&D subject and one wherein a capability to model all of the many effects required for prediction of fast shutdown characteristics in ITER remains a key R&D subject (see Section 3.4.7).

3.4.7. Disruption Modeling and Integration of Effects

The preceding presentations of the physics bases for disruption and disruption-related effects approach their respective subjects and reactor-tokamak extrapolation principles in a topical manner, as if the effects are separated. However, as has already been noted in these Sections, there are obvious connections among the topics, and the sequence of disruption events and effects that starts with MHD precursor growth and ends with current termination comprises an integrated cause-and-effect cascade in which the preceding phases and events in the sequence play an important role in determining the further evolution of the sequence (Fig. 3-80). This is particularly true for disruptions in elongated tokamaks, where vertical instability and the resulting dynamic evolution of the plasma equilibrium plays a key role and for disruptions in reactor tokamaks with high plasma energy levels, where the impurity generation effects of the energy deposited in the thermal quench phase can be expected to significantly modify the subsequent characteristics of the current quench and runaway conversion phases.

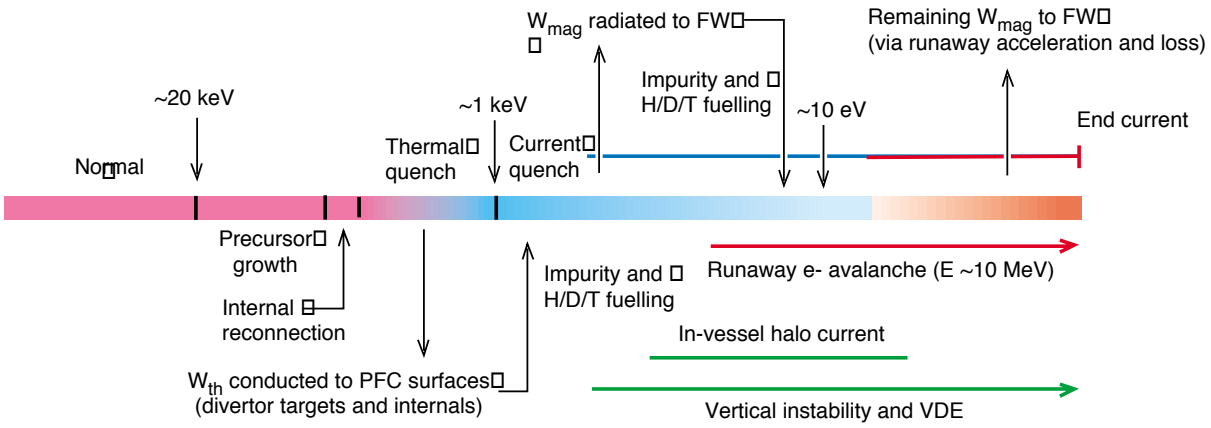

FIG. 3-80. Disruption and disruption-related effects (schematic)

Explicit consideration of the cause-and-effect aspect of the disruption sequence is especially applicable for prediction of disruption effects in reactor tokamaks, since mechanisms absent in present disruptions — especially massive plasma-facing-surface ablation and the potential for knock-on avalanche runaway generation — are expected to lead to effects in reactor tokamak

disruptions that may differ from the effects and even the disruption sequence seen in present tokamaks. This difference leads to the statement made earlier that definitive prediction of disruption characteristics and effects for reactor tokamaks will ultimately require a disruption model that incorporates consideration of all of the relevant physics mechanisms and their cause-and-effect interconnections. The basis for such an 'integrated' disruption model is the subject of this Section.

3.4.7.1. Integrated disruption modeling

The integrated sequence of events that will comprise disruption in a reactor tokamak is in principle susceptible to predictive modeling or simulation, and simulations that incorporate at least partial consideration of the various elementary effects involved — dynamic plasma equilibrium evolution, impurity influx and resulting plasma resistivity increase and radiation losses, and runaway growth and losses — have already proven useful in being able to interpret present experimental data and to help show how this data extrapolates to reactor plasma conditions. In some cases (e.g., current quench duration or runaway electron conversion by the knock-on avalanche mechanism), the physics effects involved are relatively simple and 'single-effect' modeling is sufficient to establish a bounding or 'worst-case' basis for the effects that are possible in the reactor plasma regime. However, for examples like runaway conversion, where worst-case calculations raise serious design and operation questions, there is a clear need to extend single-effect modeling to a more integrated basis in which all relevant considerations — including the effects of MHD activity, plasma motion and deformation (including the effects of non-axisymmetry) and the effects of wall- or surface-generated impurities—are taken into account in a self-consistent manner. This type of integrated modeling capability offers the promise of being able to turn the schematic sequence of effects illustrated in Fig. 3-80 into quantitative prediction for future tokamaks and ITER. Such modeling also offers the promise of being able to establish likely — as opposed to worst-case bounds — for major reactor system design basis loading conditions. The resulting more-self-consistent set of design specifications may be appreciably easier to satisfy than the present simultaneous combination of worst-case limits.

The development and validation of an integrated modeling capability has been identified as an important goal for ITER Physics R&D. The material that follows comprises discussion of the key considerations involved and summarizes the status of integrated modeling development. As the presentation shows, certain modeling basis elements and techniques are well established and validated, but other key aspects of integrated modeling remain as future R&D goals.

Modeling the full scope of disruption and ensuing effects on a 'first-principles' MHD-instability-based integrated basis is a formidable challenge and one that is likely not amenable to resolution within a foreseeable period of time. Furthermore, while a predictive model that starts from MHD precursor development is a laudable physics-understanding goal, the complexities of the non-linear MHD evolution that lead to onset of the thermal quench, the difficulties of modeling the resulting stochastic 3-D (three-dimensional) MHD effects on energy and particle transport, and the fact that the important design-relevant consequences of disruptions start with onset of the thermal quench (fast-α losses owing to MHD precursors are an exception, see Section 3.4.5), a more direct 2-D approach that starts with empirical or semi-empirical models of the thermal quench and the ensuing current profile broadening is indicated. Figure 3-81 shows a schematic illustration of the resulting modeling approach, with various key modeling basis elements (or modules) indicated. This schematic is presented here to provide a framework for the discussion of the various modeling elements that are needed for an integrated model: it is not intended to necessarily be a definitive concept for how an integrated model should be configured.

As the Figure shows, a 2-D (two-dimensional) dynamic equilibrium and transport model forms the kernel of the disruption modeling capability and provides a self-consistent means of dynamically accounting for the plasma energy and particle (both thermal and superthermal) inventories. Accounting for the magnitude and evolution of these inventories, particularly the current profile, is a key consideration that is central to calculating the plasma equilibrium in a manner that self-consistently reflects both the plasma evolution and the effects of the surrounding electromagnetic environment [*i.e.*, the toroidal and poloidal electrical conductivities and electrical connection scheme of the torus vessel and in-vessel systems and also the configuration of poloidal

field (PF) coil system]. For disruptions with time-scales comparable to or longer than the response time of the plasma equilibrium control system, consideration of passive and active response of the PF system is also required.

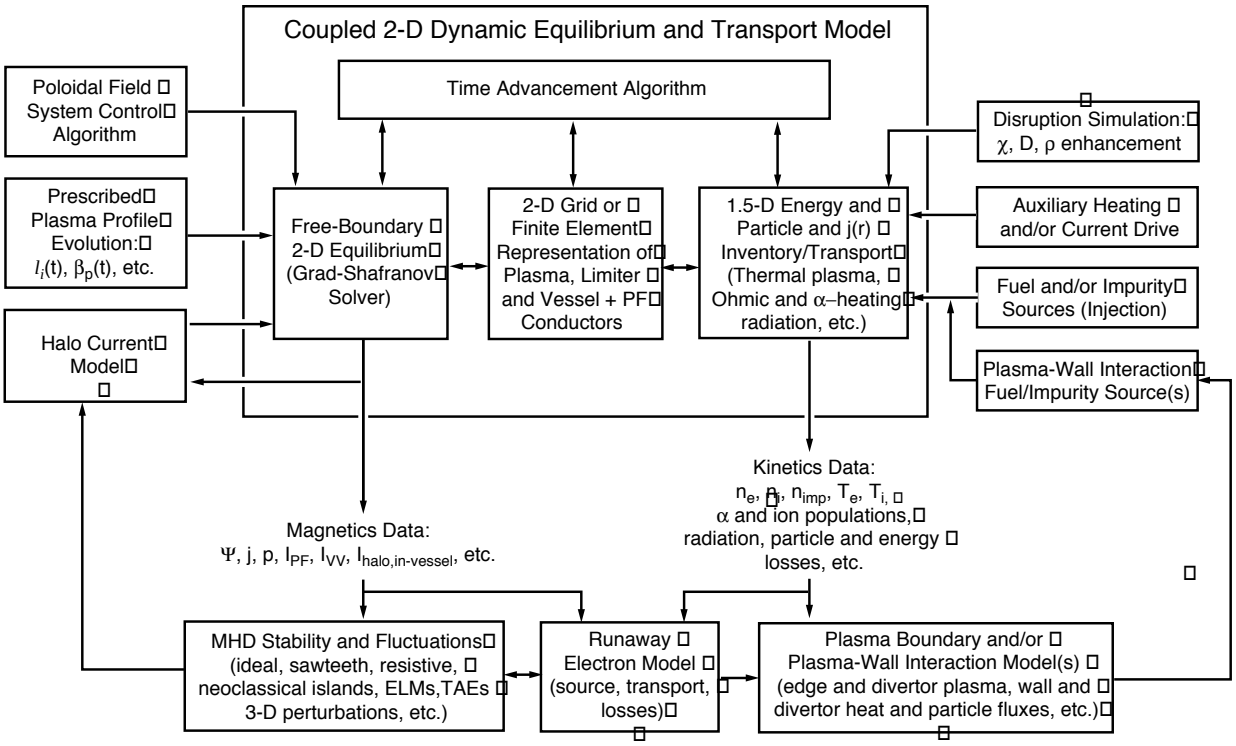

FIG. 3-81. Integrated disruption model schematic with basic and optional modeling elements. Major interactions in the model are identified (see text below) but the interactions shown are not intended to be exhaustive

In the basic coupled model schematic illustrated in Fig. 3-81, the evolution of the plasma energy and particle content and of the resulting current and pressure profiles are calculated internally by means of a 1.5-D (flux-surface-averaged) transport model that is internally coupled to the Grad-Shafranov 2-D equilibrium solver. The effects of disruption onset (thermal and current quench) are simulated by corresponding transient enhancements of the energy diffusion and particle transport coefficients and by transient and/or permanent enhancement of the plasma resistivity. The enhancement factors and durations of the enhancements are chosen (for the case of interpretation of experimental data) to achieve the observed thermal and current quench durations

and the observed positive current rise and/or current profile broadening (l_i decrease). For simulations of disruptions in future reactor tokamaks, the enhancement parameters are typically chosen to yield the projected thermal and current quench durations (see Section 3.4.2) or can be systematically varied to conduct parametric studies of the sensitivity of disruption effects to the enhancement parameters and other uncertain modeling basis parameters (see below).

Simulation of the underlying MHD instability mechanisms responsible for disruption onset by transport and/or resistivity enhancement ensures that the resulting calculation of the plasma evolution is based upon a fully self-consistent accounting of plasma energy, particle content and entropy. However, it is also possible to calculate the equilibrium evolution without transport calculations by instead prescribing the time evolution of the equilibrium parameters (l_i and β_p) and the plasma resistivity or temperature during the current decay. Here it is necessary to select profile evolutions that mimic either the experimental data (including the after-thermal-quench current rise, if present) or which yield similarly self-consistent results for the simulation of future tokamak disruptions.

Three auxiliary modules are shown in Fig. 3-81: these modules respectively support axisymmetric halo current modeling (essential to realistic modeling of the VDE phase of a disruption), a pellet/impurity injection modeling module (for study of fast shutdown implementation and effects) and a plasma-facing-surface particle and impurity source model. These modules plus the 2D equilibrium/inventory kernel constitute what can be considered to be a basic 'fully-integrated' disruption model.

Options for MHD stability assessment and self-consistent instability (fluctuation) calculation, 3-D plasma deformation calculation (with linkage to the halo current model) and for detailed plasma-facing-surface power deposition and ablation calculations are also shown. These additions are optional, in part owing to the fact that they constitute refinements to the basic disruption/VDE model and in part owing to the likelihood that the required modeling calculations may have to be implemented separately (off-line, so to speak) from the basic integrated model calculations.

A runaway electron model is also shown. This model, which is optional for the case of present experiments where runaway effects are negligible, is likely critical to the modeling of reactor disruptions, VDEs and fast shutdown where runaway conversion effects are potentially much more significant (see Section 3.4.4 and Section 3.4.5).

Simplification of the basic model to a 2-D equilibrium basis is a presently necessary aspect of integrated disruption modeling. A fully self-consistent 3-D MHD model of equilibrium and stability is in principle desirable, but the computational challenges are significant and even simplified models of such effects presently lie at the boundary of the state-of-the-art (see further discussion of 3-D and MHD fluctuation effects below).

3.4.7.2. Dynamic equilibrium modeling of disruptions and VDEs

Modeling efforts aimed at simulating disruption effects based on 2-D dynamic equilibrium models have been underway for a number of years and have been applied for both interpretation of data from present experiments and for making estimates of disruption and VDE characteristics in reactor tokamaks and various ITER designs. To date, the majority of this data interpretation and future-tokamak simulation effort has been conducted with the Tokamak Simulation Code (TSC) [3.345], but more recently there has been similar development and application of disruption and VDE simulation models embodied in the DINA [3.346] and MAXFEA [3.347] dynamic equilibrium codes. A standard TSC disruption model has been developed which can simulate many features of a disrupting plasma during both the thermal quench and current quench phases. When the predictions of this model have been compared detailed experimental data, generally good agreement is found [3.280, 3.284, 3.348]. This agreement, however, comes from adjustment of key modeling parameters in the simulation to match experimental results, and while there is a reasonable basis for then extrapolating these parameters to future tokamaks, the TSC and all similar disruption models are still semi-empirical, and the resulting predictions for future tokamaks therefore remain somewhat sensitive to the extrapolation basis. Nevertheless, TSC and similar

models provide the best present basis for self-consistently predicting the anticipated characteristics of future tokamak disruptions and VDEs.

Disruption Plasma Load Cases. Estimation of the electromagnetic loads that disruptions and VDEs produce in reactor tokamak torus-vessel and in-vessel components is a key consideration in the concept development and design of such future tokamaks. The TSC code and disruption/VDE model is being used to provide an axisymmetric model of a disrupting plasma to compute loads for the engineering analysis of the internal components of the ITER vacuum vessel and the vacuum vessel itself. A detailed TSC structural model [3.349] with 1154 filaments was built on the then-current (1996) basis of the ITER geometry modified to account for more recent developments (ca 1997) in the first wall design. The axisymmetric-equivalent ITER structure model in TSC incorporates modeling features found to be important by the 3-D structure analysis code SPARC [3.350]. The structure model is implemented by the use of 15-cm by 15-cm ($\Delta R \times \Delta Z$) zones that have specified toroidal conductivity, or for electrically-isolated components with no continuous toroidal connection (*e.g.*, the nuclear shield and divertor cassette modules) groups of zones with zero net current constraints imposed. The model also has poloidal connections and connection breaks defined which respectively allow and prevent poloidal current flow. These modeling features permit the full toroidal and poloidal complexity poloidal of the ITER vessel and in-vessel structures to be described in an equivalent 2-D axisymmetric modeling sense. A poloidal cross-section representation of the overall model appears in Fig. 3-82 below.

To date, five design-basis disruption scenarios have been developed with TSC for the ITER 21 MA, 5.7 T design. These scenarios differ in details of the initial conditions (initial Z displacement) and in the halo temperature. In all cases, the disruption was modeled by letting the thermal conduction suddenly increase to a value 10^6 times its disruptive level. The scenarios include four VDE cases and one fast radial case. The initial equilibrium for all cases corresponded closely an ITER end-of-burn equilibrium with $\beta_p = 0.9$ and $l_i\,(3) = 0.9$.

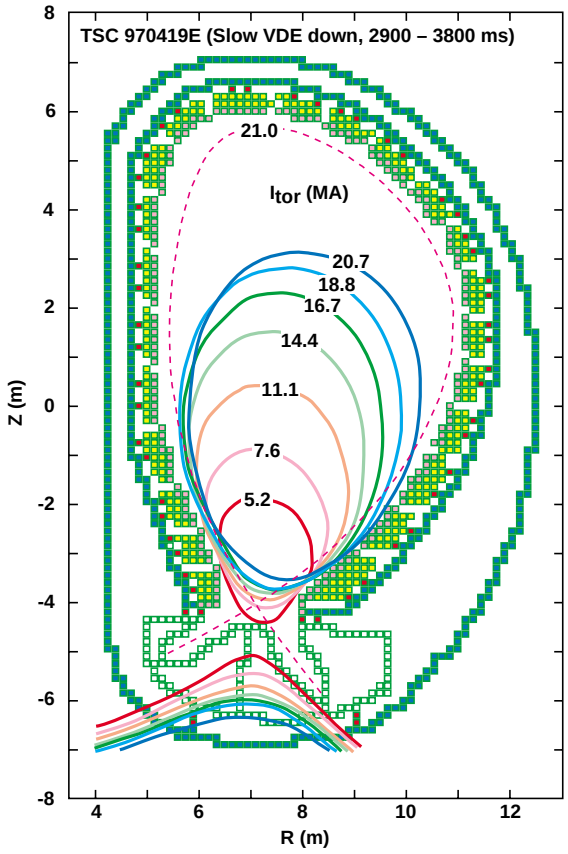

FIG. 3-82. Plasma configuration and toroidal current for a slow VDE in ITER. TSC simulation model. Compare with the configuration evolution for the Alcator C-Mod 'vertical disruption' shown in Fig. 3-59, Section 3.4.3.

The VDE cases consist of an upward or downward vertical drift lasting until $q_{95} = 1.5$, a fast (~ 2 ms) thermal quench, and a current quench of duration 11 to 900 ms. Contributions from toroidal currents, induced poloidal currents, and "plasma-wall" poloidal current flowing between plasma halo and plasma facing components were included in the analysis. The slowest VDE case (900 ms current quench, shown in Fig. 3-82) gave the largest plasma-wall poloidal current, 5.0 MA, the largest poloidal current in the structure, 3.9 MA, and the extreme net vertical force on the entire structure, -120 MN (Fig. 3-83). However, at least three additional cases are required to specify the extreme pressures in the ITER vessel, backplate divertor components, first wall, and radial connecting straps. For a given case, the vertical force evolution differs significantly for

different structural components. More recent TSC simulations have also explored the plasma/halo temperature modeling parameter sensitivities of disruption characteristics and vessel and in-vessel loadings. These sensitivity studies have yielded results similar to the DINA sensitivity studies described below.

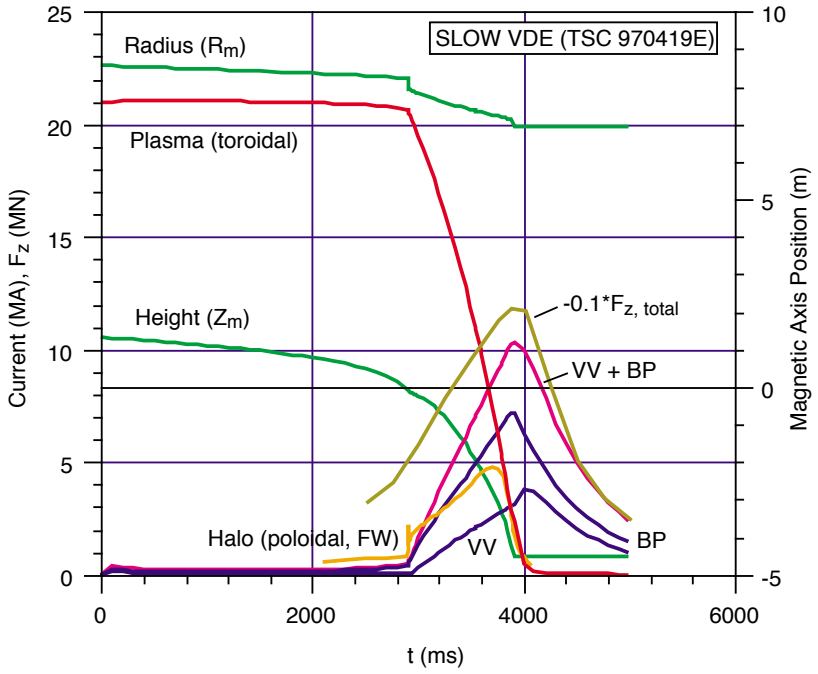

FIG. 3-83. Plasma, torus vacuum vessel (VV) and backplate (BP) toroidal currents and in-vessel poloidal halo current and axial (Z) force for the slow ITER VDE shown in Fig. 3-82. Compare with the current waveforms for the Alcator C-Mod VDE shown in Fig. 3-59, Section 3.4.3

The TSC simulations of the type shown above incorporate a detailed in-vessel and vessel model (note the number of modeling elements shown in Fig. 3-82) and hence yield great detail at the individual modeling element level about the resulting time-histories of the in-vessel currents and forces. Detailed knowledge of the component-level variation of the magnitude and time-history forces is potentially important for validation of the structural response of the overall vessel and in-vessel system and for the design of the component attachment and electrical connections. However, each TSC simulation requires significant execution time on a major computer, so it is not possible to easily study many disruption scenario cases or to exhaustively explore the effects of

variations in, for example, the halo modeling basis parameters. To perform these sensitivity and scoping type of calculations, a large number of disruption simulations using the DINA code [3.351, 3.346] have also been performed. These include simulations of DIII-D and ITER disruptions. The DINA code utilizes a semi-analytic halo model and prescribed plasma profile evolutions. In its typical embodiment, it is much faster to run than TSC, but it does not have the same level of structure detail with regard to the in-vessel halo currents. It has therefore been used to explore worst-case disruptions for ITER and to test sensitivities to plasma core and halo modeling assumptions [3.352] (Fig. 3-84). When the DINA simulations were compared with a corresponding TSC case and with limited TSC halo parameter variation scans, the results from the two codes are found to be in substantial agreement.

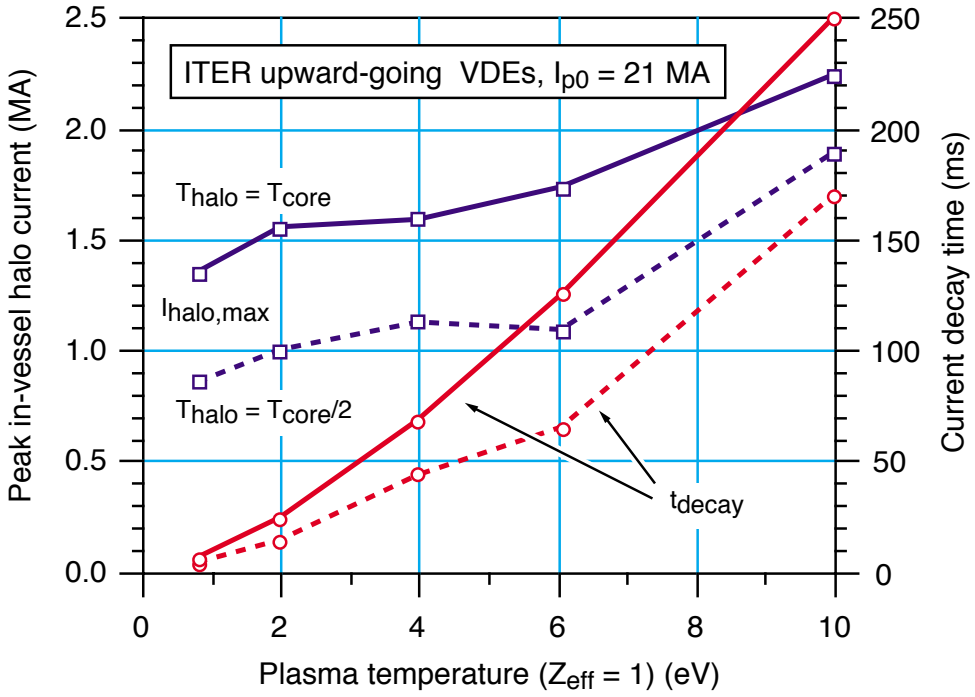

FIG. 3-84. Halo current magnitude and current decay time versus plasma temperature and halo temperature (= T_{core} or $T_{core}/2$), as obtained in DINA simulations of upward-going ITER VDEs. The minimum projected ITER current quench duration of 50 ms corresponds for these two halo assumptions to core temperatures of 3 and 4.5 eV (consistent with impurity radiation cooling, see Section 3.4.2) and corresponding peak in-vessel halo currents of about 1.6 MA and 1.2 MA. The tendency of peak halo current to increase with higher core and/or halo temperature (and hence also with increasing current quench duration) is clearly shown.

3.4.7.3. Pellet injection and fast shutdown modeling

Several special-purpose models of impurity injection shutdown in tokamaks (see Section 3.4.5) and the associated development of runaway electrons have begun to appear [3.297, 3.353]. A TSC 'killer pellet' modeling is being developed and verified by detailed modeling of well diagnosed experiments in TFTR, DIII-D and JT-60 (see Section 3.4.5), and there has been preliminary application of the model to ITER. TSC now incorporates a multi-pellet ablation and mass distribution model (including the effects of 'back-averaging', see Section 3.4.5), the full ADPAC impurity radiation model, and criteria to indicate when the evolving 2-D equilibrium becomes unstable to 3-D modes. The TFTR modeling worked very well [3.354], with TSC being able to reproduce the plasma current, OH current, diamagnetic loop, and bolometry measurements on the low Krypton concentration shots that were predicted to remain axisymmetric stable, but unable to directly predict the rapid current decay in the high Krypton concentration shots. The stability indications in TSC did predict that the high Krypton concentration shots should become MHD unstable: this is consistent with the rapid current decay observed for the high-Kr cases. Coupling of a calculation of the resulting 3-D MHD fluctuations to the basic 2-D TSC plasma evolution model remains as a future TSC model development task, as does inclusion of 3-D plasma deformation halo current asymmetry model and a runaway electron model.

A knock-on avalanche runaway conversion model based upon the formulation given in Section 3.4.4 has recently been incorporated in the DINA disruption model and has been used to simulate runaway conversion and deposition in upward-going ITER VDEs (see data in Fig. 3-84, Section 3.4.4). The results of this first 2-D dynamic modeling of runaway conversion confirm the quantitative estimates of runaway conversion obtained with 1-D 'static' models [3.297], albeit with the caveat common to all present runaway models that the possible loss-enhancing effects of MHD fluctuations on runaway losses during the avalanche conversion phase are not yet incorporated (see discussion in Section 3.4.4 and Section 3.4.5)

For future application of TSC (or other similar codes) to ITER shutdown with low-Z pellets, the energy transport model may need to include a better calculation of hydrogenic and low-Z impurity radiation transport. Here calculations of hydrogen and impurity line-radiation transport at high densities with the CRETIN code [3.355] show that line-radiation 'trapping' effects can be important and can appreciably decrease radiative cooling for high-density shutdown. This finding indicates that detailed radiation transport calculations may need to be incorporated or simulated in modeling of low-Z injection shutdown scenarios for ITER and reactor tokamaks.

3.4.7.4. Halo current models

The halo current models incorporated in present 2-D equilibrium models are axisymmetric and semi-empirical: one typically specifies the halo temperature (or equivalent electrical conductivity) plus the halo width. The effects of toroidal asymmetry, which are not incorporated in such models are presently added in an *ad hoc* manner in the subsequent 'engineering application' of the modeling data. A more-self-consistent and/or 'physics-based' non-axisymmetric halo current model is highly desirable, but the challenges of the required 3-D equilibrium and stability modeling required have not yet been resolved and experimental data relating halo current asymmetry to 3-D plasma column deformation are too sparse to provide anything more than initial insight into the possible cause (or causes) for the halo current toroidal asymmetry. Here a relatively simple model [3.290] has been developed by Pomphrey and co-workers of a 3-D helical kink-deformed plasma in contact with a wall, leading to a non-axisymmetric halo-current pattern. This model leads to a relation between halo current fraction I_H/I_P and halo toroidal peaking factor TPF that depends only on a single parameter, $\Delta a/a$, which measures the saturated amplitude of the kink instability. Choosing $\Delta a/a < 0.3$ gives good agreement with nonlinear 3D MHD [3.356] calculation for the maximum saturated amplitude of an external kink mode, and also seems to encompass the experimental data (see Section 3.4.3).

Along similar lines, insight into the origin of the lateral forces on the JET vacuum vessel associated with VDEs has been obtained in terms of corresponding measurements of a tilted and

radially-displaced plasma column [3.288]. However, predictive application of this modeling premise or the Pomphrey 3-D deformation premise into a 2-D simulation code remains as a future disruption model development and verification task.

3.7.4.5. Further model development

The A*Thermal code [3.357], developed by A. Hassanein includes a very complete description of the effects of large heat fluxes on the divertor and first wall. We should consider coupling this code to the TSC code to more self-consistently calculate the impurity influx into the plasma during the disruption from the divertor region.

For the killer pellet modeling, a number of effects need to be included in the modeling. We must incorporate the TFTR observation [3.318] that a sawtooth is induced when the pellet reaches the q = 1 surface, include a runaway electron model, develop a model for runaway interaction with wall, develop a better characterization of the onset and the consequences of a MHD event, and continue to refine the model by detailed calibration with experiments.

Three-dimensional MHD code calculations are needed to better understand the physical basis for the difference between impurity pellet fueling for inside and outside launch, to better understand how a pellet induces a MHD event, and to understand under which circumstances magnetic surfaces reform during a disruption, and for a more self-consistent calculation of non-axisymmetric halo currents during a disruption.

REFERENCES

[3.1] D. BOUCHER, F. LOUCHE, N. KARULIN, ITER JOINT CENTRAL TEAM, ITER HOME TEAMS, *ITER Fusion Performance Projections*, in *Controlled Fusion and Plasma Physics* (Proceedings 24th European Physical Society Conference, Berchtesgarten 1997, Europhysics Conference Abstracts, Geneva ,1997) **21A Part III** 953-957

[3.2] J. FREIDBERG, *Ideal Magnetohydrodynamics*, Plenum Press, New York (1987)

[3.3] F. TROYON, R. GRUBER, H. SAURENMANN, S. SEMERMZATO, S. SUCCI, *MHD Limits to Plasma Confinement*, Plasma Phys. Control. Fusion **26** (1984) 209-215

[3.4] G. BATEMAN, *MHD Instabilities*, MIT Press, Cambridge MA (1978)

[3.5] L. L. LAO, H. ST. JOHN, R. D. STAMBAUGH, A. G. KELLMAN, W. PFEIFFER, *Reconstruction of Current Profile Parameters and Plasma Shapes in Tokamaks,* Nuclear Fusion **25** (1985) 1611-1622

[3.6] L. L. LAO, J. R. FERRON, R. J. GROEBNER, W. HOWL, H. ST. JOHN, E. J. STRAIT, T. S. TAYLOR, *Equilibrium Analysis of Current Profiles in Tokamaks*, Nuclear Fusion **30** (1990) 1035-1049

[3.7] F. J. HELTON, T. S. WANG, *MHD Equilibrium in Non-Circular Tokamak with Field-Shaping Coil Systems*, Nuclear Fusion **18** (1978) 1523-1533

[3.8] J. WESLEY, H-W. BARTELS, D. BOUCHER, A. COSTLEY, L. DEKOCK, YU. GRIBOV, M. HUGUET, G. JANESCHITZ, P-L. MONDINO, V. MUKHOVATOV, A. PORTONE, M. SUGIHARA, I. YONEKAWA, *Plasma Control Requirements and Concepts for ITER*, Fusion Technology **32** (1997) 495-525

[3.9] F. TROYON *et al*, Plasma Phys. Controlled Fusion **26** (1984) 209

[3.10] E. J. STRAIT, *Stability of high beta tokamak plasmas*, Phys. Plasmas **1**, 1415-1431 (1994)

[3.11] O. SAUTER, R. J. LAHAYE, Z. CHANG, D.A. GATES, Y. KAMADA, H. ZOHM, A. BONDESON, D. BOUCHER, J. D. CALLEN, M. S. CHU, T. A. GIANAKON, O. GRUBER, R. W. HARVEY, C. C. HEGNA, L. L. LAO, D. A. MONTICELLO, F. PERKINS, A. PLETZER, A. H. REIMAN, M. ROSENBLUTH, E. J. STRAIT, T. S. TAYLOR, A. D. TURNBULL, F. WAELBROECK, J. C. WESLEY, H. R. WILSON, R. YOSHINO, *Beta limits in long-pulse tokamak discharges*, Phys. Plasmas **4** (1997) 1654-1664

[3.12] G. T. A HUYSMANS, G. CORDEY, C. GORMEZANO, A. C. C. SIPS and B D. J. TUBBING, *ν* Dependence of the Beta Limit in JET*, in Controlled Fusion and Plasma Physics (Proc. 24th European Physical Society Conf., Berchtesgarten 1997), Europhysics Conference Abstracts, Geneva (1997), **21A Part IV** 1857-1860

[3.13] T. S. TAYLOR, E. A LAZARUS, M. S. CHU, J. R. FERRON, F. J. HELTON, W. HOWL, G. L. JACKSON, T. H. JENSEN,Y. KAMADA, A. G. KELLMAN, L. L. LAO, R. J. LA HAYE, J. A. LEUER, J. B. LISTER, T. H. OSBORNE, R. T. SNIDER, R. D. STAMBAUGH, E. J. STRAIT, A. D. TURNBULL, *Profile Optimization and High-Beta Dischargaes and Stability of High-Elongation Plasmas in the DIII-D Tokamak*, in *Plasma Physics and Controlled Nuclear Fusion Research 1990,* (Proceedings 13th IAEA. Conference, Washington DC, 1990) IAEA Vienna (1991), **Vol. 1** 177-194

[3.14] Y. KAMADA, R. YOSHINO, K. USHIGUSA, Y. NEYATANI, T. OIKAWA, O. NAITO, S. TOKUDA, H. SHIRAI, T. TAKIZUKA, T. OZEKI, M. AZUMI, T. HATAE, T. FUJITA, S. TAKEJI, M. MATSUKAWA, Y. KOIDE, T. FUKUDA, S. ISHIDA, JT-60 TEAM, *High Triangularity Discharges with Improved Stability and Confinement in JT-60U*, Fusion Energy 1996 (Proceedings 16th IAEA Conference, Montreal 1996), IAEA Vienna (1997) **Vol. 1** 247-258

[3.15] M. N. ROSENBLUTH, J. HOGAN, D. BOUCHER, A. BONDESON, P. BARABASCHI, B. COPPI, L. DEGTYAREV, S. W. HANEY, H. GOEDBLOED, T. C. HENDER, H. HOLTIES, G. HUYSMANS, W. KERNER, J. MANICKAM, A. A. MARTYNOV, S. MEDVEDEV, D. A. MONTICELLO, T. OZEKI, L. D. PERALSTEIN, F. PERKINS, A. PLETZER, F. PORCELLI, P.-H. REBUT, S. TOKUDA, A. D. TURNBULL, L. VILLARD, J. WESLEY, ITER Joint Central Team, ITER Home Teams, *ITER Plasma Modeling and MHD Stability Limits*, in *Plasma Physics and Controlled Nuclear Fusion Research 1994* (Proceedings Fifteenth International Conference. on Plasma Physics and Controlled Fusion Research, Seville 1994), IAEA Vienna 1995, **Vol. 2** 517-524

[3.16] A. BONDESON, L. VILLARD, D. J. WARD, D. WERMEILLE, J. P. GOEDBLOED, H. A. HOLTIES, T. C. HENDER, G. T. A. HUYSMANS, W. KERNER, *MHD stability of ITER equilibria*, NET Report 107, Commission of the European Communities, DG XII (1995)

[3.17] S. TOKUDA, T. OZEKI, *Stability Analysis of External Kink Mode for ITER L-Mode Profiles*, JAERI-Research 94-013 (1994); S. Tokuda, T. Ozeki, *Stability Analysis of External Kink Mode for ITER H-Mode Profiles,* JAERI-Research 94-030 (1994)

[3.18] A. D TURNBULL, L. D. PEARLSTEIN, R. BULMER, L. L. LAO, R. J. LA HAYE, *On the Operational Beta Limit in Sawtoothing Discharges*, General Atomics Report GA-A22907 (to be submitted to Nuclear Fusion)

[3.19] H. ZOHM, *Edge localized modes (ELMs),* Plasma Physics and Controlled Fusion **38**, 105-128 (1996)

[3.20] C. KESSEL, J. MANICKAM, G. REWOLDT, T. M. TANG, *Improved Plasma Performance in Tokamaks with Negative Magnetic Shear*, Phys. Rev. Lett. **72**, 1212-1215 (1994)

[3.21] T. OZEKI, M. AZUMI, S. ISHIDA, T. FUJITA, *Violation of the Mercier criterion in reversed shear confinement configuration in tokamaks*, Plasma Phys. Control. Fusion **40** (1998) 871-877

[3.22] S. ISHIDA, T. FUJITA, H. AKASAKA, N. AKINO, K. ANNOU, T. AOYAGI, T. ARAI, K. ARAKAWA, M. AZUMI, R. BUDNY, S. CHIBA, O. DA COSTA, N. EBISAWA, T. FUJII, T. FUKUDA, A. FUNAHASI, L. GRISHAM, S. GUNJI, K.

HAMAMATSU, Y. HASEGAWA, T. HATAE, S. HIGASHIJIMA, H. HIRATSUKA, S. HIRAYAMA, A. HONDA, M. HONDA, N. HOSOGANE, H. ICHIGE, S. IDE, Y. IKEDA, M. ISAKA, A. ISAYAMA, N. ISEI, Y. ISHII, N. ISOZAKI, K. ITAMI, T. ITOH, T. IWAHASHI, Y. KAMADA, A. KAMINAGA, T. KASHIWABARA, M. KAWAI, Y. KAWAMATA, Y. KAWANO, D. KAZAMA, M. KAZAMA, M. KIKUCHI, H. KIMURA, T. KIMURA, H. KISHIMOTO, Y. KISHIMOTO, S. KITAMURA, K. KIYONO, K. KODAMA, Y. KOIDE, S. KOKUSEN, T. KONDOH, S. KONOSHIMA, J. KOOG, G. J. KRAMER, H. KUBO, K. KURIHARA, G. KURITA, M. KURIYAMA, Y. KUSAMA, K. MASAKI, T. MATSUDA, T. MATSMOTO, M. MATUKAWA, T. MIURI, N. MIYA, K. MIYACHI, H. MIYATA, Y. MIYO, K. MOGAKI, M. MORI, M. MORIMOTO, S. MORIOKA, S. MORIYAMA, M. NAGAMI, A. NAGASHIMA, K. NAGASHIMA, S. NAGAYA, O. NAITO, Y. NAKAMURA, M. NEMOTO, Y. NEYATANI, T. NISHITANI, N. OGIWARA, T. OHGA, M. OHSAWA, T. OHSHIMA, T. OIKAWA, T. OKABE, J. OKANO, K. OMORI, Y. ONOSE, H. OOHARA, T. OZEKI, M. SAIDOH, M. SAIGUSA, N. SAITO, A. SUKASAI, S. SAKATA, S. SAKURAI, T. SASAJIMA, M. SATO, S. D. SCOTT, M. SEIMIYA, H. SEIKI, M. SEKI, M. SHIMADA, K. SHIMUZU, M. SHIMONO, S. SHINOZAKI, H. SHIRAI, M. SHITOMI, K. SUGANUMA, T. SUGIE, H. SUNAOSHI, M. TAKAHASHI, S. TAKAHASHI, S. TAKEJI, H. TAKENAGA, T. TAKIZUKA, H. TAMAI, M. TERAKADO, K. TOBITA, S. TOKUDA, T. TOTSUKA, Y. TOYOKAWA, N. TOYOSHIMA, K. TSUCHIYA, TSUGITA, Y. TSUKAHARA, T. TUDA, Y. URAMOTO, K. USHIGUSA, K. USUI, J. YAGYU, M. YAMAGIWA, M. YAMAMOTO, T. YAMAMOTO, O. YAMASHITA, K. YOKOKURA, H. YOSHIDA, M. YOSHIDA, R. Yoshino, *Achievement of High Fusion Performance in JT-60U Reversed Shear Discharges*, Phys. Rev. Lett. **79** (1997) 3917-3921

[3.23] R. J. LA HAYE, J. D. CALLEN, T. A. GIANAKON, C. C. HEGNA, L. L. LAO, C. REN, O. SAUTER, E. J. STRAIT, T. S. TAYLOR, H. R. WILSON, *Metastable Beta Limit in DIII-D*, in *Controlled Fusion and Plasma Physics* (Proc. 24th European Physical Society Conference, Berchtesgarten 1997, Europhysics Conference Abstracts, Geneva ,1997) **21A Part III** 1121-1124

[3.24] M. F. F. NAVE, S. ALI-ARSHAD, B. ALPER, B. BALET, H. J. DE BLANK, D. BORBA, C. D. CHALLIS, M. G. VON HELLERMAN, T. C. HENDER, G. T. A. HUYSMANS, W. KERNER, G. J. KRAMER, F. PORCELLI, J. O'ROURKE, L. PORTE, G. J. SADLER, P. SMEUDERS, A. C. C. SIPS, P. M. STUBBERFIELD, D. STORK, R. REICHLE, J. A. WESSON, W. ZWINGMANN, *MHD Activity in JET Hot Ion H-Mode Discharges*, Nucl. Fusion **35** (1995) 409-429

[3.25] D. J. CAMPBELL *et al*, Phys. Rev. Lett. **60,** 2148 (1988)

[3.26] M. N. BUSSAC, R. PELLAT, D. EDERY, J. L. SOULE, Phys. Rev. Lett. **35** (1975) 1638

[3.27] H. LUTJENS, A. BONDESON, G. VLAD, *Ideal MHD Stability of Internal Kinks in Circular and Shaped Tokamaks*, Nucl. Fusion **32** (1992) 1625-1636

[3.28] V. D. SHAFRANOV, Zh. Tech. Fiz. **40**, 241 (1970) [Sov. Phys-Tech Phys **15**, 175 (1970)].

[3.29] VON GOELER, S. STODIEK and N. SAUTHOFF, Phys Rev Lett **33**, 1201 (1974).

[3.30] M. N. ROSENBLUTH, R. Y. DAGAZIAN, P. H. RUTHERFORD, Phys. Fluids **16** (1973) 1894

[3.31] B. COPPI, R. GALVAO, R. PELLAT, M. N. ROSENBLUTH, P. H. RUTHERFORD, Fiz. Plazmy **2**, 961 (1976) [Sov. J. Plasma Phys. **2**, 533 (1976)]

[3.32] B. B. KADOMTSEV, Fiz. Plazmy **1**, 710 (1975) [Sov. J. Plasma Phys. **1**, 389 (1976)].

[3.33] P. A. SWEET, in *Electromagnetic Phenomena in Cosmic Physics*, edited by B. Lenhert (Cambridge Univ. Press, 1958), p.123

[3.34] E. N. PARKER, J. Geophysical Research **62**, 509 (1957)

[3.35] A. F. DANILOV, YU. N. DNESTROVSKI, D. P. KOSTOMAROV and A. M. POPOV, Fiz. Plazmy **2**, 187 (1976) [Sov. J. Plasma Phys. **2**, 93 (1976)]

[3.36] B. V. WADDELL, D. A. MONTICELLO, M. N. ROSENBLUTH, R. B. WHITE, Nucl. Fusion **16** (1976) 528-532; W. PARK, D. A. MONTICELLO, R. B. WHITE, S. C. JARDIN, *Non-linear Saturation of the Internal Kink Mode*, Nucl. Fusion **20** (1980) 1181-1198)

[3.37] G. ARA *et al,* Ann. Phys. **112**, 443 (1978)

[3.38] M.A. DUBOIS, D.A. MARTY, G. POCHELON, *Method of Cartography of q = 1 Islands during Sawtooth Activity in Tokamaks*, Nucl. Fusion **20** (1980) 1355-1362

[3.39] A. W. EDWARDS *et al*, Phys. Rev. Lett. **57**, 210 (1986)

[3.40] H. SOLTWISCH, W. STODIEK, J. MANICKAM and J. SCHLUTER, *Plasma Phys. Contr. Nuclear Fusion Res 1986* (Vienna, IAEA), Vol I, p. 433;
J. O'ROURKE, Plasma Phys. Contr. Fusion **30**, 1475 (1991);
A. WELLER et al, Phys. Rev. Lett. **59**, 2303 (1987);
R. D. GILL, A. W. EDWARDS, D. PASINI, A. WELLER, *Snake-Like Density Perturbations in JET*, Nucl. Fusion **32** (1992) 723-735;
T. OSBORNE et al, Phys Rev. Lett. **49** (1982) 734-737

[3.41] Y. NAGAYAMA, M. YAMADA, W. PARK, E. D. FREDERICKSON, A. C. JANOS, K. M. MCGUIRE, G. TAYLOR, *Tomography of full sawtooth crashes on the Tokamak Fusion Test Reactor*, Phys. Plasmas **3** (1996) 1647-1655

[3.42] F. M. LEVINTON, S. H. BATHA, M. YAMADA, M. C. ZARNSTROFF, Phys. Fluids B **5** (1993) [missing issue!] 2554-

[3.43] D. WROBLEWSKI, L. K. HUANG, H. W. MOOS, Phys. Rev. Lett. **61** (1988), 1724;
H. WEISEN, G. BORG, B. JOYE, J. B. LISTER, Phys. Rev. Lett. **62** (1989), 434.

[3.44] D. J. CAMPBELL, R. D. GILL, C. W. GOWERS, J. A. WESSON, D. V. BARTLETT, C. H. BEST, S. CODA, A. E. COSTLEY, A. EDWARDS, S. E. KISSEL, R. M. NIESTADT, H. W. PIEKAAR, R. PRENTICE, R. T. ROSS, B. J. D. TUBBING, *Sawtooth Activity in Ohmically Heated JET Plasmas*, Nucl. Fusion **26** (1986) 1085-1092

[3.45] J. A. WESSON, A. W. EDWARDS, R. S. GRANETZ, *Spontaneous m = 1 Instability in the JET Sawtooth Collapse*, Nucl. Fusion **31** (1991) 111-116

[3.46] W. PFEIFFER, *Double-Sawtooth Oscillations in the Doublet III Tokamak*, Nucl. Fusion **25** (1985) 673-679

[3.47] D. CAMPBELL and D. PEARSON, empirical scaling laws for the sawtooth period (private communication)

[3.48] J. A. WESSON, Plasma Phys. Contr. Fusion **28**, 243 (1986)

[3.49] S. MIGLIUOLO, *[Review Paper:] Theory of Ideal and Resistive m = 1 Modes in Tokamaks*, Nucl. Fusion **33** (1993) 1721-1754

[3.50] J. F. DRAKE, T. M. ANTONSEN, A. B. HASSAM, N. T. GLADD, *Stabilization of the tearing mode in high-temperature plasma*, Phys. Fluids **26** (1983), 2509-2528

[3.51] F. PORCELLI, S. MIGLIUOLO, *Ion viscosity stabilization of resistive internal kink modes*, Phys. Fluids **29 (1996)**, 1741-1743

[3.52] S. MIGLIUOLO, F. PEGORARO and F. PORCELLI, *Stabilization of collisional drift-tearing modes at the brteakdown of the constant-Ψ approximation,* Phys. Fluids B **3** (1991), 1338-1345

[3.53] S. C. COWLEY, R. M. KULSRUD, T. S. HAHM, *Linear stability of tearing modes*, Phys. Fluids **29** (1986), 3230 -3244

[3.54] F. PORCELLI, *Collisionless m=1 Tearing Mode*, Phys. Rev. Lett. **66** (1991) 425-428

[3.55] L. ZAKHAROV and B. ROGERS, *Two-fluid magnetohydrodynamic description of the internal kink mode in tokamaks*, Phys. Fluids B **4** (1992) 3285-3301

[3.56] F. M. LEVINTON L. ZAHKAROV, S. H. BATHA, J. MANICKAM, M. C. ZARNSTORFF, *Stabilization and Onset of Sawteeth in TFTR*, Phys. Rev. Lett. **72** (1994) 2895-2898

[3.57] F. PORCELLI, Plasma Phys. Contr. Fusion **33**, 1601 (1991), and references therein.

[3.58] K. MCGUIRE et al, Phys.Rev. Lett **50**, 891 (1983)

[3.59] F. PORCELLI, D. BOUCHER and M. N. ROSENBLUTH, *Model for the sawtooth period and amplitude*, Plasma Phys. Control. Fusion **38** (1996), 2163-2186

[3.60] M. D. KRUSKAL and C. R. OBERMAN, Phys.Fluids **1**, 275 (1958)

[3.61] T. M. ANTONSEN and A. BONDESON, *Influence of trapped thermal particles on internal kink modes in high temperature tokamaks*, Phys.Fluids B **5** (1993) 4090-4098

[3.62] G. FOGACCIA, F. ROMANELLI, *On the stability of the internal kink mode in the banana regime*, Phys. Plasmas **2** (1995) 227-240

[3.63] J. A. WESSON, *Sawtooth Reconnection*, Nucl. Fusion **30** (1990) 2545-2549

[3.64] M. OTTAVIANI and F. PORCELLI, *Nonlinear Collisionless Magnetic Reconnection*, Phys. Rev. Lett. **71** (1993) 3802-3805

[3.65] A. Y. AYDEMIR, Phys. Fluids B **4** (1992), *Nonlinear studies of m=1 modes in high-temperature plasmas*, 3469-3470 (1992)

[3.66] L. E. ZAKHAROV, B. ROGERS, S. MIGLIUOLO, Phys. Fluids B **5** (1993) [missing issue!] 2498-

[3.67] R. G. KLEVA, J. F. DRAKE, F. L. WAELBROECK, *Fast reconnection in high temperature plasmas*, Phys. Plasmas **2**, 23 (1995)

[3.68] A. Y. AYDEMIR, J.C. WILEY and D.W. ROSS, *Toroidal studies of sawtootrh oscillations in tokamaks,* Phys. Fluids B **1,** 774-787 (1989)

[3.69] A. J. LICHTENBERG, *Stochasticity as the Mechanism for the Disruptive Phase of the m = 1 Tokamak Oscillations*, Nucl. Fusion **24** (1984) 1277-1289

[3.70] C. G. GIMBLETT and R. J. HASTIE, *Calculation of the post-crash state and 1-1/2 D simulation of sawtooth cycles*, Plasma Phys. Control. Fusion **36** (1994) 1439-1455

[3.71] I. VOITSEKHOVICH, X. LITAUDON, D. MOREAU, T. ANIEL, A. BÉCOULET, M. EBRA, E. JOFFRIN, F. KAZARIAN-VIBERT, Y. PEYSSON, *Thermal Electron Transport in Regimes with Low and Negative Magnetic Shear in Tore Supra*, Nucl. Fusion **37** (1997) 1715-1733

[3.72] V. P. BHATNAGAR, D. F. H. START, J. JACQUINOT, F. CHALAND, A. CHERUBINI, F. PORCELLI, *Local Magnetic Shear Control in a Tokamak via Fast Wave Minority Ion Current Drive: Theory and Experiments in JET*, Nucl. Fusion **34** (1994) 1579-1603

[3.73] F. PERKINS, R. W. HARVEY, M. MAKOWSKI, M. N. ROSENBLUTH, *Prospects for Electron Cyclotron Current Drive Stabilzation of Neoclassical Tearing Modes in ITER*, in *Controlled Fusion and Plasma Physics* (Proceedings 24th European Physical Society Conference, Berchtesgarten 1997, Europhysics Conference Abstracts, Geneva ,1997) **21A Part III** 1017-1020

[3.74] C. MERCIER, *A Necessary Condition for Hydromagnetic Stability of Plasma with Axial Symmetry*, Nucl. Fusion **1** (1960) 47-53

[3.75] F. PORCELLI, M. N. ROSENBLUTH, *Modified Mercier Criterion*, Plasma Phys. Control. Fusion **40** (1998) 481-492

[3.76] Z. CHANG, J. D. CALLEN, E. D. FREDERICKSON, R. V. BUDNY, C. C. HEGNA, K. M. MCGUIRE, M. C. ZARNSTORFF, TFTR GROUP, *Observation of Nonlinear Neoclassical Pressure-Gradient-Driven Tearing Modes in TFTR*, Phys. Rev. Lett. **74** (1995) 4663-4666

[3.77] D. A. GATES, A. M. EDWARDS T. C. HENDER, B. LLOYD, A. W. MORRIS, M. O' BRIEN, D. C. ROBINSON, M. VALOVIC, C. D. WARRICK, G. A. WHITEHURST, H. WILSON, COMPASS-D and RF HEATING TEAMS, *The Effect*

of Current Profile Control on the β-Limit in the COMPASS-D Tokamak, in *Controlled Fusion and Plasma Physics* (Proceedings 22nd European Physical Society Conference, Bournemouth 1995, Europhysics Conference Abstracts, Geneva,1995) **19C Part IV** 117-120

[3.78] R. J. LA HAYE, L. L. LAO, E. J. STRAIT, T. S. TAYLOR, *High Beta Tokamak Operation in DIII-D Limited at Low Density/Collisionality by Resistive Tearing Modes*, Nucl. Fusion **37** (1997) 397-401

[3.79] H. ZOHM, M. MARASCHEK, G. PAUTASSO, M. SCHITTENHELM, S,. SESNIC, M. SOKOLL, W. SUTTROP, M. ALEXANDER, M. BESSENRODT-WEBERPALS, A. BOOZER, H. J. DE BLANK, J. C. FUCHS, J. GERNHARDT, O. GRUBER, T. KASS, M. KAUFMANN, P. T. LANG, K. LACHNER, H. MEISTER, V. MERTENS, R. NEU, F. WÖLFL, ASDEX UPGRADE TEAM, ECRH-TEAM, ICRH-TEAM, NBI-TEAM, *MHD Stability and Disruption Physics in ASDEX Upgrade*, Plasma Phys. Control. Fusion **37** (1995) A313-A324

[3.80] D. A. GATES, B. LLOYD, A. W. MORRIS, G. MCARDLE, M. R. O' BRIEN, M. VALOVIC, C. D. WARRICK, H. R. WILSON, COMPASS-D TEAM, ECRH TEAM, *Neoclassical Islands on COMPASS-D*, Nucl. Fusion **37** (1997) 1593-1606

[3.81] H. ZOHM, D. A. GATES H. R. WILSON, G. GANTENBEIN, O. GRUBER, S. GÜNTER, M. MARASCHEK, A. W. MORRIS, M. SOKOLL, D. WAGNER, ASDEX UPGRADE TEAM and COMPASS-D TEAM, *Neoclassical MHD in ASDEX Upgrade and COMPASS-D*, Plasma Phys. and Control. Fusion **39** (1997) B237-B246

[3.82] G. HUYSMANS, *Neoclassical Tearing Modes in JET*, presentation to the 8th ITER Disruption, Plasma Control and MHD Expert Group Meeting, San Diego,11-14 May 1998 (private communication, 1998)

[3.83] T. OZEKI, *Preliminary Investigation of Neoclassical Tearing Mode in JT-60U,* presentation to the 8th ITER Disruption, Plasma Control and MHD Expert Group Meeting, San Diego,11-14 May 1998 (private communication, 1998)

[3.84] J. D. CALLEN, W. X. QU, K. D. SIEBERT, B. A. CARRERAS, K. C. SHAING, D. A. SPONG, *Neoclassical MHD equations, instabilities and transport in tokamaks*, in *Plasma Physics and Controlled Nuclear Fusion Research 1986* (Proceedings 11th IAEA International Conference, Kyoto), IAEA Vienna 1987, **Vol. 2** 157-166

[3.85] R. CARRERA, R. D. HAZELTINE, M. KOTSCHENREUTHER, *Island bootstrap current modification of the nonlinear dynamics of the tearing mode*, Phys. Fluids **29** (1986) 899-901

[3.86] A. I. SMOLYAKOV, A. HIROSE, E. LAZZARO, G. B. RE, J. D. CALLEN, *Rotating nonlinear islands in a tokamak plasma*, Phys. Plasmas **2** (1995) 1581-1598

[3.87] H. R. WILSON, J. W. CONNOR, R. J. HASTIE, C. C. HEGNA, *Threshold for neoclassical islands in a low collision frequency tokamak*, Phys. Plasmas **3** (1996) 248-265

[3.88] R. FITZPATRICK, *Helical temperature perturbations associated with tearing modes in tokamak plasmas,* Phys. Plasmas **2** (1995) 825-838

[3.89] T. A. GIANAKON, C. C. HEGNA, J. D. CALLEN, *Computational modeling of neoclassical and resistive magnetohydromagnetic tearing modes in tokamaks*, Phys. Plasmas **3** (1996) 4637-4645

[3.90] JET TEAM (presented by G. T. A. HUYSMANS), R. LA HAYE, H. R. WILSON, *Observation of Neoclassical Tearing Modes in JET*, IIAEA-F1-CN-69 EXP3/04, to be presented at the 1998 IAEA Fusion Energy Conference

[3.91] F. L. WAELBROEK, R. FITZPATRICK, *Rotation and Locking of Magnetic Islands*, Phys. Rev. Lett. **78** (1997), 1703-1706

[3.92] Z. CHANG, E. D. FREDERICKSON, J. D. CALLEN, K. M. MCGUIRE, M. G. BELL, R. V. BUDNY, C. E. BUSH, D. S. DARROW, A. C. JANOS, L. C. JOHNSON, H. K. PARK, S. D. SCOTT, J. D. STRACHAN, E. J. SYNAKOWSKI, G. TAYLOR, R. M. WIELAND, M. C. ZARNSTORFF, S. J. ZWEBEN, TFTR TEAM, *Transport Effects of Low (m,n) MHD Modes on TFTR Supershots*, Nucl. Fusion **34** (1994) 1309-1336

[3.93] Z. CHANG, J. D. CALLEN, *Global Energy Confinement Degradation Due to Macroscopic Phenomena in Tokamaks*, Nucl. Fusion **30** (1990) 219-233

[3.94] C. C. HEGNA, J. D. CALLEN, *On the stabilization of neoclassical magnetodynamic tearing modes using localized current drive or heating*, Phys. Plasmas **4** (1997) 2940-2945

[3.95] R. H WEENING, A. BONDESON, Comments on Plasma Phys. **15** (1992) 77;
A. Bondeson, in *Controlled Fusion and Plasma Physics*, Proc. 20th EPS Conf., Lisboa 1993 (European Physical Society, Geneva 1993).

[3.96] C. KESSEL, J. MANICKAM, G. REWOLDT, W. M. TANG, *Improved Plasma Performance in Tokamaks with Negative Magnetic Shear,* Phys. Rev. Lett. **72** (1994) 1212-1215; J. Manickam, M. S. Chance, S. C. Jardin, C. Kessel, D. Monticello, N. Pomphrey, A. Reiman, C. Wang, L. E. Zakharov, *The prospects for magnetohydrodynamic stability in advanced tokamak regimes*, Phys. Plasmas **1** (1994) 1601-1605

[3.97] D. PFIRSCH, H. TASSO, *A theorem on MHD-instability of plasmas with resistive walls*, Nucl. Fusion **11** (1971) 259-260

[3.98] T. H. JENSEN, M. S. CHU, J. Plasma Phys. **30** (1983) 57

[3.99] C. G. GIMBLETT, *On Free Boundary Instabilities Induced by a Resistive Wall,* Nucl. Fusion **26** (1986) 617-625

[3.100] A. BONDESON, M. PERSSON, *Stabilization by Resistive Walls and q-Limit Disruptions in Tokamaks*, Nucl. Fusion **28** (1988) 1887-1891

[3.101] L. E. ZAKHAROV, S. V. , PUTVINSKII, Sov. J. Plasma Phys. **13** (1987) 68.

[3.102] E. J. STRAIT *et al*, in *Plasma Physics and Controlled Nuclear Fusion Research 1988*, Proc. 12th Int. Conf. (IAEA, Vienna 1989), Vol. 1, p. 83.

[3.103] E. J. STRAIT, T. S. TAYLOR, A. D. TURNBULL, J. R. FERRON, L. L. LAO, B. RICE, O. SAUTER, S. J. THOMPSON, D. WRÓBLEWSKI, *Wall Stabilization of High-Beta Tokamak Discharges in DIII-D*, Phys. Rev. Lett. **74** (1995) 2483-2486

[3.104] A. M. GAROFALO, J. BIALEK, M. S. CHU, E. D. FREDERICKSON, R. J. GROEBNER, R. J. LA HAYE, L. L. LAO, G. A. NAVRATIL, B. W. RICE, S. A. SABBAGH, J. T. SCOVILLE, E. J. STRAIT, T. S. TAYLOR, A. D. TURNBULL, DIII-D TEAM, *Study of Resistive Wall Mode in DIII-D*, to be published in Controlled Fusion and Plasma Physics (Proceedings 25th European Physical Society Conference, Prague1998, Europhysics Conference Abstracts, Geneva ,1998)

[3.105] M. S. CHU, J. M. GREENE, T. H. JENSEN, R. L. MILLER, A. BONDESON, R. W. JOHNSON, M. E. MAUEL, *Effect of toroidal plasma flow and flow shear on global magnetohydrodynamic MHD modes*, Phys. Plasmas **2** (1995) 2236-2241

[3.106] M. OKABAYASHI *et al*, in *Plasma Physics and Controlled Nuclear Fusion Research 1988*, Proc. 12th Int. Conf. (IAEA, Vienna 1989), **Vol. 1**, p. 275

[3.107] M. OKABAYASHI, N. POMPHREY, J. MANICKAM, D. J. WARD, R. E. BELL, R. E. HATCHER, R. KAITA, S. M. KAYE, H. W. KUGEL, B. LEBLANC, F. M. LEVINTON, D. W. ROBERTS, S. SESNIC, Y. SUN, H.TAKAKASHI, *Role of the Stabilizing Shell in High-β, Low-q Disruptions in PBX-M*, Nucl. Fusion **36** (1996) 1167-1188

[3.108] A. BONDESON, D. J. WARD, *Stabilization of External Modes in Tokamaks by Resistive Walls and Plasma Rotation*, Phys. Rev. Lett. **72** (1994) 2709-2712

[3.109] D. J. WARD, A. BONDESON, *Stabilization of ideal modes by resistive walls in tokamaks with plasma rotation and its effect on the beta limit*, Phys. Plasmas **2** (1995) 1570-1580

[3.110] D. J. WARD, *The effect of partial poloidal wall sections on the wall stabization of external kink modes*, Phys. Plasmas **3** (1996) 3653-3660

[3.111] R. BETTI, J. P. FREIDBERG, *Stability Analysis of Resistive Wall Kink Modes in Rotating Plasmas*, Phys. Rev. Lett. **74** (1995) 2949-2952

[3.112] N. POMPHREY, S. C. JARDIN, J. BIALEK, M. S. CHANCE, D. A. D'IPPOLITO, J. M. FINN, R. FITZPATRICK, J. L. JOHNSO, C. E. KESSEL, J. MANICKAM, D. A. MONTICELLO, J. R. MYRA, M. ONO, W. PARK, A. H. REIMAN, G. REWOLDT, W. M. TANG, E. J. VALEO, L. E. ZAKHAROV, *MHD Regimes and Feedback Stabilization in Advanced Tokamaks*, in Plasma Physics and Controlled Nuclear Fusion Research 1994 (Proceedings Fifteenth International Conference on Plasma Physics and Controlled Fusion Research, Seville 1994), IAEA Vienna 1995, **Vol. 3** 251-260

[3.113] R. FITZPATRICK, A. Y. AYDEMIR, *Stabilization of the resistive shell mode in tokamaks*, Nucl. Fusion **36** (1996) 11-38

[3.114] A. B. MIKHAILOVSKII, B. N. KUVSHINOV, Plasma Phys. Reports **21** (1995) 802 [Fizika Plazmy **21** (1995) 849].

[3.115] A. BONDESON, M. S. CHU, *Inertia and ion Landau damping of low-frequency magnetohydrodynamical modes in tokamaks*, Phys. Plasmas **3** (1996) 3013-3022

[3.116] J. M. FINN, *Stabilization of ideal plasma resistive wall modes in cylindrical geometry: The effect of resistive layers*, Phys. Plasmas **2** (1995) 3782-3791

[3.117] A. BONDESON, H. X XIE, *Stability of ideal and resistive modes in cylindrical plasmas with resistive walls and plasma rotation*, Phys. Plasmas **4** (1997) 2081-2089

[3.118] R. FITZPATRICK, T. H. JENSEN, *Stabilization of the resistive wall mode using a fake rotating shell*, Phys. Plasmas **3** (1996) 2641-2652

[3.119] C. M. BISHOP, Plasma Phys. Control. Fusion **31** (1989) 1179-xxxx

[3.120] T. H. JENSEN , R. FITZPATRICK, *Resistive Wall Feedback Stabilization*, Phys. Plasmas **4** (1997) 2997-3000

[3.121] T. H. JENSEN, *A study of the efficiency of 'intelligent shells'*, Phys. Plasmas **5** (1998) 192-195

[3.122] M. F. F. NAVE, J. A. WESSON, *Mode Locking in Tokamaks*, Nucl. Fusion **30** (1990) 2575-2583

[3.123] ZOHM H et al, Europhys Lett **11** (1990) 745

[3.124] D. G. GATES, T. C. HENDER, *Resistive Wall Induced Forbidden Bands of Mode Rotation Frequency on the COMPASS-D Tokamak*, Nucl Fusion **36** (1996) 273-282

[3.125] J. A. SNIPES, D. J. CAMPBELL, P. S. HAYNES, T. C. HENDER, M. HUGON, P. J. LOMAS, N. J. LOPES CARDOZO, M. F. F. NAVE, F. C. SCHÜLLER, *Large Amplitude Quasi-Stationary MHD Modes in JET*, Nucl. Fusion **28** (1988) 1085-1097

[3.126] T. C. HENDER, R. FITZPATRICK, A. W. MORRIS, P. G. CAROLAN, R. D. DURST, T. EDDLINGTON, J. FERREIRA, S. J. FIELDING, P. S. HAYNES, J. HUGILL, I. J. JENKINS, R. J. LA HAYE, B. J. PARHAM, D. C. ROBINSON, T. N. TODD, M. VALOVIC, G. VAYAKIS, *Effect of Resonant Magnetic Perturbations on COMPASS-C Tokamak Discharges*, Nucl. Fusion **32** (1992) 2091-2117

[3.127] J. T. SCOVILLE, R. J. LA HAYE, A. G. KELLMAN, T. H. OSBORNE, R. D. STAMBAUGH, E. J. STRAIT, T. S. TAYLOR, *Locked Modes in DIII-D and a Method for Prevention of the Low Density Mode*, Nucl. Fusion **31** (1991) 875-890

[3.128] G. M. FISHPOOL , P. S. HAYNES, *Error Field Instabilities in JET*, Nucl. Fusion **34** (1994) 109-119

[3.129] D. E. ROBERTS, D. SHERWELL, J. D. FLECTCHER, G. NOTHNAGEL, J. A. M. DE VILLIERS, *Major Disruptions Induced by Helical Coils on the Tokoloshe Tokamak*, Nucl. Fusion **31** (1991) 319-340

[3.130] R. YOSHINO, Y. NEYATANI, N. ISEI, Y. KOIDE, Y. KAWANO, A. TANGA, D. J. CAMPBELL, M. F. JOHNSON, L. ROSSI, *Disruption Amelioration Experiments in JT-60U and JET*, in Plasma Physics and Controlled Nuclear Fusion Research (Proceedings 15th IAEA Conference, Seville 1994) IAEA Vienna (1995), **Vol 1** 685-695

[3.131] R. FITZPATRICK, T. C. HENDER, *The interaction of resonant magnetic perturbations with rotating plasmas*, Phys. Fluids B **3** (1991) 644-673

[3.132] M. DE BENDETTI, R. J. BUTTERY, D. GATES, T. C. HENDER, E. LAZZARO, P. LEAHY, A. W. MORRIS, F. RIMINI, A. SANTAGIUSTINA, B. TUBBING, *Plasma interaction with error fields on JET and COMPASS-D,* to be published in Controlled Fusion and Plasma Physics (Proceedings 25th European Physical Society Conference, Prague 1998, Europhysics Conference Abstracts, Geneva,1998)

[3.133] T. H. JENSEN, A. W. LEONARD, R. J. LA HAYE, M. S. CHU, *Effects of plasma flow on error field islands*, Phys. Fluids B **3** (1991) 1650-1656

[3.134] R. FITZPATRICK, *Interaction of Tearing Modes with External Structures in Cylindrical Geometry*, Nucl. Fusion **33** (1993) 1049-1084

[3.135] R. FITZPATRICK, T. C. HENDER, *Effect of a static external magnetic perturbation on resistive mode stability in tokamaks*, Phys. Plasmas **1** (1994) 3337-3355

[3.136] R. J. LA HAYE, J. T. SCOVILLE, *A method to measure poloidal field coil irregularities in toroidal plasma devices*, Rev. Sci. Instrum. **62** (1991) 2146

[3.137] J. W. CONNOR , J. B. TAYLOR, *Scaling Laws for Plasma Confinement*, Nucl. Fusion **17** (1977) 1047-1056

[3.138] R. J. LA HAYE, A. W. HYATT, J. T. SCOVILLE, *Non-linear Instability to Low m,n = 1 Error Fields in DIII-D as a Function of Plasma Fluid Rotation and Beta*, Nucl. Fusion **32** (1992) 2119-2126.

[3.139] R. T. CROSSLAND, R. J. HAYWARD, T. N. TODD, P. S. HAYNES, J. W. HILL, A. W. MORRIS, P. NICHOLSON, R. A. CROOK, *COMPASS TF coil dynamic vertical preload device and PF coil alignment using a fixed coil array*, in *Fusion Technology 1990* [Proceedings of the 16th Symposium on Fusion Technology (SOFT), London 1990], Pergammon Press, Oxford (1991) **Vol. 1** 632-635

[3.140] R. J. BUTTERY, D. J. CAMPBELL, M. DE BENEDETTI, D. GATES, T. C. HENDER, P. LEAHY, A. W. MORRIS, A. SANTAGUISTINA, B. TUBBING, JET TEAM, COMPASS-D TEAM, *Error Field Thresholds, Harmonics and Scaling Studies on JET and COMPASS-D and Implications for ITER*, in Controlled Fusion and Plasma Physics (Proceedings 24th European Physical Society Conference, Berchtesgarten 1997, Europhysics Conference Abstracts, Geneva ,1997) **21A Part I** 265-269.

[3.141] P. G. CAROLAN, A. M. EDWARDS, R. FITZPATRICK, C. G. GIMBLETT, T. C. HENDER, A. W. MORRIS, R. O'CONNELL, J. V. SCANLAN, *Correction of Error Field Locked Modes in COMPASS-D*, in Controlled Fusion and Plasma Physics (Proceedings 24th European Physical Society Conference, Montpellier 1994, Europhysics Conference Abstracts, Geneva ,1994) **18B Part I** 214-127

[3.142] R. J. LA HAYE, *Physics of Locked Modes in ITER*, *Error Field Limits, Rotation for Obviation and Measurement of Field Errors*, General Atomics Report GA-A22468 (1997)

[3.143] A. SANTAGIUSTINA, S. ALI ARSHAD, D. J. CAMPBELL, G. D`ANTONA, M. DE BENEDETTI, A. M. EDWARDS, G. FISHPOOL, E. LAZZARO, R. J. LA HAYE, A. W. MORRIS, R. ÖSTRÖM, L. ROSSI, F. SARTORI, P. SAVRUKHIN, M. TABELLINI, B. J. TUBBING, A. TANGA, G. ZULLO, *Studies of Tearing Mode Control in JET*, in Controlled Fusion and Plasma Physics (Proceedings 22nd European Physical Society Conference, Bournemouth 1995, Europhysics Conference Abstracts, Geneva,1995) **19C Part IV** 461-464

[3.144] F. WAGNER, G. BECKER, K. BEHRINGER et al, Phys. Rev. Lett. **49** (1982) 1408-1411

[3.145] M. F. F. NAVE, P. SMEULDERS, T. C. HENDER, P. J. LOMAS, B. ALPER, P. BAK, B. BALET, J. P. CHRISTIANSEN, S. CLEMENT, H. P. L. DE ESCH, N. HAWKES, G. T. A. HUYSMANS, T. T. C. JONES, R. KÖING, K. LAWSON, J. LINERTAT, A. MAAS, F. B. MARCUS, D. P. O'BRIEN, A. ROOKES, R. SARTORI, M. F. STAMP, B. SCHUNKE, P. R. THOMAS, K. THOMSEN, *An Overview of MHD Activity at the Termination of JET Hot Ion Modes*, Nucl. Fusion **37** (1997) 809-824

[3.146] M. F. F. NAVE, G. T. A. HUYSMANS, B. BALET, B. DE ESCH, R. GIANELLA, C. GOWERS, T. JONES, R. KONIG, P. LOMAS, V. V. PARAIL, F. RIMINI, B. SCHUNKE, P. THOMAS, *Discharge optimisation and the control of MHD modes*, in *Controlled Fusion and Plasma Physics* (Proceedings 24th European Physical Society Conference, Berchtesgarten 1997, Europhysics Conference Abstracts, Geneva ,1997) **21A Part I** 1-4

[3.147] SUTTROP W et al 1996 *Proc 23rd EPS Conf (Kiev)* Vol **I** p 47

[3.148] T. KASS, S GÜNTER, M. MARASCHEK, W. SUTTROP, H. ZOHM, ASDEX UPGRADE TEAM, *Characteristics of type I and type III ELM precursors in ASDEX Upgrade,* in Controlled Fusion and Plasma Physics (Proceedings 24th European Physical Society Conference, Berchtesgarten 1997, Europhysics Conference Abstracts, Geneva ,1997) **21A Part IV** 1521-1524

[3.149] Y. KAMADA, K. USHIGUSA, O. NAITO, Y. NEYATANI, S. ISHIDA, T. FUJITA, R. YOSHINO, M. KIKUCHI, M. MORI, H. NINOMIYA, *ELMy H-mode with high-β_N and high-β_p in JT-60U*, Plasma Phys. Control. Fusion **36** (1994) A123-A128

[3.150] H. ZOHM, T. H. OSBORNE, K. H. BURRELL, M. S. CHU, E. J. DOYLE, P. GOHIL, D. N. HILL, L. L. LAO, A. W. LEONARD, T. S. TAYLOR, A. D. TURNBULL, *ELM Studies on DIII-D and a Comparison with ASDEX Results*, Nucl. Fusion **35 (**1995) 543-550

[3.151] T. H. OSBORNE, R. J. GROEBNER, L. L. LAO, A. W. LEONARD, R. MAINGI, R. L. MILLER, G. D. PORTER, D. M. THOMAS, R. E. WALTZ, *Scaling of ELM and H-mode pedestal characteristics in ITER shaped discharges in the DIII-D tokamak,* in *Controlled Fusion and Plasma Physics* (Proceedings 24th European Physical Society Conference, Berchtesgarten 1997, Europhysics Conference Abstracts, Geneva ,1997) **21A Part III** 1101-1104

[3.152] R. L. MILLER, Y. R. LIN-LIU, T. H. OSBORNE, T. S. TAYLOR, *Ballooning mode stability for self-consistent pressure and current profiles at the H-mode edge*, in

Proceedings of 6th IAEA Technical Committee Meeting on H-mode Physics, Kloster Seeon 1997, Plasma Phys. Control. Fusion **40** (1998) 753-756

[3.153] JET TEAM (presented by M. KEILHACKER), *Latest JET results in deuterium and deuterium-tritium plasmas,* Plasma Phys. Control. Fusion **39** (1997) B1-B18

[3.154] J. A. SNIPES, R. S. GRANETZ, M. GREENWALD, A. E. HUBBARD, I. H. HUTCHINSON, J. IRBY, J. KESNER, S. MIGLUOLO, T. SUNN PEDERSON, J. RAMOS, J. RICE, P. C. STEK, Y. TAKASE, S. M. WOLFE, *ELMs and fast edge fluctuations in Alcator C-Mod*, in *Proceedings of 6th IAEA Technical Committee Meeting on H-mode Physics, Kloster Seeon 1997*, Plasma Phys. Control. Fusion **40** (1998) 765-770

[3.155] H. WEISEN, M. J. DUTCH, F. HOFMANN, Y. MARTIN, J-M MORET, C. NIESWAND, Z. A. PIETRZYK, R. A. PITTS, A. POCHELON, *Effect on confinement of edge-localized-modes in TCV*, Plasma Phys. Control. Fusion **38** (1996) 1415-1419

[3.156] S. J. FIELDING, J. D. ASHALL, P. G. CAROLAN, A. COLTON, D. GATES, J. HUGILL, A. W. MORRIS, M. VALOVIC, COMPASS-D TEAM, ECRH-TEAM, *The H-mode in COMPASS-D*, Plasma Phys. Control. Fusion **38** 1091-1102

[3.157] S. M. KAYE, J. L. DUNLOP, T. S. HAHM, S. SESNIC, W. TANG, J. H. HARRIS, P. RONEY, W. DAVIS, *ELM-related fluctuations in PBX-M H-modes*, Plasma Phys. Control. Fusion **36** (1994) A135-A140

[3.158] W KERNER, O. POGUTSE, R. VAN DER LINDEN, *Ideal interchange instability near the separatrix in the SOL and its relation to ELMs*, Plasma Phys. Control. Fusion **39** (1997) 757-778

[3.159] JET TEAM (presented by G. C. VLASES, *Effect of divertor configuration on plasma performance in JET*, in *Fusion Energy 1996* (Proceedings 16th IAEA Conference, Montreal 1996), IAEA Vienna (1997) **Vol. 1** 371-383

[3.160] W. SUTTROP, O. GEHRE, J. C. FUCHS, H. REIMERDES, W. SCHNEIDER, J. SCHWEINER, ASDEX UPGRADE TEAM, *Effects of type-I edge-localised modes on transport in ASDEX Upgrade*, in *Proceedings of 6th IAEA Technical Committee Meeting on H-mode Physics, Kloster Seeon 1997*, Plasma Phys. Control. Fusion **40** (1998) 771-774

[3.161] M. SUGIHARA, presentation to the ITER Divertor Database Expert Group Meeting March 1997

[3.162] E. GAUTHIER, A. CHANKIN, S. CLEMENT, P. COAD, S. DAVIES, G. FISHPOOL, J. LINGERTAT, G. MATTEWS, *ELM Dynamics and Power Deposition in the JET Divertor*, in *Controlled Fusion and Plasma Physics* (Proceedings 24nd European Physical Society Conference, Berchtesgarten 1997, Europhysics Conference Abstracts, Geneva ,1997) **21A Part I**, 61-64

[3.163] A. JANOS, J. HASTIE, K. MCGUIRE, E. FREDERICKSON, *Bursts of electron cyclotron emission during ELMs and high β disruptions in TFTR,* 1996 Plasma Phys. Control. Fusion **38** 1373-1979

[3.164] K. NAGASHIMA, T. SHOJI, Y. MIURA, *Investigation of Edge Localized Mode in the JFT-2M Tokamak*, Nucl. Fusion **36** (1996) 335-345

[3.165] R. J. BUTTERY, D. A. GATES, A. COLTON, H. DE BLANK, S. J. FIELDING, T. C. HENDER, A. W. MORRIS, M. MARASCHEK, M. SCHITTENHELM, W. SUTTROP, M. VALOVIC, *ELM Related MHD Activity on the COMPASS-D Tokamak Compared with ASDEX-Upgrade*, in *Controlled Fusion and Plasma Physics* (Proceedings 22nd European Physical Society Conference, Bournemouth 1995), Europhysics Conference Abstracts, Geneva ,1995 **19C Part III** 273-277

[3.166] S. ALI-ARSHAD, D. CAMPBELL, A. COLTON, P. CRIPWELL, L. DE KOCK, G. J. KRAMER, M. F. F. NAVE, G. F. NEILL, *ELM Precursors in JET*, in *1992 International Conference on Plasma Physics* (Proceedings 19th EPS Conference on Controlled Fusion and Plasma Physics, Innsbruck 1992), Europhysics Conference Abstracts, Geneva, 1992 **16C Part I** 227-230

[3.167] GILL R D et al 1996 *Proc 23rd EPS Conf (Kiev)* Vol **1** p167;
M. F. F. NAVE, B. ALPER, P. SMEULDERS, S. ALI-ARSHAD et al, Observations of MHD activity in JET high-performance plasmas, in *Proceedings International Conference on Plasma Physics, Foz Do Iguacu Brazil, 1994*, AIP Conference Proceedings **345** (1995) 58-65

[3.168] A. L. COLTON, R. J. BUTTERY, S. J. FIELDING, D. A. GATES, T. C. HENDER, J. HUGILL, A. W. MORRIS, M. VALOVIC, COMPASS-D TEAM, ECRH TEAM, *ELM studies in the COMPASS-D tokamak*, Plasma Phys. Control. Fusion **38** (1996) 1359-1365

[3.169] M VALOVIC, M. EDWARDS, D. GATES, S. J. FIELDING, T. C. HENDER, J. HUGILL, A. W. MORRIS, COMPASS TEAM, *L-H Transitions and ELMs on COMPASS-D*, in *Proccedings 21st EPS Conference on Controlled Fusion and Plasma Physics, Montpellier 1994*, Europhysics Conference Abstracts, Geneva, 1994, **18B Part I** 318-321

[3.170] H. REIMERDES, A. POCHELON, W. SUTTROP, PH. GUITTIENNE, H. WEISEN, *Toroidally Asymmetric ELM precursor oscillations in the TCV tokamak,* in *Controlled Fusion and Plasma Physics* (Proceedings 24th European Physical Society Conference, Berchtesgarten 1997, Europhysics Conference Abstracts, Geneva ,1997) **21A Part II** 533-537

[3.171] M. HIRSCH, E. HOLZHAUER, J. BALDZUHN, R. BRAKE, S. FIEDLER, T. GEIST, P. GRIGULL, H. J. HARTFUß, J. HOFMANN, R. JAENICKE, J. KOPONEN, F. WAGNER, A. WELLER, H. WOBRIG, W7-AS TEAM, *Dynamic behaviour of the H-mode transport barrier in W7-AS stellarator,* in *Controlled Fusion and Plasma Physics* (Proceedings 24th European Physical Society Conference, Berchtesgarten 1997, Europhysics Conference Abstracts, Geneva ,1997) **21A Part III** 1601-1604

[3.172] J. W. CONNOR, *A review of models for ELMs [Review article]*, Plasma Phys. Control. Fusion **40** (1998) 191-213; also J. W. Conner, *Edge-localised-modes — physics and theory*, in *Proceedings of 6th IAEA Technical Committee Meeting on H-mode Physics, Kloster Seeon 1997*, Plasma Phys. Control. Fusion **40** (1998) 531-542.

[3.173] J. MANICKAM, *The role of edge current density on kink mode stability and its implication for magnetohydrodynamic activity associated with edge localized modes*, Phys Fluids B **4** (1992) 1901-1908

[3.174] G. T. A. HUYSMANS, H. J. DE BLANK, W. KERNER, J. P. GOEDBLOED, M. F. F. NAVE, *MHD Stability Modes of Edge Localized Modes in JET Discharges*, in *1992 International Conference on Plasma Physics* (Proceedings 19th EPS Conference on Controlled Fusion and Plasma Physics, Innsbruck 1992), Europhysics Conference Abstracts, Geneva, 1992 **16C Part I** 247-251

[3.175] J. W. CONNOR, R. J. HASTIE, H. R. WILSON, R. L. MILLER, *Magnetodynamic stability of tokamak edge plasmas*, Phys. Plasms **5** (1998) 2687-2700; also
J. W. CONNOR and H. R. WILSON, in *Theory of Fusion Plasmas* (eds J. W. Connor, E. Sindoni and J. Vaclavik), Editrice Compositori, Bologna 1997, 441

[3.176] O. POGUTSE, J. G. CORDEY, W. KERNER, B. SCHUNKE, *Edge Modes as ELM Events*, in *Controlled Fusion and Plasma Physics* (Proceedings 22nd European Physical Society Conference, Bournemouth 1995, Europhysics Conference Abstracts, Geneva ,1995) **19C Part I** 277-280

[3.177] ASDEX TEAM, *The H-Mode of ASDEX*, Nucl. Fusion **29** (1989) 1959-2040

[3.178] G. T. A. HUYSMANS, C. D. CHALLIS, M. ERBA, W. KERNER, V. V. PARAIL, *Influence of edge Currents an Pressure Gradients on the MHD Stability of Low-n External Kink Modes,* in *Controlled Fusion and Plasma Physics* (Proceedings 24th European Physical Society Conference, Bournemouth 1995, Europhysics Conference Abstracts, Geneva ,1995) **19C Part I** 201-204

[3.179] Y-T LAU, *A linear analysius for edge-localized mode precursors*, Plasma Phys. Control. Fusion **38** (1996) 1393-1396

[3.180] S-I. ITOH, K. ITOH, A. FUKUYAMA, Y. MIURA, JFT-2M GROUP, *Edge Localized Mode Activity as a Limit Cycle in Tokamak Plasmas*, Phys. Rev. Lett. **67** (1991) 2485-2488

[3.181] H. ZOHM, ASDEX-UPGRADE TEAM, [ASDEX-UPGRADE] NI and ICRH GROUp, *Dynamic Behavior of the L-H Transition*, Phys. Rev. Lett **72** (1994) 222-225

[3.182] I. A. VOJTSEKHOVICH, A. YU. DNESTROVSKIJ, V. V. PARAIL, *Self-Consistent Description of L-H Mode Transition Dynamics in Tokamaks*, Nucl. Fusion **35** (1995) 631-640

[3.183] V. B. LEBEDEV, P. H. DIAMOND, I. GRUZINOVA, B. A. CARRERAS, *A minimal dynamical model of edge localized mode phenomena*, Phys. Plasmas **2** (1995) 3345-3359

[3.184] S-I. ITOH, K. ITOH, A. FUKUYAMA, M. YAGI, *Edge Localized Modes as New Bifurcation in Tokamaks*, 1996 Phys. Rev. Lett. **76** 920-923

[3.185] S-I. ITOH, S. TODA, M. YAGI, K. ITOH, A. FUKUYAMA, *Physics of collapses: probabilistic occurrence of ELMs and crashes*, in *Proceedings of 6th IAEA Technical Committee Meeting on H-mode Physics, Kloster Seeon 1997*, Plasma Phys. Control. Fusion **40** (1998) 737-740

[3.186] O. POGUTSE, W. KERNER, V. GRIBKOV, S. BAZDENKOV, M. OSIPENKO, *The resistive interchange convection in the edge of tokamak plasmas* Plasma Phys. Control. Fusion **36** (1994) 1963-1985

[3.187] W. HORTON, G. HU, G. LAVAL, *Turbulent Ttransport in mixed states of convective cells and sheared flows,* Phys. Plasmas **3** (1996) 2912-2933

[3.188] T. S. TAYLOR, *Physics of advanced tokamaks*, Plasma Phys. Controlled Fusion **39** B47-B73 (1997)

[3.189] D. BOUCHER, Y. BARANOV, B. FISCHER, X. LITAUDON, D. MOREAU, W. M. NEVINS, V. PARAIL, F. X. SÖLDNER, I. VOITSEKHOVITCH, ITER JOINT CENTRAL TEAM, ITER HOME TEAMS, *ITER Scenarios Including Non-Inductive Steady-State Operation*, in *Fusion Energy 1996* (Proceedings 16th IAEA Conference, Montreal 1996, IAEA Vienna 1997) **Vol. 2** 945-952

[3.190] S. A. SABBAGH, R. A. GROSS, M. E. MAUEL, G. NAVRATIL, M. G. BELL, M. BITTER, N. BRETZ, R. V. BUDNY, C. E. BUSH, M. CHANCE, P. EFTHIMION, E. D. FREDRICKSON, R. HATCHER, R. J. HAWRYLUK, S. P. HIRSHMAN, A. JANOS, S. JARDIN, D. JASSBY, J. MANICKAM, D. MCCUNE, K. M. MCGUIRE, S. MEDLEY, D. MUELLER, Y. NAGAYAMA, D. K. OWENS, M. OKABAYASHI, H. PARK, A. RAMSEY, B. STRATTON, E. SYNAKOWSKI, G. TAYLOR, R. WEILAND, M. C. ZARNSTORFF, J. KESNER, E. S. MARMAR, J. L. TERRY, *High poloidal beta in the Tokamak Fusion Test Reactor limited by a natural inboard poloidal field null,* Phys. Fluids B **3** (1991) 2277-2284

[3.191] M. E. MAUEL, G. A. NAVRATIL, S. A. SABBAGH, S. H. BATHA, M. G. BELL, R. V. BUDNY, C. E. BUSH, A. CAVALLO, M. S. CHANCE, C. Z. CHENG, P. C. EFTHIMION, E. D. FREDEREICKSON, G. Y. FU, R. J. HAWRYLUK, A. C. JANOS, D/ L. JASSBY, F. LEVINTON, J. MANICKAM, D. C. MCCUNE, K. M. MCGUIRE, S. S. MEDLEY, D. R. MIKKELSEN, D. MUELLER, Y. NQAGAYAMA, D. K. OWENS, H. K. PARK, A. T. RAMSEY, B. C. STRATTON, E. J. SYNAKOWSKI, G. TAYLOR, R. M. WIELAND, M. YAMADA, M. C. ZARNSTORFF, S. J. ZWEBEN, *Achieving high fusion reactivity in high poloidal beta discharges in TFTR*, in *Plasma Physics and Controlled Nuclear Fusion Research 1994* (Proceedings Fourteenth International Conference on Plasma Physics and Controlled Fusion Research, Würzburg 1992), IAEA Vienna 1993, **Vol. 1** 205-218

[3.192] Y. KAMADA, K. USHIGUSA, Y. NEYATANI,). NAITO, T. OZEKI, Y. KAWANO, R. YOSHINO, H. KUBO, T. FUJITA, S. ISHIDA, M. SATO, Y. KOIDE, S. TAKEJI, S. SAKURAI, K. TSUCHIYA, J. MANICKAM, M. MATSUOKA, M. KIKUCHI, M. MORI, H. NINOMIYA, M. AZUMI, JT-60U TEAM, *Steady-State High Performance in JT-60U*, in *Plasma Physics and Controlled Nuclear Fusion Research 1994* (Proceedings Fifteenth International Conference on Plasma Physics and Controlled Fusion Research, Seville 1994), IAEA Vienna 1995, **Vol. 1** 651-661

[3.193] J. R. FERRON, L. L. LAO, T. S. TAYLOR, Y. A. KIM, E. J. STRAIT, D. WROBLEWSKI, *Improved Confinement and Stability in the DIII-D Tokamak Obtained Through Modification of the Current Profile,* Phys. Fluids B **5** (1993) 2532-2539

[3.194] G. T. HOANG, C. GIL, E. JOFFRIN, D. MOREAU, A. BECOULET, P. BIBET, J. P. BIZARRO, R. V. BUNDY, J. CARRASCO, J. P. COULON, C. DE MICHELIS, T. DUDOK DE WIT, P. MONIER-GARBET, M. GONICHE, R. GUIRLET, T. HUTTER, S. M. KAYE, J. LASALLE, L. LAURENT, P. LECOUSTEY, X. LITAUDON, M. MATTIOLI, Y. PEYSSON, A.-L. PECQUET, G. REY, S. A. SABBAGH, B. SAOUTIC, G. TONON, J. C. VALLET, *Improved Confinement in High l_i Lower Hybrid Driven Steady State Plasmas in Tore Supra*, Nucl. Fusion **34** (1994) 75-85

[3.195] X. LITAUDON, R. ARSLANBEKOV, G. T. HOANG, E. JOFFRIN, F. KAZARIAN-VIBERT, D. MOREAU, Y. PEYSSON, P.BIBET, P. FROISSARD, M. GONICHE, G. REY, J FERRON, K. KUPFER, Plasma Phys. Controlled Fusion **38** (1996) 1603-1626

[3.196] S. IDE, O. NAITO, T. FUJITA, T. OIKAWA, M. SEKI, JT-60 TEAM, *Application of LHCD to Sustainment and Control of a Reversed Magnetic Shear Plasma in JT-60U*, in *Fusion Energy 1996* (Proceedings 16th IAEA Conference, Montreal 1996, IAEA Vienna 1997) **Vol. 3** 253-264

[3.197] S. IDE, T. FUJITA, O. NAITO, M. SEKI, *Sustainment and modification of reversed magnetic shear by LHCD on JT-60U*, Plasma Phys. Controlled Fusion, **38 (1996)** 1645-1652

[3.198] JET TEAM (presented by C. GORMEZANO), *Optimisation of JET Plasmas with Current Profile Control*, in *Fusion Energy 1996* (Proceedings 16th IAEA Conference, Montreal 1996, IAEA Vienna 1997) **Vol. 1** 487-495

[3.199] F. M. LEVINTON, M. C. ZARNSTORFF, S. H. BATHA, M. BELL, R. E. BELL, R. V. BUDNY, C. BUSH, Z. CHANG, E. D. FREDRICKSON, A. JANOS, J. MANICKAM, A. RAMSEY, S. A. SABBAGH, G. L. SCHMIDT, E. J. SYNAKOWSKI, G. TAYLOR, *Improved Confinement with Reversed Magnetic Shear in TFTR*, Phys. Rev. Lett. **75** (1995) 4417-4420

[3.200] E. J. STRAIT, L. L. LAO, M. E. MAUEL, B. W. RICE, T. S. TAYLOR, K. H. BURRELL, M. S. CHU, E. A. LAZARUS, T. H. OSBORNE, S. J. THOMPSON, A. D. TURNBULL, *Enhanced Confinement and Stability in DIII-D Discharges with Reversed Magnetic Shear*, Phys. Rev. Lett. **75** (1995), 4421-4424

[3.201] T. FUJITA, S. IDE, H. SHIRAI, M. KUKUCHI, O. NAITIO, Y. KOIDE, S. TAKEJI, H. KUBO, S. ISHIDA, *Internal Transport Barrier for Electrons in JT-60U Reversed Shear Discharges*, Phys. Rev. Lett. **78** (1997), 2377-2380

[3.202] M. G. BELL, S. BATHA, M. BEER, R. E. BELL, A. BELOV, H. BERK, S. BERNABEI, M. BITTER, B. BREIZMANN, N. L. BRETZ, R. BUDNY, C. E. BUSH, J. CALLEN, S. CAUFFMAN, C. S. CHANG, Z. CHANG, C. Z. CHENG, D. S. DARROW, R. O. DENDY, W. DORLAND, H. DOUNG, P. C. EFTHIMION, D. ERNST, H. EVENSON, N. J. FISCH, R. FISHER, R. J. FONCK, E. D. FREDEREICKSON, G. Y. FU, H. P. FURTH, N. N. GORELENKOV, V. YA. GOLOBOROD'KO, B. GREK, L. R. GRISHAM, G. W. HAMMETT, R. J. HAWRYLUK, W. HEIDBRINK, H. W. HERMANN, M. C. HERRMANN, K. W. HILL, J. HOGANM, B. HOOPER, J. C. HOSEA, W. A. HOULBERG, M. HUGHES, D. L. JASSBY, F. C. JOBES, D. W. JOHNSON, R. KAITA, S. KAYE, J. KESNER, J. S. KIM, M. KISSICK, A. V. KRASILNIKOV,

H. KUGEL, A. KUMAR, N. T. LAM, P. LAMARCHE, B. LEBLANC, F. M. LEVINTON, C. LUDESCHER, J. MACHUZAK, R. P. MAJESKI, J. MANICKAM, D. K. MANSFIELD, M. MAUEL, E. MAZZUCATO, J. MCCHESNEY, D. C. MCCUNE, G. MCKEE, K. M. MCGUIRE, D. M. MEADE, S. S. MEDLEY, D. R. MIKKELSEN, S. V. MIRNOV, D. MUELLER, Y. NAGAYAMA, G. A. NAVRATIL, R. NAZIKIAN, M. OKABAYASHI, M. OSAKABE, D. K. OWENS, H. K. PARK, W. PARK, S. F. PAUL, M. P. PETROV, C. K. PHILLIPS, M. PHILLIPS, P. PHILLIPS, A. T. RAMSEY, B. RICE, M. H. REDI, G. REWOLDT, S. REZNIK, A. L. ROQUEMORE, J. ROGERS, E. RUSKOV, S. A. SABBAGH, M. SASAO, G. SCHILLING, G. L. SCHMIDT, S. D. SCOTT, I. SEMENOV, T. SENKO, C. H. SKINNER, T. STEVENSON, E. J. STRAIT, B. C. STRATTON, J. D. STRACHAN, W. STODIEK, E. SYNAKOWSKI, H. TAKAHASHI, W. TANG, G. TAYLOR, M. E. THOMPSON, S. VON GOELER, A. VON HALLE, R. T. WALTERS, S. WANG, R. WHITE, R. M. WIELAND, M. WILLIAMS, J. R. WISLON, K. L. WONG, G. A. WURDEN, M. YAMADA, V. YAVORSKI, K. M. YOUNG, L. ZAKHAROV, M. C. ZARNSTORFF, S. J. ZWEBEN, *Deuterium-tritium plasmas in novel regimes in the Tokamak Fusion Test Reactor*, Phys. Plasmas **4** (1997) 1714-1724

[3.203] E. A. LAZARUS, M. S. CHU, J. R. \FERRON, F. J. HELTON, J. T. HOGAN, A. G. KELLMAN, L. L. LAO, J. B. LISTER, T. H. OSBORNE, R. SNIDER, E. J. STRAIT T. S. TAYLOR, *Higher beta a higher elongation in the DIII-D tokamak*, Phys. Fluids B **3** (1991) 2220-2229

[3.204] S. A. SABBAGH, E. D. FREDRICKSON, D. K. MANSFIELD, M. G. BELL, S. H. BATHA, R. E. BELL, R. V. BUDNY, C. E. BUSH, Z. CHANG, R. J. HAWRYLUK, D. W. JOHNSON. F. M. LEVINTON, J. MANICKAM, K. M. MCGUIRE, D. MUELLER, F. PAOLETTI, H. K. PARK, A. T. RAMSEY, C. H. SKINNER, E. J. SYNAKOWSKI, H. TAKAHASHI, G. TAYLOR, L. E. ZAKHAROV, M. C. ZARNSTORFF, *Deuterium-Tritium TFTR Plasmas with High-Internal Inductance*, in *Fusion Energy 1996* (Proceedings 16th IAEA Conference, Montreal 1996, IAEA Vienna 1997) **Vol. 1** 921-930

[3.205] T. OZEKI, M. AZUMI, T. TSUNEMATSU, K. TANI *et al.*, *Profile control for a stable high β_p tokamak with a large bootstrap current*, in Plasma Physics and Controlled Nuclear Fusion Research 1992 (Proceedings 14th IAEA Conference, Würzburg 1992, IAEA Vienna 1993) **Vol. 2** 187-194

[3.206] A. D. TURNBULL, T. S. TAYLOR, Y. R. LIN-LIU, H. ST. JOHN, *High Beta and Enhanced Confinement in a Second Stable Core VH-Mode Advanced Tokamak*, Phys Rev. Lett. **74 (**1995) 718-721

[2.207] L. LAO, K. H. BURRELL, T. S. CASPER, V. S. CHAN, M. S. CHU, J. C. DEBOO, E. J. DOYLE, R. D. DURST, C. B. FOREST, C. M. GREENFIELD, R. J. GROEBNER, F. L. HINTON. Y. KAWANO, E. A. LAZARUS, Y. R. LIN-LIU, M. E. MAYEL, W. H. MEYER, R. L. MILLER, G. A. NAVRATIL, T. H. OSBORNE, Q. PENG, C. L. RETTIG, G. REWOLDT, T. L. RHODES, B. W. RICE, D. P. SCHISSEL, B. W. STALLARD, E. J. STRAIT, W. M. TANG, T. S. TAYLOR, A. D. TURNBULL, R. E. WALTZ, DIII-D TEAM, *Rotational and magnetic shear stabilization of magnetodynamic modes and turbulence in DIII-D high performance discharges*, Phys. Plasmas **3** (1996) 1953-1958

[3.208] E. D. FREDRICKSON, S. A. SABBAGH, M. G. BELL, D. MANSFIELD, S. BATHA, Z. CHANG, F. LEVINTON, K. M. MCGUIRE, M. OKABAYASHI, G. TAYLOR, H. TAKAHASI, M. HUGHES, J. MANICKAM, M. PHILLIPS, L. ZAKHAROV, *The stability of advanced operational regimes on the Tokamk Fusion Test Reactor,* Phys. Plasmas **4** (1997) 1589-1595

[3.209] J. MANICKAM, N. POMPHREY, A. M. M. TODD, *Ideal MHD Stability Properties of Pressure Driven Modes in Low Shear Tokamaks*, Nucl. Fusion **27** (1987) 1461-1472

[3.210] J. MANICKAM, E. FREDRICKSON, Z. CHANG, M. OKABAYASHI, M .BELL, R. BUDNY, W. PARK, G. SCHMIDT, M. C. ZARNSTORFF, F. LEVINTON, S. BATHA, T. C. HENDER, C. G. GIMBLETT, R. J. HASTIE, M. PHILLIPS, M. H. HUGHES, S. A. SABBAGH, *MHD Stability Sudies in Reversed Shear Plasmas in TFTR ,* in *Fusion Energy 1996* (Proceedings 16th IAEA Conference, Montreal 1996, IAEA Vienna 1997) **Vol. 1** 453-461

[3.211] E. J. STRAIT, T. A. CASPER, M. S. CHU, J. R. FERRON, A. GAROFARO, C. M. GREENFIELD, R. J. LA HAYE, L. L.LAO, E. A. LAZARUS, R. L. MILLER, G. A. NAVRATIL, C. REN, B. W. RICE, I. SEMENOV, A. C. C. SIPS, F. X. SÖLDNER, B. W. STALLARD, T. S. TAYLOR, A. D. TURNBULL, DIII-D TEAM, *Stability of negative central magnetic shear discharges in the DIII-D tokamak*, Phys. Plasmas **4** (1997)1783.-1791

[3.212] W. PARK, Z. CHANG, E. FREDRICKSON, G. Y. FU, N. POMPHREY, H. R. STRAUSS, L. E. SUGIYAMA, in *3D Simulation Studies of Tokamak Plasmas Using MHD and Extended-MHD Models,* in *Fusion Energy 1996* (Proceedings 16th IAEA Conference, Montreal 1996, IAEA Vienna 1997) **Vol. 2** 411-422

[3.213] Z. CHANG, R. NAZIKIAN, G.-Y. FU, R. B. WHITE, S. J. ZWEBEN, E. D. FREDERICKSON, S. H. BATHA, M. G. BELL, R. E. BELL, R. V. BUDNY, C. E. BUSH, L. CHEN, C. Z. CHENG, D. DARROW, B. LEBLANC, F. M. LEVINTON, R. P. MAJESKI, D. K. MANSFIELD, K. M. MCGUIRE, H. K. PARK, G. REWOLDT, E. J. SYNAKOWSKI, W. M. TANG, G. TAYLOR, S. VON GOELER, K. L. WONG, L. ZAKHAROV, TFTR GROUP, *Alpha-driven magnetohydrodynamics (MHD) and MHD-induced alpha loss in the Tokamak Fusion Test Reactor*, Phys. of Plasmas **4** (1997) 1610-1616

[3.214] R. NAZIKIAN, S. H. BATHA, M. G. BELL, R. E. BELL, R. V. BUDNY, C. E. BUSH, Z. CHANG, Y. CHEN, C. Z. CHENG, D. S. DARROW, H. H. DUONG, P. C. EFTHIMION, E. D. FREDERICKSON, G. Y. FU, N. N. GORELENKOV, B. LEBLANCE, F. M. LEVINTON, R. MAJESKI, E. MAZZUCATO, S. S. MEDLEY, H. K. PARK, M. P. PETROV, D. A. SPONG, E. J. SYNAKOWSKI, G. TAYLOR, S. VON GOELER, R. B. WHITE, K. L. WONG, S. J. ZWEBEN, *Observation of Alpha Partickle Driven Toroidal Alfvén Eigenmodes in TFTR DT Plasmas*, in *Fusion Energy 1996* (Proceedings 16th IAEA Conference, Montreal 1996, IAEA Vienna 1997) **Vol. 1** 281-292

[3.215] H. KIMURA, S. MORIYAMA, M. SAIGUSA, Y. KUSAMA, T. OZEKI, G. J. KRAMER, T. FUJITA, T. OIKAWA, T. FUJII, M. NEMOTO, K. HAMAMATSU, O. DACOSTA, S. ISHIDA, Y. KAMADA, T. KONDOH, A. MORIOKA, Y. NEYATANI, K. KOBITA, V. I. AFANASSIEV, JT-60 TEAM, *ICRF Heating and TAE Modes in Reactor-Relevant JT-60U Discharges,* in *Fusion Energy 1996*

(Proceedings 16th IAEA Conference, Montreal 1996, IAEA Vienna 1997) **Vol. 3** 295-305

[3.217] S. TAKEJI *et al*., JAERI-Research 97-047, 10 (1997)

[3.216] S. ISHIDA, S. TAKEJI, A. ISAYAMA, N. ISEI, T. OZEKI, T. FUJITA, Y. KAMADA, Y. NEYETANI, *Disruptive Beta Limits for High Performance Discharges in JT-60U*, in *Controlled Fusion and Plasma Physics* (Proceedings 24th European Physical Society Conference, Berchtesgarten 1997, Europhysics Conference Abstracts, Geneva ,1997) **21A Part II**, 489-492.

[3.218] T. OZEKI, M. AZUMI, Y. ISHII, Y. KISHIMOTO, G. Y. FU, T. FUJITA, G. REWOLDT, M. KIKUCHI, Y. KAMADA, H. KIMURA, Y. KUSAMA, M. SAIGUSA, S. IDE, H. SHIRAI, *Physics issues of high bootstrap current tokamaks*, Plasma Phys. Control. Fusion **39** (1997), A371-A380

[3.219] E. A. LAZARUS, G. A. NAVRATIL, C. M. GREENFIELD, E. J. STRAIT, M. E. AUSTIN, K. H. BURRELL, T. A. CASPER, D. R. BAKER, J. C. DEBOO, E. J. DOYLE, R. DURST, J. R. FERRON, C. B. FOREST, P. GOHIL, R. J. GROEBNER, W. W. HEIDBRINK, R.-M. HONG, W. A. HOULBERG, A. W. HOWARD, C.-L. HSIEH, A. W. HYATT, G. L. JACKSON, J. KIM, L. L. LAO, C. J. LASNIER, A. W. LEONARD, J. LOHR, R. J. LA HAYE, R. MAINGI, R. L. MILLER, M. MURAKAMI, T. H. OSBORNE, L. J. PERKINS, C. C. PETTY, C. L. RETTIG, T. L. RHODES, B. W. RICE, S. A. SABBAGH, D. P. SCHISSEL, J. T. SCOVILLE, R. T. SNIDER, G. M. STAEBLER, B. W. STALLARD, R. D. STAMBAUGH, H. E. ST. JOHN, R. E. STOCKDALE, P. L. TAYLOR, D. M. THOMAS, A. D. TRUNBULL, M. R. WADE, R. WOOD, D WHYTE, *Higher Fusion Power Gain with Current and Pressure Profile Control in Strongly Shaped DIII-D Tokamak Plasmas*, Phys. Rev. Lett. **77** (1996), 2714-2717

[3.220] T. FUJITA, S. IDE, H. KIMURA, T. OIKAWA, S. TAKEJI, H. SHARAI, T. OZEKI, Y. KAMADA, S. ISHIDA, JT-60 TEAM, *Enhanced core confinement in JT-60U reversed shear discharges*, in *Fusion Energy 1996* (Proceedings 16th IAEA Conference, Montreal 1996, IAEA Vienna 1997) **Vol. 1** 227-237

[3.221] M. GREENWALD, J. L. TERRY, S. M. WOLFE, S. EJIMA, M. G. BELL, S. M. KAYE, G. H. NEILSON, 'A new look at density limits in tokamaks', Nucl Fusion **28** 2199 (1988).

[3.222] V. MERTENS, A. HERRMANN, A. KALLENBACH, M. KAUFMANN, J. NEUHAUSER, et al., 'Edge and divertor physics in ASDEX Upgrade with emphasis on density limit characteristics', *Fusion Energy 1996* (Proc 16th Int Conf, Montreal, 1996) Vol 1, 413, IAEA, Vienna (1997).

[3.223] M MURAKAMI, J D CALLEN AND L A BERRY, '??' Nucl Fusion **16** 347 (1976).

[3.224] S J FIELDING, J HUGILL, G M MCCRACKEN, J W M PAUL, R PRENTICE, P E STOTT, 'High-density discharges with gettered torus walls in DITE', Nucl Fusion **17** 1382 (1977).

[3.225] A GIBSON, '??', Nucl Fusion **16** 546 (1976).

[3.226] P M REBUT AND B J GREEN, 'Effect of impurity radiation on tokamak equilibrium', *Plasma Physics and Controlled Nuclear Fusion Research 1976* (Proc 6th Int Conf, Berchtesgaden, 1976) Vol 2, 3, IAEA, Vienna (1977).

[3.227] N OHYABU, 'Density limit in tokamaks', Nucl Fusion **9** 1491 (1979).

[3.228] D E T F ASHBY AND M H HUGHES, 'The thermal stability and equilibrium of peripheral plasma', Nucl Fusion **21** 911 (1981).

[3.229] D J CAMPBELL, P A DUPERREX, A W EDWARDS, R D GILL, C W GOWERS et al, 'Sawteeth and disruptions in JET', *Plasma Physics and Controlled Nuclear Fusion Research 1986* (Proc 11th Int Conf, Kyoto, 1976) Vol 1, 433, IAEA, Vienna (1987).

[3.230] J. A. WESSON, R. D. GILL, M. HUGON, F. C. SCHÜLLER, J. A. SNIPES, D. J. WARD, D. V. BARTLETT, D. J. CAMPBELL, P. A. DUPERREX, A. W. EDWARDS, R. S. GRANETZ, N. A. O GOTTARDI, T. C. HENDER, E. LAZZARO, P. J. LOMAS, N. LOPES CARDOZO, K. F. MAST, M. F. F. NAVE, N. A. SALMON, P. SMEULDERS, P. R. THOMAS, B. J. D. TUBBING, M. F. TURNER, A. WELLER, *Disruptions in JET*, Nuc. Fusion **29** (1989) 641-666

[3.231] C G LOWRY, D J CAMPBELL, N GOTTARDI, K LAWSON, G VLASES, 'Density limits in JET with beryllium', *Controlled Fusion and Plasma Heating* (Proc 17th Euro Conf, Amsterdam, 1990), Vol 14B, Part I, European Physical Society (1990) 339.

[3.232] A STÄBLER, H NIEDEMAYER, R LOCH et al, '??', *Controlled Fusion and Plasma Physics* (Proc 16th Euro Conf, Venice, 1989), Vol 13B, Part I, European Physical Society (1989) 23.

[3.233] A STÄBLER, K MCCORMICK, V MERTENS, E R MÜLLER, J NEUHAUSER et al, 'Density limit investigations on ASDEX', Nucl Fusion **32** 1557 (1992).

[3.234] Y KAMADA, N HOSOGANE, R YOSHINO, T HIRAYAMA, T TSUNEMATSU, 'Study of the density limit with pellet fueling in JT-60', Nucl Fusion **31** 1827 (1991).

[3.235] M G BELL, G L SCHMIDT, P C EFTHIMION, B GREK, R A HULSE et al, 'Attainment of high plasma densities in TFTR with injection of multiple deuterium pellets', Nucl Fusion **32** 1585 (1992).

[3.236] T W PETRIE, A G KELLMAN, M ALI MAHDAVI, 'Plasma density limits during ohmic, L mode and ELMing H-mode operation in DIII-D', Nucl Fusion **33** 929 (1993).

[3.237] M KEILHACKER AND THE JET TEAM, 'Overview of results from the JET tokamak using a beryllium first wall', Physics of Fluids B **2** 1291 (1990).

[3.238] A M MESSIAEN, J ONGENA, U SAMM, B UNTERBERG, G VAN WASSENHOVE et al, 'High confinement and high density with stationary plasma and strong edge radiation in the TEXTOR-94 tokamak', Phys Rev Lett **77** 2487 (1996).

[3.239] B LIPSCHULTZ, B LABOMBARD, E S MARMAR, M M PICKRELL, J L TERRY, R WATTERSON, S M WOLFE, 'Marfe: an edge plasma phenomenon', Nucl Fusion **24** 977 (1984).

[3.240] O GRUBER et al, '??', Plasma Phys Control Fusion ?? ?? (1997).

[3.241] T E STRINGER, 'A theory of Marfes', *Controlled Fusion and Plasma Physics* (Proc 12th Euro Conf, Budapest, 1985), Vol 9F, Part I, European Physical Society (1985) p.86.

[3.242] J NEUHAUSER, W SCHNEIDER, R WUNDERLICH, 'Thermal instabilities and poloidal asymmetries in the tokamak edge plasma', Nucl Fusion **26** 1679 (1986).

[3.243] J F DRAKE, 'Marfes: radiative condensation instability in tokamak edge plasma', Phys Fluids **30** 2429 (1987).

[3.244] S R CHOUDHURY AND P K KAW, 'Ionization and edge density gradient effects on MARFE instabilities in tokamak plasmas', Phys Fluids B **1** 1646 (1989).

[3.245] J A WESSON AND T C HENDER, 'An extended treatment of MARFE stability', Nucl Fusion **33** 1019 (1993).

[3.246] A DE PLOEY, R A M VAN DER LINDEN, G T A HUYSMANS, M GOOSSENS, W KERNER, J P GOEDBLOED, 'Marfes: a magnetohydrodynamic stability study of two-dimensional tokamak equilibria', Plasma Phys Control Fusion **39** 423 (1997).

[3.247] D J CAMPBELL, S CLEMENT, N GOTTARDI, C GOWERS, P HARBOUR et al, 'The density limit in JET diverted plasmas', *Controlled Fusion and Plasma Heating* (Proc 21st Euro Conf, Montpellier, 1994), Vol 18B, Part I, European Physical Society (1994) 2.

[3.248] B LIPSCHULTZ, J GOETZ, B LABOMBARD, G M MCCRACKEN, J L TERRY et al, 'Dissipative divertor operation in the Alcator C-Mod tokamak', J Nucl Mater **220-222** 50 (1995).

[3.249] N ASAKURA, N HOSOGANE, K ITAMI, S TSUJI, M SHIMADA et al, 'Heat and particle transport in the divertor and remote radiative cooling on JT-60U', *Plasma Physics and Controlled Nuclear Fusion Research 1994* (Proc 15th Int Conf, Seville, 1994) Vol 1, 515, IAEA, Vienna (1995).

[3.250] S L ALLEN, A S BOZEK, N H BROOKS, D A BUCHENAUER, K H BURRELL et al, 'Recent DIII-D divertor research', Plasma Phys Control Fusion **37** A191 (1995).

[3.251] K LACKNER, R CHODURA, M KAUFMANN, J NEUHAUSER, K G RAUH, W SCHNEIDER, '??', Plasma Phys Control Fusion **26** 105 (1984).

[3.252] K BORRASS, 'Disruptive tokamak density limit as a scrape-off layer/ divertor phenomenon', Nucl Fusion **31** 1035 (1991).

[3.253] K BORRASS, R SCHNEIDER, R FARENGO, 'A scrape-off layer based model for Hugill-Greenwald type density limits', Nucl Fusion **37** 523 (1997).

[3.254] D J CAMPBELL, A BICKLEY, A CHANKIN, S CLEMENT, S J DAVIES et al, 'Studies of reactor-relevant H-mode regimes in the JET pumped divertor', Plasma Phys Control Fusion **38** 1497 (1996).

[3.255] K LANG, K BÜCHL, J C FUCHS, O GEHRE, O GRUBER et al, 'Pellet refueling of ELMy H-mode discharges beyond the Greenwald limit in ASDEX Upgrade, *Controlled*

Fusion and Plasma Physics (Proc 22nd Euro Conf, Bournemouth, 1995), Vol 19C, Part II, European Physical Society (1995) 449.

[3.256] M ALI MAHDAVI S L ALLEN, N H BROOKS, R BASTASZ, L R BAYLOR *et al*, 'Divertor plasma physics experiments in the DIII-D tokamak', *Fusion Energy 1996* (Proc 16th Int Conf, Montreal, 1996) Vol 1, 397, IAEA, Vienna (1997).

[3.257] M KAUFMANN, J SCHWEINZER, M ALBRECHT, M ALEXANDER, K ASMUSSEN *et al*, 'Overview of ASDEX Upgrade results', *Fusion Energy 1996* (Proc 16th Int Conf, Montreal, 1996) Vol 1, 79, IAEA, Vienna (1997).

[3.258] P. T. LANG, K. BÜCHL, M. KAUFMANN, R. S. LANG, V. MERTENS, H. W. MÜLLER, J. NEUHAUSER, 'High-Efficiency Plasma Refueling by Pellet Injection from the Magnetic High-Field Side into ASDEX Upgrade', Phys Rev Lett **79** 1487-1490 (1997)

[3.259] R RAMAN, F MARTIN, B QUIRION, M ST ONGE, J-L LACHAMBRE *et al*, 'Experimental demonstration of nondisruptive, central fueling of a tokamak by compact toroid injection', Phys Rev Lett **73** 3101 (1994)

[3.260] P. FRANZEN, V. MERTENS, G. NEU, T. ZEHETBAUER AND ASDEX UPGRADE TEAM: "Online Confinement Regime Identification for the Discharge Control System at ASDEX Upgrade"; 23rd Europ. Conf. on Fusion and Plasma Physics, Kiev, (Ukraine), 1996

[3.261] T. ZEHETBAUER, P. FRANZEN, G. NEU, V. MERTENS, G. RAUPP, W. TREUTTERER, D. ZASCHE AND ASDEX UPGRADE TEAM: "Plasma Regime Guided Discharge Control At ASDEX Upgrade" Proc. 19th Symposium on Fusion Technology, Lisboa (P), 1996

[3.262] B. KADOMSTEV, Plasma Phys. (Rus.) (1975) **1** N1, 710.

[3.263] B. KADOMSTEV, O. POGUTSE JETPh **65** (1973) N2, 575.

[3.264] S. MIRNOV, I. SEMENOV, *Observation of disruptive-instability fine structure in a tokamak*, in Proceedings 6th International Conference on Plasma Physics and Controlled Nuclear Fusion Research, Berchtesgaden 1976, Nucl. Fusion suppl. (1977), **Vol. 1** 291-301

[3.265] F. KARGER, K. LACKNER, G. FUSSMAN, B. CANNICI, *et al.*, *On the origin of the disruptive instability in the Pulsator I Tokamak*, in Proceedings 6th International Conference on Plasma Physics and Controlled Nuclear Fusion Research, Berchtesgaden 1976, Nucl. Fusion suppl. (1977), **Vol. 1** 267-277

[3.266] S. MIRNOV, I. SEMENOV, 8th EPS Conf. (1977) **1**, 45

[3.267] E. FREDRICKSON, Z. CHANG, R. BUDNY, D. DARROW, E. MAZZUCATO, R. NAZIKAN, A. JANOS, K. M. MCGUIRE, R. MAJESKI, C. PHILLIPS, G. SCHILLING, G. TAYLOR, R. WILSON, S. ZWEBEN, S. MIRNOV, I. SEMENOV, *Advances in Understanding of Disruptions and MHD in TFTR*, in *Controlled Fusion and Plasma Physics* (Proceedings 22nd European Physical Society Conference, Bournemouth 1995, Europhysics Conference Abstracts, Geneva ,1995) **19C Part III**, 045-048

[3.268] P. L. TAYLOR, A. G. KELLMAN, B. W. RICE, D. A. HUMPHREYS, *Experimental Measurements of the Current, Temperature and Density Profile Changes during a Disruption in the DIII-D Tokamak*, Phys. Rev. Lett. **76** (1996) 916-919

[3.269] R. WOLF, JET-IR(93)08, 73

[3.270] P. V. SAVRUKHIN, E. S. LYADINA, D. A. MARTYNOV, D. A. KISLOV, V. I. POZNYAK, *Coupling of Internal m = 1 and m = 2 Modes at Density Limit Disruptions in the T-10 Tokamak*, Nucl. Fusion **34** (1994) 317-336

[3.271] F.C. SCHÜLLER, *Disruptions in Tokamaks*, in *Plasma Physics and Controlled Fusion* **37** (1995) (Proceedings 22nd European Physics Society Conference on Controlled Fusion and Plasma Physics, Bournemoth,1995) A135-A162

[3.272] R.YOSHINO *et al.*, 4th Disruption, Plasma Control and MHD Expert Group Meeting, Naka, November 1996.

[3.273] D. MUELLER, M. G. BELL, E. FREDEREICKSON, A. C. JANOS, F. C. JOBES, L. C. JOHNSON, E. J. LAWSON, R. MARSALA, D. K. OWENS, H. PARK, A. T. RAMSEY, T. SENKO, H. TAKAHASHI, G. TAYLOR, K.-L. WONG, *Disruption Avoidance on TFTR*, Fusion Technology **30** (1996) 251-257

[3.274] S. PUTVINSKI, R. AYMAR, D. BOUCHER, C. Z. CHENG, J. W. CONNER, J. G. CORDEY, A. E. COSTLEY, F. ENGELMANN, N. FUJISAWA, M. FUJIWARA, J. JACQUINOT, R. KHAYRUTDINOV, H. KISHIMOTO, S. V. KONOVALOV, A. KUKUSHKIN, B. KUTEEV, V. LUKASH, S. MIRNOV, D. MOREAU, V. MUKHOVATOV, W. M. NEVINS, F. W. PERKINS, A. R. POLEVOI, D. POST, N. PUTVINSKAYA, M. N. ROSENBLUTH, O. SAUTER, N. SAUTHOFF, M. SHIMADA, Y. SHIMOMURA, YU. A. SOKOLOV, R. D. STAMBAUGH, T. TAKIZUKA, N. UCKAN, M. WAKATANI, J. WESLEY, J. WILLIS, R. YOSHINO, K. YOUNG, *ITER Physics*, in *Fusion Energy 1996* (Proceedings 16th IAEA Conference, Montreal 1996), IAEA Vienna (1997) **2** 737-753

[3.275] J. WESLEY, N. FUJISAWA, S. ORTOLANI, S. PUTVINSKI, M. N. ROSENBLUTH, *Disruption, Vertical Displacement Event and Halo Current Characterization for ITER*, in *Fusion Energy 1996* (Proceedings 16th IAEA Conference, Montreal 1996), IAEA Vienna (1997) **2** 971-978

[3.276] J. D. CALLEN, B. V. WADDELL, B. CARRERAS, M. AZUMI, P. J. CATTO, H. R. HICKS, J. A. HOLMES, D. K. LEE, S. J. LYNCH, J. SMITH, M. SOLER, K. T. TSANG, J. C. WHITSON, *Magnetic 'islandography' in tokamaks,* in *Plasma Physics and Controlled Nuclear Fusion Research 1978*, (Proceedings 7th IAEA Conference, Innsbruck 1978), **Vol. I** 415-431

[3.277] R. YOSHINO, Y. NEYATANI, N. ISEI, M. MATSUKAWA, N. HOSOGENE, *Operational Scenarios to Avoid Disruptions in JT-60U*, J. Plasma and Fusion Res. **70** (1994)1081-1101

[3.278] J. WESLEY, N. FUJISAWA, S. PUTVINSKI and M. N. ROSENBLUTH, *Assessment of Disruption and Disruption-Related Physics Basis for ITER*, in *17th IEEE/NPSS Symposium on Fusion Engineering*, (Proceedings 17th SOFE, San Diego 1997), IEEE, Piscataway New Jersey (1998), **Vol. 1** 483-490

[3.279] R. S. GRANETZ, I. H. HUTCHINSON, J. SORCI, J. H. IRBY, B. LABOMBARD, D. GWINN, *Disruptions and Halo Currents in Alcator C-Mod,* Nucl. Fusion **36** (1996) 545-556

[3.280] R. O. SAYER, Y.-K. M. PENG, S. C. JARDIN, A. G. KELLMAN, J. C. WESLEY, *TSC Plasma Halo Simulation of a DIII-D Vertical Displacement Event*, Nucl. Fusion **33** (1993) 969-978

[3.281] R. YOSHINO, Y. NAKAMURA, Y. NETATANI, *Avoidance of VDEs During Plasma Current Quench in JT-60U*, Nucl. Fusion **36** (1996) 295-307

[3.282] P. NOLL, R. AIGLE, M. L. BROWNE, D. CORBYN, T. ERIKSSON, C. FROGER, M. HUGUET, H. NIEDERMEYER, P. H. REBUT, A. SANTAGIUSTINA, L. SONNERUP, J. R. WATKINS, J. WESSON, *Stabilization of Vertical Position and Control of Plasma Shape in JET*, in *Fusion Engineering* (Proc. 11th Symposium on Fusion Engineering, Austin 1985), IEEE, New York (1986), **Vol. 1** 33-40

[3.283] E. J. STRAIT, L. L. LAO, J. L. LUXON, E. E. REIS, *Observation of Poloidal Current Flow to the Vacuum Vessel wall During Vertical Instabilities in the DIII-D Tokamak*, Nucl. Fusion **31** (1991) 527-534

[3.284] W. H. KUGEL, N. ASAKURA, R. BELL, ..., *Title = ???*, Controlled Fusion and Plasma Phys. (Proceedings 16th Eur. Conf. Venice 1989) Vol. **13B**, Part I, European Physical Society 1989, 199-xxx

[3.285] O. GRUBER, G. PAUTASSO, U. SEIDEL, K. BÜCHL, K. LACKNER, V. MERTENS, F. MAST, M. SCHITTENHELM, W. SUTTROP, M. ULRICH and THE ASDEX UPGRADE TEAM, *Disruptions in Vertically Elongated ASDEX Upgrade Plasmas*, in *Plasma Physics and Controlled Nuclear Fusion Research* (Proceedings 15th IAEA Conference, Seville 1994), IAEA Vienna (1995), **1** 675-684

[3.286] A. TANGA and the JET TEAM, *Disruptions and Vertical Displacement Events in JET*, in *Fusion Energy 1996* (Proceedings 16th IAEA Conference, Montreal 1996), IAEA Vienna (1997) **Vol. 1** 723-730

[3.287] V. RICCARDO, P. ANDREW, A. KAYE, P. NOLL, T. RAIMONDI, *Asymmetric Vertical Displacement Events at JET*, in *17th IEEE/NPSS Symposium on Fusion Engineering* (Proceedings 17th SOFE, San Diego 1997), IEEE, Piscataway New Jersey (1998), **Vol. 1** 112-115

[3.288] P. ANDREW, P. NOLL, V. RICCARDO, *The Relation Between Halo Currents and Plasma Displacement/Deformation in JET*, in *17th IEEE/NPSS Symposium on Fusion Engineering* (Proceedings 17th SOFE, San Diego 1997), IEEE, Piscataway New Jersey (1998), **Vol. 1** 108-1151

[3.289] A. SAKASAI and the JT-60 TEAM, *High Performance and Steady-State Experiments on JT-60U*, in *17th IEEE/NPSS Symposium on Fusion Engineering*, (Proceedings 17th SOFE, San Diego 1997), IEEE, Piscataway New Jersey (1998), **Vol. 1** 18-25

[3.290] N. POMPHREY, J. BIALEK, W. PARK, *Modeling the Toroidal Asymmetry of Poloidal Halo Currents in Conducting Structures*, Nucl. Fusion **38** (1998) 449-466

[3.291] A. C. JANOS, E. D. FREDERICKSON, K. M. MCGUIRE, S. H. BATHA, M. G. BELL, M. BITTER, R. BUNDY, C. E. BUSH, P. C. EFTHIMION, R. J. HAWRYLUK, K. W. HILL, J. C. HOSEA, F. C. JOBES, D, W, JOHNSON, F. LEVINTON, D. K. MANSFIELD, D. M. MEADE, S. S. MEDLEY, D. A. MONTICELLO, D. MUELLER, Y. NAGAYAMA, D. K. OWENS, H. K. PARK, W. PARK, D. E. POST, J. SCHIVELL, J. D. STRACHAN, G. TAYLOR, M. ULRICKSON, S. VON GOELLER, E. WILFRID, K. L. WONG, M. YAMADA, K. M. YOUNG, M. C. ZARNSTORFF, S. J. ZWEBEN, TFTR GROUP, *Disruptions in the TFTR Tokamak*, in *Plasma Physics and Controlled Fusion Research 1992* (Proceedings 14th IAEA Conference Würzburg 1992) IAEA Vienna 1993 **1** 527-539

[3.292] G. MARTIN, M. CHATELIER, C. DOLOC, *New Insight into Runaway Electrons Production and Confinement*, in *Controlled Fusion and Plasma Physics* (Proceedings 22nd European Physical Society Conference, Bournemouth 1995), Europhysics Conference Abstracts, Geneva ,1995, **19C Part II,** 41-44

[3.293] R. D. GILL, *Generation and Loss of Runaway Electrons Following Disruptions in JET*, Nucl. Fusion **33** (1993) 1613-1625

[3.294] R. YOSHINO, T. KONDOH, Y. NEYATANI, K. ITAMI, Y. KAWANO, N. ISEI, *Fast plasma shutdown by killer pellet injection in JT-60U with reduced heat flux on the divertor plate and avoiding runaway generation*, Plasma Phys. Control. Fusion **39** (1997) 313-332

[3.295] YU. A. SOKOLOV, *'Multiplication' of accelerated electrons in a tokamak,* JETP Letters **29** (1979) [translation Pis'ma v Zhurnal Eksperimental'noi i Teoreticheskoi Fiziki **29** (1979)] 244-246

[3.296] R. JAYAKUMAR, H. H. FLEISHMANN, S. ZWEBEN, *Collisional avalanche exponentiation of runaway electrons in electrified plasmas,* Phys. Lett. **A172** (1993) 447-451

[3.297] S. PUTVINSKI, N. FUJISAWA, D. POST, N. PUTVINSKAYA, M. N. ROSENBLUTH, J. WESLEY, *Fast Plasma Termination by Impurity Fueling*, Journal Nucl. Materials **241-243** (1997) 316-321

[3.298] M. N. ROSENBLUTH, S. V. PUTVINSKI, *Theory for Avalanche of Runaway Electrons in Tokamaks*, Nucl. Fusion **37** (1997) 1355-1362

[3.299] G. FUSSMAN, *On the Motion of Runaway Electrons in Momentum Space*, Nucl. Fusion **19** (1979) 327-334.

[3.300] J. W. CONNOR, R. J. HASTIE, *Relativistic limitations on runaway electrons*, Nucl. Fusion **15** (1975) 415-424

[3.301] R. JASPERS, K. H. FINKEN, G. MANK, F. HOENEN, J. A. BOEDO, N. J. LOPES CARDOZO, F. C. SCHÜLLER, *Experimental Investigation of Runaway Electron Generation in TEXTOR*, Nucl. Fusion **33** (1993) 1775-1785

[3.302] R. JASPERS, N. J. LOPES CARDOZO, F. C. SCHÜLLER, K. H. FINKEN, T. GREWE, G. MANK, *Disruption Generated Runaway Electrons in TEXTOR and ITER*, Nucl. Fusion **36** (1996) 367-373

[3.303] I. M. PANKRATOV, R. JASPERS, K. H. FINKEN, I. ENTROP, G. MANK, *Control of Runaway Electron Secondary Generation by Changing Z_{eff}*, Nucl. Fusion **38** (1998) 279-286

[3.304] Y. KAWANO, R. YOSHINO, Y. NEYATANI, T. KONDOH, N. ISEI, S. ISHIDA, K. TOBITA, T. HATAE, K. ITAMI, A. SAKASAI, JT-60U TEAM, *Fast Current Shutdown Scenario for Major Disruption Softening in JT-60U*, in Fusion Energy 1996 (Proceedings 16th IAEA Conference, Montreal 1996), IAEA Vienna (1997) **1** 345-357

[3.305] Y. KAWANO, R. YOSHINO, Y. NEYATANI, T. KONDOH, N. ISEI, S. ISHIDA, K. TOBITA, T. HATAE, K. ITAMI, A. SAKASAI, JT-60U TEAM, *Suppression of Runaway Electrons during Disruptive Discharge Terminations in JT-60U*, in Controlled Fusion and Plasma Physics (Proceedings 24th European Physical Society Conf., Berchtesgarten 1997), Europhysics Conference Abstracts, Geneva ,1997, **21A Part II** 501-504

[3.306] S. LUCKHARDT, private communication: *'Runaway bursts and plasma mixing during DIII-D killer pellet experiments'* (1997)

[3.307] S. TOKUDA, private communication: *'Effect of Magnetic Perturbations on Runaway Electrons Generation',* presented to the ITER Disruption, Plasma Control, and MHD Expert Group Meeting (September 1997)

[3.308] H. E MYNICK, J. D. STRACHEN, *Transport of runawy and thermal electrons due to magnetic microturbulence,* Phys. Fluids **24** (1981) 695-702

[3.309] L. LAURENT, J. M. RAX, *Stochastic instability of runaway electrons in tokamaks*, Europhys. Lett. **11** (1990) 219-224

[3.310] A. J. RUSSO, *Effect of Ripple on Runaway Electrons in Tokamaks*, Nucl. Fusion **31** (1991) 117-126

[3.311] M. N. ROSENBLUTH, P. B. PARKS, D. POST, S. PUTVINSKI, N. PUTVINSKAYA, H. A. SCOTT, *Runaway Electrons and Fast Plasma Shutdown*, in Fusion Energy 1996 (Proceedings 16th IAEA Conference, Montreal 1996), IAEA Vienna (1997) **2** 979-986

[3.312] M. SCHITTENHELM, *Runaway Generation during Disruptions in ITER Taking Account of Particle Trapping*, in *Controlled Fusion and Plasma Physics* (Proceedings 24th European Physical Society Conf., Berchtesgarten 1997), Europhysics Conference Abstracts, Geneva ,1997, **21A Part III** 985-988

[3.313] M. N. ROSENBLUTH, private communication: '*Neoclassical peaking effects in avalanche runaway generation*' (1997)

[3.314] R. YOSHINO, private communication: *'Runaways Termination'*, presented to the ITER Disruption, Plasma Control, and MHD Expert Group Meeting (September 1997)

[3.315] G. MARTIN, private communication: *'Localization of photo-neutron activated regions on the Tore Supra inboard limiter'* (1997)

[3.316] R. YOSHINO, private communication: '*Intense Helium Gas Puffing in JT-60U*', presented to the ITER Disruption, Plasma Contrrol, and MHD Expert Group Meeting (March 1997).

[3.318] P. L. TAYLOR, private communication: *'Massive He gas puff results'*, in '*Runaway Electron Studies in DIII-D Disruptions'* presented to the ITER Disruption, Plasma Control, and MHD Expert Group Meeting (May1998)

[3.318] G. L. SCHMIDT, private communication: *'MHD activity in TFTR pellet injection experiments'* (1997)

[3.319] B. V. KUTEEV, V. YU. SERGEEV, S. SUDO, *Emergency Discharge Quench or Rampdown by a Noble Gas Pellet*, Nucl. Fusion **35** (1995) 1167

[3.320] G. PAUTASSO, K. BÜCHL, J. C. FUCHS, O. GRUBER, A. HERRMANN, K. LACKNER, P. T. LANG, K. F. MAST, M. ULRICH, H. ZOHM, *Use of Impurity Pellets to Control Energy Dissipation During Disruption*, Nucl. Fusion **36** (1996) 1291-1297

[3.321] A. G. KELLMAN, J. W. CUTHERBERTSON, T. E. EVANS, D. A. HUMPHREYS, A. W. HYATT, G. L. JAHNS, T. JERNIGAN, C. J. LASNIER, R. L. LEE, J. A. LEUER, S. LUCKHARDT, M. J. SCHAFFER, P. L. TAYLOR, D. G. WHYTE, D. WROBLEWSKI, J. ZHANG, *Disruption Studies in DIII-D*, in *Fusion Energy 1996* (Proceedings 16th IAEA Conference, Montreal 1996)**,** IAEA Vienna (1997) **1** 739-746

[3.322] R. S. GRANETZ, I. H. HUTCHINSON, J. SORCI, D. T. GARNIER, J. H. IRBY, B. LABOMBARD, E. S. MARMAR, ALCATOR GROUP, *Disruptions, Halo Currents and Killer Pellets in Alcator C-Mod*, in *Fusion Energy 1996* (Proceedings 16th IAEA Conference, Montreal 1996), IAEA Vienna 1997) **1** 757-762

[3.323] G. L. SCHMIDT, S. ALI-ARSHAD, D. BARTLETT, A. CHANKIN, S. CLEMENT, M. GADEBERG, P. KUPSCHUS, D. O'BRIEN, R. REICHLE, G. SADLER, A. TANGA, *Potential Safe Termination by Injection of Polypropylene Pellets in JET*, in *Controlled Fusion and Plasma Physics* (Proc. 22nd European Physical Society Conf. Bournemouth 1995), Europhysics Conference Abstracts, Geneva ,1995, **19C, Part IV** 21-24

[3.324] G. L. SCHMIDT, E. FREDERICKSON, private communication: *Impurity Injection on TFTR*, in *U.S. Disruption Physics R&D Report for FY 1997* (U.S. ITER Home Team Report ITER/US/97/PH-14, August 1997)

[3.325] P. B. PARKS, R. J. TRUNBULL, *Effect of transonic flow in the ablation cloud on the lifetime of a solid hydrogen pellet in a plasma*, Phys. Fluids **21** (1978) 1735-1741

[3.326] S. L. MILORA, W. A. HOULBERG, L. L. LENGYEL, V. MERTENS, *Pellet Fueling [Review Article]*, Nucl. Fusion **35** (1995) 657-754

[3.327] S. C. JARDIN, *TSC Analysis of TFTR Impurity Injection Experiments*, in *U.S. Disruption Physics R&D Report for FY 1997* (U.S. ITER Home Team Report ITER/US/97/PH-14, August 1997)

[3.328] D. G. WHYTE, T. E. EVANS, A. G. KELLMAN, D. A. HUMPHREYS, A. W. HYATT, T. C. JERNIGAN, R. L. LEE, S. L. LUCKHARDT, P. B. PARKS, M. J. SCHAFFER, P. L. TAYLOR, *Energy Balance, Radiation and Stability During Rapid Plasma Termination via Impurity Pellet Injections on DIII-D,* in *Controlled Fusion and*

Plasma Physics (Proceedings 24th European Physical Society Conf., Berchtesgarten 1997), Europhysics Conference Abstracts, Geneva ,1997, **21A Part III,** 1137-1140

[3.329] R. YOSHINO, Y. NAKAMURA, Y. NEYATANI, *Plasma Equilibrium Control during the Slow Plasma Current Quench with Avoidance of Plasma-Wall Interaction in JT-60U*, Nucl. Fusion **37** (1997) 1161-1166

[3.330] R. YOSHINO, J. KOGA, T. TAKEDA, *Sensor Algorithms of the Plasma Vertical Position to Avoid a Vertical Displacement Event During Plasma-Current Quench on JT-60U*, Fusion Technology **30** (1996) 237-250

[3.331] Y. NEYATANI, R. YOSHINO, private communication: *Halo Current Measurement in JT-60U*, presentation to ITER Disruption, Plasma Control and MHD Expert Group Meeting (September 1997)

[3.332] Y. NAKAMURA, R. YOSHINO, Y. NEYATANI, *Mechanism of Vertical Displacement Events in Disruptive Discharges*, Nucl. Fusion **36** (1996) 643-656

[3.333] R. YOSHINO, M. OHSAWA, *Fluctuations in Plasma Equilibrium Control on JT-60U*, Fusion Technology **30** (1996) 159-166

[3.334] Y. NAKAMURA, R. YOSHINO, N. POMPHREY, S. C. JARDIN, *β_p-collapse-induced vertical displacement event in high β_p tokamak disruption,* Plasma Phys. and Contr. Fusion **38** (1996) 1791-1804

[3.335] A. C. JANOS, E. D. FREDERICKSON, R. V. BUNDY, D. S. DARROW, K. M. MCGUIRE, S. J. ZWEBEN, *Characterization of Alpha Particle Loss During Disruptions in TFTR During Deuterium-Tritium Operation*, Nucl. Fusion **36** (1996) 475-493

[3.336] M. N. ROSENBLUTH, S. V. PUTVINSKI, P. B. PARKS, *Liquid Jets for Fast Plasma Termination in Tokamaks*, Nucl. Fusion **37** (1997) 955-966

[3.337] R. S. GRANETZ, private communication: *Massive D pellet injection in Alcator C-Mod*, presented to the ITER Disruption, Plasma Control, and MHD Expert Group Meeting (September 1997); also R. S. Granetz, M. Greenwald, D. Mossessian, *Massive D_2 Killer Pellet Injection Experiments on Alcator C-Mod*, in *U.S. Disruption Physics R&D Report for FY 1997* (U.S. ITER Home Team Report ITER/US/97/PH-14, August 1997)

[3.338] H. SCOTT, *Radiation Transport Calculations for Killer Pellets for ITER,* in *U.S. Disruption Physics R&D Report for FY 1997* (U.S. ITER Home Team Report ITER/US/97/PH-14, August 1997)

3.339] E. D. FREDERICKSON, K. MCGUIRE, Z. CHANGE. A. JANOS, M. BELL, R. V. BUDNY, C. E. BUSH, J. MANICKAN, H. MYNICK, R. NAZIKAN, G. TAYLOR, *β limit disruptions in the Tokamak Fusion Test Reactor,* Phys. Plasmas **2** (1995) 4216-4229

[3.340] V,. MERTENS, C. AUBANEL, O. GRUBER, M. KAUFMANN, G. NEU, G. RAUPP, H. RICHTER, W. TREUTTERER, D. ZASCHE, TH. ZEHETBAUER,

ASDEX UPGRADE TEAM, NBI TEAM AND ICRH TEAM, *Plasma Performance Optimization in ASDEX Upgrade*, Fusion Technology **32** (1997) 459-467

[3.341] D. WRÓBLEWSKI, G. L. JAHNS, J. A. LEUER, *Tokamak Disruption Alarm Based on a Neural Network Model of the High-β Limit*, Nucl. Fusion **37** 725-741

[3.342] G. RAUPP, O. GRUBER, A. KALLENBACH, V. MERTENS, G. NEU, B. STEREIBL, W. TREUTTERER, , TH. ZEHETBAUER, D. ZASCHE, ASDEX UPGRADE TEAM, *Discharge Supervision Control on ASDEX Upgrade*, Fusion Technology **32** (1997) 444-458

[3.343] A. W. MORRIS, T. C. HENDER, J. HUGILL, P. S. HAYNES *et al.*, Feedback stabilization of disruption precursors in a tokamak, Phys. Rev. Lett. **64** (1990)1254-1257

[3.344] D. A. KISLOV, V. V. ALIKAEV, YU. V. ESIPCHUK, A. M. KAKURIN, A. YA. KISLOV, D. A. MARTYNOV, G. E. NOTKIN, K. A. RAZUMOVA, A. V. SUSHKOV, V. V. VOLKOV, *The m = 2, n = 1 mode suppression by ECRH on the T-10 tokamak*, Nucl. Fusion **37** (1997) 339-350

[3.345] S. C. JARDIN, N. POMPHREY, J. DELUCIA, *Dynamical modeling and position control of tokamaks*, J. Comput. Physics **66** (1986) 481-507

[3.346] R. KHAYRUTDINOV, V. LUKASH., *Studies of plasma equilibrium and transport in a tokamak fusion device with the inverse-variable technique*, J. of Comput. Physics **109** (1993) 193-201

[3.347] P. BARABASCHI: MAXFEA finite-element dynamic equilbrium modelling code, personal communication, 1998

[3.348] B. J. MERRILL, S. C. JARDIN, M. ULRICKSON, M. BELL, *Dynamics and energy flow in a disrupting tokamak plasma,* Fusion Engineering and Design **15** (1991) 163-180

[3.349] R. O. SAYER, *TSC Filamentary Representation of the ITER Vacuum Vessel, Blanket and Divertor*, in U.S. Disruption Physics R&D Report for FY 1997 (U.S. ITER Home Team Report ITER/US/97/PH-14, August 1997)

[3.350] D. W. WEISSENBERGER, *SPARC Version 1:1 User Manual*, PPPL-2494, Princeton Plasma Physics Laboratory, January 1988

[3.351] R. KHAYRUTDINOV, V. LUKASH., Plasma Physics Reports **22** (1996) 91-xx

[3.352] D. HUMPHREYS, A. G. KELLMAN, *Scoping Studies of ITER Disruption Scenarios Using the DINA Code*, in U.S. Disruption Physics R&D Report for FY 1997 (U.S. ITER Home Team Report ITER/US/97/PH-14, August 1997)

[3.353] S. C. CHIU, et al., *Fokker-Plank Simulations of Knock-on Runaway Electron Generation in Tokamaks*, paper 2B02, 1997 International Sherwood Fusion Theory Conference, April 1997, Madison, Wisconsin.

[3.354] S. C. JARDIN, Z. CHANG, E. FREDERICKSON, G. L. SCHMIDT, A. KELLMAN, D. HUMPHREYS, T. EVANS, D. WHYTE, P. TAYLOR, B.

MERRILL, *Modeling of Impurity Pellet Injection Experiments in TFTR and DIII [sic] and Implications for Fast Safety Shutdown of ITER* (paper 3R12), Bull. Am. Phys. Soc. **41** (1996) 1435

[3.355] H. A. SCOTT, W. MAYLER, *GLF-a simulation code for X-ray lasers*, Applied Physics B **58** (1994) 35-43

[3.356] A. SYKES, J. A. WESSON, *Title = ?*, in *Plasma Physics and Controlled Nuclear Fusion Research 1980* (Proceedings. 8th International Conference, Brussels1980), IAEA Vienna (1981), **Vol. 1** 237-2xx.

[3.357] A. HASSANIEN, et al., *Modeling Plasma/Material Interactions During a Tokamak Disruption*, Argonne National Laboratory, ANL/FPP/TM 271 (1994).

LIST OF TABLES

LIST OF FIGURES

FIG. 3-4. β_N versus internal inductivity in DIII-D. Maximum normalized beta obtainable in both positive and negative shear plasmas increases with internal inductivity.

FIG. 3-5. Ideal' and 'Non-ideal' beta limits in otherwise similar DIII-D plasmas: the high heating power discharge (84643) reaches a disruptive ideal β-limit at $\beta_N \approx 4l_i \approx 4.4$ after ~0.2 s; the lower-power long-pulse discharge (86144) with otherwise similar parameters has onset of an m = 2, n = 1 'neoclassical tearing mode' and a 'soft' β-limit at $\beta_N \approx 2$ after ~1.5 s (see Section 3.2.3)

FIG. 3-6. ITER simulation discharge in JET (1.7 T, 1.7 MA, $\beta_{N,max} \approx 3$, limited by available heating power) [3.12]

FIG. 3-7. Measured and calculated ideal MHD ballooning onset criterion (α/q^2) for a JET 'ITER simulation discharge' with $\beta_N = 3.8$, close to the ideal MHD limit [3.12]. The plasma is close to or at marginal ideal MHD stability over nearly the whole cross-section

FIG. 3-8. Beta limits for n=1 external kink modes as a function of ψ_{frac}, the poloidal flux fraction associated with truncation for H-mode profiles. Truncation outside $q \approx 4$ leads to a converged value of the β limit.

FIG. 3-9. Computed n = 1 mode growth rate and edge normal displacement as a function of increasing β_N, for $q(0) < 1$ and $q(0) > 1$, with and without the presence of a stabilizing conducting wall [3.18]. The pressure profiles and wall position used for this calculation are derived from DIII-D discharge 82205 at 3665 ms. The β_N of the experimental discharge, which was ideal MHD stable, is indicated: other β_N values examined in the calculation were obtained by scaling the experimental profile as explained in the text. The finite growth rate and mode amplitude for $q(0) = 0.95$ and $\beta_N \leq 3$ are ascribed to an internal rather than external mode. The presence of absence of a wall has no effect on the comparative instability of the $q(0) < 1$ case. The applicable ideal-MHD external kink pressure for instability inferred from this analysis is $\beta_N \cong 3$

FIG. 3-10. Schematic illustration of sawtooth oscillation features: temperature and safety factor profile waveforms and evolution in an idealized circular cross-section tokamak plasma. See Figures in Section 3.2.2.6 for similar data from simulations of ITER sawteeth.

FIG. 3-11. Comparison of predicted critical shear for sawtooth onset with measured shear, both evaluated at the measured q = 1 radius. Data for TFTR L-mode and supershot plasmas, all with $q(0) < 1$

FIG. 3-12. Simulation [3.59] of plasma temperature and safety factor profiles before and after sawtooth reconnection in a 1.5 GW ignited-burn ITER plasma. See Fig. 3-13 for time waveforms for this simulation.

FIG. 3-13. Simulation of ignition and sustained 1.5-GW burn in a 21-MA ITER plasma. The first sawtooth occurs about 200 s after initial heating and a stable 70-s period sawtooth cycle develops by 300 s. This cycle continues indefinitely (the simulation here ends arbitrarily at 400 s). The plasma profiles before and after a sawtooth reconnection are shown in Fig. 3-12. The effect of the reconnection on fusion power, β_p and l_i is barely discernible.

FIG. 3-14. Simulation of a m = 2, n = 1 neoclassical island in an ignited ITER plasma. The low value of the tearing mode parameter $\Delta' = -2.6$ in this simulation produces a large island that can be expected to have a significant impact on energy transport and hence on achievable beta. Simulation by Alexander Pletzer with the PEST-3 stability code

FIG. 3-15. Measured island widths in various tokamaks compared with neoclassical tearing mode theory predictions: a) m/n = 4/3 neoclassical tearing mode in TFTR compared with the prediction of the neoclassical island evolution equation from [3.76]. (b) m/n = 3/2 neoclassical tearing mode in DIII-D compared to theoretical predictions (calculated using measured parameters) with either the ion polarization current term included or the cross-island transport term included. Time history of $\beta_p(t)$ as determined by the equilibrium reconstruction code EFIT is also shown. (c) m/n=2/1 mode during an ECRH power ramp down in COMPASS-D, compared to theoretical predictions [3.80]. Measured $\beta_p(t)$ (from diamagnetic loop) is also shown.

FIG. 3-16. Soft X-ray tomographic reconstructions of saturated n = 2 neoclassical modes in JET at $\beta_N = 2.4$ (left) and $\beta_N = 3.4$ (right). At the lower β_N, the mode has both m = 2 and m = 3 harmonics; at higher β_N, the m = 2 harmonic dominates. The data plots show the perturbation of the SXR emission at one toroidal azimuth angle: green = small; blue = positive; red = negative. The axisymmetric equilibrium flux surfaces are superimposed.

FIG. 3-17. Neoclassical mode growth rate (dw/dt) versus island width w and poloidal beta β_p. There is threshold $\beta_{p,crit}$ for mode growth and for $\beta_p > \beta_{p,crit}$, a critical island width w_{crit} for mode growth. For $\beta_p > \beta_{p,crit}$, the saturated mode width increases linearly with increasing β_p. For simplicity, details of the sensitivity of w_{crit} to β_p and to the comparative importance of the ion-polarization and cross-island transport effects (and hence plasma collisionality) are omitted here (see [3.80]).

FIG. 3-18. Dynamics of neoclassical mode onset and subsequent confinement and temperature profile effects in ASDEX Upgrade (pulse #8216). An m = 3, n = 2 neoclassical mode develops at t = 1.5 s and persists for the balance of the beam-heated phase of the discharge. Note the drop in β_N at fixed beam power after mode onset and lack of recovery of the full pre-onset beta despite a further ~30% increase in beam power (both indicating confinement deterioration). Thomson scattering electron temperature profile data confirm the presence a 3/2 island and a ~ 7-cm wide profile flattening at q ~ 1.5 when the neoclassical mode is present

FIG. 3-19. Comparisons of neoclassical mode onset data from the ITER database with the predictions of two threshold model scalings. Left (a): β_N at the point of onset of MHD, plotted vs. $(\nu_e^*)^{0.3}$, a proposed scaling for the onset of MHD from cross-

island transport threshold model. Right (b): β_N vs. $\nu_i/\varepsilon\omega^*$, an important parameter in determining the critical island width in the ion polarization current threshold model (large threshold width for $\nu_i/\varepsilon\omega^* > 0.3$, small threshold width for $\nu_i/\varepsilon\omega^* < 0.3$). The dashed vertical lines represent the spread due to a 15% uncertainty in the measured temperature at the rational surface. The following caveats apply to the interpretation of the database: (1) TFTR data have rapid power increases and the value $\nu_i/\varepsilon\omega^*$ goes from above the threshold value to well below in ~200 ms, (2) solid data points for JET and DIII-D are for mode onset; open points are for no mode onset, and (3) The COMPASS-D data is for plasmas with $T_e > T_i$ (ECRH heating), while all other data are with neutral beam heating.

FIG. 3-20. DIII-D discharge #80111 illustrating plasma rotation stabilization of a non-rotating m=3, n=1 RWM (detected by saddle-loop magnetics data, second panel). The RWM develops for $\beta_N > \beta_{N,ideal}$, but is resistively stabilized (limited in amplitude) by the effect of plasma rotation at the q = 3 surface. As the q = 3 rotation slows, the mode grows in a corresponding manner. When the q = 3 rotation ceases, the wall stabilization ceases to be effective, the RWM grows rapidly on a wall-resistance time scale (~5 ms) and the high-β_N phase terminates owing to severe confinement deterioration. Data reproduced from [3.103].

FIG. 3-21. Resistive wall mode growth rate and slip frequency and plasma mode (ideal n = 1 external kink) growth rate versus resistive wall position, for a plasma with pressure 30% above the wall-at-infinity external kink beta limit and $\omega_{rot}/\omega_A = 0.06$. A finite-width wall position window (shaded domain) for simultaneous plasma and RWM stability exists.

FIG. 3-22. Marginal wall position versus normalized beta for plasma and resistive wall modes. The plasma mode is stable for a wall located inside marginal position and the RWM is stable for a wall located outside the marginal position. A finite wall-position stability window (shaded region) exists in this case for $\beta_N \leq 4.2$. The calculation here is for a relatively broad pressure profile with a central-to-volume-average pressure ratio = 1.7.

FIG. 3-23. Possible implementation of an 'intelligent shell' scheme for feedback stabilization of RWMs. The system comprises a sensor array S_{ij} electronically coupled to a corresponding actively-driven feedback coil array P_{ij}. With sufficient feedback gain and bandwidth, the sensor array surface appears to be a resistance-less conductor and the relevant RWM(s) are stabilized.

FIG. 3-24. Calculation based on a model described in [3.122] of 2,1 resistive tearing mode slowing and locking in a JET ohmic plasma. An initial plasma rotation velocity ω = 2000 s^{-1} is assumed in this example.

FIG. 3-25. Plasma response to externally-applied 2,1 RMP in COMPASS-C [3.126]. A 1-kA coil current produces a 13 G radial 2,1 field at the plasma surface. Toroidal field is 1.1 T in these experiments. The mode penetration threshold density is well described by a theoretical model (detailed in [3.126]) that includes the effect of strong poloidal flow damping. The viscosity time scale τ_v (see discussion in text) is

a parameter in the model: the model curves shown are for the experimentally-measured range of τ_v. A model without poloidal damping fails to describe the data.

FIG. 3-26. Error-field coil currents for 2,1 mode penetration and locking in low-density Ohmic plasmas (2 x 10^{19} m^{-3}) in COMPASS-D. Mode locking occurs whenever the magnitudes of the currents in the 3,1 and 2,1 coils exceed the boundary indicated by the demarkation between the unshaded and shaded domains. These domains and the boundary presumably extend as shown in a anti-symmetrical fashion for negative $I_{2,1}$

FIG. 3-27. Error-field penetration threshold (B_{pen}/B_t) in COMPASS-D (R = 0.56 m), DIII-D (R = 1.7 m) and JET (R = 2.95 m), scaled for $n_e = 1.6 \times 10^{19}$ m^{-3} and $q_{95} = 3.3$. The error field harmonic mix varies among the three experiments. The data plotted are the equivalent 2,1 field as evaluated using Eq. (3-10) for COMPASS-D and JET and Eq. (3-11b) for DIII-D. The single-experiment toroidal field scalings (α_B) given in Table 3-II are also shown.

FIG. 3-28. Error field tolerance versus β for DIII-D beam-heated H-mode plasmas

FIG. 3-29. Divertor region D_α intensity in a typical DIII-D plasma with slowly increasing neutral beam injection power. Low-amplitude Type III ELMs appear after the L-H transition when low NBI power is applied and disappear as power is slowly increased. Larger Type I ELMs with increasing frequency appear at high power. Summarized from a more-complete data set presented in [1], Figure 2

FIG. 3-30. Magnetic fluctuation amplitude and divertor D_α intensity indications of an 'outer mode' MHD event in a JET hot-ion H-mode deuterium discharge (No. 33648). The 100-ms outer mode MHD event results in a corresponding transient increase in divertor D_α and also initiates an prompt and irreversible deterioration of plasma energy confinement and DD neutron yield. Applied NBI power is constant for the full data period (12-14 s) shown. Summarized from a more-complete data set presented in Ref [3.145], Fig. 1.

FIG. 3-31. H-mode operational diagram for ASDEX Upgrade presented in terms of the measured electron temperature and density 2 cm inside the separatrix (this location corresponds to the top of the H-mode pedestal). Boundaries indicating different types of confinement regime are marked (Kaufmann et al, 1997). The limiting bound of edge pressure (nT) corresponds closely to the predicted pressure gradient for onset of ideal MHD ballooning ('ideal ballooning limit'). —Same as FIG. 3-49.

FIG. 3-32. Ideal MHD ballooning stability comparison data for Type I ELMs in DIII-D plasmas with ITER-like shape (q varies). The pressure gradient measured prior to Type I ELM onset consistently exceeds twice the calculated ideal ballooning gradient threshold.

FIG. 3-33. Plasma edge operational space diagram for ITER. The projected ITER edge operation conditions (n, T) lie along the ideal MHD ballooning instability limit contour in the upper right corner of the diagram, at $n \approx 8 \times 10^{19}$ m^{-3}, $T \approx 4$ keV, in the region where Type I ELMs are present, and where Type III ELMs and excessive edge impurity radiation losses are avoided.

FIG. 3-34. Plasma magnetic configuration reconstruction and profile data for a NBI-heated reversed-shear plasma in DIII-D. The toroidal current density (j_{tor}) and safety factor (q) profile data are derived in this case from MSE measurements of the in-plasma vertical (Z) component of the poloidal field. The radius of the reverse-shear region (shaded) is about half of the minor radius. The pressure gradient steepens within the shear reversal radius. Data reproduced from [3.200].

FIG. 3-35. LHCD shear reversal in Tore Supra [R = 2.4 m, a = 0.72 m (circular cross-section), B = 1.3 T, $n_{e0} = 3 \times 10^{19}\ m^{-3}$]. A LHCD-sustained quasi-steady-state RS region develops within 3 s of application of 2.5 MW of 3.7 GHz LHCD. T he HXR data shows the approximate LH power deposition profile. Approximately half of the 0.4-MA plasma current is LH-driven. Safety factor profiles are inferred from Faraday rotation measurements of the in-plasma field direction. Data reproduced from [3.195].

FIG. 3-36. Plasma current and l_i waveforms for a representative DIII-D current rampdown experiment. Current density profiles obtained from equilibrium reconstructions supplemented with MSE data are shown in the right-hand panel. Data reproduced from [3.193]

FIG. 3-37. Energy confinement versus l_i in DIII-D. The normalization basis used here is the so-called DIII-D/JET empirical scaling which accurately describes H-mode confinement in both experiments. Reproduced from [3.193] with multiple data indicated by shaded domains (typical data shown to indicate error bars)

FIG. 3-38. Energy confinement (relative to ITER89P scaling) and peak β_N in DIII-D L-mode current-rampdown plasmas. Explicitly-calculated ideal MHD ballooning limits for various l_i are also shown. Experimental and MHD stability data from [3.193] with the $\beta_N = 4l_i$ empirical scaling added here for comparison.

FIG. 3-39. Peak normalized β (from diamagnetic measurements, fast-ion pressure included) as a function of plasma internal inductance l_i as obtained in TFTR NBI-heated plasmas. β_N-l_i trajectories for two current rampdown cases are shown. The highest β_N case ends in disruption. The symbol-coded data show the peak β_N values reached (without disruption) in various current rampdown and constant-current cases. Data for 'standard' TFTR supershot plasmas are also shown. The rampdown plasmas transiently achieve higher β_N and l_i. Reproduced from [3.190], with $\beta_N = 4l_i$ and $2l_i$ empirical scalings added.

FIG. 3-40. High-n ballooning stability analysis for a TFTR current-rampdown plasma (0.85→0.4 MA). The measured pressure gradient in the outer half of the plasma is found to be close to the calculated first-stable-region pressure gradient limit (first stability boundary).

FIG. 3-41. Comparison of calculated (from the PEST stability code) and measured radial displacements for the n = 1 'infernal mode' MHD precursor that precedes disruption in TFTR RS plasmas. The mode is localized near the q_{min} radius and combines kink and ballooning instability features. The precursor growth rates are commensurate with ideal MHD. Data reproduced from [3.208].

FIG. 3-42. Density, temperature and safety factor profiles for a high-performance JT-60U RS discharge with edge safety factor $q_{95} \approx 3.5$ (from [3.216]). Note the relatively large minor radius of the reversed-shear region and the pronounced effect of the ITB on plasma core energy and particle confinement.

FIG. 3-43. MHD stability analysis for the RS discharge illustrated in Fig. 3-42. Calculations with the ERATO-J code show the presence of a coupled kink-ballooning instability that is localized around the radial position of the ITB (note that the data plotted are for the radius-weighted mode displacement $\rho\xi$, where ρ is the normalized radius derived from the flux surface volume). Reproduced from [3.216] with RS and ITB indications added.

FIG. 3-44. Normalized beta versus edge safety factor for high-l_i and RS plasma experiments (solid data symbols). Theoretical ideal MHD stability limits for proposed ITER, TPX and reactor-candidate plasmas are also shown (open symbols). Calculated beta limits for positive-shear (PS) and RS ITER cases are indicated. The corresponding β_N needed in ITER for 1.5 GW fusion power is also shown: the arrows indicate the β_N 'headroom' relative to the ideal MHD limit.

FIG. 3-45. Plasma operation domains and density limits in the ASDEX-Upgrade tokamak. Adapted from Ref. [3.222], Fig. 8. The $\bar{n}_e - P_{sep}$ trajectories for several 0.8-MA discharges with time-varying density and/or heating power are shown. The shaded region encompass the inferred domain for the L-mode phase. The high-density boundary of this domain is disruptive. The 'MARFE limit' curve within the L-mode region shows the onset density at which the divertor MARFE expands into the bulk plasma and full divertor detachment develops

FIG. 3-46. Hugill diagram for JET limiter plasmas following introduction of beryllium evaporation and a beryllium limiter [3.237]. The points show densities normalized by B_T/R achieved in plasmas with various forms of heating. The two dashed lines illustrate the density limits in earlier OH/ICRF and NBI experiments with a mainly-carbon first wall For a given q_{cyl}, the largest values of the Murakami parameter after the introduction of beryllium represent densities 30-50% beyond the Greenwald density. The tendency for the normalized limiting density to increase with power input is also shown in the data.

FIG. 3-47. Greenwald diagram for L- and H-mode plasmas in JET. Gas-fueled plasmas attained densities 30% beyond the Greenwald value with little confinement degradation, while pellet fueled plasmas reached higher densities (after [3.233]).

FIG. 3-48. Above-Greenwald pellet-fueling experiments in ASDEX-U and DIII-D.

FIG. 3-49. H-mode operational diagram for ASDEX Upgrade presented in terms of the measured electron temperature and density 2 cm inside the separatrix (this location corresponds to the top of the H-mode pedestal). Boundaries indicating different types of confinement regime are indicated [3.257]. The limiting bound of edge pressure (nT) corresponds closely to the pressure gradient for onset of ideal MHD ballooning. The 'limiting density' for H-mode operation is approximately 7×10^{19} m^{-3} (cf. the similar H-mode limit shown in Fig. 3-45). — Same as FIG. 3-31 —

FIG. 3-50. Sustained above-Greenwald H-mode operation in ASDEX-U with feedback-controlled high-field-side pellet injection fueling and 10 MW NBI heating (from [3.258]).

FIG. 3-51. Soft X-ray tomographic reconstruction of the development of a major disruption in T-10. Contours of equal SXR emission; high-emission region diagonally shaded. Frames A-F (at 60 μs intervals): m = 1 precursor growth; frames G-L (Δt = 830 μs total, interval varies): m = 2 mode growth; frames M-T (Δt = 230 μs total, interval varies somewhat): m = 1 and m = 2 modes coalesce and 'cold' bubble enters plasma column (frame T).

FIG. 3-52. Typical disruption in JET (ohmic plasma). The slow and fast phases of the thermal quench, the ensuing positive current rise and negative voltage spike and the subsequent onset of the current quench are shown. Precursor growth occurs during a period that may extended from up to 100 ms before thermal quench [3.230]. Note that the zero of the plasma current axis is suppressed: only the first part of the current quench is shown

FIG. 3-53. Disruption frequency versus effective safety factor ($q_{eff} \approx 1.25\ q_{95}$) in JT-60U. Only disruptions during current flattop are included. A wide range of experiments and plasma parameters are included in the data set. Data and analysis courtesy of R. Yoshino on behalf of the JT-60 Team

FIG. 3-54. Thermal quench times $\tau_{1\text{-}2}$ (delay between initial and final quench) and τ_2 (fast quench) for various tokamaks, plotted as a function of plasma minor radius. Extrapolation to ITER (a = 2.8 m) yields $\tau_{1\text{-}2} \approx 20$ ms and $\tau_2 \approx 1$ ms.

FIG. 3-55. Plasma current and thermal energy and inner divertor target power and cumulative thermal energy during a disruption (pulse 6134) in ASDEX-U. In this example, about 20% of the initial plasma thermal energy reaches the inner target at the end of the thermal quench. The remainder of the target energy comes from the dissipation of magnetic energy in the current quench, which is accompanied by a VDE (vertical motion toward the divertor). The authors conclude in this example that there is significant loss of plasma thermal energy by radiation upstream of the divertor. Data courtesy of O. Gruber for the ASDEX-U Team

FIG. 3-56. Toroidal asymmetry ratio, inboard/outboard divertor target ratio and total energy accountability (referenced to plasma thermal energy) in various DIII-D single-null divertor disruptions and VDEs. The horizontal arrangement of the data within the four groups is for presentation purposes only and has no significance. Data and analysis by A. Hyatt, C. L. Lasnier, R. L. Lee, A. Kellman

FIG. 3-57. Time-average current quench times (for ΔI_p = 60 %) divided by plasma cross section area versus plasma current density before disruption. The normalized quench times for three electron temperatures as inferred from a simple radiative power balance model are compared with the experimental data.

FIG. 3-58. Histogram of current quench times (100% linear decay) derived from 80%-20% and 90%-10% current thresholds in Alcator C-Mod. Current magnitudes are measured relative to the initial before-disruption plasma current. Data and analysis by R. Granetz

FIG. 3-59. (a) (a) Upper figure: Magnetic flux reconstructions at 0.6-ms intervals during a disruption and subsequent vertical displacement in Alcator C-Mod. The arrows show the poloidal projection of halo current flow. The halo circuit in the plasma scrape-off actually follows a helical path, in order to be force-free. (b) Lower figure: Plasma current, vertical motion, and in-vessel halo currents in the upper and lower portions of the vacuum vessel wall. In this example of a downward-going displacement, halo current in the upper portion of the vessel is essentially zero.

FIG. 3-60. Measured vertical disruption forces in ASDEX-U compared with the product of maximum halo current (measured) and toroidal field. The mean slope of the data implies an effective in-vessel halo current flow length of about 0.4 m ($\sim 0.8a_o$). The toroidal conductivity of nearby in-vessel components is negligible, so in this case, halo current provides the entire vertical stabilizing force on the plasma.

FIG. 3-61. Peak total halo current ($I_{h,max}$) versus pre-disruption plasma current (I_{p0}) for disruptions in various elongated tokamaks. The data is for plasmas with vertical elongation $1.5 \le \kappa_X \le 2.0$, where κ_X is the elongation at the separatrix.

FIG 3-62. Halo current density measured at 10 toroidal locations around the Alcator C-Mod divertor: (a) A relatively peaked `filament' of halo current is seen to rotate twice around the torus. (b) The same data plotted in a different manner, showing the predominantly n = 1 structure of the toroidal asymmetry.

FIG. 3-63. Halo currents in the Alcator C-Mod divertor structure (ten electrically-isolated decants) at three 100-μs intervals near the time of maximum halo current. Halo current at a given time is largely localized within 4 of the 10 decants. The TPF varies between 2.5 and 3.8. The distribution rotates toroidally at a frequency of 1.4 kHz

FIG. 3-64. Toroidal peaking of halo currents in various tokamaks, for plasmas with $1.5 \le \kappa_X \le 2$. High peaking factors occur only at low halo current fraction. The hyperbolic curves show limiting bounds for the data. The bounds in the various tokamaks on the normalized maximum halo current at $q_{95} = 3$ derived from the data in Fig. 3-61 are also shown.

FIG. 3-65. Plasma disruption leading to runaway conversion in JET [3.293]). Loss of plasma thermal energy (fall in soft X-ray emission), onset of runaway conversion (current plateau at 1 MA) and subsequent onset of quasi-continuous runaway losses (indicated by sustained hard X-ray emission) are shown. Equilibrium control is maintained following conversion and the 1-MA runaway discharge persists for several seconds. Note the suppression of the current waveform zero

FIG. 3-66. Avalanche production of runaways during the flattop phase of a low-density TEXTOR discharge (from [3.301]): synchrotron emission intensity (infra-red wavelengths, λ = 3-8 μm) and plasma line-average density. The initial quasi-exponential growth of runaway content (indicated by the IR intensity) and subsequent reduction in growth rate following a plasma density increase are evident. The synchrotron radiation spectrum shows that the maximum runaway energy is about 20 MeV

FIG. 3-67. Runaway conversion in a simulated ITER “disruption” (actually a fast plasma shutdown obtained with 1% Xe injection, [3.297]). The initial rate of thermal

current decay corresponds to ~300 ms decay time. Onset of appreciable avalanche growth at 100 ms (I ~12 MA) results in the prompt conversion of the remaining plasma current to runaway current. The final magnitude of current conversion is only weakly sensitive to assumptions about the initial seed runaway number, initial current quench rate and so forth

FIG. 3-68. Runaway generation in JT-60U versus normalized fluctuation amplitude $\widetilde{B}_{r\ n=1}/B_t$ and current quench rate (from [3.304]). In the shaded region no runaways are observed either with or without excitation of the DCW (external helical field) coil. Use of the DCW expands the runaway-free domain (see mitigation discussion in text below)

FIG. 3-69. Plasma equilibrium evolution during an ITER VDE with runaway conversion, as simulated with DINA dynamic equilibrium code. The well-known tendency for upward-going VDEs to impact on a limited portion of the upper-inboard first wall is clearly shown. In this case, the termination phase of the VDE is a 10-MA runaway current channel. Simulation data courtesy of V. Lukash and R. Khayrudinov

FIG. 3-70. Fast plasma shutdown in a beam-heated JT-60U plasma [3.130]. Ne pellet injection produces rapid radiation of the plasma thermal energy and a non-disruptive current quench. The hard X-ray emission indicates that runaway electrons are produced during the current quench (see §3.4.4).

FIG. 3-71. Calculated penetration of solid krypton pellets into a high-temperature (ignited burn) ITER plasma (a = 3.0 m, reproduced from [3.319]).

FIG. 3-72. Disruption and pellet-injection fast shutdown in ASDEX Upgrade. Fast shutdown (Ne pellet) results in reduced vessel vertical force (inferred from the measured halo current) and absence of significant thermal quench loading on the divertor. Note also the absence of a positive plasma current spike and reduction of the divertor target heating associated with the current quench.

FIG. 3-73. Halo current data for DIII-D VDEs (vertical control disabled) and pellet shutdown (also with control disabled). Datum points show peak normalized halo current magnitude and TPF (see §3.4.3) at time of maximum halo current; typical trajectories (versus time during the current decay) of I_h/I_{p0} and TPF for VDE and Ne pellet VDE are also shown. Pellet-injected VDEs have lower halo current magnitude and toroidal asymmetry.

FIG. 3-74. Direction of plasma axis motion in after-disruption VDEs in JT-60U versus initial vertical position of the magnetic axis and current quench time (from [3.323]). The angles referred to in the Figure legend give the direction of the initial axis motion: 0° = radially outward, 90° = vertically upwards, etc. Plasmas with initial position ~10 cm above the midplane exhibit passive neutral stability for quench times in the 5-25 ms range. Compare with Fig. 3-75.

FIG. 3-75. Calculation with a TSC model of the initial displacement of the JT-60U plasma magnetic axis 1 ms after a simulated thermal quench [3.332]. The initial position Z_o of the plasma magnetic axis before the quench is varied relative to the machine midplane (Z = 0). The field index parameter n chosen for the modeling results in a plasma with an initial elongation of about 1.6. The neutral point is about 10 cm above the midplane (*cf.* data in Fig. 3-74)

FIG. 3-76. Thermal and current quench durations for fast plasma shutdown in ITER with various quantities (masses in g) and species (xenon, beryllium and deuterium) of injected impurity. From simulation data in [3.297], presented to show the effect of after-injection density increase. The relative magnitude of the resulting runaway (RA) conversion is shown by the width of the shaded umbra that surrounds the lines joining the datum points for each species. The predicted density enhancement threshold for unconditional runaway avoidance ('No RA', see §3.4.4), the limit on maximum current quench duration set by VDE/halo-current mitigation (see §3.4.4) and the limit on minimum thermal quench time set by first-wall surface melting(see text above) are indicated.

FIG. 3-77. Neural-net disruption prediction in DIII-D. After training, the neutral net successfully predicts the β_{Na} at which disruption occurs in plasmas in which the disruption threshold is not well-described by β_{Na} = constant. Here β_{Na} is an on-line signal that provides a relative measure of the normalized total beta (Troyon coefficient). Depending on the threshold basis chosen, a 'look-ahead' time ≥ 100 ms for prediction of an impending disruption is achieved.

FIG. 3-78. 'Prediction' of a beta-limit disruption in TFTR. Actual β_N and calculated MHD stability limit critical β_N (defined at r/a = 0.33) for a selection of non-disrupting TFTR supershots (open data symbols, time and pressure profile vary over the data set, critical β_N obtained by off-line MHD stability calculation) and comparison of the calculated and actual β_N for Shot #76778, a high-performance DT pulse, which disrupted upon reaching the 'predicted' stability limit.

FIG. 3-79. Plasma control autonomy and disruption avoidance during an ASDEX-U discharge. Corrective actions ('repair procedures', in this case reduction of the injected neon) taken by the control system upon detection of loss of HRH mode (high-radiation H-mode) allow the mode to be recovered. The disruption that would have otherwise occurred is avoided.

FIG. 3-80. Disruption and disruption-related effects (schematic)

FIG. 3-81. Integrated disruption model schematic with basic and optional modeling elements. Major interactions in the model are identified (see text below) but the interactions shown are not intended to be exhaustive

FIG. 3-82. Plasma configuration and toroidal current for a slow VDE in ITER. TSC simulation model. Compare with the configuration evolution for the Alcator C-Mod 'vertical disruption' shown in Fig. 3-59, Section 3.4.3

FIG. 3-83. Plasma, torus vacuum vessel (VV) and backplate (BP) toroidal currents and in-vessel poloidal halo current and axial (Z) force for the slow ITER VDE shown in Fig. 3-82. Compare with the current waveforms for the Alcator C-Mod VDE shown in Fig. 3-59, Section 3.4.3

FIG. 3-84. Halo current magnitude and current decay time versus plasma temperature and halo temperature (= T_{core} or $T_{core}/2$), as obtained in DINA simulations of upward-going ITER VDEs. The minimum projected ITER current quench duration of 50 ms corresponds for these two halo assumptions to core temperatures of 3 and 4.5 eV (consistent with impurity radiation cooling, see §3.4.2) and corresponding peak in-

vessel halo currents of about 1.6 MA and 1.2 MA. The tendency of peak halo current to increase with higher core and/or halo temperature (and hence also with increasing current quench duration) is clearly shown.